Lasse Løvstakken

# Signal processing in diagnostic ultrasound: Algorithms for real-time estimation and visualization of blood flow velocity

Doctoral thesis
for the degree of Philosophiae Doctor (PhD)

Trondheim, February 2007

Norwegian University of Science and Technology
Faculty of Medicine
Department of Circulation and Medical Imaging

# Signalbehandling i diagnostisk ultralyd: Algoritmer for sanntids fremstilling av blodstrøm

Lasse Løvstakken

**Bakgrunn:**
Ultralyd fargedoppler er en medisinsk avbildningsmodalitet som viser blodets hastighet og retning i et to- eller tredimensjonalt område i kroppen, hvor unormal blodsstrøm kan oppdages og undersøkes. Metoden har vist seg svært nyttig ved diagnose av sykdom som manifesterer seg i hjerte- og karsystemet, for eksempel ved deteksjon og gradering av hjerteklafflekkasjer, eller ved gradering av forsnevringer i arterier grunnet plakk og avleiringer. Begrensninger i dagens dopplerbaserte metoder gjør at informasjonen som fremstilles kan være vanskelig tilgjengelig og upålitelig.
I denne avhandlingen undersøkes det om mer avanserte signalbehandlingsmetoder kan benyttes for å oppnå en mer nøyaktig og brukervennlig fargedoppleravbildning, med et overordnet mål om en økt diagnostisk sikkerhet i klinikk ved bruk av denne avbildningsmodaliteten.

**Resultater:**
En viktig del av databehandlingen i fargedoppler består av å skille det svake blodsignalet fra omliggende vevssignal. En ny algoritme er i denne avhandlingen beskrevet for å adaptivt skille ut blodstrømssignalet selv i vanskelige forhold med kraftig vevsbevegelse. Algoritmen kan taes i bruk i dagens systemer, og vil for eksempel kunne bedre ikke-invasive undersøkelser av blodstrøm i kransarterier.
Videre er et simuleringsstudium utført, hvor en alternativ metode for estimering av blodstrømshastighet basert på statistisk modellering er undersøkt. Det vises her at slik modellbasert estimering vil kunne gi mer nøyaktige målinger av blodstrømshastighet, spesielt når hastigheten er lav som ved avbildning av små blodkar.
Dagens dopplerbaserte metoder er begrenset til bare å kunne måle blodets hastighetskomponent langs ultralydstrålen. En ny metode for sanntids visualisering av blodets bevegelse i en vilkårlig retning i ultralydbildet er her beskrevet. Den nye metoden kan gi en mer riktig og intuitiv fremstilling av de faktiske blodstrømsforhold. Den kliniske nytten av den nye metoden er videre undersøkt i fire forskjellige kliniske applikasjoner, hvor det vises at den mer detaljerte retningsinformasjonen som er tilgjengelig kan gi en økt diagnostisk sikkerhet sammenliknet med tradisjonell fargedoppler.

*Overnevnte avhandling er funnet verdig til å forsvares offentlig for graden philosophiae doctor (PhD). Disputas finner sted i auditoriet, medisinsk teknisk forskningssenter, mandag 19. februar 2007, kl. 12:15*

# Abstract

Ultrasound Color Flow Imaging (CFI) has become a valuable tool in a wide range of medical applications where information about blood flow can be related to the diagnosis of disease, as for instance in the cardiovascular system. The modality provides a map of blood velocity and direction in a two- or three-dimensional region of interest, where abnormal blood flow patterns can be detected and investigated.

The work presented in this thesis is devoted to the development of CFI signal processing for improved estimation and visualization of blood velocity. The thesis consists of three technical contributions, and one chapter describing preliminary clinical and experimental results of using one of the methods described. The different contributions are written in article form and can be read individually. A thorough background chapter is also included to introduce the unfamiliar reader to concepts and challenges present in ultrasound imaging and CFI specifically.

Two thesis chapters address the problem of separating the weak signal from blood in CFI, typically dominated by signal from surrounding tissue. In chapter three, an adaptive filter approach for the removal of this clutter signal prior to velocity estimation is described. An adaptive filter algorithm suitable for real-time performance is developed, and shown to provide satisfactory results even in excessive tissue clutter conditions. In chapter four, a different approach for dealing with the clutter signal is described. Assuming the statistical properties of the clutter signal known, we analyze the properties of maximum likelihood estimation (MLE) of blood velocity, compared to conventional methods. We further address issues related to the practical implementation of this model-based estimation scheme.

A technique for the visualization of the two-dimensional blood velocity vector has previously been introduced. In chapter five, the real-time implementation of this technique, called Blood Flow Imaging (BFI), is described and evaluated. The method is not limited by angle-dependency or velocity aliasing as conventional CFI, and is shown to have potential within different imaging contexts. Finally in chapter six, clinical and experimental pilot studies are described where the potential of the BFI modality has been investigated. It is shown that BFI can provide a more detailed and intuitive image of flow conditions, that can be beneficial in both vascular and cardiac applications when the blood flow direction plays a major role. Through the investigations, practical restrictions and potential improvements of the current implementation have also been mapped.

# Preface

This thesis is submitted in partial fulfilment of the requirements for the degree of PhD at the Norwegian University of Science and Technology (NTNU). The research was funded by the Research Council of Norway (NFR), and was carried out at the Department of Circulation and Medical Imaging, NTNU. The main supervisor has been Professor Hans Torp, and co-supervisor has been Professor Rune Haaverstad, both from the Department of Circulation and Medical Imaging, NTNU.

**Acknowledgements**

Several people have been involved in the thesis work presented and deserve my gratitude. First of all, I would like to give my respect to my supervisor, Professor Hans Torp. His creative mind and profound knowledge of ultrasound imaging has been a source of inspiration and confidence throughout the course of the thesis, and he has always been supportive and encouraging. I would also like to thank my co-supervisor Professor Rune Haaverstad for his genuine interest in my work, and for a rewarding cooperation.

Further I would like to express my gratitude towards all co-authors who have contributed to the results in the thesis, and especially to Steinar Bjærum for his contributions throughout the project period. My clinical investigations have been inspiring, and have involved several people. I want to thank Siri A. Nyrnes and Bjørn O. Haugen, Nicola Vitale and Khalid Ibrahin, Frank Lindseth and Geirmund Unsgaard, and Agnar Tegnander. I would also like to thank the people at GE Vingmed Ultrasound for always being available for questions and support. My fellow colleagues and friends at the Department of Circulation and Medical Imaging have contributed both socially as well as academically.

Finally, I would like to thank my family for their unconditional love and support, and my dear Hanne for her love and encouragements.

Trondheim, December 12, 2006

Lasse Løvstakken

# Table of Contents

# Chapter 1

# Introduction

Lasse Løvstakken
Dept. Circulation and Medical Imaging, NTNU

The concept of diagnostic ultrasound imaging is about the use of ultrasonic pressure waves to image the human interior for diagnostic purposes. Today's ultrasound imaging systems provide physicians with valuable tools for investigating abnormalities related to the human anatomy, physiology, and hemodynamics, and are used routinely in diagnosis in a range of clinical contexts [1, 2]. Ultrasound imaging is a non-invasive technique without any known harmful effects [3–5], and provides images of both soft tissue and blood flow at a high imaging frame rate.

Systematic investigations of using ultrasound for imaging began in the late forties [6, 7], and many research teams have since then been involved in the technical development leading to today's real-time imaging equipment. Important fundamental research have been performed in areas of acoustics, piezo-electric material technology and transducer design, electronic circuits and digital technology, and statistical signal processing [8–12]. Engineers have worked in close collaboration with clinicians, who have adopted the new experimental techniques for clinical use [13–16]. It is this combined effort of extensive research in both the technical and clinical community that has pushed the development to where we are today.

One of the most important developments since the beginning of ultrasound imaging research, has been the introduction of Doppler ultrasound systems for measuring blood flow velocity. The first systems appeared in the sixties and through the seventies [17–21], and the clinical foundation rationalizing its use as a noninvasive diagnostic tool was established by the late seventies and early eighties [22–27]. Since its introduction, a continuous development has extended the functionality of ultrasound Doppler instruments. One of the most successful technologies to appear has been color flow imaging (CFI) systems. The CFI modality allows for the investigation of blood flow velocity and direction in a distributed region of interest [28, 29], and is today used in a wide range of clinical applications where information about blood flow can be related to the diagnosis of disease. Estimated blood flow velocities and directions are encoded in different colors and superimposed on a B-mode image of the anatomy, where areas of abnormal flow related to pathology can be located and investigated.

Real-time systems offering CFI were introduced in the mid-eighties [30, 31].

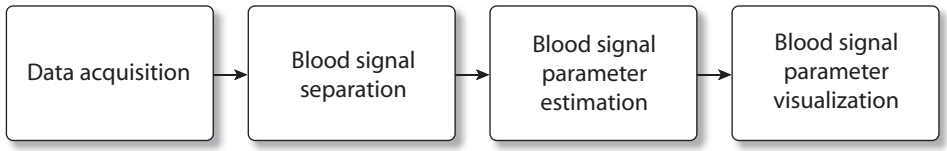


Figure 1.1: Building blocks of CFI processing.

Since then, general developments in ultrasound technology and research efforts have improved the modality in terms of an increased sensitivity and frame rate, and with regards to signal processing algorithms. However, the estimation of blood velocity in CFI is a challenging task. Issues related to conventional estimation schemes [31] limits the diagnostic value of CFI in many clinical contexts. Further, although quantitative Doppler measurements are obtained, the use of CFI is arguably qualitative, used mostly for the visual detection and evaluation of abnormal flow patterns. Improved CFI performance may be gained by using more sophisticated signal processing, which could increase the diagnostic confidence in clinical evaluations and also the quantitative use of CFI in the future. Due to the rapid increase of computational power in recent years, this goal should now also be feasible while retaining the real-time operation associated with ultrasound imaging.

The thesis work presented in upcoming chapters is dedicated to the task of improving CFI algorithms for blood flow detection, velocity estimation, and visualization. In the following sections the motivation behind the thesis work will be given in more detail, the aims of the study will be formalized, and summaries of the thesis contributions will be presented. A certain degree of knowledge about ultrasound imaging and specifically CFI is assumed. However, more detailed background information of these concepts and references for further reading is included in Chapter 2.

## 1.1 Motivation and problem formulation

In color flow imaging the velocity and direction of blood flow is estimated in a distributed region of interest, i.e., for multiple range gates in depth and in several beam directions. The CFI acquisition is based on a pulsed-wave approach, and the information available for processing is the received Doppler-signal sampled through several pulse emissions. It is not practical to estimate the complete Doppler spectrum for each spatial position, and parameters reflecting the properties of the spectrum are instead estimated from the received signal and encoded in colors on display. Typically, the mean signal power, and the mean frequency and bandwidth of the Doppler signal is estimated. To obtain a frame rate sufficient for following the dynamics of the flow in the cardiovascular system, few temporal samples (8-16) are available for processing. This fact makes the detection of blood and estimation of blood velocity a challenge.

The building blocks of CFI processing is shown Fig. 1.1. After data acquisition, 8-16 temporal samples are available for each range gate. These signal vectors are first

processed to isolate the signal from blood, before the blood signal spectrum parameters are estimated and further visualized using a color scheme on display. Several aspects of this processing scheme needs to be addressed.

At the signal separation stage, the temporal signal vectors received at each range gate are high-pass filtered to remove the dominating signal from surrounding tissue, present due to reverberations and beam sidelobes [32, 33]. Conventional filters may not provide a sufficient separation when the tissue velocity approaches the blood velocity range of interest. This could happen due to excessive muscle contractions such as for the myocardium, due to the movement of the vessel wall in response to an incoming flow pressure pulse, and due to a relative movement of the ultrasound probe and patient. When imaging peripheral vessels with low velocity blood flow, this problem may become severe. An inadequate separation of the blood signal will add a signal dependent bias to subsequent velocity estimates, and may cause visible artifacts in the image from falsely colored tissue regions.

At the blood velocity estimation stage, an autocorrelation approach is usually employed to estimate the mean signal power, and the mean frequency and bandwidth of the Doppler signal [31]. The autocorrelation method (ACM) is limited in several aspects. The method is based on phase-shift information, and aliasing artifacts will occur when the movement of blood scatterers between pulse acquisitions correspond to a phase-shift of more than $\pm\pi$ radians. This problem frequently obscures the velocity information in CFI. The autocorrelation approach does further not utilize the full bandwidth information available in the received signal. By exploiting the wideband nature of ultrasound pulsed-wave imaging, velocity estimates with a lower variance and beyond the Nyquist limit may be obtained [34–37]. The autocorrelation method can also only estimate the axial velocity component of blood, leading to angle-dependent estimates where the actual blood direction must be interpreted based on a priori information of the angle between the ultrasound beam and vessel of interest. Despite that alternative estimation schemes have been proposed, the autocorrelation method has remained the algorithm of choice in commercial CFI systems. This is partly due to its low computational demands and robustness in poor signal-to-noise conditions.

At the visualization stage, the Doppler spectrum parameters are encoded using a color table for display. Due to the limitations of the velocity estimation algorithm used, the parametric color image may be prone to misinterpretation due to angle-dependencies and aliasing artifacts. Further, for each image point a decision is made if the gray-scaled tissue image or colored flow image is to be displayed. This arbitration approach is usually necessary to cover for artifacts resulting from an inadequate signal separation, but may also limit the visualization of low-velocity flow in smaller vessels.

A more in-depth review of the limitations in conventional CFI processing from a method perspective is given in Chapter 2. From the user point of view, the main artifacts encountered in CFI as a result from its limitations are *flashing artifacts*, *angle-dependency artifacts*, *aliasing artifacts*, and *color blooming*. These artifacts are best described through an example. A color flow image of the carotid bifurcation is shown in Fig. 1.2, taken at the time of the systole. Blood flow from the common carotid artery divides into two branches, one branch supplying blood flow to the brain called the internal carotid artery, and one branch supplying blood flow to the face called

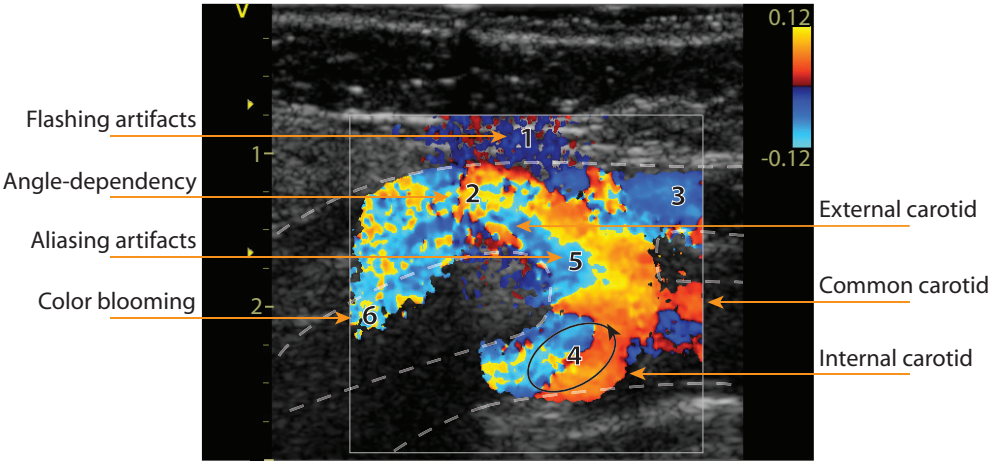


Figure 1.2: A color flow image of the carotid bifurcation, taken at the time of the systole. Different artifacts caused by limitations of the conventional CFI algorithms have been indicated to the left of the image.

the external carotid artery. The color scale in the upper right corner of the image indicates that blood flow directed upwards, towards the transducer, is represented by colors from red to yellow for an increasing velocity magnitude, while flow directed downwards, away from the transducer, is represented by colors from blue to cyan. The color image is displayed on top of a gray-scaled image of the anatomy. Artifacts present due to the limitations of the conventional algorithm are indicated to the left of the image. In the following, a brief explanation of the different artifacts and their consequences for the example in Fig. 1.2 will be given.

**Flashing artifacts:** These artifacts may occur due to an inadequate attenuation of the tissue clutter signal when separating the blood flow signal. Clutter signal present after filtering may then be falsely colored in the resulting image. The term flashing artifacts is used because the artifacts appear suddenly, and are typically only present in parts of the cardiac cycle. Flashing artifacts may confuse the physician, and may also conceal important flow information. In Fig. 1.2, these artifacts can be observed in the area marked 1, and are in this case introduced when the vessel wall moves in response to the incoming flow pressure pulse.

**Angle-dependency artifacts:** These artifacts occur because the current estimation algorithm only measure the axial blood velocity component. This leads to color images that are prone to misinterpretation, and that may conceal important information about the presence of eddies and turbulence. In Fig. 1.2, the impact of angle-dependency artifacts is visible in several areas of the flow image. In the area marked 2, flow in the external (upper) branch of the carotid artery changes direction compared to the ultrasound beam. The corresponding change

in the sign of the axial velocity component measured then also changes the color displayed in the image. The absence of lateral flow information is further visible in the area marked 3, a smaller branch of the artery. Although colored in blue indicating a direction downwards, it is difficult to see how the vessel itself is angled compared to the ultrasound beam, and therefore some uncertainty as to what direction the blood actually flows. Even further, there is a stenosis at the beginning of the internal (lower) branch of the example carotid artery, just right to the area marked 4. This stenosis induces a flow eddie not clearly visualized by the axial velocity component alone. For the given example, the color region of the flow eddie might equally well be interpreted as an aliasing artifact.

**Aliasing artifacts:** These artifacts occur when the velocity of the blood scatterers are above the maximum limit determined by the sampling rate of the Doppler signal, i.e., the pulse repetition frequency. Velocity magnitudes above the maximum measurable will wrap around the velocity scale and be visualized with a false velocity value. In Fig. 1.2, aliasing artifacts can be observed in the area marked 5, in the flow going to the external (upper) branch of the carotid. This flow region is colored in both red and blue colors indicating different flow directions, although one uniform direction of flow is present. Comparing the aliasing region to the flow eddie region in 4, one can observe the confusion aliasing artifacts can make.

**Color blooming artifacts:** These artifacts occur due to the limited spatial resolution of ultrasound imaging, which leads to a fundamental overlap between blood and tissue signal in certain areas of the image. This problem is further aggravated when the spatial resolution in the flow image is reduced to achieve a sufficient sensitivity. When the flow and tissue images are combined, the color image may cover immediate tissue such as vessel walls. In Fig. 1.2, color blooming can be observed in the area marked 6.

In summary, current limitations in conventional CFI may lessen its diagnostic value and complicate its use in the clinic.

## 1.2 Aims of study

The aims of this thesis work will now be presented and formalized. Starting in general terms, the overall aim of this work is to address shortcomings of the conventional color flow imaging modality, and to look for solutions to make the modality more accurate and accessible with less demands for image interpretation. Further, a secondary aim is to focus on solutions suitable for real-time performance. Refering to the CFI block diagram in Fig. 1.1, improvements can certainly be conceived at all processing stages shown. In this work, the scope has been restricted to the latter three stages covering blood signal separation, and blood velocity estimation and visualization. Several important topics of research are therefore not pursued in this work. Two examples of improved data acquisition in CFI could be the development of new pulsing strategies

for increased frame rate, and the use of coded excitation for increased sensitivity while retaining spatial resolution when imaging peripheral vessels. Such improvements would in general be beneficial for subsequent signal processing.

Important progress have been made in the signal separation stage in recent years, where the use of adaptive signal processing have received increased attention. Adaptive clutter filters have shown potential for more properly removing the tissue clutter signal even in excessive clutter conditions [38, 39]. This work is continued here, and is considered as one of the main topics of the thesis. At the velocity estimation stage, several new estimators have been proposed since the presentation of the original real-time autocorrelation algorithm. Both improved axial one-dimensional as well as two-dimensional velocity vector estimators have been proposed [34–37, 40–42]. In this study, we investigate the topic of improved axial velocity estimation as well as two-dimensional velocity estimation and visualization. The latter is considered the second main topic of the thesis. The final formalized aims of the thesis study now becomes:

**Aim 1:** Address current limitations of blood signal separation in color flow imaging, and specifically the use of adaptive signal processing for this purpose.

**Aim 2:** Address limitations of blood velocity estimation in color flow imaging, and specifically solutions for the determination and visualization of the full velocity vector.

**Aim 3:** Address solutions suitable for real-time performance.

## 1.3 Summary of presented work

In the following subsections, a summary of the original contributions of the thesis work will be presented. The thesis consists of four original contributions as listed in Table 1.1, three technical papers and a chapter containing preliminary results from clinical collaborations. Of the technical papers, two have been published, and one is in press for publication in an international peer-reviewed journal. The clinical collaboration work includes a series of pilot studies performed to investigate the clinical value of the new real-time blood flow imaging technique described in one of the technical papers included (Chapter 5). The results from the clinical collaborations will be submitted for publication in peer reviewed clinical journals in the near future. Extended abstracts of each thesis contribution will now be given.

**Contribution no. 1: (chapter 3)**
**Real-time adaptive clutter rejection filtering in color flow imaging using power method iterations**

Lasse Løvstakken[1], Steinar Bjærum[2], Kjell Kristoffersen[2], Rune Haaverstad[1], and Hans Torp[1]
[1] Dept. Circulation and Medical Imaging, NTNU
[2] GE Vingmed Ultrasound, Horten, Norway

The received ultrasound signal from blood flow is dominated by a clutter signal component from surrounding tissue. This clutter signal is present in vessel lumens due

**Table 1.1: Original contributions in thesis**

| # | Chapter | Contribution title | Topic | Publication status |
|---|---|---|---|---|
| 1 | 3 | Real-time adaptive clutter rejection in color flow imaging using power method iterations | Blood signal separation | Published Sept. 2006 |
| 2 | 4 | Optimal velocity estimation in color flow imaging in presence of clutter | Blood signal separation | Accepted for publication Oct. 2006 |
| 3 | 5 | Blood Flow Imaging - A new real-time 2-D flow imaging technique | Blood velocity estimation and visualization | Published Feb. 2006 |
| 4 | 6 | Clinical applications of BFI | Blood velocity estimation and visualization | Unpublished work |

to reverberations, beam sidelobes, and also the thickness of the ultrasound imaging plane. The clutter signal can be as high as 50-80 dB in signal power compared to that of blood flow, and must be accounted for to be able to properly estimate the blood flow parameters such as blood signal power, velocity, and velocity spread. Otherwise, a false detection of blood flow and biased flow parameter estimates will result. The art of removing the tissue clutter signal is referred to as clutter rejection, and is in normal cases of tissue movement removed from the received signal by a conventional finite impulse response (FIR), infinite impulse response (IIR), or polynomial regression high-pass filter prior to velocity estimation [32, 33]. However, when the tissue movement becomes excessive such as when imaging the beating heart, conventional high-pass filtering does not provide sufficient clutter attenuation. It may also be desired to image the slowly moving flow present in peripheral vessels. When the tissue velocity becomes comparable to that of blood flow however, it becomes more difficult to separate the blood flow signal using conventional filters. More advanced clutter filtering algorithms are therefore needed that can remove the clutter signal component in normal as well as more excessive cases of tissue movement.

In this paper we propose a new algorithm for real-time adaptive clutter rejection filtering in ultrasound color flow imaging. The algorithm is based on regression filtering using eigenvectors of the estimated signal correlation matrix as a basis for representing the clutter signal. This method has previously been proposed by other authors [38, 39], but has been considered to suffer from drawbacks that lessen its practical value. It has been considered too computationally demanding for real-time processing in general CFI applications, and further not been considered sufficiently robust with regards to filtering the various mixtures of blood and tissue signal present throughout the image.

We show that it is feasible to implement the algorithm using today's desktop

computers by the iterative power method for eigenvector estimation. We further introduce a new adaptive algorithm for selecting the proper order of the filter, needed to make the technique sufficiently robust in all image regions. Background theory of the method and the filter algorithm is presented in detail, and the filter algorithm performance and computational demands is compared to that of FIR, IIR, and polynomial regression filtering. Examples are also included which confirms that by adapting the clutter rejection filter to estimates of the clutter signal statistics, an improved attenuation of the clutter signal can be achieved in normal as well as more excessive cases of tissue movement.

*This paper was published in the IEEE Transactions on Ultrasonics, Ferroelectrics, and Frequency Control, vol. 52, no. 9, Sept. 2006. It is presented in its original form.*

**Contribution no. 2: (chapter 4)**
**Optimal velocity estimation in ultrasound color flow imaging in presence of clutter**

Lasse Løvstakken[1], Steinar Bjærum[2], and Hans Torp[1]
[1] Dept. Circulation and Medical Imaging, NTNU
[2] GE Vingmed Ultrasound, Horten, Norway

In color flow imaging (CFI), the rejection of tissue clutter signal has been treated separately from blood velocity estimation, by high-pass filtering the received Doppler signal. However, the small number of temporal samples available results in high-pass clutter filters with a long transition band in order to achieve sufficient stop band attenuation. The complete suppression of the clutter signal is therefore difficult to achieve without affecting the subsequent velocity estimates, and this often leads to suboptimal performance [32]. The aim of this work is to provide new insight into the potential of using more advanced estimation schemes, and specifically more advanced methods of dealing with the tissue clutter signal. A different approach to velocity estimation is investigated based on statistical modeling.

Simulations were setup to investigate how a maximum likelihood estimation (MLE) scheme including statistical models of both clutter and blood compared to the conventional technique of clutter filtering before using the autocorrelation method (ACM) for blood velocity estimation. Based on simplified models of the signal from clutter and blood, an analytic expression for the Cramer-Rao lower bound (CRLB) was found, and used to determine the existence of an efficient maximum likelihood estimator of blood velocity in CFI when assuming full knowledge of the clutter statistics. We further simulated and compared the performance of the MLE to that of the ACM using finite impulse response (FIR) and polynomial regression clutter filters. Two signal scenarios were simulated, representing realistic signals received when imaging a central and peripheral vessel respectively.

Simulations showed that an efficient MLE did not exist for practically usable packet sizes ($< 16$). However, by including 3-9 independent spatial points, the MLE variance

approached the CRLB in both scenarios. On the other hand, using an equal amount of averaging, the ACM was approximately unbiased only for the central scenario, and then only in the clutter filter pass band with a variance of up to four times the CRLB. The ACM suffered from a severe bias in the filter transition region in both scenarios, and a significant performance gain was here achieved using the MLE.

For practical use, the clutter signal properties needs to be estimated from the received signal. We finally replaced the known clutter statistics with an estimate obtained from low-rank approximations of the sample correlation matrix. Used in the model-based framework, this method came close to the performance of the MLE, and may be an important step towards a practical model-based estimator including tissue clutter with optimal performance.

*This paper has been accepted for publication in the IEEE Transactions on Ultrasonics, Ferroelectrics, and Frequency Control, Oct. 2006. It is presented in its original form.*

**Contribution no. 3: (chapter 5)**
**Blood Flow Imaging - A new real-time 2-D flow imaging technique**

Lasse Løvstakken[1], Steinar Bjærum[2], Ditlef Martens[2], and Hans Torp[1]
[1] Dept. Circulation and Medical Imaging, NTNU
[2] GE Vingmed Ultrasound, Horten, Norway

One of the major shortcomings of conventional color flow velocity estimation schemes is the limitation of only being able to measure the axial velocity component. The lateral component of the flow may contain important information about the hemodynamics of the flow, for instance of turbulence and eddie formation. By not giving the complete picture of the flow conditions, the display of current color flow imaging is therefore lacking and prone to misinterpretation. Quite some research have been put into finding alternative methods capable of determining the full velocity vector, but none have yet proved sufficiently robust for clinical use, and are still considered experimental.

In this work a new method that successfully visualize both the axial and lateral flow velocity component in real-time is presented. Due to its ability to portrait the complete image of the actual flow in a non-parametric way, the method has been named Blood Flow Imaging (BFI). The BFI modality relies on the preservation and display of the speckle pattern originating from the blood scatterers. The movement of this speckle pattern is correlated to the movement of the blood scatterers for short time periods. By using beam interleaving techniques, smaller sub-images are acquired at a frame rate equal to the pulse repetition frequency (PRF), capturing the speckle movement. The blood signal speckle pattern images are produced by B-mode processing high-pass filtered signal packets from a given sample volume. An amplitude normalization procedure is needed to compensate for the mean power variation between packets. By displaying subsequent speckle pattern images acquired at the PRF in slow motion, the blood flow can be visually tracked from frame to frame.

BFI is a qualitative technique, as no attempt is made to measure the full velocity

vector. However, BFI has been combined with conventional CFI, offering both quantitative axial Doppler measurements and qualitative velocity vector visualization. The combined display modality has several advantages compared to conventional CFI. The presentation of blood flow is more intuitive, requiring less interpretation, and also provides new information of flow direction not present in conventional CFI. The speckle pattern movement is further not limited by aliasing as the CFI velocity estimates, and therefore visualizes a higher dynamic range of blood velocities.

The method was first introduced in the thesis work of Bjærum [43]. Since then, the method has been implemented in real-time on a commercial scanner system and optimized for different clinical applications. The method especially has potential in vascular imaging, but also shows potential in other clinical applications.

*This paper was published in the IEEE Transactions on Ultrasonics, Ferroelectrics, and Frequency Control, vol. 53, no. 2, Feb. 2006. It is presented in its original form.*

**Contribution no. 4: (chapter 6)**
**Clinical applications of BFI**

Lasse Løvstakken et al.
Dept. Circulation and Medical Imaging, NTNU

The limitations of conventional color flow imaging (CFI) related to angle-dependency and velocity aliasing may often obscure information about the true blood flow direction and velocity. A new real-time flow mapping technique called Blood Flow Imaging (BFI) has been introduced, able to visualize the two-dimensional vector flow direction, not limited by aliasing. The method also presents flow at an increased frame rate compared to CFI. In a series of clinical pilot studies, we evaluated potential benefits of the new method in cardiovascular and neurovascular surgery, in pediatric cardiology, and in peripheral vascular imaging. The studies were made possible with the help of many dedicated technical and clinical researchers at St.Olavs University Hospital and at Sintef Health Research, in Trondheim, Norway.

In cardiovascular surgery, the potential of BFI was evaluated as a tool for intra-operative quality control of flow in coronary anastomoses. In a porcine model, technically perfect as well as pathological left internal mammary artery (LIMA) to left anterior descending (LAD) coronary artery anastomoses were created. A study was setup where independent observers rated both modalities in aspects related to blood direction and velocity magnitude. Results indicated that BFI could more properly portrait the complex flow conditions, and required less interpretation than CFI.

In neurovascular surgery, the visualization of blood flow is challenging due to the complex vascular architecture. The potential of BFI combined with navigation technology was evaluated for intra-operative flow visualization in cerebral aneurisms and arteriovenous malformations (AVM). The directional information provided by BFI showed potential for increasing the certainty in separating feeding arteries from draining veins in AVMs, and to in general reduce the amount of interpretation needed for identifying vessels of interest in the complex vasculature.

The flow across atrial septal defects (ASD) may be difficult to detect due to overlapping B-mode and color images, caused by trade-offs between spatial resolution and frame rate. A study was setup to investigate if the increased frame rate and directional information provided by the speckle pattern movement in BFI could increase the certainty of ASD evaluations in children. Results indicated this to be the case by more properly visualizing the movement of blood across the septum, and for separating true flow across the septum from color artifacts.

When imaging vessels on a sub-millimeter scale, conventional tissue-flow arbitration may obscure flow due to strong clutter components and low blood velocities. A new transparent mixing technique replacing arbitration has been introduced with BFI. We evaluated the technique in treatment of tendinosis, requiring ultrasound imaging of small vessels ($<$ 1mm) for guiding needle incisions. Using the new technique, no flow information was lost due to arbitration, and flashing artifacts were less intrusive. The speckle movement also helped highlight actual flow in the surrounding noise floor.

*Unpublished work. Clinical papers are in progress, and the results presented will be taken from these pending papers.*

## 1.4 Publication list

During the course of the thesis work, both written and oral contributions have been made to national and international conferences and journals. Some of these contributions have been included in the thesis, while some have not. The following is a list of all published material produced during the course of the thesis between Jan. 2003 and Dec. 2007.

**Peer reviewed papers**

1. L. Løvstakken, S. Bjærum, and H. Torp, "Optimal Velocity Estimation in Color Flow Imaging in Presence of Clutter Noise", *Accepted for publication in the IEEE Transactions on Ultrasonics, Ferroelectrics, and Frequency Control*, Oct. 2006

2. L. Løvstakken, S. Bjærum, K. Kristoffersen, and H. Torp, "Real-Time Adaptive Clutter Rejection Filtering in Color Flow Imaging Using Power Method Iterations", *IEEE Transactions on Ultrasonics, Ferroelectrics, and Frequency Control*, vol. 53, no. 9, pp. 1597-1608, Sept. 2006

3. L. Løvstakken, S. Bjærum, D. Martens, and H. Torp, "Blood Flow Imaging - A New Real-Time, 2-D Flow Imaging Technique", *IEEE Transactions on Ultrasonics, Ferroelectrics, and Frequency Control*, vol. 53, no. 2, pp. 289-299, 2006

4. K. S. Ibrahim, L. Løvstakken, I. Kirkeby-Garstad, H. Torp, H. Vik-Mo, N. Vitale, R. Mårvik, and R. Haaverstad, "Effect of the cardiac cycle on the LIMA-LAD anastomosis assessed by ultrasound", *Accepted for publication in Asian Cardiovascular and Thoracic Annals*, Sept. 2006

**Conference proceeding papers**

1. L. Løvstakken, T. A. Tangen, S. Bjærum, and H. Torp, "Optimal velocity estimation in Color Flow Imaging in presence of clutter", *Proceedings of the IEEE International Ultrasonics Symposium*, Oct. 2006

2. L. Løvstakken, S. Bjærum, D. Martens, and H. Torp, "Real-time Blood Motion Imaging - A 2D Blood Flow Visualization Technique", *Proceedings of the IEEE International Ultrasonics Symposium*, vol. 1, pp. 602-605, 2004

3. L. Løvstakken, R. Haaverstad, P. Aadahl, S. Bjærum, S. Samstad, and H. Torp, "Quality Control of Off-Pump Coronary Heart Surgery using Ultrasound Color Flow Imaging with Adaptive Clutter Rejection Filters", *Proceedings of the IEEE International Ultrasonics Symposium*, vol. 2, pp. 1602-1605, 2003

**Abstracts**

1. L. Løvstakken and H. Torp, "Blood Flow Imaging (BFI) En ny metode for visualisering av 2D blodstrømsforhold med ultralyd", *Årsmøte for Norsk Forening for Ultralyddiagnostikk (NFUD)*, 2006

2. L. Løvstakken, S. Bjærum, K. Kristoffersen, R. Haaverstad, and H. Torp, "Real-time Adaptive Clutter Rejection Filtering in Color Flow Imaging Using Power Method Iterations", *IEEE International Ultrasonics Symposium - Abstracts*, 2005

3. B. Amundsen, L. Løvstakken, S. Samstad, H. Torp, and S. Slørdahl, "Blood Flow Imaging by ultrasound improved visualisation of flow direction in carotid stenoses using speckle tracking", *European Heart Journal Abstract Supplement*, 2005

4. B. Amundsen, L. Løvstakken, S. Samstad, H. Torp, and S. Slrdahl, "Ny ultralydmetode for bedre framstilling av flowretning i carotis-stenoser: Blood Flow Imaging (BFI)", *Hjerteforum*, nr. 3, 2005

5. H. Torp and L. Løvstakken, "Decomposition of flow signals into basis functions: Performance advantages, disadvantages, and computational complexity", *IEEE International Ultrasonics Symposium - Abstracts*, 2004

6. K. S. Ibrahim, L. Løvstakken, I. Kirkeby-Gaarstad, H. Torp, R. Mårvik, and R. Haaverstad, "Effect of the cardiac cycle and ultrasonic mode on the LIMA-LAD anastomosis in epicardial imaging", *Scandinavian Society for Research in Cardiothoracic Surgery meeting*, 2004

7. K. S. Ibrahim, L. Løvstakken, I. Kirkeby-Gaarstad, H. Torp, H. Vik-Mo, and R. Haaverstad, "Cardiac cycle and ultrasound mode does not influence the intraoperative epicardial assessment of the LIMA-LAD anastomosis", *First Conference of Arab Faculties of Medicine Society and first Conference of Jordanian Faculties of Medicine, 2004*

## 1.5 Concluding remarks

This thesis work is a contribution to the research performed in recent years with the aim of improving the color flow imaging modality. Due to the continuing advances in computing power, advanced signal processing can now be performed while retaining the real-time operation that has become one of the trademarks of ultrasound imaging. The goal of achieving an even more accurate and accessible real-time CFI modality is therefore considered feasible.

The thesis work have addressed the topics of clutter rejection and two-dimensional velocity vector determination and visualization. Results on the topic of clutter rejection include a new real-time adaptive algorithm, that is able to reject the clutter signal and retain the blood signal even in excessive cases of tissue motion. Further, a simulation study analyzing the potential of model-based estimation including both the blood and clutter component has been described, which shows that much can be gained by algorithms which combine velocity estimation and clutter rejection.

In the topic of two-dimensional velocity vector determination and visualization, a new real-time flow imaging modality has been described that successfully visualizes both the axial and lateral component of flow. The new technique is qualitative, but has been combined with conventional CFI to also provide parametric Doppler information. The combined modality provides a more intuitive display of blood flow, and also provides information of the true flow conditions not previously available. The new modality has been evaluated through four different clinical pilot studies, where it has shown potential in vascular as well as cardiac applications.

Technological advances are often made through several individual research efforts that contribute to a common solution. Hopefully, the thesis work will also be useful for further research by others. Through the use of advanced signal processing techniques, the role of ultrasound color flow imaging is expected to be further increased in the future clinic, by offering a more efficient evaluation of flow conditions, and an increased diagnostic confidence.

#### Future work

The thesis work should be further developed. A short list of future work is included here. For an in-depth discussion please refer to the individual chapters.

The proposed adaptive clutter rejection algorithm should be further evaluated in-vivo, and the limitations of eigenvector regression should be analyzed in more detail, especially for low-velocity blood flow conditions. Model-based estimation including both the clutter and blood signal component may increase the estimation accuracy in CFI. Practical and computationally feasible methods of such estimation schemes should be further investigated.

Regarding BFI, more work should be done to investigate the use of long, high-bandwidth pulses such as the chirp excitation. This could help increase penetration while retaining fine-grained speckle images. The real-time BFI modality should also be evaluated in adult cardiac applications using a transesophagel probe, where it is possible to come close to the heart. In the near future, an increase in parallel

receive beamforming is expected which may increase the performance of BFI when imaging deeper vessels and in cardiac applications. Work should then be performed to investigate new potential applications of BFI. The extension to 3-D BFI may then also become feasible. Finally, work should be done to investigate potential misinterpretations of the speckle pattern movement.

The future of ultrasound imaging in general and specifically of CFI is continually evolving. Current trends in real-time 3-D ultrasound imaging is at the moment is pushing the technology forward, and will also offer new possibilities for improved 2-D imaging. Also, new techniques and applications will be available on continually smaller instruments due to advances in miniaturization of electronic circuits and digital technology. This will open up a market of new users in point-of-care (POC) applications. As these users will be non-experts, more accessible and intuitive modalities and applications will be important.

## 1.6 Thesis outline

The thesis is organized as follows. In in chapter 2, a thorough background of ultrasound imaging and specifically color flow imaging is given. This foundation should put the unfamiliar reader capable of understanding the problems and work presented in the following chapters. In chapter 3-5 the technical thesis papers are presented. The papers are included as originally published, but have been adapted to the book layout. In chapter 6, four preliminary clinical and experimental studies are described, where the value of the new real-time BFI modality is evaluated.

# References


[1] C. Rumack, S. Wilson, and J. Charboneau, *Diagnostic ultrasound*. St. Louis: Elsevier Mosby, 2005.

[2] H. Feigenbaum, W. Armstrong, and T. Ryan, *Feigenbaum's echocardiography, 6th edition*. Philadelphia: Lippincott Williams & Wilkins, 2005.

[3] S. Barnett, G. ter Haar, M. Ziskin, W. Nyborg, K. Maeda, and J. Bang, "Current status of research on biophysical effects of ultrasound," *Ultrasound Med. Biol.*, vol. 20, pp. 205–218, 1994.

[4] S. Barnett, G. T. Haar, M. Ziskin, H. Rott, F. Duck, and K. Maeda, "International recommendations and guidelines for the safe use of diagnostic ultrasound in medicine," *Ultrasound Med. Biol.*, vol. 26, pp. 355–366, 2000.

[5] S. Barnett and D. Maulik, "Guidelines and recommendations for safe use of doppler ultrasound in perinatal applications," *J. Mater. Fetal Med.*, vol. 10, pp. 75–84, 2001.

[6] B. Goldberg, R. Gramiak, and A. Freimanis, "Early history of diagnostic ultrasound: the role of american radiologists," *AJR. Am. J. Roentgenol.*, vol. 160, pp. 189–194, 1993.

[7] S. Levi, "The history of ultrasound in gynecology 1950-1980," *Ultrasound Med. Biol.*, vol. 23, pp. 481–552, 1997.

[8] K. Beach, "1975-2000: a quarter century of ultrasound technology," *Ultrasound Med. Biol.*, vol. 18, pp. 377–388, 1992.

[9] P. Wells, "Ultrasonics in medicine and biology," *Phys. Med. Biol.*, vol. 22, pp. 629–669, 1977.

[10] P. Wells, "Ultrasound imaging," *J. Biomed. Eng.*, vol. 10, pp. 548–554, 1988.

[11] P. Wells, "The present status of ultrasonic imaging in medicine," *Ultrasonics*, vol. 31, pp. 345–352, 1993.

[12] P. Wells, "Ultrasound imaging," *Phys. Med. Biol.*, vol. 51, pp. R83–R98, 2006.

[13] L. Nelson, "Echoes from the past: history of obstetric ultrasound," *J. Ultrasound Med.*, vol. 22, pp. 667–671, 2003.

[14] R. Meyer, "History of ultrasound in cardiology," *J. Ultrasound Med.*, vol. 23, pp. 1–11, 2004.

[15] R. Kane, "Intraoperative ultrasonography: history, current state of the art, and future directions," *J. Ultrasound Med.*, vol. 23, pp. 1407–1420, 2004.

[16] J. Haller, T. Slovis, D. Babcock, and R. Teele, "Early history of pediatric ultrasound (circa 1960-1985)," *J. Ultrasound Med.*, vol. 23, pp. 323–329, 2004.

[17] D. Baker, H. Stegall, and W. Schlegel, "A sonic transcutaneous blood flowmeter," *Proc., 17th Ann. Conf. Eng. Med. Biol.*, vol. 6, 1964.

[18] P. Peronneau and F. Leger, "Doppler ultrasonic pulsed blood flowmeter," *Proc. 8th Int. Conf. Med. Biol. Eng.*, pp. 10–11, 1969.

[19] P. Wells, "A range-gated ultrasonic doppler system," *Med. Biol. Eng.*, vol. 7, pp. 641–652, 1969.

[20] D. Baker, "Pulsed ultrasonic doppler blood-flow sensing," *IEEE Trans. Sonics Ultrason.*, vol. 17, pp. 170–185, 1970.

[21] F. Barber, D. Baker, A. Nation, D. Strandness, and J. Reid, "Ultrasonic duplex echo-doppler scanner," *IEEE Trans. Biomed. Eng.*, vol. 21, pp. 109–113, 1974.

[22] S. Johnson, D. Baker, R. Lute, and H. Dodge, "Doppler echocardiography. the localization of cardiac murmurs," *Circulation*, vol. 48, pp. 810–822, 1973.

[23] J. Holen, R. Aaslid, K. Landmark, and S. Simonsen, "Determination of pressure gradient in mitral stenosis with a non-invasive ultrasound doppler technique," *Acta Med. Scand.*, vol. 199, pp. 455–460, 1976.

[24] A. Brubakk, B. Angelsen, and L. Hatle, "Diagnosis of valvular heart disease using transcutaneous doppler ultrasound," *Cardiovasc. Res.*, vol. 11, pp. 461–469, 1977.

[25] D. FitzGerald and J. Drumm, "Non-invasive measurement of human fetal circulation using ultrasound: a new method," *Br. Med. J.*, vol. 2, pp. 1450–1451, 1977.

[26] L. Hatle, A. Brubakk, A. Tromsdal, and B. Angelsen, "Noninvasive assessment of pressure drop in mitral stenosis by doppler ultrasound," *Br. Heart J.*, vol. 40, pp. 131–140, 1978.

[27] W. McCallum, C. Williams, S. Napel, and R. Daigle, "Fetal blood velocity waveforms," *Am. J. Obstet. Gynecol.*, vol. 132, pp. 425–429, 1978.

[28] P. Wells, "Ultrasonic colour flow imaging," *Phys. Med. Biol.*, vol. 39, pp. 2113–2145, 1994.

[29] K. Ferrara and G. DeAngelis, "Color flow mapping," *Ultrasound in Medicine & Biology*, vol. 23, pp. 321–345, 1997.

[30] M. Eyer, M. Brandestini, D. Phillips, and D. Baker, "Color digital echo/doppler image presentation," *Ultrasound Med. Biol.*, vol. 7, pp. 21–31, 1981.

[31] C. Kasai, K. Namekawa, A. Koyano, and R. Omoto, "Real-time two-dimensional blood flow imaging using an autocorrelation technique," *IEEE Trans. Sonics Ultrason.*, vol. 32, pp. 458–464, 1985.

[32] H. Torp, "Clutter rejection filters in color flow imaging: A theoretical approach," *IEEE Trans. Ultrason., Ferroelec., Freq. Contr.*, vol. 44, pp. 417–424, 1997.

[33] S. Bjaerum, H. Torp, and K. Kristoffersen, "Clutter filter design for ultrasound color flow imaging," *IEEE Trans. Ultrason., Ferroelec., Freq. Contr.*, vol. 49, pp. 204–216, 2002.

[34] O. Bonnefous and P. Pesque, "Time domain formulation of pulse-doppler ultrasound and blood velocity estimation by cross correlation," *Ultrason. Imaging*, vol. 8, pp. 73–85, 1986.

[35] K. Ferrara and V. Algazi, "A new wideband spread target maximum likelihood estimator for blood velocity estimation. i. theory," *IEEE Trans. Ultrason., Ferroelec., Freq. Contr.*, vol. 38, pp. 1–16, 1991.

[36] T. Loupas, J. Powers, and R. Gill, "An axial velocity estimator for ultrasound blood flow imaging, based on a full evaluation of the doppler equation by means of a two-dimensional autocorrelation approach," *IEEE Trans., Ultrason., Ferroelec., Freq. Contr.*, vol. 42, pp. 672–688, 1995.

[37] S. Alam and K. Parker, "The butterfly search technique for estimation of blood velocity," *Ultrasound in Medicine & Biology*, vol. 21, pp. 657–670, 1995.

[38] S. Bjaerum, H. Torp, and K. Kristoffersen, "Clutter filters adapted to tissue motion in ultrasound color flow imaging," *IEEE Trans. Ultrason., Ferroelec., Freq. Contr.*, vol. 49, pp. 693–704, 2002.

[39] D. Kruse and K. Ferrara, "A new high resolution color flow system using an eigendecomposition-based adaptive filter for clutter rejection," *IEEE Trans. Ultrason., Ferroelect., Freq. Contr.*, vol. 49, pp. 1384–1399, 2002.

[40] B. Dunmire, K. Beach, K. Labs, M. Plett, and D. Strandness, "Cross-beam vector doppler ultrasound for angle-independent velocity measurements," *Ultrasound Med. Biol.*, vol. 26, pp. 1213–1235, 2000.

[41] G. Trahey, J. Allison, and O. von Ramm, "Angle independent ultrasonic detection of blood flow," *IEEE Trans. Biomed. Eng.*, vol. 34, pp. 965–967, 1987.

[42] J. Jensen and P. Munk, "A new method for estimation of velocity vectors," *IEEE Trans. Ultrason., Ferroelect., Freq. Contr.*, vol. 45, pp. 837–851, 1998.

[43] S. Bjærum, *Detection and visualization of moving targets in medical ultrasound imaging, paper H: Blood Motion Imaging: A new blood flow imaging technique.* Trondheim, Norway: NTNU, 2001.

# Chapter 2

# Background

Lasse Løvstakken
Dept. Circulation and Medical Imaging, NTNU

The following chapter contains information that is included to give the unfamilar reader a short introduction to diagnostic ultrasound imaging and conventional methods and terms used in this context. It also includes more in-depth information about the concept of color flow imaging (CFI), the modality under investigation in this thesis work. An overview of conventional methods is given, and current challenges and limitations are reviewed. A review is finally given on previous work in the two main topics of the thesis work, that of two-dimensional velocity estimation and adaptive clutter filtering in CFI.

## 2.1 Diagnostic ultrasound imaging

### 2.1.1 Background

The history of diagnostic ultrasound traces back to the 1940s, when the concept of using ultrasound to image the human interior was conceived based on knowledge of pulse-echo imaging from SONAR and technology from ultrasonic metal flaw detectors available at the time. This emerging technology matured during the forties, and by the end of the decade systematic research into its diagnostic use began in several research groups over the world. Some of the first descriptions of diagnostic ultrasound imaging was reported in the early fifties through the pioneering work of Wild and Reid, Howry and Bliss, and Edler and Hertz [1–3]. An important foundation for the use of this technology in medicine was the discovery of new piezoelectric materials in the mid-forties, which allowed for the generation of short high frequency pulses in the MHz range.

As a diagnostic tool, ultrasound was first conceived as a tool for tissue characterization, i.e. with the ability to differentiate between different types of tissue such as cancerous and normal tissue. Although research in this area is still ongoing, this goal has arguably still not been reached today [4, 5]. Demonstrations of ultrasound imaging equipment were presented in the fifties. However, it was not until the advent of transistor technology that equipment could be made that would allow for mainstream use. The first commercial B-mode (brightness mode) instruments became available in

the early sixties, offering static images of the human interior based on the received signal envelope. Further advances in transistor technology lead to the first real-time B-mode scanners in the late sixties and through the seventies [6–8].

From the late fifties, effort was also put into registering movement with ultrasound through the Doppler shift of the received signal. The first effort is usually attributed to Satumora in 1957 [9]. The first commercial Doppler instruments appeared in the sixties based on the continuous wave (CW) approach, which did not include any depth information. Pulsed wave (PW) Doppler instruments for measuring blood flow velocity at specific depths was described in the late sixties [10–12]. The development of the scan converter further allowed for duplex operation of both Doppler and B-mode imaging in the late seventies, while real-time two-dimensional Doppler mapping became feasible in the mid-eighties. A formidable development has taken place due to dedicated research in both the technical and clinical community [13, 14].

Ultrasound imaging is today used in a wide range of clinical contexts. Perhaps the most well known application is that in obstetrics and fetal medicine [15], where ultrasound examinations are used to investigate the health of the fetus during pregnancies. Clinical research in this area has been extensive since the late sixties, and ultrasound examinations can today reveal many potential health risks, reducing the morbidity and mortality of newborns. Due to its high imaging frame rate, ultrasound has also found particular use in the diagnosis of cardiovascular decease, where the dynamics of the heart muscle and the blood flow in the heart and arteries are important measures. The development of Doppler ultrasound for measuring blood flow and tissue velocities, has provided physicians with a valuable tool for diagnosis in the cardiovascular system [16, 17]. Ultrasound imaging is further used in many other areas of medicine, such as the screening for breast cancer in women, detection of abnormalities and cancer in the internal organs. It is also used intraoperatively in for instance heart- and neurosurgery as a tool for quality control. For a more complete description of ultrasound imaging techniques and applications in medicine, please refer to one of the many textbooks available, such as [18–21].

In the following subsections, a brief look at the basic principles of ultrasound imaging, and at the design of modern ultrasound imaging systems will be given.

### 2.1.2 Basic principles of ultrasound imaging

Ultrasound is defined as pressure waves with frequencies above the human audible range of 20 kHz. Pressure waves propagate through a medium. In diagnostic ultrasound imaging, longitudinal pressure wave pulses with center frequencies in the range of 2-15 MHz are transmitted into the human tissue. As the pressure wave propagate, it interacts with different tissue characteristics through scattering and attenuation processes. This fundamental mechanism is the foundation of ultrasound imaging. The pressure amplitude of the backscattered ultrasound can be registered and used to form an image of the different tissue media present.

The properties of a tissue medium can be described by a given density $\rho$ and compressibility $\kappa$. It is the local differences in density and compressibility that causes the scattering of ultrasound. The basic equation governing pressure wave propagation

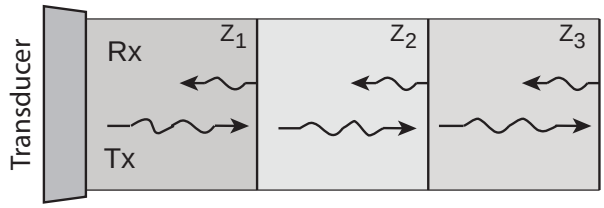


Figure 2.1: The concept of pulse-echo ultrasound imaging. An ultrasound pulse is emitted into the tissue, and is scattered at interfaces between different types of tissue $Z_1$, $Z_2$, and $Z_3$. The backscattered signal is received by the same transducer and form the basis for the ultrasound image.

can be derived by considering the conservation of mass and momentum. Assuming a homogenous medium, and linear propagation where the displacement of scattering volumes is linearly proportional to the change in pressure, the basic equation governing the propagation of a pressure wave $p(\mathbf{r}, t)$ is given by [22]

$$\nabla^2 p(\mathbf{r}, t) - \frac{1}{c^2} \frac{\partial^2 p(\mathbf{r}, t)}{\partial t^2} = 0, \tag{2.1}$$

where $\mathbf{r}$ is a spatial position vector, $t$ is time, and $c = \frac{1}{\sqrt{\rho\kappa}}$ is the speed of sound in the medium. The speed of sound in human tissue has been measured to be 1540 m/s on average, with only a small range for different types of soft tissue [23]. The assumption of a constant value for the speed of sound is fundamental in conventional ultrasound imaging, and allows for a simple conversion between imaging depth and receive time in pulse-echo operation.

The ultrasonic waves are attenuated as they travel through the tissue due to power absorptions, scattering losses, and the geometric spreading of the ultrasound beam [22]. This attenuation limit the penetration depth in ultrasound imaging. Because the spatial resolution of an ultrasound image is proportional to the frequency of the transmitted pulse, one would in principle use higher frequencies. Unfortunately the attenuation of ultrasonic waves is frequency dependent, and the optimal working frequency is a compromise between resolution and penetration. The attenuation in human soft tissue is usually approximated to be 0.5 dB/cmMHz one way [24].

Conventional ultrasound imaging is pulse-echo imaging, a concept illustrated in Fig. 2.7. An ultrasound transducer transfers pressure waves into the tissue, and also receives the backscattered signal produced as the wave encounters differences in tissue properties across its path. The backscattered signal is a measure of the different tissue properties and can be used to form an image. Scattering objects can be divided into three basic types. An object large compared to the wavelength of the transmitted pulse will reflect the ultrasound wave in a specular way. Scattering objects comparable to the wavelength will scatter the ultrasound wave directionally. Finally, scattering objects small compared to the wavelength will scatter the incoming ultrasound wave in an omnidirectional way, so-called Rayleigh scattering. As an example, specular

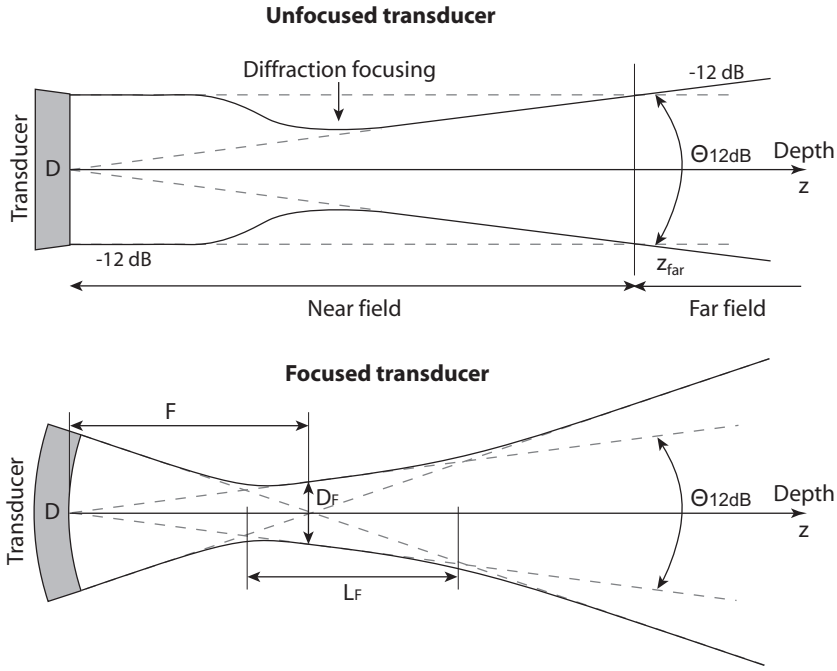


Figure 2.2: The beam profile of a plane unfocused (upper) and focused transducer (lower). The course of the unfocused beam can be divided in to a near field and far field region. In the near field diffraction effects are prominent and cause a convergence of the beam known as diffraction focusing. By focusing, a narrow beam width can be achieved in the near field over a limited depth region.

reflectors could be structures such as bone or vessel walls, while Rayleigh scattering results when the ultrasound beam encounters the small red blood cells. Combinations of these scattering processes are typically present throughout an ultrasound image.

### Beam formation

When the wavelength of the transmitted pressure wave becomes small compared to the transmitting aperture, the sound beam generated will become directional. This is the case for the unfocused ultrasound beam illustrated in the upper schematic of Fig. 2.2. It is useful to divide the course of the sound beam into specific regions in depth, the near and far field. In the near field diffraction effects are prominent. These effects are present due to the limited aperture used, and will cause the beam to converge, a phenomenon called diffraction focusing. The extreme near field is often defined as the region where the beam is a close replica in width to that of the aperture used. The far field is defined as the region where the pressure wave amplitude fall off at a fixed rate. The transition between the near and far field is for a plane circular transducer

given by

$$z_{far} = \frac{D^2}{2\lambda}, \tag{2.2}$$

where $D$ is the diameter of the aperture, and $\lambda$ is the wavelength of the emitted pulse. The one way beam width is usually defined as the -12 dB drop in signal power. As an example, consider a transducer with an aperture diameter of 2 cm and a center frequency of 2.5 MHz. The start of the far field region is then given by

$$z_{far} = \frac{0.02^2 \cdot 2.5e6}{2 \cdot 1540}\ cm = 32\ cm \tag{2.3}$$

In other words, ultrasound image formation is made in the near field of the transducer.

The beam can be focused by curving the aperture, by using a lens, or by using transducer arrays and electronic delays between the different array elements. When focusing the far field is effectively brought into the near field, and a narrow beam width can then be achieved at a specific depth in a limited region. In order to achieve efficient focusing, the focus point must lie in the near field of the beam as defined for a circular transducer in (2.2). A focused beam profile is shown in the lower schematic of Fig. 2.2. The beam width $D_F$ determines the lateral resolution of the imaging system, and is for a focused transducer given by (-3 dB beam width)

$$D_F = \frac{\lambda}{D}F = F_{\#}\lambda, \tag{2.4}$$

where $F$ is the distance to the focus point, $D$ is the aperture diameter, $\lambda$ is the wavelength. $F_{\#}$ is the focus distance measured in apertures, the F-number of the imaging system. The focal depth $L_F$ of the beam defines the effective depth region of uniform beam width as given at the focus depth. The (-1 dB) focal depth is given by

$$L_F = 4 \cdot \lambda F_{\#}^2. \tag{2.5}$$

For a transducer aperture of 2 cm with a center frequency emission of 2.5 MHz, focused at 7 cm, the beam width and focus depth is equal to

$$D_F = \frac{0.07 \cdot 1540}{0.02 \cdot 2.5e6}\ cm = 0.22\ cm, \quad L_F = 4 \cdot \frac{0.07^2 \cdot 1540}{0.02^2 \cdot 2.5e6}\ cm = 3.0\ cm \tag{2.6}$$

The F-number defines the lateral resolution in focus as given by (2.4), and is therefore desired to be low to achieve a narrow beam width. However as seen in (2.5), the depth of focus is proportional to the F-number squared. Using too low F-numbers may therefore concentrate the sound energy in a small region along the beam axis, and the appropriate F-number must therefore be optimized according to a given transducer design and application.

The beam shape can be further optimized using *apodization*, *dynamic aperture*, and *dynamic focus*. The concept of apodization is to weight the individual elements according to a window function. This will reduce the beam sidelobe level at the expense of a broader mainlobe. Dynamic aperture is further used to create a more uniform beam width in depth, by reducing the aperture size used at closer depths on receive to keep the F-number as constant as possible. The concept of dynamic focus is to sweep the focus electronically on receive according to depth.

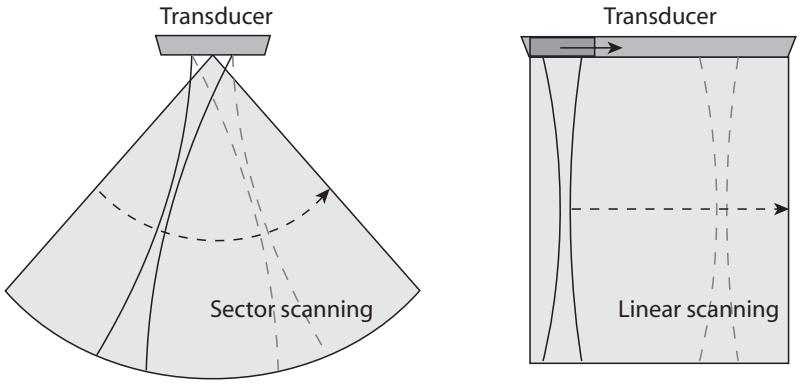


Figure 2.3: Two common ultrasound scanning modes, the sector and linear scan.

### Image formation

Image formation is done by sweeping the ultrasound beam over a region of interest, and registering the backscattered signal in each direction. The sweeping of the beam is today typically done electronically using transducer arrays, but is also still done mechanically in certain applications, for instance in high frequency imaging systems. Sweeping the beam electronically can be done in different ways. Two standard techniques are depicted in Fig. 2.3. The sector scan uses transmission delays on the array elements to not only focus the beam, but also to steer the beam in a desired direction. This is called phased array imaging, and is most widely used in cardiac applications where the acoustic window between the ribs is limited. To be able to steer the beam at larger angles, the array elements must be small compared to the wavelength in order to achieve efficient focusing and to avoid grating lobes. Grating lobes are repetitions of the mainlobe in space due to the division of the aperture into elements. A common design criteria is to require an element size of $a = \lambda/2$, which in theory allows for efficient steering in a sector of 90 degrees without grating lobes.

Another type of sweeping is the linear scan. A larger aperture is typically used, with larger elements of size $\sim 1.5\lambda$ as steering requirements are limited. A smaller subaperture is used to form a beam at a given offset from the center of the transducer. This subaperture is swept over the aperture to produce a rectangular image region. Linear scans are used in vascular and abdominal applications. In abdominal applications it is also common to curve the transducer aperture to achieve a broader field of view and a better contact with the abdomen, so-called curvilinear arrays.

### Display modes

Several different display modes have been introduced since the beginning of ultrasound imaging. The most basic display modality today is the B-mode modality, which shows a two-dimensional image of tissue in gray scale. Images are made based on the

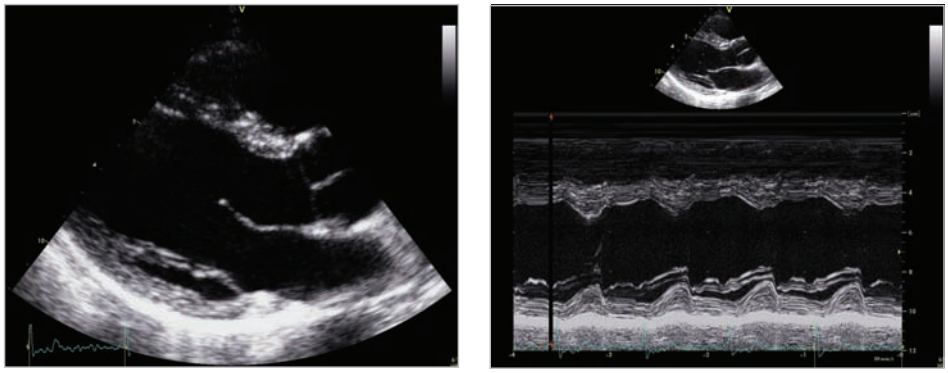


Figure 2.4: The B-mode and M-mode imaging of a healthy human heart.

received signal envelope. Due to the high dynamic range of the received signal from different tissue structures, the signal is logarithmically compressed before display to show both weak and strong echoes simultaneously. In B-mode, a high spatial resolution is important in order to resolve close targets. A high frame rate is also desired in many clinical applications to investigate the dynamics of structures.

Another common modality is the M-mode (motion mode), which displays the envelope of the acquired signal along a specific beam direction over time. This one-dimensional modality has a very high imaging frame rate and is suitable for investigating rapid movements of tissue structures, for instance the movement of the heart valves. M-mode images along curved lines, called curved M-mode, is also used based on two-dimensional acquisitions. In Fig. 2.4, a standard B-mode and M-mode image of a healthy human heart is shown.

In addition to the two major tissue imaging modalities described, a number of Doppler related modalities have been introduced. Continuous wave (CW) and pulsed wave (PW) spectral Doppler is used to investigate the blood flow distribution in the heart and arteries. Two-dimensional Doppler mapping, or color flow imaging (CFI), became a standard modality in the early nineties, and shows the distribution of flow velocities in a region of interest. Duplex operation of both B-mode and spectral Doppler or CFI, and triplex modalities of all three is also available on modern systems.

Static and electrocardiogram-gated 3-D images have been available for some time for abdominal imaging using mechanically steered transducers. In recent years, dynamic three-dimensional imaging has also become available. Using 2-D array technology, real-time 3-D images of the heart anatomy and blood flow can be obtained. The new information available can for instance be beneficial in the diagnosis of the heart valve disease.

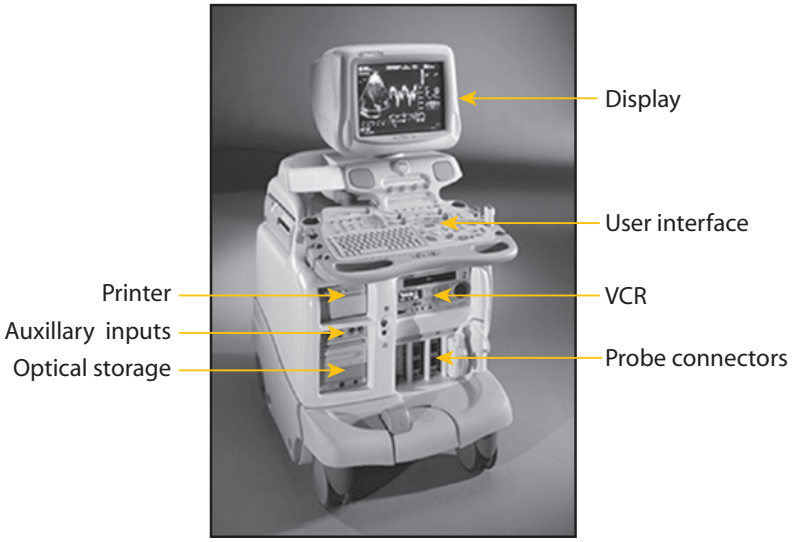


Figure 2.5: An example of a modern high-end ultrasound scanner, the GE Vivid 7 ultrasound system (image courtesy of GE Healthcare). The different parts of the system has been labeled.

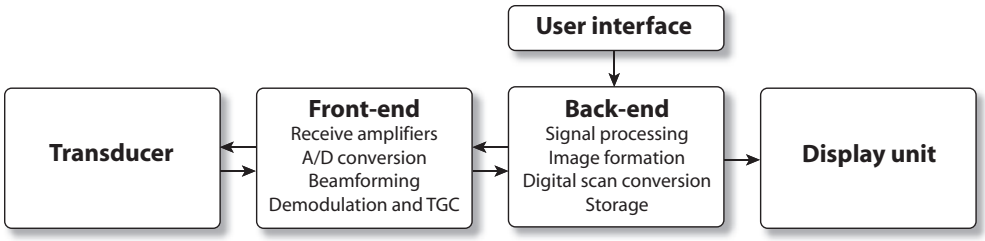


Figure 2.6: Block diagram of a modern generic ultrasound system.

### 2.1.3 Building blocks of an ultrasound imaging system

A modern high-end scanner is shown in Fig. 2.5. These systems contain a user interface and display, probe connectors, an optical storage unit, ECG and other auxiliary input connectors, a thermal printer, and often units for supporting old recordings such as a VCR. Modern systems are designed to be portable within hospital buildings, but laptop size systems are now also available which includes most of the functionality of high-end scanners. The basic building blocks and signal chain of a modern ultrasound imaging system is shown in Fig. 2.6, and will be described in the following subsections.

### Transducer

The transducer is an indispensable part of the ultrasound imaging system, responsible for the transmission and reception of ultrasonic pressure waves. A typical transducer today consists of an array of piezoelectric elements. On transmission, these piezoelectric elements vibrate in response to an external electric field, creating ultrasonic waves. On receive, the piezoelectric elements vibrate in response to an external pressure, producing an electrical signal. Ultrasound pulse emission timing and array element apodization can be controlled electronically, and allows for flexible beam shaping and electronic focusing and steering of the beam. Transducers come in different shapes and sizes designed for specific clinical applications. Also, due to the limited frequency bandwidth of the currently available piezoelectric ceramic materials, transducers also have to be designed to work in a specific frequency range, based on the demands of penetration in a given clinical application. For instance, a transducer designed for cardiac imaging has to be small enough to fit between the human ribs, and might operate in a frequency range from 2-4 MHz in order to achieve sufficient penetration to cover the heart. A transducer for imaging peripheral vessels on the other hand, can be considerably larger and might operate at frequencies of 7-14 MHz due to shallow penetration depths. The subject of transducer design is comprehensive, and out of scope for this introductory chapter. For more information on the subject please refer to [22]. Challenges for the future include the design of two-dimensional arrays for high-quality 3-D imaging, and broadband designs for multi-frequency operation and non-linear imaging.

### Front-end

The front-end of the ultrasound system consists of dedicated hardware for controlling the transmission and reception of ultrasonic waves. The delays needed to focus the ultrasound beam in a given direction are calculated and used to transmit ultrasound pulses in directions according to the given scanning mode. After transmission, the system enters receive mode. Depth dependent preamplification is needed to exploit the full dynamic range of the A/D convertors. The received signal from the transducer elements are then beamformed in a given direction by a delay-and-sum procedure. A receive filter matched to the bandwidth of the received signal is applied to maximize the signal-to-noise ratio. Since the attenuation of ultrasound is frequency dependent, the receive filter is often swept to follow the changes in frequency content over depth. Echoes from deeper structures are attenuated more than echoes from shallow structures, and to image both near and far echoes simultaneously, a depth dependent amplification is applied to the signal, called time-gain compensation. The beamformed signal finally goes through a complex demodulator, where the RF-signal is transferred to baseband, and downsampled to reduce the amount of data for later processing. Much of the signal processing has in modern systems been moved to the back-end of the system, however it is also common to used dedicated hardware for this purpose in the front-end.

#### Back-end

In modern systems the back end of an ultrasound system typically consists of a conventional desktop computer, and is responsible for tasks such as user interfacing, signal processing, image preparation and scan conversion, and archive storage of ultrasound recordings. In modern systems, the back end tasks are performed in software running on a real-time aware operating system. User interface tasks are typically first administered by the back end. For instance, the selection of a specific image modality by the user, will first be administered by the back end computer, which further communicates with and sets up the front-end for new operation. The rapid development of computer technology has moved increasingly more tasks to the back-end of the system. Processing tasks such as image filtering, Doppler processing, and scan conversion are now feasible to do in software, which is much more flexible and cost effective than previous hardware solutions. The development of high performance graphics cards in recent years, have also made real-time rendering of 3-D ultrasound images feasible at a low cost. Systems for research are now available where beamforming can be done in software. In the long run, even real-time beamforming in software will most likely become feasible.

### 2.1.4 Ultrasound image quality

#### Spatial resolution

The spatial resolution is defined as the minimum spacing between targets that still can be distinguished by the imaging system. In ultrasound imaging the spatial resolution is theoretically given by the center frequency and bandwidth of the emitted pulse, the aperture diameter, and the focus depth. The theoretical radial resolution is related to the temporal length of the emitted pulse through the following relation:

$$\Delta r = \frac{c \cdot T_{pulse}}{2} = \frac{c}{2 \cdot B_{pulse}}, \tag{2.7}$$

where $B_{pulse}$ is the pulse bandwidth. The radial resolution is at first hand limited by the transducer bandwidth, and is further degraded by frequency dependent attenuation which shifts the frequency contents of the received pulse towards zero. In B-mode imaging the radial resolution is in the range of wavelengths, while in Doppler modes it is increased to achieve sufficient sensitivity to the weaker blood signal level. The lateral resolution is given by a beam width measure as defined in (2.4), and is therefore dependent on the ratio between the focus depth and aperture (the F-number), and the wavelength of the emitted pulse. The lateral image resolution is broadened outside of the beam axis focus.

The total imaging system resolution can be described through the point spread function (PSF), which is defined as the image of an infinitely small point. In Fig. 2.7, the pulse-echo point spread function for pulse center frequency of 2.5 MHz with a relative bandwidth of 60%, using a F-number of 2 on both transmit and receive is shown. As can be observed in the figure, the ultrasound imaging system has a limited region of support in the Fourier space. In the lateral direction, the imaging system

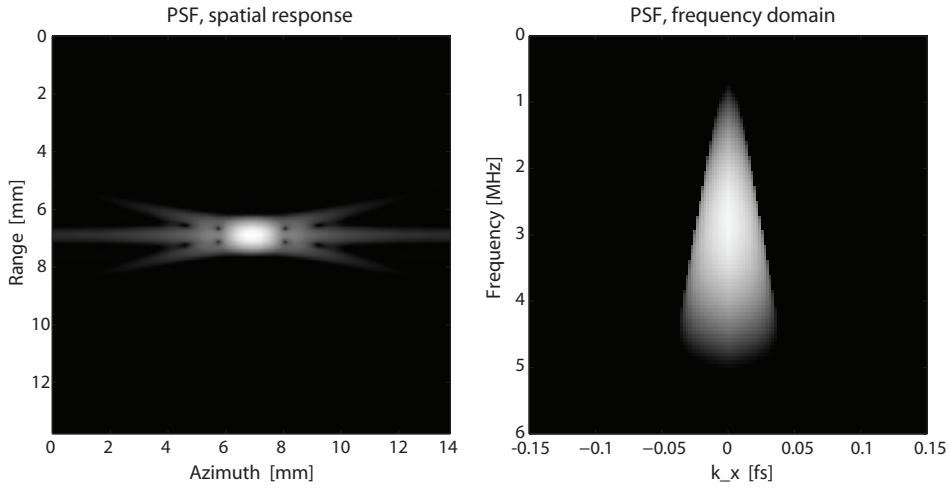


Figure 2.7: Example of a two-way point spread function (PSF) of an ultrasound imaging system. The PSF is given in focus of a transducer using an F-number of 2 on both transmit and receive. A pulse with center frequency of 2.5 MHz with a relative bandwidth of 60% was used.

exhibits a low-pass character, while in the axial direction a bandpass character is given. It is this bandpass character that gives the speckle pattern and anisotropic properties of the ultrasound images [25].

### Contrast resolution

The contrast resolution is defined as the ability of the imaging system to differentiate between two regions of different scattering properties. In ultrasound imaging these scattering properties are given by local changes in compressibility and density. The contrast resolution in ultrasound imaging is degraded by beam sidelobes and by acoustic noise such as reverberations and phase front aberrations. The contrast resolution is a local characteristic, and depends both on system design and the imaging object through the inferred acoustic noise. It is therefore difficult to give an absolute measure of this property for ultrasound imaging.

### Factors corrupting image quality

Several factors limit the quality in ultrasound images. These are related to both fundamental physical phenomenons and to system design.

**Reverberations:** Conventional ultrasound imaging operates in the Born approximation regime, where only one scattering process is assumed before the wave is received at the receiving transducer. In reality, the ultrasound wave may be scattered multiple times across its path, called reverberations. Due to

reverberations, signal from specific scatterers are received multiple times, and ghost images are then produced which degrade the contrast resolution of the image.

**Phase front aberrations:** In conventional ultrasound imaging, the tissue medium is assumed homogenous, and the speed of sound therefore assumed constant. In reality, different types of tissue are present with varying speeds of sound. When different parts of the beam wavefront travel through different types of tissue, the varying speed of sound will cause the wavefront to be distorted. This is termed phase front aberration. Phase front aberration infers a less efficient focusing, which result in a degradation in lateral resolution due to a broadened mainlobe, and in contrast resolution due to an increased sidelobe level.

**Frequency dependent attenuation:** Due to the frequency dependent characteristics of the attenuation of ultrasound in tissue, the received signal center frequency will shift towards lower frequencies during propagation. This center frequency shift results in a degradation of the spatial resolution and penetration which is aggravated for increasing depths.

**Beam sidelobes:** Due to the finite aperture used when imaging, beam sidelobes will be present. Scatterers present in the beam side lobes will be registered on receive, and in effect degrades the contrast resolution of the image. By using apodization of the individual elements on the transducer array, it is possible to trade a wider mainlobe for a lower sidelobe level.

**Grating lobes:** Due to the division of the aperture in array elements the beam pattern will be reproduced periodically in space. The angle between the grating lobes and the mainlobe is determined by the size of the individual array elements, called the pitch. Grating lobes may infer visible image artifacts, and degrade the contrast resolution as for beam sidelobes.

### 2.1.5 Ultrasound Doppler imaging

When a transmitted ultrasound wave is reflected from a moving scatterer, the wave will experience a shift in frequency. This is termed the Doppler effect, named after Christian Doppler who first described the phenomenon [26]. The Doppler effect plays with our sense of time by contracting or expanding the timescale of waves as they are emitted from a moving source or reflected of a moving target. In ultrasound pulse-echo imaging both of these cases occur. The scaling of the temporal axis can then be shown to be given by [27]

$$\alpha = \frac{c + v\cos\theta}{c - v\cos\theta} \approx (1 + \frac{2v\cos\theta}{c}), \tag{2.8}$$

where $\theta$ is the angle between the scatterer velocity vector and the ultrasound beam direction, and $v\cos\theta$ is the axial component of the scatterer velocity, defined as positive towards the ultrasound transducer. The corresponding shift in frequency is then given

by:

$$f_d = \alpha f_0 - f_0 = 2f_0 \frac{v \cos\theta}{c}, \tag{2.9}$$

where, $f_d$ is termed the Doppler shift, and $f_0$ is the emitted frequency. The equation is valid as long as $v \cos\theta \ll c$.

The Doppler principle can be used to measure the velocity of both tissue and blood with ultrasound. Tissue velocities are typically quite low compared to blood flow, but with some exceptions. The contractions of the myocardium can for instance be in the range around 10 cm/s, while the movement of the heart valves can have velocities as high as 50 cm/s. For blood flow the velocities range up to 1 m/s for normal flow, while stenotic and valve insufficiency flow can reach as high as 6 m/s. Imaging with a pulse center frequency of 2.5 MHz, this means that Doppler shifts can range up to 19500 kHz. In diagnostic ultrasound, the Doppler shifts are hence in the human audible range.

For blood the received signal from an insonified sample volume is a sum of contributions from a large number of scatterers, each producing a Doppler shift according to their given velocity and direction. The received signal is therefore made up of a spectrum of different velocities. Further, as each scatterer is observed in a finite time interval, a non-zero bandwidth is given for each velocity. This is termed the transit time effect.

The velocity spectrum within a sample volume can be investigated by spectral analysis of the received signal. As the Doppler shift is in the audible range, it is also common to generate sound through a set of speakers for the physicians to interpret. This was in fact how the early Doppler instruments strictly operated, before real-time spectral analysis became computationally feasible. An increasing scatterer velocity causes an increasing Doppler shift and therefore a higher pitch of the sound. Two different Doppler modalities have become standard, based on either a continuous wave (CW) excitation, or a pulsed wave (PW) excitation approach. A brief description will now be given. For a more thorough description please refer to [21, 22, 27, 28].

### Continuous-wave Doppler

In continuous-wave Doppler (CW-Doppler), a single frequency signal is continuously transmitted into the tissue, while the backscattered signal is simultaneously received, typically by a different part on the same transducer aperture. The sample volume in CW-Doppler is given by the overlap between the transmit and receive beam. Doppler shifts from all scatterers moving in this large region of overlap are therefore observed, and in practice no range resolution is available in CW-Doppler. The main advantage of the CW approach is that it is not limited by a maximum measurable velocity, as a continuous recording of the Doppler signal is obtained.

The magnitude and sign of the Doppler frequency can be obtained by quadrature demodulation. Consider the CW emission given by

$$e(t) = \cos(2\pi f_0 t) = Re\{e^{i2\pi f_0 t}\}, \tag{2.10}$$

where $f_0$ is the emitted sinusoidal frequency. Assuming the received signal at time $t$ to be a delayed, scaled, and Doppler shifted version of the emitted signal at time $t_0$, we get:

$$r(t) = A\big(\alpha(t-t_0)\big) \cdot e\big(\alpha(t-t_0)\big) = A\big(\alpha(t-t_0)\big) \cdot \cos\big(2\pi f_0 \alpha(t-t_0)\big). \tag{2.11}$$

The complex analytic signal can be obtained through the Hilbert transform, and is given by:

$$\tilde{r}(t) = \tilde{A}\big(\alpha(t-t_0)\big) \cdot e^{i2\pi\alpha f_0(t-t_0)} \tag{2.12}$$

Mixing the received analytic signal with the quadrature reference signal $e^{-i2\pi f_0 t}$ then yields:

$$\begin{aligned} r_{IQ}(t) &= \tilde{A}\big(\alpha(t-t_0)\big) \cdot e^{i2\pi\alpha f_0(t-t_0)} \cdot e^{-i2\pi f_0 t} \\ &= \tilde{A}\big(\alpha(t-t_0)\big) \cdot e^{i2\pi(\alpha f_0 - f_0)t - i2\pi\alpha f_0 t_0} = \tilde{A}\big(\alpha(t-t_0)\big) \cdot e^{i2\pi f_d t + i\phi_0}, \end{aligned} \tag{2.13}$$

revealing the complex Doppler signal.

### Pulsed-wave Doppler

In pulsed-wave Doppler (PW-Doppler), a series of pulses are emitted into the tissue at a constant pulse repetition frequency (PRF), phase-coherent with respect to the transmission carrier frequency $f_0$, and range-gated on receive to achieve range resolution as in regular pulse-echo imaging. As the pulses interact with moving scatterers, they are reflected and shifted in frequency according to (2.9). In PW-Doppler, the pulse length need to be shorter than $T_P = 1/PRF$ in order to achieve range resolution. This requirement and the fact that the change in pulse bandwidth due to attenuation can be large compared to the Doppler shift itself, makes it difficult to measure the Doppler shift directly as in CW-Doppler [27]. Instead, an approach based on analyzing the difference in subsequently emitted pulses is taken. Due to the axial movement of the scatterer, the received signal from consecutive emissions will be delayed an amount proportional to the axial velocity. A simplified example for a single scatterer will illustrate this. The emitted pulse typically consist of a burst of sinusoidal oscillations, as given in complex form by

$$e(t) = g(t)e^{i2\pi f_0 t}, \tag{2.14}$$

where $g(t)$ is the complex envelope of the pulse and $f_0$ is the pulse carrier frequency. Given a single scatterer at depth $r_0$ with velocity $v$ and angle $\theta$ compared to the ultrasound beam. Pulses are emitted at intervals of $T_P$ seconds. The received complex signal from a pulse emitted at time $t$ can then be described by

$$r_m(t) = e\big(\alpha(t-t_m)\big), \tag{2.15}$$

where $\alpha$ is the time compression factor given in (2.8), and $t_m$ is the relative time from pulse emission to reception for pulse number $m$, given by

$$t_m = \frac{2r_0}{c} + \frac{2v\cos\theta m T_P}{c} = t_0 + m\tau. \tag{2.16}$$

The relation between two consecutive pulses then becomes

$$r_m(t) = e\big(\alpha(t - t_m)\big) = e\big(\alpha(t - t_0 - \frac{2v\cos\theta m T_P}{c})\big) = r_{m-1}(t - \tau), \tag{2.17}$$

which in this ideal case is a delayed version of the previous pulse, given by the displacement of the scatterer in the axial direction. The velocity of the scatterer can be found either by trying to estimate $\tau$ directly from consecutive RF-signals, or by sampling the resulting change in phase compared to the carrier frequency between consecutive pulses. Conventional PW-Doppler uses the latter method. Inserting (2.14) into the expression for $r_m(t)$ gives

$$r_m(t) = g\big(\alpha(t - t_m)\big)e^{i2\pi f_0\alpha(t-t_0-m\tau)} = g(\alpha(t - t_m))e^{i2\pi f_0\alpha(t-t_0)}e^{i\phi(m)}, \tag{2.18}$$

where the additional phase function $\phi(m)$ is given by

$$\phi(m) = 2\pi f_0\alpha\frac{2v\cos\theta T_P}{c}m. \tag{2.19}$$

The frequency of this phase function then becomes

$$f_\phi = \frac{1}{2\pi}\frac{\phi(m) - \phi(m-1)}{T_P} = 2f_0\alpha\frac{v\cos\theta}{c} \approx f_d, \tag{2.20}$$

where the instantaneous frequency is approximated by a discrete derivative. As seen, the instantaneous Doppler shift is actually an artifact in pulsed Doppler systems. The equation is valid for $v\cos\theta \ll c$. This signal is termed the complex Doppler signal, or simply the Doppler signal. In practical systems, the complex Doppler signal is obtained by removing the carrier frequency through complex demodulation. The sign of the Doppler shift can be obtained by inspecting the phase relationship between the in-phase and quadrature components [20, 21].

## 2.2 Color Flow Imaging

### 2.2.1 Background

Color flow imaging (CFI) is a modality that provides an image of flow velocity and direction in a two- or three-dimensional region of interest. In this way, the distributed flow presence throughout an image region can be observed, abnormal flow patterns can be detected and investigated, and quantitative measurements of flow velocities can be combined with area estimates to produce volume flow. The information acquired by CFI is encoded in a color image, hence its name, and is combined with B-mode imaging of tissue to provide an image of both the tissue anatomy and flow conditions. The modality has been given different names, and other well used synonyms and acronyms include color flow mapping (CFM) and color-Doppler imaging (CDI), the latter is most often used in the clinical community.

In today's high-end ultrasound systems, the CFI modality is integrated along with B-mode and M-mode imaging, and also PW- and CW-Doppler modes. Duplex and

triplex imaging where combinations of the modalities are also available. The CFI modality both alone and in combination with spectral Doppler has proven valuable in many different clinical contexts, such as in cardiology, obstetrics and gynecology, pediatrics, vascular surgery, and more [18, 19]. The method has perhaps found particular use in the diagnosis of the cardiovascular system, where it for instance is used to locate and evaluate heart valve insufficiencies, septum defects, and artery plaque stenosis.

Color flow imaging provides quantitative measurements of the axial velocity and direction of blood flow. However, the method is despite of this mostly used in a qualitative way for the visual detection of areas of abnormal blood flow patterns. These areas are then further examined using the more detailed spectral display of CW- and PW-Doppler. The reason for the non-quantitative use can be related to basic limitations in temporal resolution of the velocity measurements compared to the spectral Doppler techniques, but can also be attributed to limitations of current estimation schemes with regards to velocity aliasing and angle-dependencies.

The history of ultrasound CFI began in the late seventies, when multi range gate (MRG) PW systems were introduced to estimate the flow velocity along several range gates in depth [29]. This allowed for the measurement of velocity profiles. The concept of color flow imaging emerged as a natural extension of these MRG PW instruments, by also estimating the flow velocity along several beams directions. The first two-dimensional color flow images were produced by processing data from MRG Doppler system scanned over a region of interest [30, 31].

The estimation of the complete Doppler spectrum in each range gate is an unpractical solution in CFI, and research efforts were put into finding efficient and accurate algorithms for estimating representative spectral parameters such as the mean Doppler frequency. This approach had previously been abandoned in the context of PW-Doppler systems when real-time spectral processing became feasible [32], but was once again a relevant issue for MRG Doppler and CFI methods. In CFI the estimation procedure is particulary challenging due to short ensemble lengths available for processing. Time-domain algorithms became the practical solution, and several estimators were proposed for real-time estimation of the first three spectral moments, signal power, mean frequency, and frequency spread in the CFI context [32–35].

The first real-time CFI systems were introduced in the mid-eighties. They were based on the autocorrelation approach introduced to the ultrasound community by Namekawa and Kasai [36, 37]. The method had earlier been described and used in the weather radar community [38–40], where real-time color-Doppler imaging was demonstrated as early as the mid-seventies [41]. The autocorrelation estimator has prevailed, and is today the standard algorithm used in most commercial scanner systems. Since the first real-time systems, the modality has been improved in different aspects. The first commericial system was actually based on electronic scanning using phased-array transducers. However, the potential of electronic scanning could not be fully exploited for CFI at this time, and mechanically scanned transducer systems were soon after introduced with better performance. It was first by the advent of digital front-end technology that the advantages of electronic scanning really could be utilized through beam interleaving and parallel beamforming techniques,

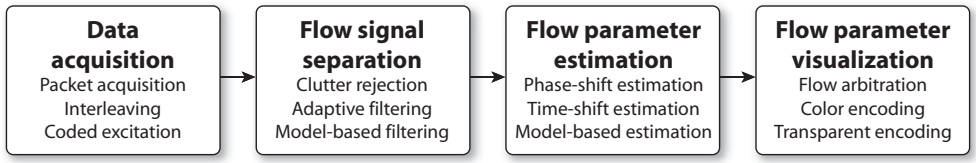


Figure 2.8: Block diagram of basic CFI processing.

increasing the flexibility and frame rate. Digital systems have further eased the implementation of new algorithms, for instance the implementation and evaluation of more advanced clutter rejection filtering, which has received much attention due to its major influence on the resulting images. The computational power of today's desktop computers are now at a stage where the CFI processing can be done in software, which further increases the flexibility. The latest technology to appear is real-time dynamic three-dimensional color flow imaging based on data acquired using 2-D phased-array transducers. This modality take full advantage of the increased processing power of current CPUs, and also the massive development in graphic card performance that has taken place in recent years, making it possible to do real-time three-dimensional rendering of image volumes.

In the following subsections, a detailed look at the inner workings of CFI systems will be given, and some aspects not covered in the thesis papers will also be included. An in-depth description of CFI systems and algorithms has also been given by Jensen [27], Angelsen and Torp [42], Wells [43], and Ferarra [44]. Detailed descriptions of clinical applications of CFI can for instance be found in [18, 19, 21].

### 2.2.2 Building blocks of ultrasound CFI

A block diagram illustrating the basic signal processing blocks of CFI is given in Fig. 2.8. At each processing stage in the figure, a number of subtopics are listed which will be explained in coming sections. The processing described is based on the assumption of using transducer arrays, where the ultrasound beam can be steered and focused electronically in the desired directions. In this way subsequent beams has discrete positions in space, which is contrary to mechanical transducers where the beam is swept continuously over the image region of interest. After the data acquisition of a complete CFI frame, $N_P$ discrete number of temporal samples is available for processing for each sample bin in the image. This temporal signal vector $\boldsymbol{x}$ is first processed to remove the clutter signal from tissue structures, which is referred to as the blood signal separation stage. After the separation of the blood flow signal, the estimation of parameters reflecting properties of the flow is performed. Typically, the mean velocity of blood scatterers, the blood signal power, and also the blood velocity spread within the sample volume is estimated. The estimated parameters are conventionally encoded in different colors and visualized superimposed on a gray-scaled B-mode image of the tissue anatomy. The CFI processing will now be described in more detail.

### 2.2.3 Data acquisition

The data acquisition in CFI is based on a pulsed wave approach. The ultrasonic beam is scanned over the region to be imaged, and a series of $N_P$ pulses are transmitted and received in each beam direction. This acquisition scheme is referred to as packet acquisition, and the number of pulses $N_P$ is called the packet size. There are several challenges in CFI acquisition. Blood flow parameters are estimated for every range gate along the beam. To investigate local changes in the two-dimensional velocity distribution, a high spatial resolution and therefore the use of high-bandwidth pulses is desired. However, assuming the pulse energy constant, the signal-to-noise ratio of the received signal from blood can be shown to be inversely proportional to the bandwidth of the emitted pulse [45], and to achieve a sufficient sensitivity, longer pulses must most often be used. This compromises the spatial resolution, and also requires a separate acquisition of B-mode images. If the acoustic energy of the emitted pulse is limited by restrictions set on the emitted pulse amplitude, one way to retain both a high spatial resolution and sufficient sensitivity could be to use coded excitation [46, 47]. For instance, a longer pulse with high bandwidth such as the chirp excitation could be transmitted, and deconvolved on receive for pulse compression.

Another challenge is that of frame rate. In order to achieve a good separation of the blood flow signal component and high quality velocity estimates, it is desired to have a high packet size. However, in order to follow the dynamics of the flow, a high imaging frame rate is required. This restricts the packet size to typically 8-16 samples depending on the clinical application. The frame rate can be increased by reducing the lateral beam sampling, however this will reduce the spatial resolution and therefore the quality of the image, and a compromise is again made. In modern scanner systems, multi-line acquisition (MLA) is often available, where several receive beams are generated per transmit beam, increasing the frame rate at the expense of more beamforming hardware [48, 49]. With the introduction of real-time 3-D color flow imaging using 2-D arrays, the problem of frame rate has become even more critical. More MLA could be performed, but these methods also introduces image artifacts. The number of MLA is also limited by demands of sensitivity, as a broader transmit beam must be used.

The received signal along each beam is sampled throughout the image depth at a high sampling rate ($\sim 50$ MHz) and is referred to as the fast-time signal. For a given range depth, the signal formed from subsequent beam acquisitions is referred to as the slow-time signal. This concept is shown in Fig. 2.9, illustrating the received and beamformed signal along a direction containing a strong stationary scatterer at $z_0$, a moving scatterer around $z_1$, and a thermal noise component. Combined, the fast-time and slow-time signal from a given range gate form the complete signal foundation of CFI velocity estimators. The corresponding Fourier space content is shown to the right. As can be seen, the blood flow signal of interest is spread in two frequency dimensions. The angle $\phi$ is related to the velocity of the scatterers through the Doppler equation.

The rate of subsequent pulse transmissions, the pulse repetition frequency (PRF), determines the sampling rate of the slow-time signal. The slow-time signal variation must therefore lie below PRF/2, the Nyquist rate, in order to be properly represented.

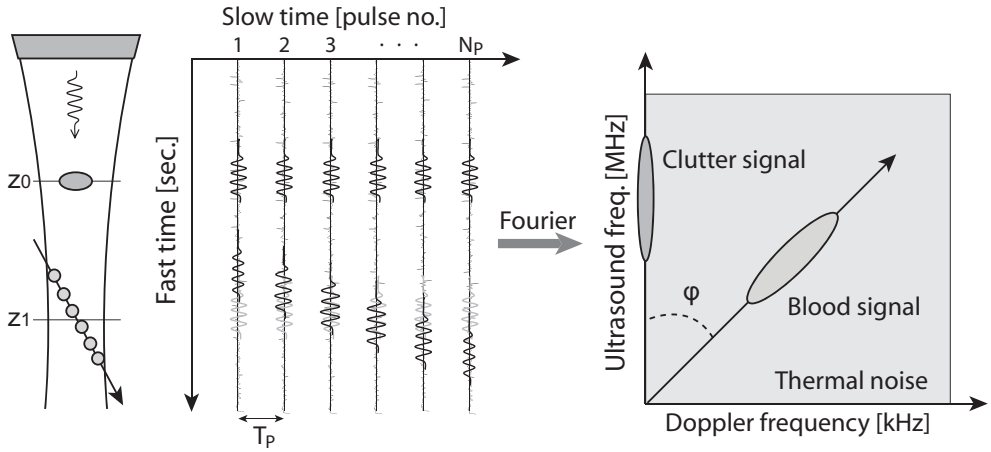


Figure 2.9: An illustration of the input signal foundation in CFI. In the example a strong stationary tissue scatterer is positioned at $z_0$ and a weaker moving blood scatterer is positioned around $z_1$. The signal along the ultrasound beam is termed the fast-time signal, while the signal from subsequent beams at a specific range is termed the slow-time signal. To the right the two-dimensional Fourier content and frequency spread of the different signal components is illustrated.

For velocity estimators utilizing the slow-time signal only, the PRF used is therefore proportional to the maximum velocity measurable before aliasing occurs. The depth of the image scan determines the maximum PRF available before ambiguities as to where the signal is obtained is introduced. Although this constraint is sometimes disregarded in high-PRF Doppler modalities, it is avoided in conventional CFI by waiting the appropriate time before firing a new pulse. By decreasing the PRF with a factor $k$, there is time to acquire data in $k-1$ other beam directions before transmitting the next pulse in the initial direction. This technique is termed beam interleaving [50]. The $k$ number of beams is called the interleave group size (IGS) and together form an interleave group (IG). The interleave group size (IGS) can be expressed by

$$\mathrm{IGS} = \left\lfloor \frac{\mathrm{PRF}_{\max}}{\mathrm{PRF}} \right\rfloor \cdot \mathrm{MLA}, \tag{2.21}$$

where MLA is the number of parallel receive beams acquired, and $\lfloor \cdot \rfloor$ means rounding off to the nearest integer towards $-\infty$. Beam interleaving is used to maximize the overall frame rate for a given user chosen PRF, set according to the blood velocity range of interest.

After beamforming and complex demodulation of the received signal has been performed, the signal-to-noise ratio (SNR) of the received signal is maximized by a filter matched to the received signal bandwidth. It has been shown that using a receive filter with a rectangular impulse response with length equal to the emitted pulse is close to optimal for this purpose [45].

### 2.2.4 Signal model

#### General signal model

After data acquisition, a two-dimensional signal matrix is in general given, consisting of sampled data in both fast-time and slow-time respectively, as illustrated in Fig. 2.9. In this thesis work, only the slow-time signal is considered, which means that the signal from each range gate is processed separately. The resulting received signal then reduces to a complex signal vector of $N_P$ slow-time samples, $\boldsymbol{x} = [x_1, x_2, \ ... \ , x_{N_P}]^T$.

The received slow-time signal from an insonified sample volume is in our general model assumed to consist of three signal components. A clutter component $\boldsymbol{c}$ originating from sound scattered from tissue and acoustic noise sources such as reverberation and beam sidelobes, a blood signal component $\boldsymbol{b}$ originating from sound scattered from the moving blood cells, and an electrical/thermal noise component $\boldsymbol{n}$. The general signal model is then given by

$$\boldsymbol{x} = \boldsymbol{c} + \boldsymbol{b} + \boldsymbol{n}. \tag{2.22}$$

The blood and clutter signal components originate from different scattering sources at different spatial locations, and are therefore considered statistically independent. As the bandwidth of the thermal noise after receiver filtering is large compared to the sampling frequency of the Doppler signal (PRF), it is modeled as white noise.

Assuming a zero-mean complex Gaussian process for the received signal from both blood and tissue as rationalized in the upcoming subsections, the probability density function (PDF) of the received signal vector is given by

$$p_x(\boldsymbol{x}) = \frac{1}{\pi^N |\mathbf{R}_x|} e^{-\boldsymbol{x}^{*T} \mathbf{R}_x^{-1} \boldsymbol{x}}. \tag{2.23}$$

Being Gaussian, the signal is completely characterized statistically by its second order moments. The second order moment information is then contained in the signal correlation matrix given by [51]

$$\mathbf{R}_x = \mathrm{E}\{\boldsymbol{x}\boldsymbol{x}^{*T}\}, \tag{2.24}$$

where E denotes the expectation operator. Assuming statistical independence this can further be written as

$$\mathbf{R}_x = \mathbf{R}_c + \mathbf{R}_b + \mathbf{R}_n = \mathbf{R}_c + \mathbf{R}_b + \sigma_n^2 \mathbf{I}, \tag{2.25}$$

where $\mathbf{R}_c$ is the clutter correlation matrix, $\mathbf{R}_b$ is the blood signal correlation matrix, $\sigma_n^2$ is the thermal noise variance, and $\mathbf{I}$ is the identity matrix. In this framework we do not assume stationarity.

#### Blood signal model

Blood is a medium consisting of several types of cells suspended in a fluid medium known as plasma. The main cell concentration is made up of red blood cells (RBCs),

or erythrocytes. The scattering medium in the blood plasma is mainly these red blood cells, which have a diameter of about $6 - 8\mu m$ [52]. As the scattering size is much smaller than the wavelength used in medical ultrasound imaging, the scattering properties will exhibit Rayleigh characteristics. This means that the sound scattered from blood follows a frequency dependency law for the scattering power of $f^4$.

There are two main approaches for modeling the blood medium and its ultrasound scattering characteristics. One approach models the blood as a large collection of particle objects [53, 54]. The main advantage of this approach is that the principle of superposition can be applied to sum the backscattered wavelets from each individual RBC. Another approach models the blood as a random continuum, where the insonified scattering volume is assumed to consist of many scattering RBCs, which together form a continuum whose density $\rho$ and compressibility $\kappa$ change due to fluctuations in blood cell concentration, causing the scattering of incoming ultrasound pressure waves [52, 55]. The two models can explain different properties known to exist for the scattering of blood, but neither are consistent with measurements of the backscattering coefficient in presence of phenomena such as turbulence, shear rate, and varying hematocrit [56, 57]. A unified approach where a hybrid of the two models have also been proposed to provide a higher level of accuracy [58]. A more thorough review of the different models proposed is also given here. There is a general agreement in both models, that the scattering of ultrasound from blood can be described as a zero-mean Gaussian process due to the large number of scattering red blood cells within an ultrasound resolution cell. Considering the complex demodulated signal, a corresponding complex Gaussian process is given.

The Doppler signal received from blood flow depends on the direction and velocity relative to the ultrasound beam of all scatterers in the ensemble present within a resolution cell. Each scatterer contributes to the total receive signal with a Doppler shift, and a finite Doppler bandwidth due to the limited observation time related to the movement through the sample volume. Turbulent behavior of flow will increase the Doppler signal bandwidth.

By assuming rectilinear motion, and Gaussian shaped beam profiles constant over the pulse shape, the received Doppler spectrum can also be shown to be Gaussian shaped [59].

### Tissue signal model

Tissue consist of different types of scatterers of varying size compared to the wavelength of the transmitted ultrasound pulse, and therefore exhibit different scattering characteristics. The scattering properties may further also vary with the angle of insonification. Such anisotropy can be observed for instance when imaging muscle fibers in the ventricle septum of the heart [25, 60]. Tissue characterization based on analysis of the backscattered pressure waves from ultrasound has been an area of research since the birth of diagnostic ultrasound imaging [5], but is still considered experimental.

A simplified view is taken in this work. It is well known, that when the ultrasound field insonifies a volume containing a large amount of randomly distributed scatterers,

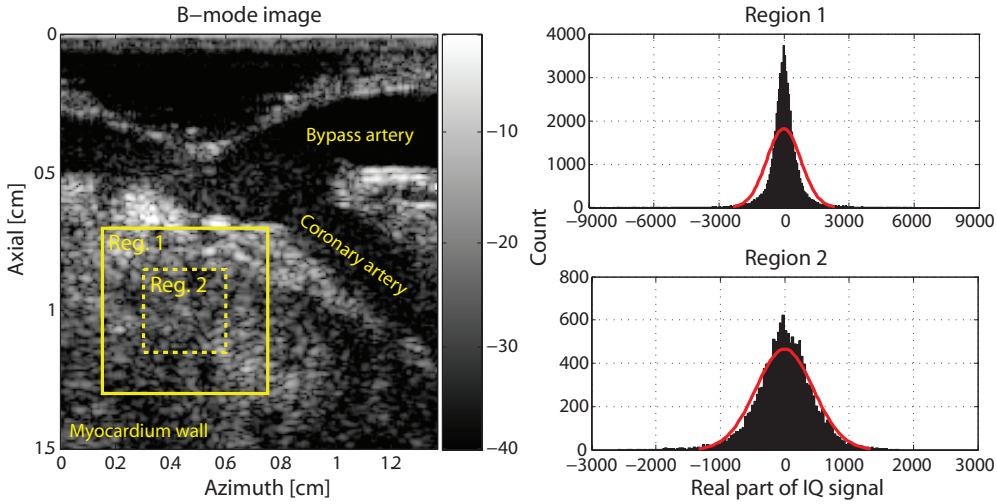


Figure 2.10: The tissue signal histogram from two different regions in the myocardium wall of a pig. As can be observed, when looking at smaller regions, the distribution of the tissue signal approaches a Gaussian shape. The data was acquired using an i13L linear array (GE Healthcare, WI, USA) with a pulse frequency of 14 MHz.

a Gaussian distributed signal results [61]. This results in what is called fully developed speckle in the ultrasound images. In parts of this thesis work where a tissue model is applied, we assume this to be the case. When considering larger regions with non-uniform scattering, a non-Gaussian distribution of the received tissue signal is typically given due to large differences in scattering strengths. It can be justified however, that when looking smaller regions in an image where a close to uniform medium is given, the distribution of the received signal from tissue approaches a Gaussian shape. An example of this is shown in Fig. 2.10, where the myocardium wall of a pig is imaged using an i13L linear array probe (GE Healthcare, WI, USA) operating at 14MHz. As can be observed, when looking at smaller sections of an image, the distribution of the tissue signal does in fact approach a Gaussian shape.

The Doppler signal from tissue results from tissue movement due to muscle contractions, and muscle vibrations in the operator holding the ultrasound probe and the patient. There may also be a relative motion of the probe against the patient skinline. The muscle contractions are typically cyclic, and are therefore accelerated. This acceleration will increase the bandwidth of the tissue Doppler spectrum. Tissue muscle vibrations were analyzed in [62], where it was modeled as a zero-mean Gaussian process, and shown to set a lower bound on the measurable Doppler shifts from blood.

### 2.2.5 Blood signal separation

Blood flow signal separation remains an important topic in CFI. Due to beam sidelobes and reverberations, signal from surrounding tissue is also present inside the vessel

lumens and the ventricles of the heart. This tissue clutter signal dominates the received signal, and is a major source of bias in subsequent estimation of blood flow parameters. Regardless of parameter estimation technique, the clutter signal must be accounted for. A similar problem exist in RADAR, where fixed target canceling (FTC) is performed to remove the stationary ground clutter component by simply subtracting subsequently acquired beams, a simple high-pass filter. In diagnostic ultrasound imaging, this problem is more elaborate. The tissue clutter can exhibit a substantial movement during the heart cycle, which complicates matters by increasing the center frequency and bandwidth of the tissue Doppler signal spectrum.

In conventional CFI algorithms, the clutter signal is removed by high-pass filtering in the slow-time domain. Due to the discrete acquisition of subsequent beams, the slow-time signal vectors must be filtered separately for each beam direction. The clutter filter in CFI should have a sufficient stop-band attenuation for removing the clutter component, and a short transition region to minimize removal of the Doppler signal from blood. For most cases a stop band damping of 80 dB would be sufficient.

For clutter filtering purposes in CFI both finite impulse response (FIR), infinite impulse response (IIR) high-pass filters, and also polynomial regression filters have been used [63–66].

### FIR filters

FIR filters can be described by an impulse response function $h(n),\ n = 0, \ldots, M-1$, where $M-1$ is denoted the filter order. With an input signal $x(n),\ n = 0, \ldots, N_P - 1$, the output signal $y(n)$ is the convolution sum given by

$$y(n) = \sum_{k=0}^{M-1} h(k)x(n-k), \tag{2.26}$$

where the first $M-1$ output samples are invalid and discarded. FIR filters have the advantage of being time invariant and easy to implement with low computational demands. On the negative end, initializing filter samples have to be discarded, leaving fewer samples for velocity estimation. As the following correlation estimates are not dependent on the phase response, improved FIR filters for CFI can be achieved by designing a minimum-phase filter [64]. A decreased variance in subsequent estimation can then also be achieved by averaging estimates achieved after filtering in both the forward and backward direction.

### IIR filters

An infinite impulse (IIR) filter can be described by the difference equation

$$y(n) = -\sum_{k=1}^{M} a_k y(n-k) + \sum_{k=0}^{M} b_k x(n-k), \tag{2.27}$$

where $M$ is denoted the filter order. This is a recursive equation, and the output samples $y(n)$ are dependent on present and past input samples as well as past output

values. Due to the small number of samples available, the transient response of the IIR filter must be reduced on the expence of a sharp steady-state filter response. The initialization of the IIR filter therefore becomes important. Several methods have been described for the initialization of IIR filters [66–68]. It has been shown that projection initialization, where the transient vector subspace is removed from the output signal by projection is superior for CFI applications [64].

#### Regression filters

Polynomial regression filters models the clutter signal by a set of orthonormal slowly varying polynomial basis functions [63, 65]. Typically, the Legendre polynomials have been used. The filter output is given as the projection of the input signal vector $\boldsymbol{x}$ onto the complement of the clutter signal basis given by

$$\boldsymbol{y} = \big(\mathbf{I} - \sum_{k=0}^{M-1} \boldsymbol{b}_k \boldsymbol{b}_k^{*T}\big)\boldsymbol{x} = \mathbf{A}\boldsymbol{x}, \tag{2.28}$$

where $\boldsymbol{b}_k$ are orthonormal basis vectors spanning the clutter signal subspace, $\mathbf{I}$ is the identity matrix and $\mathbf{A}$ is a projection matrix. The filter order is given by $M-1$. Polynomial regression filters have a high stop band attenuation, and an attractive transition region compared to FIR and IIR filters. Another specific advantage of regression filters is that no samples need to be discarded after filtering, reducing the variance in subsequent flow parameter estimation. A disadvantage of the polynomial regression filter approach is that it is not time-invariant. This causes a severe frequency distortion in the transition region of the filter [63].

In Fig. 2.11, the frequency response of the three different types of filters are shown for comparison. The main challenge of using high-pass filters to remove clutter in CFI is to achieve filters with sufficient stop-band attenuation and at the same time a sharp transition region for the short ensemble lengths available (see Section 2.2.3). Due to the resulting non-ideal frequency response of the filters, they have a negative impact on subsequent estimator accuracy [63, 64]. An insufficient stop-band attenuation for removing the clutter component will lead to a negative bias towards zero frequency for mean-frequency estimators. A long transition region of the clutter filter may remove parts of the blood flow component, causing a positive bias. Also, the white noise component becomes correlated after filtering, and contributes to a positive bias [69, 70].

### 2.2.6 Blood signal parameter estimation

In color flow imaging, the scatterer velocity is estimated by exploiting the change in the RF or baseband signal due to scatterer movement over several pulse emissions. Different approaches exist to accomplish this. The estimation of the Doppler spectrum as in PW-Doppler is not a practical solution. Few temporal samples are available and would lead to poor spectrum estimates, and the sheer amount of information would in any case be difficult to visualize properly. Instead, parameters reflecting properties

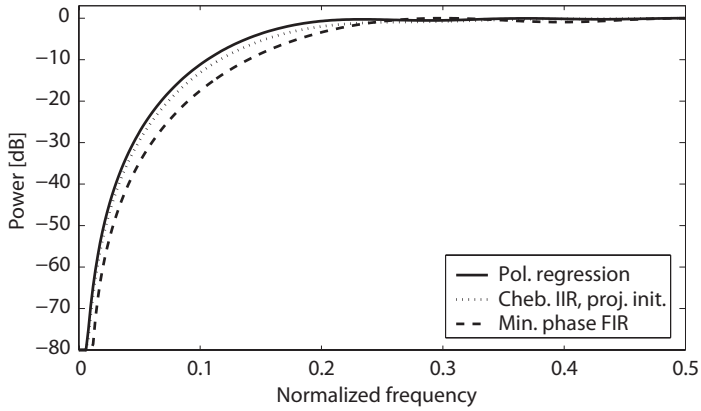


Figure 2.11: Comparison between three different types of high-pass clutter filters, a fourth order polynomial regression filter, a projection initialized Chebychev IIR filter, and a minimum-phase FIR filter. The figure is taken from [64].

of the Doppler spectrum is estimated. This process is done separately for each range bin for several beams in a region of interest.

Conventional parameters of interest in CFI are the blood flow signal power $P$ indicating the presence of blood flow, the mean frequency of the Doppler spectrum $\bar{\omega}_d$, and also the frequency bandwidth of the Doppler spectrum $B$, which relates to flow disturbance. These parameters are directly related to the first three central moments of the Doppler spectrum, which for a discrete process is given by [32, 42]

$$P = \int_{-\pi}^{\pi} G(\omega)d\omega, \quad \bar{\omega}_d = \frac{1}{P}\int_{-\pi}^{\pi} \omega G(\omega)d\omega, \quad B^2 = \frac{1}{P}\int_{-\pi}^{\pi} (\omega - \bar{\omega})^2 G(\omega)d\omega. \quad (2.29)$$

Estimation of spectral moments from short ensemble lengths is a challenging task. Much work on the subject was performed in the weather-radar community in the late seventies and early eighties parallel to the development in ultrasound imaging [40, 71], where a similar problem and data acquisition is given. Implementation wise, spectral parameter estimation can be done in the frequency or time-domain. In the frequency domain an estimate of the power spectrum $\hat{G}(\omega)$ is replaced for $G(\omega)$ in (2.29). This is however not a practical solution in CFI due to computational demands. Time-domain estimators obtain spectral parameters directly from the signal samples or through correlation analysis, and can have low computational demands.

The estimators are further characterized based on the signal information they employ. Referring to Fig. 2.9, the slow-time signal only or both the slow- and fast-time signal can be utilized. The estimators are also characterized as being either narrow or wideband estimators, based on the validity and assumption of input signal bandwidth. Narrowband estimators are in principle valid for single frequency signals, or may degrade in presence of wideband pulses, while wideband methods are valid for general wideband pulse emissions.

Phase-shift estimation is based on the fact that a displacement of the blood scatterers between pulse emissions can be related to a change in phase of the received signal compared to the demodulation frequency. Phase-shift estimation is limited by aliasing when the displacement of scatterers correspond to a phase-shift of more than $\pm\pi$. Basic phase-shift estimation utilize the slow-time signal only and are typically narrowband. Phase-shift techniques have low computational demands, and can also be done efficiently in the baseband.

Time-shift estimation is based on estimating the time delay of the received echoes due to the displacement of scatterers, tracking the scatterer movement in the received RF-signal. Methods include cross-correlation of subsequent pulse emissions, and Fourier based methods implemented in time domain. Model-based methods have also been proposed. Time-shift estimation techniques exploit both the slow- and fast-time information, and may therefore produce estimates with a lower bias and variance, and also above the aliasing limit. The improved performance may become marginal when longer pulse lengths are needed to achieve sufficient penetration. Time-shift estimation algorithms are in general much more computationally demanding than phase-shift algorithms. Also, when based on RF-data this complexity is further increased.

Several specific estimators have been proposed for the estimation of blood flow velocity in CFI. In the following subsections, a brief review of some of the most important velocity estimators will be presented. The techniques described here deals with the estimation of the axial velocity component. Experimental methods that also estimate the lateral velocity component have been given a specific review in Section 2.4.

### The autocorrelation estimator

The autocorrelation estimator was the one used to first demonstrate the feasibility of real-time two-dimensional ultrasound color flow imaging. It was introduced by Nakemawa and Kasai for diagnostic ultrasound applications in the mid-eighties [36, 37], but was earlier described in the context of weather radar by several authors [38–40], where it eventually was named the correlated pulse-pair estimator.

The autocorrelation approach estimates the three spectral parameters $P$, $\bar{\omega}_d$ and $B$ from the slow-time correlation function $R_x(m)$ at lag zero and one, given by

$$\hat{P} = \hat{R}_x(0), \quad \hat{w}_d = \angle \hat{R}_x(1), \quad \hat{B} = \sqrt{1 - \frac{|\hat{R}_x(1)|}{\hat{R}_x(0)}} \tag{2.30}$$

A simple view of of the autocorrelation mean frequency estimator can be given as follows. The correlation function $R_x(m)$ is related to the inverse Fourier transform of the Doppler spectrum through the Wiener-Kinchin theorem, which for $m = 1$ is given by

$$R_x(1) = \frac{1}{2\pi} \int_{-\pi}^{\pi} G(\omega) e^{i\omega} d\omega = \frac{e^{i\bar{\omega}_d}}{2\pi} \int_{-\pi}^{\pi} G(\omega) e^{i(\omega - \bar{\omega}_d)} d\omega. \tag{2.31}$$

As can be seen, the mean Doppler frequency $\bar{\omega}_d$ can be estimated from the phase angle of $R_x(1)$ if the imaginary part of the last integral in (2.31) is zero. This is the case

for spectra that are symmetric around the mean frequency [40], but is also a good approximation for narrowband spectra.

In practise, the autocorrelation function of lag one is estimated from the received signal sequence, $\hat{R}_x(1)$. The mean axial velocity of blood is further obtained by a scaling factor

$$\hat{v}_z = \frac{c \cdot PRF}{4\pi f_0} \angle \hat{R}_x(1) \tag{2.32}$$

The properties of the autocorrelation estimator have been examined by several authors, both in the weather radar community [38–40], and in the context of ultrasound blood velocity estimation [35, 59, 72]. The autocorrelation estimator has been shown to be an unbiased estimator of the mean spectral frequency for symmetric spectra, and in presence of white noise, and can further estimate the mean frequency over the whole frequency range from $-\pi$ to $\pi$. When utilizing spatial averaging the autocorrelation estimate has been shown to improve substantially [72]. The autocorrelation approach has also been extended to also use the fast-time signal through the simultaneous estimation of the mean fast-time frequency [73], which was shown to reduce the variance of the velocity estimates.

### The cross-correlation estimator

The cross-correlation estimator has also received much attention for blood flow velocity estimation in diagnostic ultrasound. The concept of cross-correlation estimation of blood flow velocity is in principle quite simple. As shown in Section 2.1.5, the received signal from subsequent beam emissions is delayed a given time $\tau$ due to the scatterer movement, given by

$$\tau = \frac{2\Delta z}{c} = \frac{2v \cos\theta T_P}{c}. \tag{2.33}$$

This time delay can be estimated by finding the point of maximum correlation between subsequent pulses $r_1$ and $r_2$ in a range segment, given by

$$\hat{\tau}_{max} = \arg\max R_{12}, \tag{2.34}$$

where the cross-correlation for a specific range segment in the RF-signal is estimated discretely by [27]

$$\hat{R}_{12}(m) = \frac{1}{N_S} \sum_{k=0}^{N_S-1} r_1(k) r_2(k+m), \tag{2.35}$$

where $N_S$ is the number of range samples in a given range segment. Knowing the time between pulse emissions $T_P$, the axial velocity estimate can be calculated from

$$\hat{v}_z = \frac{c}{2} \frac{\hat{\tau}_{max}}{T_P}. \tag{2.36}$$

As the velocity estimate produced by the cross-correlation technique is related to the lag of maximum correlation, it is the dominant scatterer movement that is being

tracked. The method can therefore not in general be related to the mean velocity of the ensemble insonified as the autocorrelation technique.

The cross-correlation technique applied for ultrasound blood flow velocity estimation, was described amongst others by Bonnefous [74], Foster [75], and Embree and O'Brian [76], and has been validated both in-vitro and in-vivo. The influence of different imaging system parameters on the delay estimate was described in [75]. The technique can achieve a lower variance estimate of the axial blood velocity compared to the autocorrelation approach, and is in theory not limited by aliasing. However, signal decorrelation sources will degrade the performance. The increased performance compared to the autocorrelation method is reduced when longer pulses must be used to obtained sufficient sensitivity. When also utilizing radial averaging in the autocorrelation technique, the performance of the two has been shown to be comparable in certain contexts [77].

#### Other estimators

Other estimators have been proposed since the introduction of real-time color flow imaging. Ferrara and Algazi proposed a wideband maximum likelihood estimator [78], based on a model of a slowly fluctuation range-spread target. In this approach the received signal is matched filtered to a model of the received signal of varying parameters, and parameter estimates are determined from the best match. Other wideband tracking techniques have been also proposed by Wilson [79] and Kaisar and Parker [80]. A different approach was taken by Vaitkus who proposed using a root-MUSIC estimator in CFI [81]. This estimator is based on the modeling of the blood and clutter signal components as a number of eigenvectors of the estimated signal correlation matrix. Similarly, AR modeling of the Doppler signal in CFI has also be proposed [82]. The choice of correct model order is then crucial for performance.

Although shown to have potential for velocity estimation in CFI, these methods described have not been fully validated in-vivo, and are still considered experimental.

### 2.2.7 Blood flow parameter visualization

#### Arbitration

Before display, the parametric information in CFI is combined with the tissue B-mode image for duplex operation. For each image pixel, a decision it made wether tissue of flow information is to be displayed. This hard arbitration mechanism is a way to combine the two sources of information, but it is also necessary to reduce the amount of artifacts related to the limitations of the current CFI processing. The decision is typically based on comparisons of the power and frequency estimates of the Doppler signal. An example of arbitration rule could be that higher mean frequencies indicate blood signal, but simultaneously high power estimates may indicate flashing artifacts. For this image point the tissue image should be displayed. However, such simple threshold decisions are prone to error, and artifacts therefore occur.

#### Visualization

The visualization of the estimated blood flow velocity parameters is based on color encoding [30, 43]. The most basic visualization is to encode only the mean Doppler frequency magnitude and direction. In this one-dimensional color scheme, the axial direction of flow directed towards the away from the transducer is typically encoded in different colors, while the velocity magnitude is encoded in an increased color intensity. By further using a two-dimensional color scheme where the power estimates also control the intensity of the color, a better delineation of the vessel walls can be given. In cardiac imaging, it is common to use a two-dimensional colormap based on flow velocity and bandwidth. In this mode areas of high bandwidth indicating turbulence are highlighted in green color.

Another type of CFI visualization relies only on the Doppler signal power estimate and has been named power-Doppler [83, 84]. This method is often combined with a high degree of temporal averaging to produce angiography-like images suitable for imaging of smaller vessels and low flow rates in stationary tissue, such as in abdominal imaging.

Due to the spatial extents of the point spread function in ultrasound imaging, the tissue and flow information will inherently overlap when close to one another, and lead to color blooming artifacts where the flow image may cover areas of tissue. The immediate vessel wall can for instance often be covered by the color image. This problem is further aggravated when the spatial resolution for the flow image must be reduced in order to achieve a sufficient sensitivity.

## 2.3 Adaptive clutter rejection in CFI

### 2.3.1 Filter bank approach

One approach to adaptive clutter filtering has been to select an appropriate fixed-response clutter filter for each range gate based on estimated clutter Doppler signal characteristics, such as for instance the clutter mean velocity and power. A method for iteratively selecting the appropriate cut-off frequency of polynomial regression filters has been described [85], and a method for selecting the appropriate filter from a predefined set of high-pass filters has been proposed [86].

One drawback of these methods is the ad-hoc nature of optimizing the appropriate filters for different mixtures of clutter and blood signal. Further, since the methods depend on the estimated mean frequency of the clutter signal, errors will be induced when these estimates are inaccurate. This may for instance occur inside the vessel lumen of larger arteries, where the clutter and blood signal power may become comparable. This will lead to a bias in the estimate of the mean clutter Doppler frequency. Also, accelerated clutter movement will increase the bandwidth of the clutter Doppler signal, and may also be a source of bias and variance when estimating the mean frequency of the clutter signal.

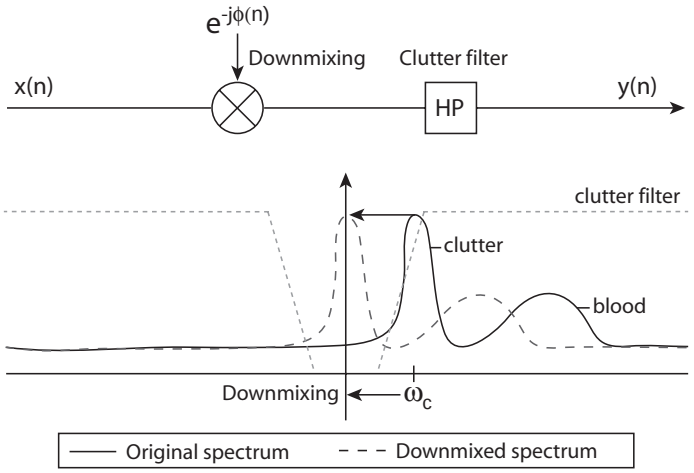


Figure 2.12: An illustration of the downmixing approach to adaptive clutter filtering. The received Doppler signal is downmixed using an estimate of the mean or varying clutter Doppler frequency.

### 2.3.2 Downmixing approach

Another adaptive filtering approach has been to process the received signal from each sample volume prior filtering. A Doppler signal downmixing technique was first proposed in [87, 88] for color flow imaging applications, and was given further elaboration in [89]. In this method, the complex slow-time Doppler signal is downmixed using a phase-function $\phi(n)$ based on estimates of the clutter Doppler frequency content, followed by a conventional non-adaptive high-pass filter. The concept is illustrated in Fig. 2.12. If successful, the clutter signal is moved to zero Doppler frequency, and a lower order clutter filter may then be used to remove the clutter component in varying conditions. This is beneficial for imaging both low and high velocities.

Estimates of the clutter Doppler frequency has been obtained using the autocorrelation approach as described in Section 2.2.6. The most simple technique performs downmixing using the estimates mean clutter Doppler frequency. The phase-function $\phi(n)$ used is then given by

$$\phi_{mf}(n) = \hat{\omega}_c n = \angle\Big[\sum_{k=1}^{N_P-2} R_x(k,1)\Big] n \tag{2.37}$$

In this way adaptation to the tissue clutter velocity is achieved. This may be satisfactory when considering the relative movement between the transducer and patient. However, as rationalized in Section 2.2.4, the tissue movement also exhibits accelerated movement. The downmixing approach can be extended to adapt to acceleration by downmixing with a varying frequency obtained from the cumulative

phase of the correlation function of lag one. In this approach, the phase-function can be given by [89]

$$\phi_{vf}(n) = \begin{cases} 0 & \text{if } n = 0 \\ \sum_{k=1}^{n} \angle \hat{R}_x(k,1) & \text{if } x = 1, \ldots, N-2 \end{cases} \tag{2.38}$$

To ensure the adaptation to the clutter signal, the autocorrelation estimates $\hat{R}_x(1)$ are averaged over a spatial region with similar characteristics.

As shown by Bjærum [89], the varying frequency approach is the most efficient of the two variants. However, the varying frequency approach must be used with caution as it may cause complications for subsequent velocity estimation. The mixing process with a varying frequency may cause artifacts in the resulting Doppler spectrum [90]. This does not occur for the constant mean frequency downmxing. A combined approach could be to use the varying frequency for power estimates, and the mean frequency downmixing for velocity estimates. By further doing arbitration based on the power estimates, flashing artifacts may be reduced. This has been proposed in a recent patent application by Germond-Rouet et al [90].

### 2.3.3 Eigenvector regression approach

A third approach to adaptive clutter rejection has been to design the clutter filter adaptively based on the received signal statistics. One such approach is eigenvector regression filtering. In this approach, the clutter signal is modeled as a linear combination of orthonormal basis vectors, obtained through the eigenvector decomposition of the signal correlation matrix. This approach to data representation and analysis has different origins and names, including principal component analysis (PCA), the Hotelling transform, and the (discrete) Karhunen-Loève transform (DKLT) [51]. Using the DKLT formulation, the received signal vector is expanded into the basis given by

$$\boldsymbol{x} = \sum_{i=1}^{N_P} \kappa_i \boldsymbol{e}_i, \qquad E\{\kappa_i \kappa_j^*\} = \begin{cases} \lambda_i & i = j \\ 0 & i \neq j \end{cases} \tag{2.39}$$

where $\boldsymbol{x}$ is a slow-time sample vector, and $\boldsymbol{e}_i$ and $\lambda_i$ are the eigenvectors and eigenvalues of the correlation matrix defined in (2.24). The expansion in (2.39) is sorted on decreasing eigenvalues $\lambda_i$, a measure of the variance or energy represented by an eigenvector $\boldsymbol{e}_i$. The DKLT follows when looking for an orthonormal basis expansion with statistically orthogonal expansion coefficients $\kappa_i$ [51]. It can be shown that this is the most efficient representation of a random process in the mean-square sense, when the expansion is truncated to use fewer than $N_P$ terms.

In the practical case, an estimated correlation matrix at a given point is obtained by averaging in a surrounding spatial region. The sample correlation matrix estimate is given by

$$\hat{\mathbf{R}}_x = \frac{1}{K} \sum_{k=1}^{K} \boldsymbol{x}_k \boldsymbol{x}_k^{*T}, \tag{2.40}$$

where $K$ number of sample vectors that are used to form the estimate. The correlation matrix is in general Hermitian symmetric and positive semidefinite, and a complete (full rank) set of eigenvectors and orthonormal eigenvalues can be estimated if the number of independent sample vectors $K$ in (4.19) is at least equal to the packet size $N_P$ [91]. The eigenvectors then span the complete signal vector space. In the context of clutter filtering, a subset of these eigenvectors are selected for representing the clutter signal component, and removed through projection filtering. The final clutter filter can be formulated as a matrix-vector multiplication as for the polynomial regression filter, given by

$$y = \left(\mathbf{I} - \sum_{i=1}^{M} \hat{\boldsymbol{e}}_i \hat{\boldsymbol{e}}_i^{*T}\right)\boldsymbol{x} = \mathbf{A}\boldsymbol{x}, \tag{2.41}$$

where $\mathbf{I}$ is the identity matrix and $\hat{\boldsymbol{e}}_i$ are the estimated eigenvectors selected for clutter representation. The filter order is defined as $M-1$, i.e., a zero order filter includes one eigenvector. As the method relies on estimation of the correlation matrix based on spatial averaging of signal vectors, the eigenvectors will represent signal components based on the average of the estimated signal statistics. Uniform statistics is therefore assumed in the averaging region. When few sample vectors are used in the averaging process, the variance of the correlation matrix estimate might also be a source of error in clutter representation.

The question remains as to how to select the proper eigenvectors for clutter representation. This aspect is crucial for the success of the algorithm. If the chosen basis does not represent most of the clutter signal, it may not be properly attenuated, and a bias in subsequent velocity estimation is inferred. Further, if eigenvectors also representing the blood signal component is included, a substantial part of the blood signal may be lost. The information available for selection of the proper basis is given by the eigenvalues and eigenvectors. The eigenvalues has information about the signal energy or variance represented by the eigenvector basis vector. A dominant signal component that constitute a large part of the total signal variance, will therefore be represented by eigenvectors with large corresponding eigenvalues. Due to the dominant and low-bandwidth nature of the clutter Doppler signal, the clutter signal energy is mostly contained in the signal subspace represented by a smaller set of eigenvectors with large corresponding eigenvalues [89]. This has been the criteria used in prior investigations [89, 92], where a fixed number of eigenvectors has been selected from the $N_P$ eigenvectors with the most dominant eigenvalues. This method follows the truncated DKLT formulation. Among alternative basis representations used for clutter filtering, such as the Legendre polynomial basis, it is optimal in removing the most of the clutter signal for a given filter order. The approach assumes that the blood signal energy is low compared to that of clutter signal. As the mixture of clutter and blood signal varies throughout an image region, the appropriate filter order also varies, and should be chosen adaptively. The filter order can be selected based on the eigenvalue spectrum information, for instance by adaptive thresholding of the eigenvalue spectrum or the eigenvalue spectrum slope.

As an alternative or extension to this approach, one can also conceive estimating the frequency content of the individual eigenvectors, and base a decision on the fact

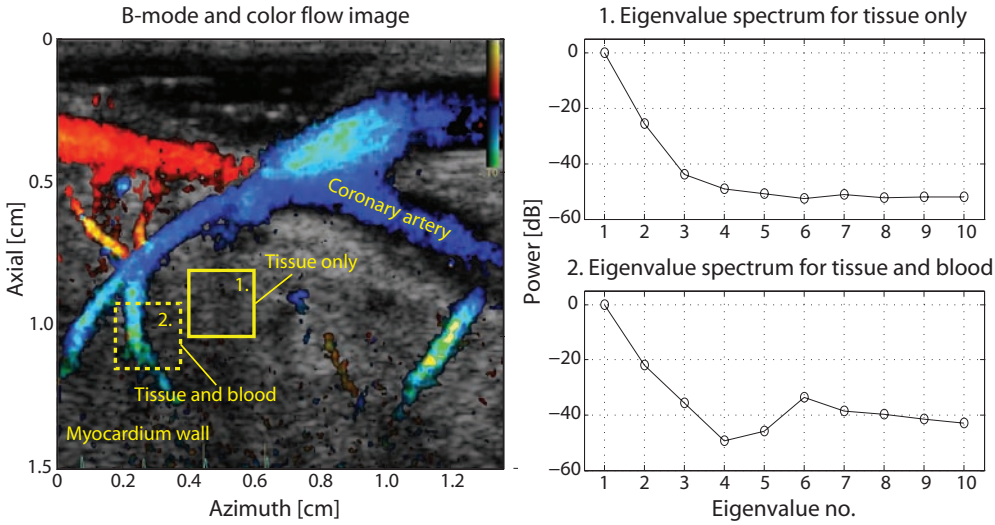


Figure 2.13: The eigenvalue spectrum from a region containing tissue signal only, and a region containing both tissue clutter and blood signal. The spectrum is sorted on increasing frequency content of the eigenvectors. As can be seen, when blood signal is introduced, it is represented by a different set of eigenvectors than that of tissue signal. The data was acquired from a beating pig myocardium using an i13L linear array (GE Healthcare, WI, USA) with a pulse center frequency of 10 MHz.

that the clutter signal typically has a lower frequency content than the signal from blood. The mean frequency of each eigenvector can for instance be estimated using the autocorrelation approach as described in Section 2.2.6. Aspects of both filter order selection schemes can be observed in Fig. 2.13. The example is based on data obtained from the beating heart of a pig, using an i13L linear array (GE Healthcare, WI, USA) with a pulse center frequency of 10 MHz. The eigenvalues have been sorted on the estimated mean frequency of each eigenvector. The clutter signal is in this example mostly represented by the first three eigenvectors. The blood signal is mostly represented by a different part of the spectrum with a higher frequency content. As can be observed by careful inspection of this example, using only the signal energy as a criteria for selecting eigenvectors would also have removed a substantial part of the blood signal if the three most dominating eigenvectors had been chosen.

An advantage of the eigenvector regression approach compared to conventional clutter filters is the fact that it can adapt to nonstationary movement. As described in Section 2.2.4, the tissue clutter signal is typically accelerated, and the received clutter signal thus exhibits this nonstationary behavior. The potential performance gain obtained from this property in a practical setting remains to be investigated.

### 2.3.4 Independent component analysis

Some efforts have been made to analyze and remove the clutter signal component by independent component analysis (ICA) [93, 94], based on the JADE algorithm described by Cardoso [95]. This is a blind signal separation approach based on the non-Gaussian characteristics of the signal components of interest. In the case of CFI, the Gaussian assumption for the blood signal component is well rationalized. For the tissue component, the different scattering characteristics throughout an image region may lead to an averaged non-Gaussian distribution. As the estimation of statistics for the signal components must be based on the assumption of uniform statistics in a region of interest, small averaging regions must be employed. As discussed in Section 2.2.4, the distribution of the tissue signal then typically approaches a Gaussian shape. Using ICA and higher-order statistics are therefore not expected to give an increase in performance compared to using a second-order Gaussian approach. The methods are therefore not properly justified for the task of clutter rejection.

## 2.4 Vector velocity imaging in CFI

### 2.4.1 Compound Doppler and related techniques

#### Compound Doppler approach

By utilizing several Doppler measurements from different beam angles, an estimate of the blood flow velocity vector can be obtained. This compound Doppler approach has been a area of research in over 30 years, and an excellent review for both PW-Doppler and CFI systems is given by Dunmire [96]. Two main approaches have been used for compound Doppler in CFI. Either combining two or three regular CFI acquisitions steered in different directions [97], or to simultaneously use separate subapertures on the same transducer array for transmit and receive [98–100]. For use in CFI the most practical approach is to transmit in one direction, and to receive and beamform from two directions in parallel using separate subapertures. This particular setup is illustrated in Fig. 2.14. In this way using parallel receive beamforming, only one frame acquisition is needed, critical for following the dynamics of the flow. The axial and lateral velocity component in this two-dimensional setup is then given by [96]

$$v_{lat} = \frac{c \cdot (f_l - f_r)}{2f_0 \cdot \sin\theta}, \qquad v_{ax} = \frac{c \cdot (f_l + f_r)}{2f_0 \cdot (1 + \cos\theta)}, \tag{2.42}$$

where $f_l$ and $f_r$ is the Doppler shift received from the left and right subaperture respectively, and $\theta$ is the angle between the receive and transmit directions. This angle can be kept constant in depth by beam steering and by gradually sliding the receive subapertures from the middle towards the ends of the transducer for increasing depths.

Limitations of the compound Doppler approach is mainly related to the problem of achieving a sufficient angle of separation between the beam directions to obtain a sufficient accuracy in velocity measurements for increasing depths. Also, for transducer

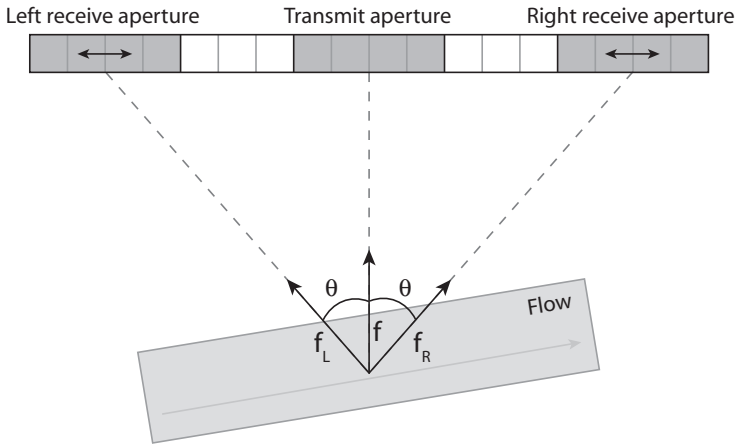


Figure 2.14: A compound Doppler approach for CFI utilizing one transmit aperture and two receive apertures beamformed in parallel.

subarray approaches, the receive apertures will be reduced in size, compromising the sensitivity. Although the compound Doppler approach has been validated to give reasonable accurate results in different vascular contexts, no mainstream system is available, and clinical studies rationalizing the use of the method are still limited [96].

### Lateral modulation approach

Another approach related to the compound Doppler technique has been proposed by Jensen and Munk [101] and Anderson [102]. The methods are based on producing a modulation in the lateral direction of the received ultrasound field, using complex apodization schemes. A scatterer movement in the lateral direction can then be registered using a phase-shift technique as in the radial direction.

The approach taken by Anderson has been called spatial quadrature, and relies on the use of a complex apodization scheme on receive to create the lateral modulation. Using odd and even apodization functions related by a Hilbert operator, an in-phase and quadrature PSF can be produced using parallel beamforming on receive. The two different receive signals are added and subtracted to produce a signal from a left and right receive subaperture, respectively, as defined by the distance between the peaks of the apodization functions.

The approach by Jensen and Munk has been named transverse oscillation. Two sinc-shaped receive apertures placed a distance apart have been used to create the lateral modulation on receive. To have a spatial modulation that only depends on the receive field, a near uniform beam is transmitted using a Gaussian transmit apodization. The in-phase and quadrature signal from the lateral modulation is directly sampled by steering two receive beams one quarter of a wavelength apart symmetrically around the transmit beam direction. This can be done by parallel beamforming in one frame acquisition.

In both methods the lateral modulation is approximated to be given through the Fraunhofer approximation as the Fourier transform of two point sources placed a distance apart. This results in a sinusoidal modulation given by

$$r_{lat}(x) = cos(2\pi \frac{D}{z\lambda} x) = cos(2\pi f_{lat} x), \tag{2.43}$$

where $D$ is the distance between the two point sources, $z$ is the depth of interest, and $\lambda$ is the wavelength of the emitted pulse.

Compared to the compound Doppler approach described above, the lateral modulation approaches uses complex apodization schemes to obtain the signal from two separated subapertures on receive. Using a Hilbert transform as in the spatial quadrature approach, is in theory identical to the compound Doppler method described. This relation was also indicated by Anderson [103]. The transverse oscillation method on the other hand, uses a narrowband approximation to the Hilbert transform, and this method is therefore at best equal to the other two.

### 2.4.2 Doppler bandwidth method

The bandwidth of the received composite Doppler signal is dependent on the spread of velocities of the scatterers present. It is further also dependent on the finite observation time of individual scatterers given as they travel through the sample volume [104, 105]. This is termed the transit-time broadening effect. Several authors have proposed models of the Doppler bandwidth variation [106–108], and the idea of estimating the lateral flow component based on the estimated Doppler bandwidth [109–111]. To obtain a bandwidth dependency independent of different beam-to-vessel angles, the methods has been based on shaping the Doppler sample volume spherically [107]. As nonstationary behavior will also contribute to the doppler spectral bandwidth, the methods are based on stationary flow assumptions.

The main challenge of this method is perhaps to obtain a robust estimate of the true Doppler signal bandwidth in a realistic setting. This can be in general be problematic in low signal-to-noise conditions. The clutter signal will also be a problem if not properly removed. This could especially be problematic in the systole part of the cardiac cycle at the time of the incoming flow pulse. The clutter rejection filter will further cause problems when the flow direction approaches a transverse direction compared to the beam, as a major part of the Doppler signal from blood may then be removed. These confounding factors has kept the Doppler bandwidth method at an experimental stage.

### 2.4.3 Speckle tracking techniques

The lateral velocity components of blood will move the blood scatterers out of the axial beam direction. As an extension to the 1-D axial cross-correlation technique, one can conceive searching for the maximum signal correlation between image acquisitions in the two-dimensional image plane, or even the three-dimensional image volume. The velocity vector can then be in principle measured based on the distance to the point of

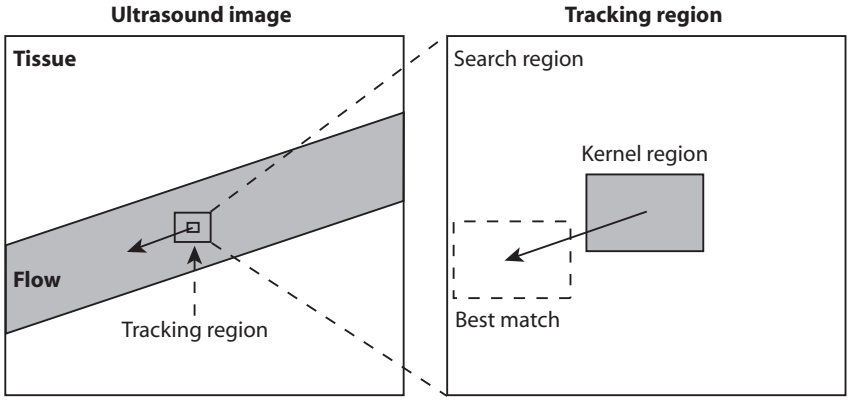


Figure 2.15: An illustration of the speckle tracking concept. The best match of a given kernel region is searched for in a larger search area of a subsequent acquisition. The velocity can be calculated based on the estimated displacement and the time between image acquisitions.

maximum correlation and the time between image acquisitions. Due to computational demands of two- or three-dimensional cross-correlation, this is difficult to do in real-time at present. However, methods have been proposed that approximate the true correlation function with similar measures. To further reduce the complexity, the methods also operate on the signal envelope rather than the RF-signal. By matching speckle pattern regions in subsequent frames an estimate of the displacement and velocity of the given pattern is given by the position of the best match. This concept, referred to as speckle tracking, is shown in Fig. 2.15 for the two-dimensional case.

Common correlation measures include the sum of absolute differences (SAD), or the sum of squared differences (SSD) of image patterns. Considering $X_0$ as the kernel region and $X_1$ to be region in a search area in a subsequent image acquisition, the SAD formula can be written as [112]:

$$\epsilon(\alpha, \beta) = \sum_{k=1}^{K} \sum_{l=1}^{L} |X_0(k, l) - X_1(k - \alpha, l - \beta)|, \tag{2.44}$$

where the quantity $\epsilon$ is termed the SAD coefficient, $K$ and $L$ defines the lateral and axial size of the kernel region, and $\alpha$ and $\beta$ defines the offset compared to the center in the search region. Pushed by the demands of multimedia video compression, SAD calculations are now an integral part of the multimedia instruction sets on modern CPUs [113], which can substantially increase the efficiency of an SAD tracking implementation.

The concept of ultrasound speckle tracking for flow velocity vector estimation was proposed at Duke University [114, 115]. This group also developed a system capable of producing approximatively 800 velocity vector estimates in real-time [116], which was analyzed in-vitro and in-vivo in a series of papers [117, 118]. Their efforts were

summarized in [112]. In general, a good correlation in velocity vector estimates was reported for regular lateral flow and high signal-to-noise ratios. Axial flow components severely decreased the accuracy of the method. Clinical in-vivo studies have not been performed.

The main limitations of the speckle tracking approach for blood flow velocity vector estimation are related to clutter filtering and speckle pattern decorrelation. To achieve a sufficient attenuation of the clutter signal while retaining the signal from blood, the imaging frame rate of the two- or three-dimensional search region must be high compared to the Doppler shifts produced by the movement of tissue. Also, when the direction of flow approaches a pure lateral direction, the Doppler shifts approaches zero, and a large part of the blood signal will be removed using traditional clutter rejection filters. Due to the lateral bandwidth of the imaging system, some blood signal will typically remain after filtering. As shown in [119], a bandpass signal is then produced, inferring an amplitude modulation in the remaining speckle pattern.

The blood flow speckle pattern rapidly decorrelates due to sources such as non-laminar flow patterns, flow velocity gradients, and out-of-plane movement in two-dimensional velocity estimation. This speckle decorrelation can severely degrade the performance of the speckle tracking procedure. Due to the bandpass nature and higher spatial frequency content in the axial direction, the decorrelation is more prominent when a substantial axial velocity component is present [120].

The high imaging frame rate of lateral subregions needed may be obtained by using beam interleaving techniques as described in Section 2.2.3. Smaller subimages are then obtained at a frame rate equal to the pulse repetition frequency. As there is no correlation of the speckle pattern between interleave groups, the speckle tracking algorithm must be performed within one group. Also, as the interleave group width shrink for increasing scan depths, so will the width of the search regions. Another approach is to track the speckle signal within groups of receive lines acquired using multiple-line acquisition (MLA) [121, 122]. In this way, very small subregions can be acquired simultaneously at a very high frame rate. Two or four times MLA is today common in high-end scanners, but this is will be further increased due to the demands of frame rate imposed by dynamic three-dimensional imaging.

Another challenge in speckle tracking is related to spatial sampling and interpolation. The movement of scatterers as estimated using speckle tracking is limited to a displacement of an integer number of beam and range samples. To ensure a sufficient overall frame rate for following the flow dynamics, the lateral sampling is limited, and interpolation methods then becomes crucial in order to estimate the movement of the scatterers with good accuracy.

In summary, although efforts have shown that speckle tracking of blood is feasible, the lack of robustness for irregular flow patterns and the challenge of clutter filtering has kept the method at an experimental stage.

## 2.5 Future directions of CFI systems

Future CFI systems has more to offer. Current trends of real-time 3-D ultrasound imaging is at the moment pushing the technology forward, and also offer new possibilities for improved 2-D imaging. Transducer, transmitter, and beamforming technology is becoming increasingly more sophisticated, and the continuing increase in computational power of standard CPUs and graphic card GPUs, opens up for the use of more advanced real-time signal processing that can be more easily implemented and evaluated.

An improved separation of flow through adaptive signal processing can be expected to improve the estimation of low-velocity flow in peripheral vessels, and to provide a better image of coronary flow in transthoracic imaging. High-frequency imaging of the microcirculation such as for the detection of angiogenesis in cancer diagnosis might also be possible in combination with more advanced clutter rejection in the future.

High-frequency imaging in the 20-80 MHz range has for practical purposes conventionally been done using mechanically steered transducers, and the CFI performance is then more challenging then for transducer arrays [123]. Current research efforts are however producing increasingly robust high-frequency arrays [124], which may increase the performance of high-frequency microcirculation imaging.

Real-time dynamic three-dimensional color flow imaging is now available, and is expected to increase the certainty of diagnosis of cardiac abnormalities such as the quantification of valve leakage area. One of the challenges of this modality is to achieve a sufficient frame rate. Currently, ECG triggering over several heart cycles is needed to obtain a sufficiently large imaging volume sector at tolerable frame rates. An increased frame rate can be expected by the use of more parallel receive beamforming, however, the number of parallel receive beams is ultimately limited by demands of penetration, as the transmit beam must be broad enough to cover all receive beams. Adaptive clutter rejection techniques may further be used to lower the packet size in CFI to achieve a higher frame rate [90].

Two- and three-dimensional vector velocity estimation has been a continuing area of research. At the moment, compound Doppler techniques and speckle tracking are perhaps the most liable candidates for accomplishing this task in the near future. Real-time operation of both these methods is today considered feasible. In high-frequency flow imaging the use of speckle tracking becomes more attractive as the signal power of blood then becomes comparable to that of tissue, and can then be tracked with less demands of clutter filtering [125].

# References


[1] J. Wild and J. Reid, "Application of echo-ranging techniques to the determination of structure of biological tissues," *Science*, vol. 115, pp. 226–230, 1952.

[2] D. Howry and W. Bliss, "Ultrasonic visualization of soft tissue structures of the body," *J. Lab. Clin. Med.*, vol. 40, pp. 579–592, 1952.

[3] I. Edler and C. Hertz, "The use of ultrasonic reflectoscope for the continuous recording of the movements of heart walls. 1954," *Clin Physiol Funct Imaging*, vol. 24, pp. 118–136, 2004.

[4] P. Wells, "Ultrasound imaging," *Phys. Med. Biol.*, vol. 51, pp. R83–R98, 2006.

[5] K. Taylor and P. Wells, "Tissue characterisation," *Ultrasound Med. Biol.*, vol. 15, pp. 421–428, 1989.

[6] J. Somer, "Electronic sector scanning for ultrasonic diagnosis," *Ultrasonics*, vol. 6, pp. 153–159, 1968.

[7] J. Griffith and W. Henry, "A sector scanner for real time two-dimensional echocardiography," *Circulation*, vol. 49, pp. 1147–1152, 1974.

[8] O. Ramm and F. Thurstone, "Cardiac imaging using a phased array ultrasound system. i. system design," *Circulation*, vol. 53, pp. 258–262, 1976.

[9] S. Satomura, "Ultrasonic doppler method for the inspection of cardiac functions," *J. Acoust. Soc. Am.*, vol. 29, pp. 1181–1185, 1957.

[10] P. Peronneau and F. Leger, "Doppler ultrasonic pulsed blood flowmeter," *Proc. 8th Int. Conf. Med. Biol. Eng.*, pp. 10–11, 1969.

[11] P. Wells, "A range-gated ultrasonic doppler system," *Med. Biol. Eng.*, vol. 7, pp. 641–652, 1969.

[12] D. Baker, "Pulsed ultrasonic doppler blood-flow sensing," *IEEE Trans. Sonics Ultrason.*, vol. 17, pp. 170–185, 1970.

[13] B. Goldberg, R. Gramiak, and A. Freimanis, "Early history of diagnostic ultrasound: the role of american radiologists," *AJR. Am. J. Roentgenol.*, vol. 160, pp. 189–194, 1993.

[14] K. Beach, "1975-2000: a quarter century of ultrasound technology," *Ultrasound Med. Biol.*, vol. 18, pp. 377–388, 1992.

[15] P. Callen, *Ultrasonography in obstetrics and gynecology, 4th edition.* Philadelphia: Elsevier/Saunders Publishing Company, 2000.

[16] A. Weyman, *Principles and Practice of Echocardiography.* Philadelphia: Lippincott Williams & Wilkins, 1993.

[17] M. Hennerici, D. Neuerburg-Heusler, M. Daffertshofer, T. Karasch, and S. Meairs, *Vascular Diagnosis With Ultrasound: Clinical References With Case Studies, 2nd edition.* New York: Thieme Medical Publishers, 2006.

[18] C. Rumack, S. Wilson, and J. Charboneau, *Diagnostic ultrasound.* St. Louis: Elsevier Mosby, 2005.

[19] H. Feigenbaum, W. Armstrong, and T. Ryan, *Feigenbaum's echocardiography, 6th edition.* Philadelphia: Lippincott Williams & Wilkins, 2005.

[20] W. McDicken, *Diagnostic ultrasonics: principles and use of instruments.* Edinburgh: Churchill Livingstone, 1991.

[21] D. Evans and W. McDicken, *Doppler ultrasound: physics, instrumentation and clinical applications, 2nd edition.* Chichester: John Wiley & Sons, 2000.

[22] B. Angelsen, *Ultrasound imaging: waves, signals, and signal processing.* Trondheim: Emantec AS, 2000.

[23] G. Ludwig, "The velocity of sound through tissues and the acoustic impedance of tissues," *J. Acoust. Soc. Am.*, vol. 22, pp. 862–866, 1950.

[24] F. Duck, *Physical properties of tissue: a comprehensive reference book.* London: Academic Press, 1990.

[25] R. Lerner and R. Waag, "Wave space interpretation of scattered ultrasound," *Ultrasound Med. Biol.*, vol. 14, pp. 97–102, 1988.

[26] A. Roguin, "Christian johann doppler: the man behind the effect," *Br. J. Radiol.*, vol. 75, pp. 615–619, 2002.

[27] J. Jensen, *Estimation of Blood Velocities Using Ultrasound - A Signal Processing Approach.* New York: Cambridge University Press, 1996.

[28] P. Atkinson and J. Woodcock, *Doppler ultrasound and its use in clinical measurement.* London: Academic Press, 1982.

[29] M. Brandestini, "Topoflow-a digital full range doppler velocity meter," *IEEE Trans. Sonics Ultrason.*, vol. 25, pp. 287–292, 1978.

[30] M. Eyer, M. Brandestini, D. Phillips, and D. Baker, "Color digital echo/doppler image presentation," *Ultrasound Med. Biol.*, vol. 7, pp. 21–31, 1981.

[31] J. Reid and M. Spencer, "Ultrasonic doppler technique for imaging blood vessels," *Science*, vol. 176, pp. 1235–1236, 1972.

[32] K. Kristoffersen and B. Angelsen, "A comparison between mean frequency estimators for multigated doppler systems with serial signal processing," *IEEE Trans. Biomed. Eng.*, vol. 32, pp. 645–657, 1985.

[33] B. Angelsen and K. Kristoffersen, "Discrete time estimation of the mean doppler frequency in ultrasonic blood velocity measurements," *IEEE Trans. Biomed. Eng.*, vol. 30, pp. 207–214, 1983.

[34] W. Barber, J. Eberhard, and S. Karr, "A new time domain technique for velocity measurements using doppler ultrasound," *IEEE Trans. Biomed. Eng.*, vol. 32, pp. 213–229, 1985.

[35] K. Kristoffersen, "Time-domain estimation of the center frequency and spread of doppler spectra in diagnostic ultrasound," *IEEE Trans. Ultrason., Ferroelec., Freq. Contr.*, vol. 35, pp. 484–497, 1988.

[36] C. Kasai, K. Namekawa, A. Koyano, and R. Omoto, "Real-time two-dimensional blood flow imaging using an autocorrelation technique," *IEEE Trans. Sonics Ultrason.*, vol. 32, pp. 458–464, 1985.

[37] K. Namekawa, C. Kasai, M. Tsukamoto, and A. Koyano, "Realtime bloodflow imaging system utilizing auto-correlation techniques," *Ultrasound Med. Biol.*, vol. Suppl 2, pp. 203–208, 1983.

[38] K. Miller and M. Rochwarger, "A covariance approach to spectral moment estimation," *IEEE Trans. Informat. Theor.*, vol. 18, pp. 588–596, 1972.

[39] D. Sirmans and B. Bumgarner, "Numerical comparison of five mean frequency estimators," *J. Appl. Meteorol.*, vol. 14, pp. 991–1003, 1975.

[40] D. Zrnic, "Spectral moment estimates from correlated pulsed pair," *IEEE Trans. Aerosp. Electron.*, vol. 13, pp. 344–354, 1977.

[41] G. Gray, R. Serafin, D. Atlas, R. Rineheart, and J. Boyajian, "Real-time color doppler radar display," *American Meteorological Society Bulletin*, vol. 56, pp. 580–588, 1975.

[42] H. Torp and B. Angelsen, *Estimation of blood velocities from Doppler signals. Ultrasound imaging, Waves, Signals, and Signal Processing vol. 2.* Trondheim: Emantec AS, 2000.

[43] P. Wells, "Ultrasonic colour flow imaging," *Phys. Med. Biol.*, vol. 39, pp. 2113–2145, 1994.

[44] K. Ferrara and G. DeAngelis, "Color flow mapping," *Ultrasound in Medicine & Biology*, vol. 23, pp. 321–345, 1997.

[45] K. Kristoffersen, "Optimal receiver filtering in pulsed doppler ultrasound blood velocity measurements," *IEEE Trans. Ultrason., Ferroelec., Freq. Contr.*, vol. 33, pp. 51–58, 1986.

[46] B. Haider, P. Lewin, and K. Thomenius, "Pulse elongation and deconvolution filtering for medical ultrasonic imaging," *IEEE Trans. Ultrason., Ferroelect., Freq. Contr.*, vol. 45, pp. 98–113, 1998.

[47] T. Misaridis, K. Gammelmark, C. Jorgensen, N. Lindberg, A. Thomsen, M. Pedersen, and J. Jensen, "Potential of coded excitation in medical ultrasound imaging," *Ultrasonics*, vol. 38, pp. 183–189, 2000.

[48] D. Shattuck, M. Weinshenker, S. Smith, and O. Ramm, "Explososcan: A parallel processing technique for high speed ultrasound imaging with linear phased arrays," *J. Acoust. Soc. Am.*, vol. 75, pp. 1273–1282, 1984.

[49] K. Thomenius, "Evolution of ultrasound beamformers," *Proceedings of the IEEE Ultrasonics Symposium, 1996*, vol. 2, pp. 1615–1622 vol2, 1996.

[50] R. Chesarek, "Ultrasound imaging system for relatively low-velocity blood flow at relatively high frame rates," *US Patent 4888694, Quantum Medical Systems, Inc.*, 1989.

[51] C. Therrien, *Discrete Random Signals and Statistical Signal Processing.* Upper Saddle River, USA: Prentice Hall Inc., 1992.

[52] B. Angelsen, "A theoretical study of the scattering of ultrasound from blood," *IEEE Trans. Biomed. Eng.*, vol. BME-27, pp. 61–67, 1980.

[53] R. Albright, "Relationship of doppler ultrasonic scattered signal characteristics to flow and beam parameters," *The Journal of the Acoustical Society of America*, vol. 59, pp. 786–789, 1976.

[54] L. Mo and R. Cobbold, "A stochastic model of the backscattered doppler ultrasound from blood," *IEEE Trans. Biomed. Eng.*, vol. 33, pp. 20–27, 1986.

[55] P. Atkinson and M. Berry, "Random noise in ultrasonic echoes diffracted by blood," *Journal of Physics A: Mathematical, Nuclear and General*, vol. 7, pp. 1293–1302, 1974.

[56] K. Shung, G. Cloutier, and C. Lim, "The effects of hematocrit, shear rate, and turbulence on ultrasonic doppler spectrum from blood," *IEEE Trans. Biomed. Eng.*, vol. 39, pp. 462–469, 1992.

[57] S. Wang and K. Shung, "In vivo measurements of ultrasonic backscattering in blood," *IEEE Trans. Ultrason., Ferroelect., Freq. Contr.*, vol. 48, pp. 425–431, 2001.

[58] L. Mo and R. Cobbold, "A unified approach to modeling the backscattered doppler ultrasound from blood," *IEEE Trans. Biomed. Eng.*, vol. 39, pp. 450–461, 1992.

[59] H. Torp, K. Kristoffersen, and B. Angelsen, "Autocorrelation technique in color flow imaging, signal model and statistical properties of the autocorrelation estimates," *IEEE Trans. Ultrason., Ferroelec., Freq. Contr.*, vol. 41, pp. 604–612, 1994.

[60] M. Aygen and R. Popp, "Influence of the orientation of myocardial fibers on echocardiographic images," *Am. J. Cardiol.*, vol. 60, pp. 147–152, 1987.

[61] R. Wagner, S. Smith, J. Sandrik, and H. Lopez, "Statistics of speckle in ultrasound b-scans," *IEEE Trans. Sonics Ultrason.*, vol. 30, pp. 156–163, 1983.

[62] A. Heimdal and H. Torp, "Ultrasound doppler measurements of low velocity blood flow: limitations due to clutter signals from vibrating muscles," *IEEE Trans., Ultrason., Ferroelec., Freq. Contr.*, vol. 44, pp. 873–881, 1997.

[63] H. Torp, "Clutter rejection filters in color flow imaging: A theoretical approach," *IEEE Trans. Ultrason., Ferroelec., Freq. Contr.*, vol. 44, pp. 417–424, 1997.

[64] S. Bjaerum, H. Torp, and K. Kristoffersen, "Clutter filter design for ultrasound color flow imaging," *IEEE Trans. Ultrason., Ferroelec., Freq. Contr.*, vol. 49, pp. 204–216, 2002.

[65] A. Hoeks, J. Vandevorst, A. Dabekaussen, P. Brands, and R. Reneman, "An efficient algorithm to remove low-frequency doppler signals in digital doppler systems," *Ultrason. Imaging*, vol. 13, pp. 135–144, 1991.

[66] A. Kadi and T. Loupas, "On the performance of regression and step-initialized iir clutter filters for color doppler systems in diagnostic medical ultrasound," *IEEE Trans. Ultrason., Ferroelec., Freq. Contr.*, vol. 42, pp. 927–937, 1995.

[67] R. Fletcher and D. Burlage, "Initialization technique for improved mti performance in phased-array radars," *Proceed. IEEE*, vol. 60, pp. 1551–1552, 1972.

[68] E. Chornoboy, "Initialization for improved iir filter performance," *IEEE Trans. Signal Process.*, vol. 40, pp. 543–550, 1992.

[69] J. Willemetz, A. Nowicki, J. Meister, F. D. Palma, and G. Pante, "Bias and variance in the estimate of the doppler frequency induced by a wall motion filter," *Ultrason. Imaging*, vol. 11, pp. 215–225, 1989.

[70] J. Rajaonah, B. Dousse, and J. Meister, "Compensation of the bias caused by the wall filter on the mean doppler frequency," *IEEE Trans. Ultrason., Ferroelec., Freq. Contr.*, vol. 41, pp. 812–819, 1994.

[71] R. Doviak and D. Zrnic, "Practical algorithms for mean velocity estimation in pulse doppler weather radars using a small number of samples," *IEEE Trans. Geosci. Remote Sensing*, vol. 21, pp. 491–501, 1983.

[72] H. Torp, K. Kristoffersen, and A. Angelsen, "On the joint probability density function for the autocorrelation estimates in ultrasound color flow imaging," *IEEE Trans. Ultrason., Ferroelec., Freq. Contr.*, vol. 42, pp. 899–906, 1995.

[73] T. Loupas, J. Powers, and R. Gill, "An axial velocity estimator for ultrasound blood flow imaging, based on a full evaluation of the doppler equation by means of a two-dimensional autocorrelation approach," *IEEE Trans., Ultrason., Ferroelec., Freq. Contr.*, vol. 42, pp. 672–688, 1995.

[74] O. Bonnefous and P. Pesque, "Time domain formulation of pulse-doppler ultrasound and blood velocity estimation by cross correlation," *Ultrason. Imaging*, vol. 8, pp. 73–85, 1986.

[75] S. Foster, P. Embree, and W. O'Brien, "Flow velocity profile via time-domain correlation: error analysis and computer simulation," *IEEE Trans., Ultrason., Ferroelec., Freq. Contr.*, vol. 37, pp. 164–175, 1990.

[76] P. Embree and W. O'Brien, "The accurate ultrasonic measurement of the volume flow of blood by time domain correlation," *Ultrasonics Symposium, IEEE 1985*, pp. 963–966, 1985.

[77] H. Torp, X. Lai, and K. Kristoffersen, "Comparison between cross-correlation and auto-correlation technique in color flow imaging," *Ultrasonics Symposium, 1993 Proceedings, IEEE 1993*, pp. 1039–1042 vol2, 1993.

[78] K. Ferrara and V. Algazi, "A new wideband spread target maximum likelihood estimator for blood velocity estimation. i. theory," *IEEE Trans. Ultrason., Ferroelec., Freq. Contr.*, vol. 38, pp. 1–16, 1991.

[79] L. Wilson, "Description of broad-band pulsed doppler ultrasound processing using the two-dimensional fourier transform," *Ultrason. Imaging*, vol. 13, pp. 301–315, 1991.

[80] S. Alam and K. Parker, "The butterfly search technique for estimation of blood velocity," *Ultrasound in Medicine & Biology*, vol. 21, pp. 657–670, 1995.

[81] P. Vaitkus and R. Cobbold, "A new time-domain narrowband velocity estimation technique for doppler ultrasound flow imaging. i. theory," *IEEE Trans. Ultrason., Ferroelec., Freq. Contr.*, vol. 45, pp. 939–954, 1998.

[82] Y. Ahn and S. Park, "Estimation of mean frequency and variance of ultrasonic doppler signal by using second-order autoregressive model," *IEEE Trans. Ultrason., Ferroelec., Freq. Contr.*, vol. 38, pp. 172–182, 1991.

[83] S. Jain, P. Fan, E. Philpot, N. Nanda, K. Aggarwal, S. Moos, and A. Yoganathan, "Influence of various instrument settings on the flow information derived from the power mode," *Ultrasound Med. Biol.*, vol. 17, pp. 49–54, 1991.

[84] J. Rubin, R. Bude, P. Carson, R. Bree, and R. Adler, "Power doppler us: a potentially useful alternative to mean frequency-based color doppler us," *Radiology*, vol. 190, pp. 853–856, 1994.

[85] S. Bjærum, H. Torp, T. Bakke, and K. Kristoffersen, *Detection and visualization of moving targets in medical ultrasound imaging, paper E: Automatic selection of the clutter filter cut-off frequency in ultrasound color flow imaging*, pp. E1–E14. Trondheim, Norway: Norwegian University of Science and Technology, 2001.

[86] Y. Yoo, R. Managuli, and Y. Kim, "Adaptive clutter filtering for ultrasound color flow imaging," *Ultrasound Med. Biol.*, vol. 29, pp. 1311–1320, 2003.

[87] L. Thomas and A. Hall, "An improved wall filter for flow imaging of low velocity flow," *Proceedings of the IEEE Ultrasonics Symposium*, vol. 3, pp. 1701–1704, 1994.

[88] P. Brands, A. Hoeks, and R. Reneman, "The effect of echo suppression on the mean velocity estimation range of the rf cross-correlation model estimator," *Ultrasound Med. Biol.*, vol. 21, pp. 945–959, 1995.

[89] S. Bjaerum, H. Torp, and K. Kristoffersen, "Clutter filters adapted to tissue motion in ultrasound color flow imaging," *IEEE Trans. Ultrason., Ferroelec., Freq. Contr.*, vol. 49, pp. 693–704, 2002.

[90] L. Germond-Rouet, L. Thanasis, and O. Bonnefous, "Clutter filtering with small ensemble lengths in ultrasound imaging," *International Patent no. WO 2005/033737 A1, Philips Electronics N.V*, 2005.

[91] G. Golub and C. V. Loan, *Matrix Computations*. Johns Hopkins University Press, 1996.

[92] D. Kruse and K. Ferrara, "A new high resolution color flow system using an eigendecomposition-based adaptive filter for clutter rejection," *IEEE Trans. Ultrason., Ferroelect., Freq. Contr.*, vol. 49, pp. 1384–1399, 2002.

[93] C. Gallippi and G. Trahey, "Adaptive clutter filtering via blind source separation for two-dimensional ultrasonic blood velocity measurement," *Ultrason. Imaging*, vol. 24, pp. 193–214, 2002.

[94] C. Gallippi, K. Nightingale, and G. Trahey, "Bss-based filtering of physiological and arfi-induced tissue and blood motion," *Ultrasound Med. Biol.*, vol. 29, pp. 1583–1592, 2003.

[95] J. Cardoso and A. Souloumiac, "Blind beamforming for non-gaussian signals," *Radar and Signal Processing, IEE Proceedings F*, vol. 140, pp. 362–370, 1993.

[96] B. Dunmire, K. Beach, K. Labs, M. Plett, and D. Strandness, "Cross-beam vector doppler ultrasound for angle-independent velocity measurements," *Ultrasound Med. Biol.*, vol. 26, pp. 1213–1235, 2000.

[97] D. Fei, C. Fu, W. Brewer, and K. Kraft, "Angle independent doppler color imaging: Determination of accuracy and a method of display," *Ultrasound in Medicine & Biology*, vol. 20, pp. 147–155, 1994.

[98] E. Papadofrangakis, W. Engeler, and J. Fakiris, "Measurement of true blood velocity by an ultrasound system," *US Patent no. 4,265,126, General Electric Company*, 1981.

[99] A. Hall and R. Bernandi, "Method for detecting two-dimensional flow for ultrasound color flow imaging," *US Patent No. 5,398,216, General Electric Company*, 1995.

[100] P. Phillips, A. Kadi, and O. von Ramm, "Feasibility study for a two-dimensional diagnostic ultrasound velocity mapping system," *Ultrasound in Medicine & Biology*, vol. 21, pp. 217–229, 1995.

[101] J. Jensen and P. Munk, "A new method for estimation of velocity vectors," *IEEE Trans. Ultrason., Ferroelect., Freq. Contr.*, vol. 45, pp. 837–851, 1998.

[102] M. Anderson, "Multi-dimensional velocity estimation with ultrasound using spatial quadrature," *IEEE Trans. Ultrason., Ferroelec., Freq. Contr.*, vol. 45, pp. 852–861, 1998.

[103] M. Anderson, "Vector flow estimator isomorphism and wall filter requirements," *Medical Imaging 2001: Ultrasonic Imaging and Signal Processing*, vol. 4325, pp. 215–226, 2001.

[104] J. Griffith, W. Brody, and L. Goodman, "Resolution performance of doppler ultrasound flowmeters," *The Journal of the Acoustical Society of America*, vol. 60, pp. 607–610, 1976.

[105] V. Newhouse, P. Bendick, and L. Varner, "Analysis of transit time effects on doppler flow measurement," *IEEE Trans. Biomed. Eng.*, vol. 23, pp. 381–386, 1976.

[106] Y. Kim and S. Park, "Modeling of doppler signal considering sample volume and field distribution," *Ultrason. Imaging*, vol. 11, pp. 175–196, 1989.

[107] A. McArdle and V. Newhouse, "Doppler bandwidth dependence on beam to flow angle," *The Journal of the Acoustical Society of America*, vol. 99, pp. 1767–1778, 1996.

[108] A. Yu, A. Steinman, and R. Cobbold, "Transit-time broadening in pulsed doppler ultrasound: a generalized amplitude modulation model," *IEEE Trans., Ultrason., Ferroelec., Freq. Contr.*, vol. 53, pp. 530–541, 2006.

[109] V. Newhouse, D. Censor, T. Vontz, J. Cisneros, and B. Goldberg, "Ultrasound doppler probing of flows transverse with respect to beam axis," *IEEE Trans. Biomed. Eng.*, vol. 34, pp. 779–789, 1987.

[110] P. Tortoli, G. Guidi, L. Mantovani, and V. Newhouse, "Velocity magnitude estimation with linear arrays using doppler bandwidth," *Ultrasonics*, vol. 39, pp. 157–161, 2001.

[111] K.-W. Yeung, "Angle-insensitive flow measurement using doppler bandwidth," *IEEE Trans., Ultrason., Ferroelec., Freq. Contr.*, vol. 45, pp. 574–580, 1998.

[112] L. Bohs, B. Geiman, M. Anderson, S. Gebhart, and G. Trahey, "Speckle tracking for multi-dimensional flow estimation," *Ultrasonics*, vol. 38, pp. 369–375, 2000.

[113] D. Boggs, A. Baktha, J. Hawkins, D. Marr, J. Miller, P. Roussel, R. Singhai, B. Toll, and K. Venkatraman, "The microarchitecture of the intel pentium 4 processor on 90nm technology," *Intel technology journal*, vol. 8, pp. 1–17, 2004.

[114] G. Trahey, J. Allison, and O. von Ramm, "Angle independent ultrasonic detection of blood flow," *IEEE Trans. Biomed. Eng.*, vol. 34, pp. 965–967, 1987.

[115] L. Bohs and G. Trahey, "A novel method for angle independent ultrasonic imaging of blood flow and tissue motion," *IEEE Trans. Biomed. Eng.*, vol. 38, pp. 280–286, 1991.

[116] L. Bohs, B. Friemel, B. McDermott, and G. Trahey, "A real time system for quantifying and displaying two-dimensional velocities using ultrasound," *Ultrasound Med. Biol.*, vol. 19, pp. 751–761, 1993.

[117] L. Bohs, B. Friemel, and G. Trahey, "Experimental velocity profiles and volumetric flow via two-dimensional speckle tracking," *Ultrasound Med. Biol.*, vol. 21, pp. 885–898, 1995.

[118] L. Bohs, B. Friemel, J. Kisslo, D. Harfe, K. Nightingale, and G. Trahey, "Three-dimensional flow images by reconstruction from two-dimensional vector velocity maps," *J. Am. Soc. Echocardiogr.*, vol. 8, pp. 915–923, 1995.

[119] S. Bjærum, *Detection and visualization of moving targets in medical ultrasound imaging, paper H: Blood Motion Imaging: A new blood flow imaging technique.* Trondheim, Norway: NTNU, 2001.

[120] B. Friemel, L. Bohs, K. Nightingale, and G. Trahey, "Speckle decorrelation due to two-dimensional flow gradients," *IEEE Trans., Ultrason., Ferroelec., Freq. Contr.*, vol. 45, pp. 317–327, 1998.

[121] L. Bohs, S. Gebhart, M. Anderson, B. Geiman, and G. Trahey, "2-d motion estimation using two parallel receive beams," *IEEE Trans. Ultrason., Ferroelect., Freq. Contr.*, vol. 48, pp. 392–408, 2001.

[122] L. Bohs, B. Geiman, M. Anderson, S. Breit, and G. Trahey, "Ensemble tracking for 2d vector velocity measurement: Experimental and initial clinical results," *IEEE Trans., Ultrason., Ferroelec., Freq. Contr.*, vol. 45, pp. 912–924, 1998.

[123] D. Goertz, J. Yu, R. Kerbel, P. Burns, and F. Foster, "High-frequency 3-d color-flow imaging of the microcirculation," *Ultrasound in Medicine & Biology*, vol. 29, pp. 39–51, 2003.

[124] J. Brown, F. Foster, E. Cherin, and G. Lockwood, "A 40 mhz linear array based on a 2-2 composite with geometric elevation focussing," *IEEE Ultrasonics Symposium Proceedings*, 2006.

[125] W. Aoudi, H. Liebgott, A. Needles, V. Yang, F. Foster, and D. Vray, "Estimation methods for flow imaging with high frequency ultrasound," *In Press, Ultrasonics*, 2006.

# Chapter 3

# Real-time adaptive clutter rejection in ultrasound color flow imaging using power method iterations

Lasse Løvstakken[1], Steinar Bjærum[2], Kjell Kristoffersen[2], Rune Haaverstad[1], and Hans Torp[1]
[1] Dept. Circulation and Medical Imaging, NTNU
[2] GE Vingmed Ultrasound, Horten, Norway

We propose a new algorithm for real-time, adaptive clutter rejection filtering in ultrasound color flow imaging (CFI) and related techniques. The algorithm is based on regression filtering using eigenvectors of the signal correlation matrix as a basis for representing clutter, a method that previously has been considered too computationally demanding for real-time processing in general CFI applications. The data acquisition and processing scheme introduced allows for a more localized sampling of the clutter statistics and, therefore, an improved clutter attenuation for lower filter orders. By using the iterative power method technique, the dominant eigenvalues and corresponding eigenvectors of the correlation matrix can be estimated efficiently, rendering real-time operation feasible on desktop computers. A new adaptive filter order algorithm is proposed that successfully estimates the proper dimension of the clutter basis, previously one of the major drawbacks of this clutter-rejection technique. The filter algorithm performance and computational demands has been compared to that of conventional clutter filters. Examples have been included which confirms that, by adapting the clutter-rejection filter to estimates of the clutter-signal statistics, improved attenuation of the clutter signal can be achieved in normal as well as more excessive cases of tissue movement and acceleration.

## 3.1 Introduction

Current color flow imaging (CFI) techniques can indicate the presence and velocity distribution of blood flow in a two-dimensional (2-D) ultrasound image in real time. These methods have become valued tools for clinicians, as they have proven to be highly useful for locating abnormal blood flow related to pathology [1, 2]. In order for CFI techniques to work properly, signals from stationary and slowly moving tissue must be removed before any attempt is made to estimate blood flow parameters. This clutter component can have a signal power of as much as 60-80 dB higher than that of blood flow, and it can infer a false detection of blood flow and biased flow velocity estimates if not sufficiently attenuated. To achieve a frame rate sufficient for following the dynamic behavior of arterial or intracardiac blood flow, few temporal samples are available for processing in CFI (typically 8-16); therefore, the task of clutter-rejection filtering is a challenge. The task has conventionally been performed by high-pass filtering the temporal samples available for each sample bin in the image. Both finite impulse response (FIR) and infinite impulse response (IIR) high-pass filters, as well as time domain polynomial regression filters have been used [3–6]. These filters have in common a fixed filter frequency response in which the filter cut-off frequency typically is adjusted according to the flow velocity range of interest in a given clinical setting.

The fixed response clutter filters can achieve sufficient clutter suppression in circumstances in which the tissue is near stationary. However, when the velocity and acceleration of the tissue movement is high, or when the tissue velocity becomes comparable to the blood flow velocities of interest, better filters are needed to properly attenuate the clutter signal component. Examples of clinical situations in which this is the case could be when imaging slow peripheral flow, or when there is excessive clutter movement, such as when imaging the coronary arteries of the beating heart. In general there also is a relative movement between the transducer and the patient that may cause problems for conventional filters. By estimating the statistical properties of the clutter from the received data, adaptive filters can be made that more accurately removes the clutter component in normal as well as more excessive cases of tissue movement. Such adaptive clutter rejection filters are the subject for this work.

Other authors have published work in this area for diagnostic ultrasound applications. One approach has been to select the most suitable, conventional, nonadaptive clutter filter from a bank of filters, based on estimated clutter characteristics [7]. Another approach introduced by Thomas and Hall [8], and given further elaboration by Bjærum et al. [9], relies on down-mixing the received Doppler signal with the estimated clutter Doppler frequency prior to clutter filtering using conventional, nonadaptive filters. A third approach, which also is the focus of this work, has been to seek an optimal clutter basis for regression filtering by using the eigenvectors of the estimated signal correlation matrix. This method was introduced for ultrasound applications by Bjærum et al. in [9], in which it was shown to be superior to the downmixing approach, but also to suffer from practical limitations. The method was further analyzed for high-frequency ultrasound applications by Kruse and Ferrara [10]. Assuming Gaussian signals, the method provides an optimal basis for regression, in maximizing the amount of clutter energy in the least amount of basis

functions. Using higher order statistics for finding optimal, independent basis functions was explored by Gallippi and Trahey [11]. Such methods of independent component analysis (ICA) may yield a more correct clutter signal basis if the Gaussian signal assumption is invalid, but they are computationally more demanding and still not properly justified.

This paper presents a new algorithm for real-time, adaptive clutter rejection filtering in CFI-related techniques, based on clutter representation by the eigenvectors of the signal correlation matrix. The method previously was shown to be superior to conventional, nonadaptive filters [9, 10, 12], but it has been considered too computationally demanding for real-time processing and has not been robust when filtering in areas containing substantial signals from blood flow as well as tissue structures. We suggest solutions to overcome these limitations by introducing a new processing and filter order selection scheme, and by using the power method for efficiently estimating the eigenvector clutter basis. A prototype of the new algorithm has been implemented and evaluated on a GE Vingmed Vivid 7 (GE Vingmed Ultrasound, Horten, Norway) ultrasound system in which filtering results show the superiority of the adaptive algorithm for the detection of blood flow in nonstationary tissue structures.

The paper has been organized as follows. In Section 3.2 some background theory is given, describing the signal model used and the theoretical views of the filter and its performance. In Section 3.3, the methods used to implement the filter and to analyze its performance are presented. In Section 3.4, results of filter analysis and filter performance compared to conventional fixed response filters are given. These results are discussed in Section 3.5. In Section 3.6, conclusions and potential future work are presented.

## 3.2 Theory

### 3.2.1 Signal model

The signal model used for the development and analysis of the algorithm follows that of Torp et al. [13]. The received signal in a given direction after beamformation is originally modeled as a zero-mean, 2-D complex Gaussian process $x(t, n)$, where $t$ is the elapsed time after pulse transmission $k$, corresponding to a depth range $r = ct/2$, and $n$ is the pulse number in the sequence of pulses emitted. The Gaussian assumption is justified by the central limiting theorem in the fact that the total received signal is a sum of contributions from a large number of independent scatterers. A 1-D clutter filter operating in the pulse-to-pulse dimension is to be developed, and the filter input signal is a sampled signal vector $\boldsymbol{x}$ consisting of $N$ temporal samples from a single sample volume, with a probability density function given by:

$$p_x(\boldsymbol{x}) = \frac{1}{\pi^N |\mathbf{R}_x|} e^{-\boldsymbol{x}^{*T} \mathbf{R}_x^{-1} \boldsymbol{x}}. \tag{3.1}$$

The received signal is assumed to consist of a clutter component $\boldsymbol{c}$ originating from sound scattered from tissue and acoustic noise sources, such as reverberation, an

electrical/thermal noise component $\boldsymbol{n}$, and a blood signal component $\boldsymbol{b}$ originating from sound scattered from the moving red blood cells. The general signal model then is given by:

$$\boldsymbol{x} = \boldsymbol{c} + \boldsymbol{n} + \boldsymbol{b}. \tag{3.2}$$

The three signal components originate from fundamentally different sources and are statistically independent. As the bandwidth of the thermal noise is much larger than the sampling frequency of the Doppler signal (PRF), it is modeled as white noise. Being Gaussian, the signal is completely characterized statistically by its second order moments. We do not assume stationarity, and the second order moment information then is contained in the signal correlation matrix given by [14]:

$$\mathbf{R}_x = \mathrm{E}\{\boldsymbol{x}\boldsymbol{x}^{*T}\}, \tag{3.3}$$

which in our case can further be written as:

$$\mathbf{R}_x = \mathbf{R}_c + \mathbf{R}_n + \mathbf{R}_b = \mathbf{R}_c + \sigma_n^2\mathbf{I} + \mathbf{R}_b, \tag{3.4}$$

where $\mathbf{R}_c$ is the clutter correlation matrix, $\mathbf{R}_b$ is the blood signal correlation matrix, $\sigma_n^2$ is the thermal noise variance, and $\mathbf{I}$ is the identity matrix.

### 3.2.2 General filter model

The general filter model used for analysis is formulated as a linear transformation in the $N$ dimensional complex vector space $\mathcal{C}^N$. This mapping can be represented by a matrix-vector multiplication as given by:

$$\boldsymbol{y} = \mathbf{A}\boldsymbol{x}, \tag{3.5}$$

where $\boldsymbol{x}$ is the input signal vector, $\mathbf{A}$ is the filter matrix, and $\boldsymbol{y}$ is the filtered signal vector. This formulation is general enough to include all conventional clutter filters such as FIR and IIR high-pass filters with linear initialization, as well as time-domain regression filters [5, 15]. The filter matrix may have complex entries, in which case a nonsymmetric filter frequency response is given.

The filter given in (3.5) is not necessarily time invariant; therefore, the frequency response cannot always be given as the Fourier transform of an impulse response. However, the frequency response can be obtained as the power of the output when the input is a complex harmonic signal, which can be shown to result in the following expression [5]:

$$H_m(\omega_2) = \frac{1}{|N-m|}\sum_k A_k(-\omega_2)^* A_{k+m}(-\omega_2)e^{-im\omega_2}, \tag{3.6}$$

where $m$ is the temporal lag in the signal correlation function, $k$ is the row number of the filter matrix, and $\omega_2$ is the temporal frequency variable in the beam-to-beam data dimension. $A_k(\omega_2)$ is the Fourier transform of row number $k$ of the filter matrix given in (3.5), defined by:

$$A_k(\omega_2) = \sum_n a(k,n)e^{-in\omega_2}. \tag{3.7}$$

For time invariant filters, it can be shown that the transfer functions for all lags, as given in (3.6), becomes equal to $|H(\omega_2)|^2$ [5]. The phase of the correlation function estimates thus is not affected by such filters.

The focus of this paper is on regression filters. The output signal then can be given as the projection of the input signal into a vector subspace, which in our case represents the complement of the subspace containing the clutter signal. The filter projection matrix for this operation is formed by [6]:

$$\mathbf{A} = \mathbf{I} - \sum_{k=1}^{K} \boldsymbol{b}_k \boldsymbol{b}_k^{*T}, \tag{3.8}$$

where $\mathbf{A}$ is the projection matrix, $\mathbf{I}$ is the identity matrix, and $\boldsymbol{b}_k$ is basis vector $k$ in a set of orthonormal basis vectors spanning the clutter signal subspace. The filter order is defined as $K-1$, i.e., a zero order filter includes one basis vector.

The Legendre polynomials are one set of orthonormal basis vectors that can be used for clutter suppression [3–5]. The resulting polynomial regression filter has been shown to have a superior frequency response compared to FIR and IIR filters for clutter filtering in CFI [6]; therefore it will be used as the main reference when comparing the efficiency of the adaptive filter algorithm developed.

### 3.2.3 Eigenvector filter basis

A more proper basis for regression filtering can be found by adapting the basis functions to the actual signal statistics. As described by Bjærum et al. [9], it is advantageous to form the clutter signal basis from a subset of the eigenvectors of the signal correlation matrix. This form of data representation and analysis has different origins and names, including principal component analysis (PCA), the Hotelling transform, and the (discrete) Karhunen-Loève transform (DKLT) [14]. Following the formulation of Karhunen and Loève, the received signal vector $\boldsymbol{x}$ in (3.2) is expanded into the orthogonal basis given by

$$\boldsymbol{x} = \sum_{i=1}^{N} \kappa_i \boldsymbol{e}_i, \qquad E\{\kappa_i \kappa_j^*\} = \begin{cases} \lambda_i & i = j \\ 0 & i \neq j \end{cases} \tag{3.9}$$

where $\boldsymbol{x}$ is the input signal vector from a given sample bin, and $\lambda_i$ and $\boldsymbol{e}_i$ are the eigenvalues and eigenvectors of the correlation matrix ordered by decreasing eigenvalue, $\lambda_1 \geq \lambda_2 \geq ... \geq \lambda_N$. The total energy of the signal equals the sum of the eigenvalues $\lambda_i$. This representation is optimal in the sense that, among all expansion in orthonormal basis vectors, it provides the best mean-square approximation of the received signal vector $x$ if the expansion is truncated to use $K < N$ basis vectors [9, 14].

The clutter subspace basis is chosen to consist of the $K$ first terms in (3.9). The rationale for this decision is that the signal variation inferred by the clutter movement is different and of higher energy than that of blood flow. Consequently, the clutter signal will be concentrated in a smaller set of eigenvectors with the largest corresponding eigenvalues [9, 10]. An illustration of a typical eigenvalue spectrum that

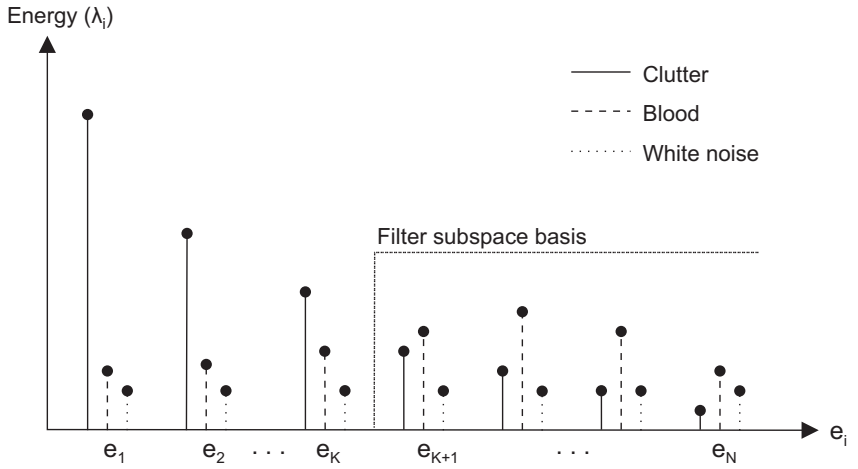


Figure 3.1: An illustration of the distribution of signal component energy over the basis given by the eigenvectors of the signal correlation matrix. Observe that the clutter signal energy is mostly distributed over the first $K$ eigenvectors with a large corresponding eigenvalue.

shows the distribution of signal components over basis functions is given in Fig. 3.1. As illustrated in the figure, most of the clutter energy is located in the directions of the first $K$ eigenvectors, and it can be removed by projecting the received signal onto the complement of this basis. If the proper clutter subspace dimension $K$ is selected, this approach will remove a maximum amount of signal from clutter while a minimum amount of signal from blood flow is lost. The resulting filter is in general complex valued; therefore, it has a nonsymmetric frequency response. In Fig. 3.2 the filter frequency response of a third order polynomial and eigenvector regression filter based on real data from moving myocardium is shown for comparison.

As emphasized in [9] and [10], selecting the proper clutter subspace basis dimension $K$ is critical for the success of the filter. Earlier methods of selecting this dimension has been based on thresholding the eigenvalues. However, this will lead only to satisfactory results if the signal vector is dominated by clutter signal. As shown in Section 3.3, this is not always the case, and a substantial part of the blood flow signal also could be removed. We propose a new adaptive method for selecting the proper subspace basis based on the gradient of the eigenvalue spectrum, as further described in Section 3.2.4.

The correlation matrix is Hermitian symmetric and positive semidefinite [14]; therefore, it is possible to find $N$ real and nonnegative eigenvalues and corresponding eigenvectors. Several methods exist for estimating the eigenvalues and eigenvectors for such matrices, where the most efficient and numerically robust methods usually are based on the singular value decomposition (SVD) or the matrix QR decomposition [16]. However, due to the small size of the correlation matrix for the given application, and because only a few of the eigenvectors with the largest eigenvalues are needed to represent the clutter signal, a different and simpler iterative method called the power

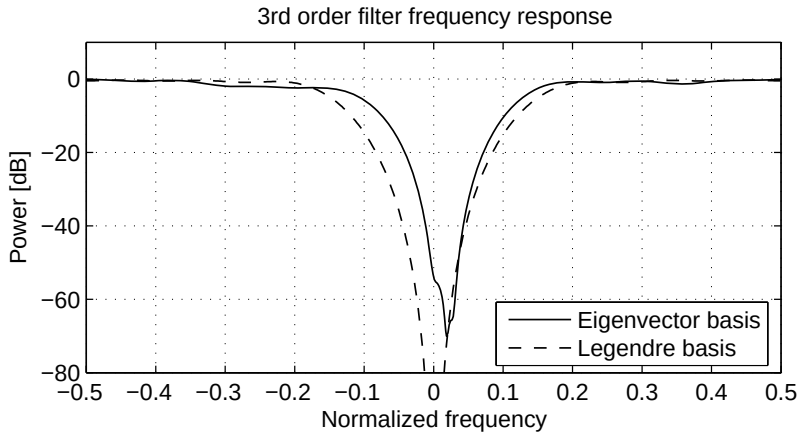


Figure 3.2: The filter frequency response of a third order polynomial and eigenvector regression filter. The adaptive eigenbasis was calculated from real data from an area of moving myocardium. Observe that the eigenvector regression filter has nonsymmetric frequency response, indicating clutter movement.

method [16] has been chosen for the estimation of the eigenvector basis. This method is highly efficient in our case, and it provides a method for directly selecting the proper clutter subspace basis. The following section describes this method in more detail.

### 3.2.4 Power method iterations

The power method is an iterative method for estimating the dominant eigenvalue and corresponding eigenvector of a matrix. It is a relatively simple method that is suited for situations in which there is a large difference between the most dominant and second most dominant eigenvalue [16]. Fortunately, this is the case in our situation in which the received signal typically consists of strong signal components from tissue in addition to signal components from blood flow and thermal noise. As only some of the eigenvectors with a large corresponding eigenvalue are needed for clutter filtering, the method also becomes computationally efficient. The method can be derived as follows.

Let $\boldsymbol{x} \in \mathcal{C}^N$ be a Gaussian distributed random vector with signal correlation matrix $\mathbf{R}_x$ as given in Section 4.2.1, and let $\boldsymbol{v}_0$ be an arbitrary vector in $\mathcal{C}^N$. The vector $\boldsymbol{v}_0$ can be written as:

$$\boldsymbol{v}_0 = \sum_{i=1}^{N} \alpha_i \boldsymbol{e}_i, \tag{3.10}$$

a linear combination of the eigenvectors $\boldsymbol{e}_i$ of $\mathbf{R}_x$, an orthonormal basis in $\mathcal{C}^N$. Further write

$$\boldsymbol{v}_k = \mathbf{R}_x^k \boldsymbol{v}_0 = \mathbf{R}_x^k \sum_{i=1}^{N} \alpha_i \boldsymbol{e}_i = \sum_{i=1}^{N} \alpha_i \mathbf{R}_x^k \boldsymbol{e}_i, \tag{3.11}$$

where $\mathbf{R}_x^k$ is $\mathbf{R}_x$ raised to the power of $k$. Because $\boldsymbol{e}_i$ are eigenvectors of $\mathbf{R}_x$, we have the relation:

$$\mathbf{R}_x^k \boldsymbol{e}_i = \lambda_i^k \boldsymbol{e}_i, \tag{3.12}$$

and (3.11) can therefore further be written as:

$$\boldsymbol{v}_k = \sum_{i=1}^{N} \alpha_i \lambda_i^k \boldsymbol{e}_i = \lambda_1^k (\alpha_1 \boldsymbol{e}_1 + \sum_{i=2}^{N} (\frac{\lambda_i}{\lambda_1})^k \alpha_i \boldsymbol{e}_i). \tag{3.13}$$

In the limit of large $k$ and if $\lambda_1 \gg \lambda_i$ for $i = 2 \ldots N$, the expression under summation in (3.13) approaches zero, and $\boldsymbol{v}_k$ then becomes equal to:

$$\lim_{k\to\infty} \boldsymbol{v}_k = \lim_{k\to\infty} \lambda_1^k (\alpha_1 \boldsymbol{e}_1 + \sum_{i=2}^{N} (\frac{\lambda_i}{\lambda_1})^k \alpha_i \boldsymbol{e}_i) = \lambda_1^k \alpha_1 \boldsymbol{e}_1, \tag{3.14}$$

a constant times the eigenvector corresponding to the most dominant eigenvalue. Normalizing this vector produces the eigenvector of interest. The eigenvalue can be estimated from the Rayleigh quotient given by:

$$\lambda_1 = \frac{\boldsymbol{e}_1^{*T} \mathbf{R}_x \boldsymbol{e}_1}{\boldsymbol{e}_1^{*T} \boldsymbol{e}_1}. \tag{3.15}$$

In this way, the most dominant eigenvalue and corresponding eigenvector can be found. The second most dominant eigenvalue and corresponding eigenvector can be found by repeating the estimation procedure after deflating $\mathbf{R}_x$ according to:

$$\mathbf{R}_x = \mathbf{R}_x - \lambda_1 \boldsymbol{e}_1 \boldsymbol{e}_1^{*T}, \tag{3.16}$$

which corresponds to setting the current most dominant eigenvalue equal to zero.

The power method converges if the modulus of the most dominant eigenvalue is unique, i.e., if $|\lambda_1| > |\lambda_2| \geq ... \geq |\lambda_N|$, and if the initial eigenvector guess is not orthogonal to the actual eigenvector. The eigenvector iterations then converge linearly at a rate proportional to $(\lambda_2/\lambda_1)^k$, and the eigenvalue iterations as calculated from the Rayleigh quotient converge linearly at a rate given by $(\lambda_2/\lambda_1)^{2k}$ [16, 17]. These properties can be used to estimate the proper dimension of the clutter subspace. A closer inspection of the eigenspectrum for different mixtures of clutter and blood flow signal reveals that the ratio between the second and the most dominating eigenvalue is substantially small only as long as clutter is present. Using the convergence rate of the power method as a measure of this property, the eigenvector iteration procedure is stopped when the rate drops below a given threshold, indicating that all or most clutter is represented by the basis thus far estimated. More details on the implementation of this method, and results of using the algorithm are given in Section 3.3.3 and Section 3.4.2, respectively.

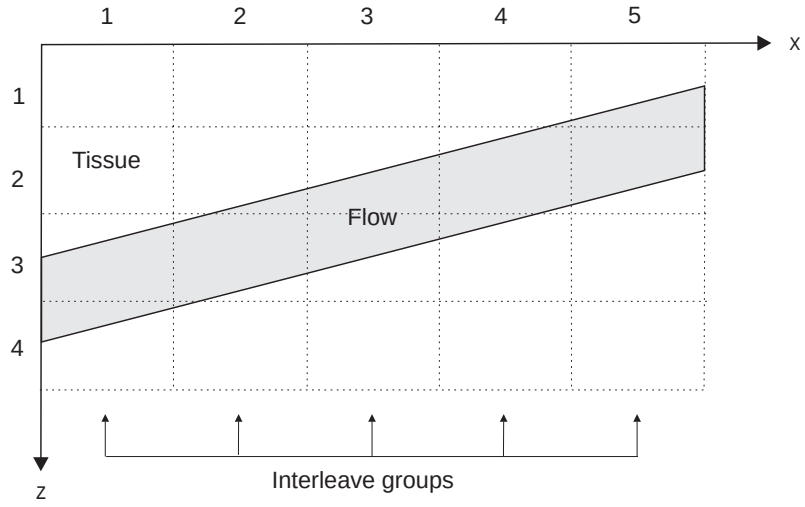


Figure 3.3: An illustration of the averaging grid used in the algorithm. The lateral (x) grid sizes coincide with the interleave group size as indicated. As can be observed, the different averaging regions may contain different mixtures of flow and tissue signal.

## 3.3 Method

### 3.3.1 Data acquisition

The data acquisition scheme used to implement the algorithm is packet acquisition as used in conventional CFI systems. The ultrasonic beam is scanned over the flow region to be imaged, and a series of $N$ pulses (typically 8-16) are transmitted in each beam direction. In each depth bin in the image, a complex signal vector of $N$ samples is formed and used for further blood flow detection and velocity estimation. The number of pulses $N$ is referred to as the packet size. For each flow image, a tissue B-mode scan is performed, and the flow and B-mode images are combined for simultaneous visualization of both blood flow and tissue structures. A parametric color display is typically used to encode the flow information. The packet acquisition scheme is combined with interleaving techniques [18], a procedure performed to maximize the frame rate for a chosen PRF. If the PRF is chosen smaller than the maximum possible for a given imaging situation, there is time to transmit in the neighboring directions. In this way, smaller parts of the total image are acquired separately, in interleave groups. Neighboring beams within interleave groups are acquired subsequently in time at the maximum PRF available. This temporal transmit scheme is advantageous when estimating the signal statistics by averaging laterally as well as radially in the image.

### 3.3.2 Estimation of second order statistics

Estimates of the correlation matrix are obtained by averaging signal vectors both laterally and radially in the image. To ensure that a maximum amount of clutter is isolated by as few eigenvectors as possible, the clutter statistics should be uniform in the averaging regions. This has been accomplished by processing separately in small regions given by a rectangular grid as shown in Fig. 3.3. A unique filter is adapted to the statistics of every grid square. For sufficiently fine grids, uniform clutter statistics is approximately given in the averaging regions, and the clutter can therefore more efficiently be represented by eigenvectors. To form a correlation matrix of full rank, the number of signal vectors averaged has to at least equal the packet size, and this is considered a lower bound for the number of signal vectors in a grid region. As shown in Fig. 3.3, the different regions may consist of signals from different mixtures of clutter and flow of varying degrees. This will affect the estimates of the correlation matrix and eigenvector basis. To ensure that the flow signal is preserved when filtering, an adaptive filter order selection algorithm is introduced, as described further in Section 3.3.3.

The formula used to estimate the correlation matrix is given by:

$$\hat{\mathbf{R}}_x = \frac{1}{K} \sum_{k=1}^{K} \boldsymbol{x}_k \boldsymbol{x}_k^{*T}, \tag{3.17}$$

where $\boldsymbol{x}_k$ is one sample vector from a spatial averaging region as illustrated in Fig. 3.3. The resulting correlation matrix is not restricted to a Toeplitz structure, and, therefore, may represent nonstationary processes. Imposing a Toeplitz structure would greatly reduce the number of computations necessary to form the estimate, but is not favorable as the clutter movement may be accelerated and, therefore, nonstationary. This also was emphasized in [9] and [10].

### 3.3.3 Adaptive filter algorithm

In Fig. 3.4, a flowchart is shown that illustrates the main steps of the filter algorithm, as well as giving an in-depth view at how power method iterations are used to estimate the proper clutter signal subspace. The complex signal vectors from a grid square are used to estimate the signal correlation matrix. This matrix is the input of the power method in which the $K$ number of eigenvectors with the most dominant eigenvalues are estimated, as illustrated in Fig. 3.1. Two main loops control the sequence of events in this algorithm. An outer loop controls the filter order, which is limited by a maximum value set as a precaution if the adaptive selection algorithm should fail. An inner loop iterates over each eigenvector estimate until the power method converges with sufficient accuracy $\epsilon$. However, if a maximum number of iterations set has been reached, the power method has failed to converge in sufficient time, and the algorithm will end. This fail-safe is in fact the adaptive order selection mechanism which ensures that mostly clutter is represented by the final filter basis. The convergence rate of the power method is related to the rate between the most dominant and second most dominant eigenvalue. This means that the method continues to estimate new eigenvectors for

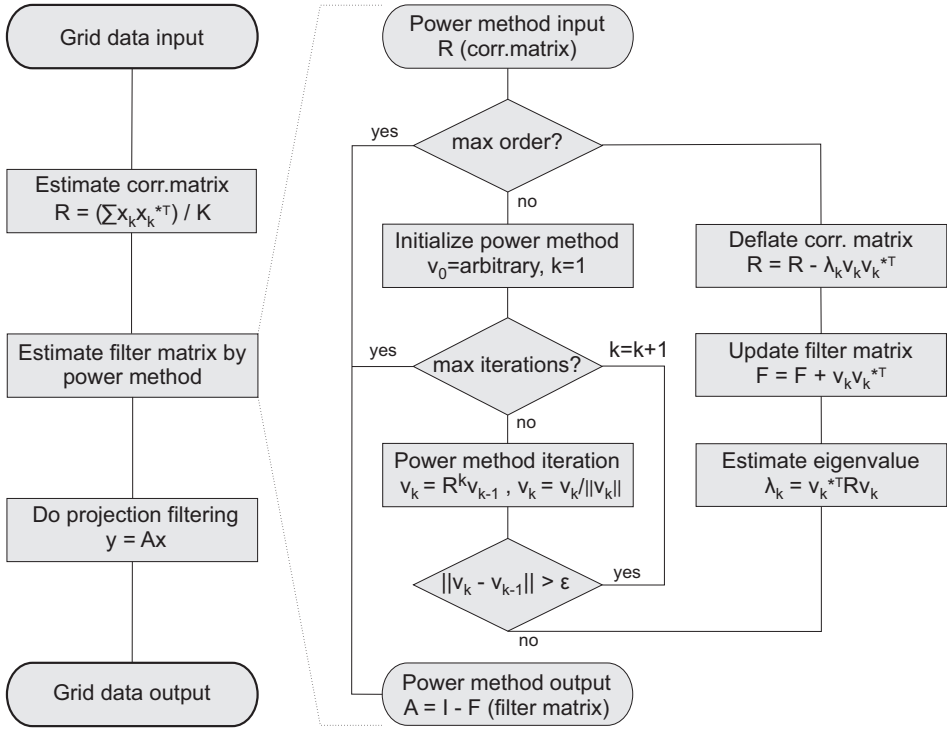


Figure 3.4: A flowchart illustrating the filter algorithm in concept. The power method iteration algorithm for estimating the eigenvectors and the filter order is shown in depth on the right-hand side. The eigenbasis estimation procedure ends if either a maximum filter order set is reached, or if the power method fails to converge to an eigenvector in a given number of iterations.

clutter representation until the eigenvalue spectrum, ordered by decreasing value, has become sufficiently flattened. The final filter projection matrix can be formed using (3.8), and the output of the main algorithm is the filtered signal vectors from the grid square in process. The procedure is repeated for every grid square. Please refer to [16] for thorough elaborations on the general power method algorithm.

The performance of general projection filters are dependent on the validity of the basis functions in representing the true clutter signal at a given spatial location. If the true clutter signal has components not contained in the signal subspace spanned by the estimated clutter basis functions, the attenuation of clutter will be degraded. This infers a poorer detection of blood flow, and it may severely affect the estimates of flow velocity and bandwidth as used in CFI algorithms. The geometric concept is illustrated in Fig. 3.5 for the case of one basis vector. If the clutter signal vector is represented by $\boldsymbol{e}_c$, and the filter basis function is given by $\hat{\boldsymbol{e}}_c$, the filter output is the projection onto the complement of $\hat{\boldsymbol{e}}_c$. This residual signal vector has $\sin^2\theta_1$ times

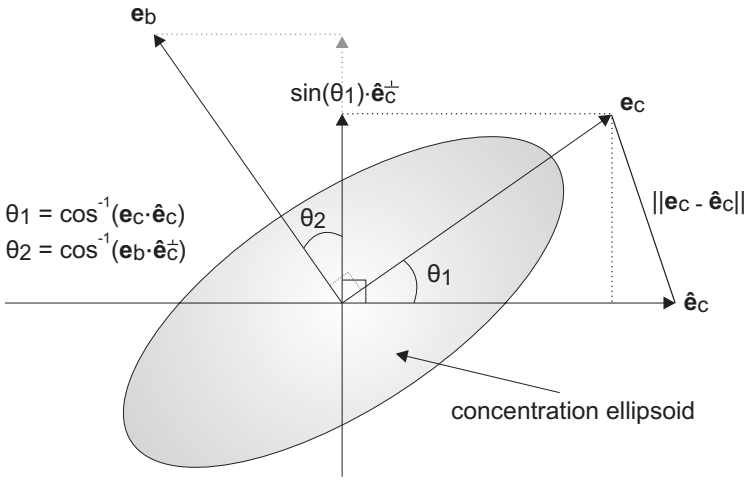


Figure 3.5: A geometric illustration of the error that may result from using an inaccurate basis vector to represent clutter. $\boldsymbol{e}_c$ represents the actual clutter signal vector, and $\hat{\boldsymbol{e}}_c$ represents the estimated basis vector. The residual signal vector after projection has $\sin^2(\theta)$ times the energy of the clutter signal vector $\boldsymbol{e}_c$.

the energy contained in the direction of $\boldsymbol{e}_c$, where $\theta_1$ is the angle between the actual clutter signal vector and basis vector approximation.

When representing the clutter signal by eigenvectors as estimated by the proposed algorithm, the misrepresentation of the clutter signal can be related to the estimation of the signal statistics, i.e., the correlation matrix, and to the estimation of the eigenvectors by the power method. When averaging, it is assumed that all sample vectors in a given region are realizations of the same process. This is not necessarily the case as different mixtures of tissue and flow signals may be present for a given region, and the estimated basis then will represent an average of this mixture. Also, as relatively few sample vectors are averaged to form the correlation matrix, the variance of the estimate also may contribute to an error. In general, the power method will converge to the dominant eigenvector. However, because the number of iterations used is limited, the estimate will not be accurate. Assuming that the error between eigenvector iterates are monotonically decreasing, the stopping criteria $\epsilon$ has been chosen so that the projection error due to the difference between the current and the previous iterate lies below a given threshold for every basis vector. This error is in decibels given by:

$$\Delta Q_k = 10\log_{10}(\sin^2(\theta_k)) \approx 10\log_{10}(||\hat{\boldsymbol{e}}_k - \hat{\boldsymbol{e}}_{k-1}||^2), \tag{3.18}$$

where $\theta_k = \cos^{-1}(\hat{\boldsymbol{e}}_k \cdot \hat{\boldsymbol{e}}_{k-1})$ is the angle between the eigenvector estimates, which for small angles can be approximated to the norm of the vector differences. As long as the attenuation error $\Delta Q_k$ lies below the maximum difference in blood flow to clutter signal power, the detection error due to the difference in vector angle is assumed negligible.

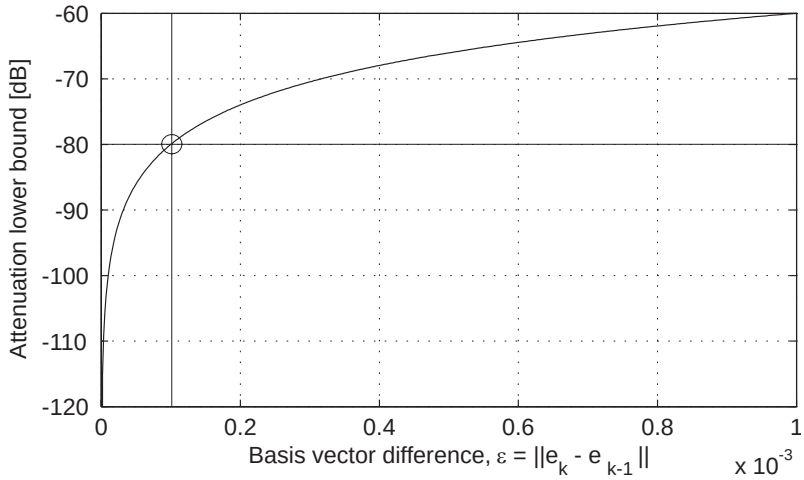


Figure 3.6: The basis vector attenuation error due to inaccuracies as given by $\epsilon = ||\boldsymbol{e}_k - \hat{\boldsymbol{e}}_{k-1}||$. The threshold $\epsilon$ is used to ensure sufficient basis vector estimation accuracy. As can be observed, an $\epsilon$ of $10^{-4}$ corresponds to at least -80 dB attenuation, which in principle should be sufficient for clutter attenuation.

This is a conservative measure, as the projection error due to one eigenvector typically is partially removed by another. In Fig. 3.6, the lower bound on attenuation for a given $\epsilon$ is shown. As seen in Fig. 3.6, an $\epsilon$ of $10^{-4}$ results in at least 80 dB clutter attenuation.

The effects of the error in basis vector representation of clutter for conventional CFI velocity estimation techniques [19], can be analyzed by using the filter frequency transfer functions as given by (3.6) and (3.7). Due to time variant filter impulse responses, the estimates of different lags of the correlation function for the Doppler signal are affected by different filter frequency transfer functions. The equations, introduced by Torp in [5], are valid for single frequency signals, and approximatively so for narrowband signals. To analyze the filter influence on the bias in mean Doppler frequency and bandwidth estimates as used in the conventional autocorrelation technique [20], only lag zero and one are needed. The bias in frequency and bandwidth due to the clutter filter then is given by:

$$\Delta f_d = \frac{\angle H_1(w)}{2\pi}, \qquad \Delta B = \sqrt{1 - \left|\frac{H_1(w)}{H_0(w)}\right|} \tag{3.19}$$

### 3.3.4 Real-time implementation

The proposed algorithm consists of three main parts, the estimation of the correlation matrix, the eigenvector basis estimation, and the clutter projection filtering. The estimation of the correlation matrix is a time-consuming part of the algorithm due to the large amount of matrix outer products needed. However, by exploiting the Hermitian symmetry of the correlation matrix, the number of complex multiplications

and additions is almost halved. It is further possible to save computations by reducing the number of signal vectors used in the correlation matrix estimate in both the radial and lateral direction of the image. We will in subsequent sections refer to this procedure as (spatial) downsampling. As indicated in Section 5.5, the amount of downsampling that can be used before the filter characteristics is affected severely, is sufficient to substantially reduce the computation time of the algorithm.

The eigenvector estimation varies in computational demands, dependent on the adaptive order and the convergence rate of the power method, which determines the number of iterations performed to produce each eigenvector. This procedure is performed for every grid region; therefore, the number of regions has a major impact on performance. Projection filtering using a complex basis, requires approximately two times the work of that using a real basis such as the Legendre polynomials, and it is a time-consuming part of the algorithm, depending on the basis dimension. The projection filter matrix is actually not calculated, as for lower order filters it is faster to do projection straight forward, one basis vector at a time.

The implementation is in general CPU cache sensitive, and loop unrolling is incorporated through the C++ compiler (Microsoft Visual C++ v7.0, Microsoft Corporation, Redmond, WA). Due to the small correlation matrix size, no special purpose data structure or linear algebra library was incorporated. The algorithm is dominated by multiplication and addition operations. Assuming a fixed-filter basis dimension $P$, the total algorithm flop count then can be calculated by counting the number of real multiplications and additions needed to produce a filtered frame of data.When including all higher order and product terms in packet size $N$ and filter basis dimension $P$, this is given by:

$$\begin{aligned} F_{tot} \simeq & \underbrace{4/k_{dwn} \cdot N^2 \cdot n_{vects})}_{F_{corr}} + \underbrace{(14NP \cdot n_{vects})}_{F_{proj}} \\ & + \underbrace{(26N^2P - 10N^2 + 18NP) \cdot n_{avg}}_{F_{eig}}, \end{aligned} \tag{3.20}$$

where $n_{vects}$ is the total number of signal vectors, $n_{avg}$ is the number of averaging regions used, and $k_{dwn}$ is the downsampling factor used when estimating the correlation matrix. The contribution of the three main parts of the algorithm has been indicated by underbracing. It is important to note that flop counting is a crude approach of measuring algorithm efficiency because it ignores overheads and aspects like subscripting and memory traffic. A listing of relevant flop counts for modern desktop CPUs is given in Table 3.1 [21]. The peak flop count is the theoretical maximum flop count for a given CPU, and the L100 and L1000 flop counts result from the more descriptive LINPACK benchmarks [22]. These benchmarks show the performance when using the optimized LINPACK library to solve the general matrix problem $Ax = b$ with a matrix size of $100x100$ and $1000x1000$, respectively. This is a relevant measure of performance in our case, as a similar algorithmic problem exists, dominated by multiplication and addition.

**Table 3.1: Flop counts for modern processors in GFlops**

| Processor | Clock rate | Peak | L100 | L1000 |
|---|---|---|---|---|
| Intel Pentium 3 | 0.9 GHz | 0.9 | 0.2 | 0.5 |
| IBM/Apple PowerPC G4 | 1.0 GHz | 2.0 | 0.3 | 1.0 |
| AMD Opteron | 2.2 GHz | 4.3 | 1.3 | 3.1 |
| **Intel Pentium 4**[1] | **3.0 GHz** | **6.0** | **1.6** | **3.2** |
| IBM/Apple PowerPC 970/G5 | 2.2 GHz | 8.8 | 1.7 | 3.8 |
| Intel Xeon | 3.6 GHz | 7.2 | 1.8 | 4.2 |

[1] The CPU used for the implementation of the real-time algorithm.

**Table 3.2: Acquisition parameters used in the clinical examples**

| Parameter | Intraoperative | Vascular |
|---|---|---|
| Clinical object | Coronary artery | Carotid artery |
| Probe | GE i13L | GE 7L |
| Probe type | Linear array | Linear array |
| Center frequency | 10 MHz | 6.7 MHz |
| Pulse length | 0.2 $\mu$s | 0.6 $\mu$s |
| F# transmit / receive | 1.4 / 1.1 | 2.5 / 1.4 |
| Beam overlap | 60 % | 20 % |
| PRF | 2.5 kHz | 1.0 kHz |
| Packet size | 10 | 12 |
| $v_{Nyquist}$ | 9.6 cm/s | 5.8 cm/s |

## 3.4 Results

In this section, results from the evaluation of the adaptive filter algorithm will be given, including examples of filtering on clinical data. Most of the clinical examples used have been acquired from pig experiments, in which coronary artery bypass grafting (CABG) surgery was performed on the beating heart, as described in [23]. Imaging the flow in the bypass anastomosis represents a major challenge for conventional clutter rejection filters due to the excessive movement of the myocardium, and it can help show the potential of adaptive filters. All data was acquired using a GE Vingmed Vivid 7 ultrasound system (GE Vingmed Ultrasound, Horten, Norway), with linear array probes suitable for the different clinical contexts. Relevant acquisition parameters for the clinical examples are given in Table 3.2.

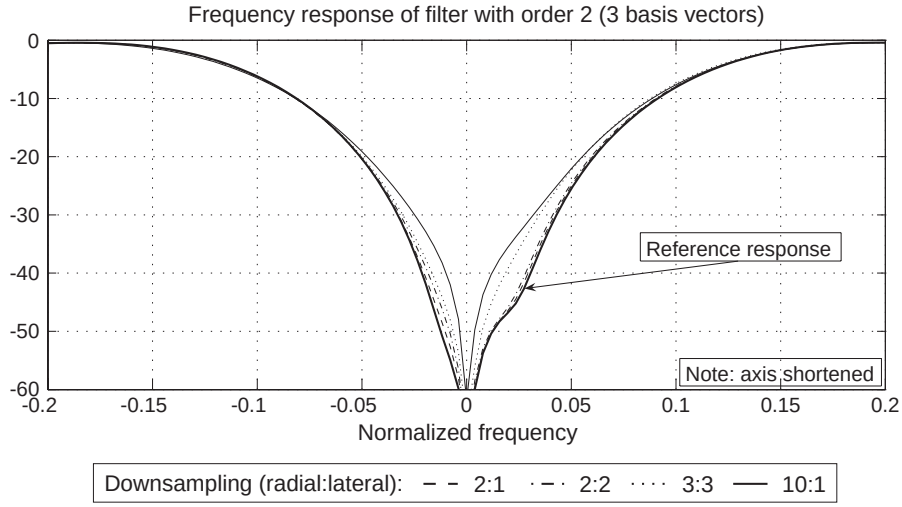


Figure 3.7: The influence of differences in filter basis due to downsampling when estimating the correlation matrix, for a case of highly nonuniform and nonstationary statistics. As can be observed, the filter characteristics change, but they are approximately the same for small downsampling factors.

### 3.4.1 Estimation of second order statistics

When reducing the number of sample vectors used in the estimate of the correlation matrix by downsampling, the variance of the estimate will increase. To see what might happen to the filter performance in such cases, the filter frequency response was calculated for different downsampling factors in an area containing highly, nonuniform and nonstationary statistics. In Fig. 3.7, the effect on the filter frequency response for a second order filter is shown in which the reference response is the fully sampled estimate. As can be seen, downsampling with factors of two in the radial and lateral direction only has small effects on the estimate.

The averaging grid size used has a major influence on how well the filter algorithm performs. This can be seen in Fig. 3.8, in which filter output using different grid sizes are shown, compared to polynomial regression filtering as a reference. The example shows coronary flow in a left internal mammary artery (LIMA) to left anterior descending (LAD) anastomosis in the early part of the diastole. First order filters are used, and the filter output is shown with a dynamic range of 40 dB. As can be observed, more effective filtering is given for finer grids. Furthermore, blocking effects due to different filter orders for different regions may become visible, as seen in the lower left image. The extreme case of using just enough samples to form a correlation matrix of full rank is given in the lower right image. As can be observed, near perfect detection can be obtained, even for the case of imaging coronary arteries in highly moving tissue structures.

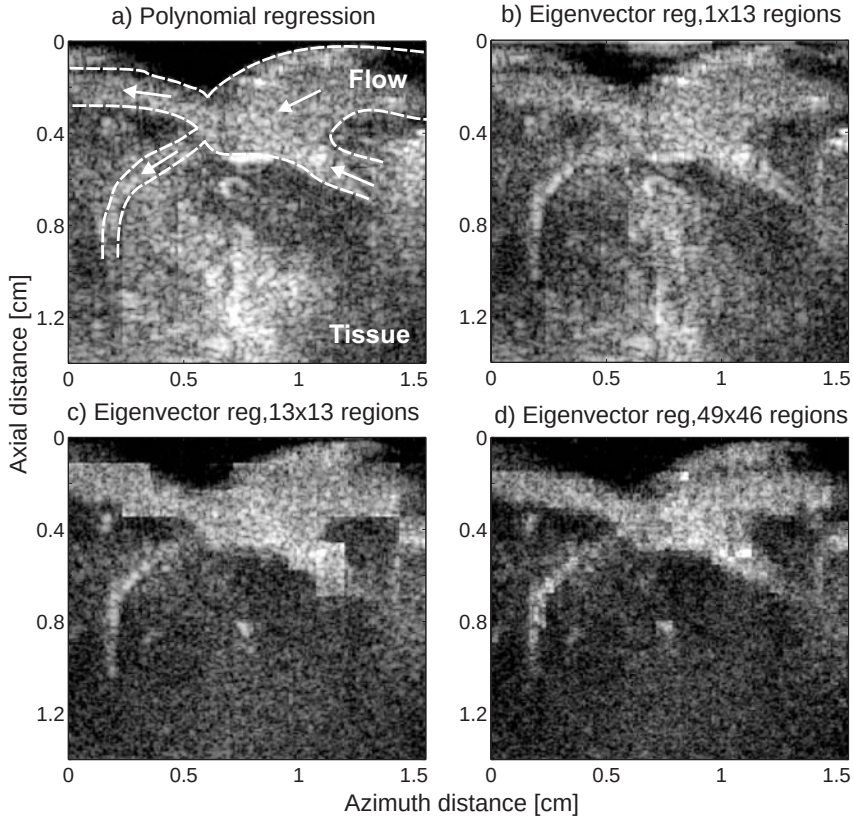


Figure 3.8: Filtering using different averaging grids (rows x cols) compared to polynomial regression filtering. The filter order is 1, and the filter output is shown with a dynamic range of 40 dB. A finer grid results in better attenuation of clutter. However, block artifacts may appear where neighboring regions have different signal characteristics.

### 3.4.2 Adaptive filter results

The success of the filter order selection mechanism is critical for the success of the filter algorithm. Two clinical examples used to evaluate this mechanism are given in Fig. 3.9. The images were filtered using a fine grid while allowing the dimension of the filter basis to vary freely. The parametric images to the right shows the filter basis dimension chosen for the different grid regions. In the reference images to the left, actual areas of flow have been illustrated. Comparing the reference images with the parametric images, one can observe that areas containing tissue and areas in which one would expect increased tissue movement get a higher filter order than areas containing blood flow signal. Also, areas containing large amounts of blood flow and little clutter, as in the vessel lumen, are given lower order filters. This shows that the filter algorithm

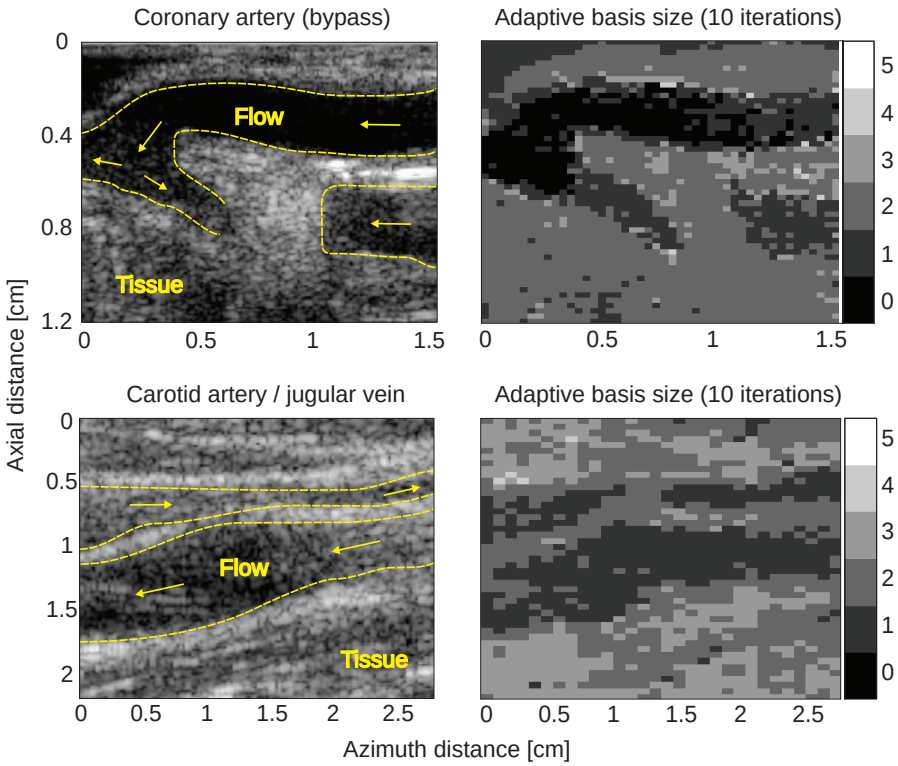


Figure 3.9: Results of the adaptive order algorithm. The filter basis dimension varies without restrictions for two different clinical examples. The parametric images to the right show the filter basis dimension chosen for each averaging region. As can be seen, the filter basis dimension is chosen to be smaller in areas of flow and reduced clutter.

is able to retain the blood flow signal while properly suppressing clutter.

Three filtering examples using data from coronary artery bypass surgery on the beating heart and from the carotid artery are shown in Fig. 3.10. The coronary images in the first two rows are from the early diastole and systole, respectively, and contain excessive tissue movement that represents a challenge for conventional, nonadaptive clutter filters. A carotid artery example image from the systole has been included in the bottom row to show how the adaptive filter order mechanism can help retain the blood flow signal for higher order filters. As a reference, the Legendre polynomial basis filter has been used. This filter has the highest stop band attenuation and steepest transition regions among the conventional fixed order filters, and it also is implemented by projection as described in Section 3.2.2. As can be seen in the coronary examples in the first two rows, the eigenvector basis is superior to the Legendre basis. This is typically the case for low-order filters (∼3rd order). However, as can be seen, using a fixed order eigenvector basis may remove parts of the blood flow components in some

areas. Looking at the rightmost images, the adaptive order eigenvector basis preserves the blood flow components in these areas and provides a better filling of the vessel lumen. In the bottom row, examples showing the carotid artery and jugular vein, a high filter order was chosen on purpose. As evident, the polynomial basis outperforms the fixed order eigenvector basis. However, by using an adaptive eigenvector basis order, superior filtering is obtained.

In Fig. 3.11, examples of typical, filter-induced bias in mean frequency and bandwidth estimators as used in the conventional autocorrelation technique are given. The bias in mean frequency and bandwidth was calculated, using the expressions in (3.19), and compared for filtering, using the eigenvector and Legendre polynomial basis. Two different contexts were investigated: filtering an area containing tissue only, and filtering an area containing both tissue and flow. The acquisition parameters for the two cases are the same as for the coronary examples. As can be seen, the bias in both mean frequency and bandwidth for the proposed filter are comparable to the Legendre polynomial basis for low filter orders, and are mainly given in the filter transition and stop band. As can be observed in the second context, including flow eigenvectors in the filter basis as for the second and third order filters, will induce a severe bias in both mean frequency and bandwidth.

### 3.4.3 Real-time performance

The average and worst case theoretical flop count of the new algorithm has been compared to that of FIR filtering, IIR filtering, and polynomial regression filtering. Projection initialized IIR filters were shown in [6] to be the only type of IIR filters with sufficient stop band attenuation for clutter rejection filtering with limited temporal samples available as in CFI; therefore, it has been used in the comparison. The total flop count of the new algorithm is a function of the amount of sample vectors, the filter order, the packet size, the degree of downsampling in correlation estimates, and the number of averaging regions used. In Fig. 3.12, the flop counts for the different filters are given when varying some of these parameters. The default values of the respective parameters are indicated by the dashed vertical line in each plot. The average case flop count for the new algorithm corresponds to an average filter order of two compared to three for the other filters. This is considered a fair estimate when many averaging areas contain uniform clutter movement or blood flow. The time spent processing per frame in milliseconds using the L100 benchmark for a Pentium 4 class CPU is given in the rightmost y-axis. Quite high theoretical frame rates can be achieved, even for fine grids, ignoring overhead associated with further processing and display. As also can be seen, downsampling when estimating the correlation matrix may substantially decrease the processing time per frame.

## 3.5 Discussion

Several aspects regarding the proposed adaptive filter algorithm and filter-order selection mechanism needs to be discussed. The main aspects that have an impact

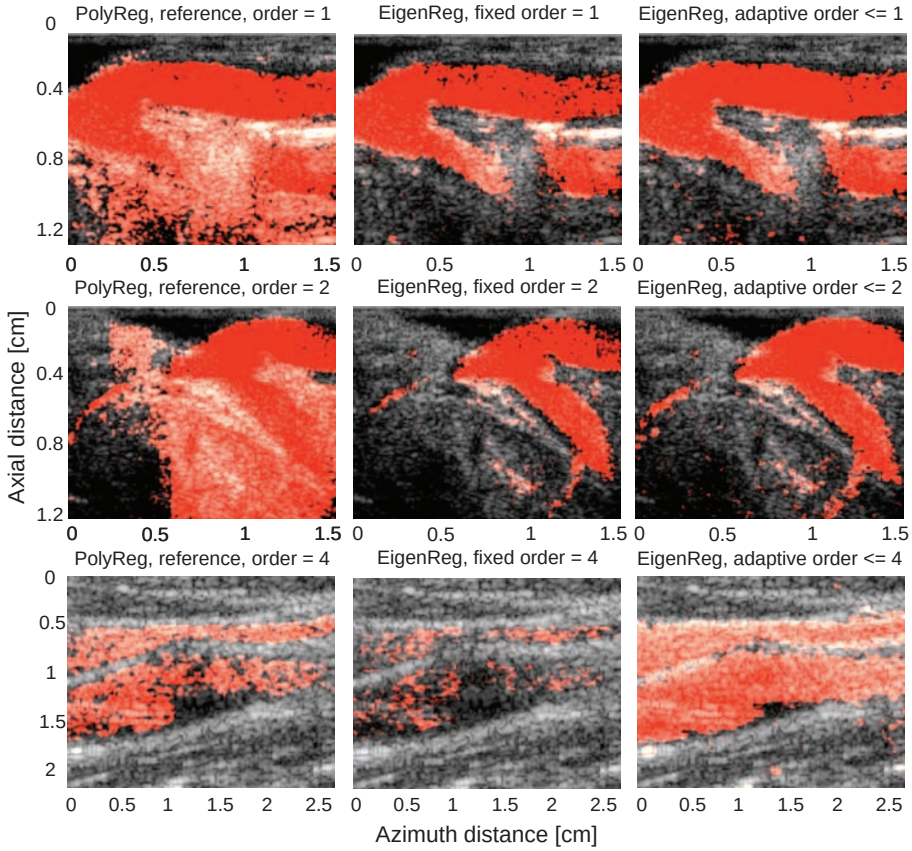


Figure 3.10: Results of filtering clinical data using the adaptive filter algorithm. The first column of images was obtained using the Legendre polynomial basis, the middle column was obtained using a fixed order eigenvector basis, and the rightmost column was obtained using eigenvector basis with adaptive order. As can be observed, improved clutter attenuation and flow preservation is achieved using the proposed algorithm.

on the filter performance are the estimation of the correlation matrix, the estimation of the eigenvectors, the selection of filter order, and the projection step performed to separate the clutter component.

The estimate of the correlation matrix is dependent on how the signal vectors are acquired and averaged. By also averaging in the lateral direction, the amount of radial averaging can be reduced, and more localized sampling of the clutter statistics can be achieved. This corresponds to lower filter order demands for representing the clutter in that area. As described in Section 3.3.1, when the user chosen PRF is less then the maximum given by the depth of the ultrasound scan, beam interleaving can be used

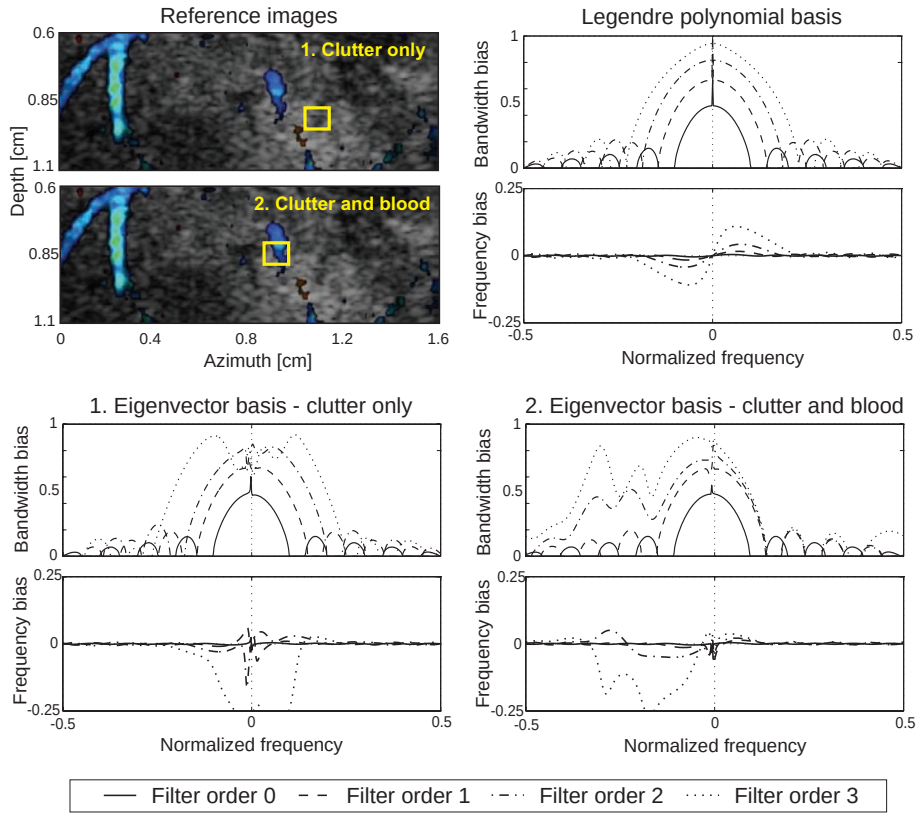


Figure 3.11: Bias in mean frequency and bandwidth estimates as calculated using (3.19) for the proposed adaptive filter basis compared to that of using a fixed Legendre polynomial basis. Two cases are presented; for data containing clutter only, and for data containing both clutter and blood flow. It can be observed that the bias is comparable as long as the filter basis does not include eigenvectors representing blood flow components. Furthermore, the bias is located in the transition and stop band of both filters.

to maximize the frame rate. This also is advantageous in our case as shorter time intervals are given between the acquisition of neighboring beams. Improved estimates then can be achieved when averaging in the lateral direction. The proper choice of averaging regions needs further elaboration. As seen in Fig. 3.8, smaller averaging regions amounts to improved attenuation of clutter, as the clutter statistics then are more uniform for each grid region. However as seen in Fig. 3.12, the computational demands for large numbers of averaging regions can be quite substantial. Using larger grid regions may lead to blocking artifacts as seen in the lower left image in Fig. 3.8. The artifacts result because different filter orders have been chosen for neighboring regions. This is especially visible when the grid regions cover both the vessel wall and

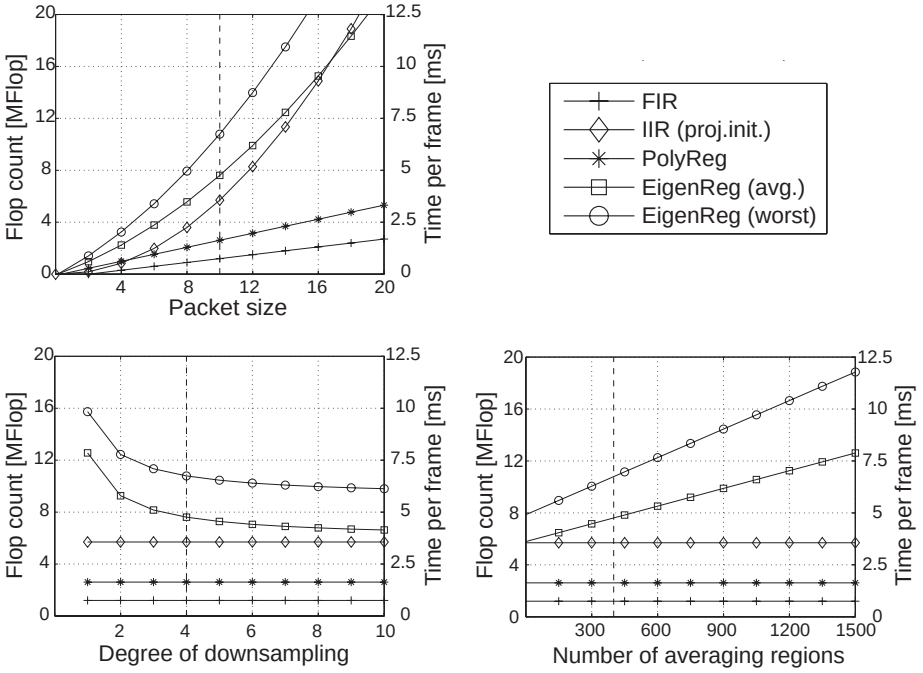


Figure 3.12: The flop count for the proposed algorithm compared to FIR filtering, IIR filtering with projection initialization, and polynomial regression filtering. Upper left, flop count versus packet size; lower left, flop count versus downsampling factor; lower right, flop count versus number of averaging regions. The default values of the respective parameters are indicated by the dashed vertical line in each plot.

lumen. The artifacts can be removed by tissue/flow arbitration as used in conventional algorithms, but this is not an optimal solution. Another approach could be to use a 2-D sliding window average, centered around each signal vector. However, as real-time operation then would be hard to obtain, this has not been considered in this work.

Downsampling amounts to an increase in variance of the correlation matrix estimate, and it may alter the filter characteristics as shown in Fig. 3.7. However, the first major eigenvectors are little affected for smaller downsampling factors and still may be used to represent the clutter. This may be due to the relatively slow movement and small bandwidth of the clutter signal. The results are by no means general, but they may indicate the validity of using small downsampling factors of 2-4 to decrease the processing time per frame. As shown in Fig. 3.12, the time used to process one frame can be substantially decreased, even for these factors.

The power method was chosen for the estimation of eigenvectors because of the small correlation matrix size and the knowledge that only a few major eigenvectors are needed. Also, if clutter signal is present, the convergence rate is rapid, using less then 10 iterations to converge with sufficient accuracy. The convergence rate of the method

can be increased further by introducing shifts as in the Rayleigh quotient method [16]. However, this method is more computationally demanding per iteration, and it will not decrease the total computation time for our case. Alternatively, a SVD could be performed. This method has good numerical properties and saves computation time by working directly on the data matrix. Although effective algorithms exist for performing the SVD [16], the small matrix size and Hermitian symmetry still favors the power method for our case.

The success of the filter order selection mechanism is crucial for the success of the filter in different mixtures of tissue and blood flow. Given an accuracy threshold $\epsilon$, a maximum number of iterations can be set that decides when the clutter is already given by the basis estimated thus far. For the different flow and tissue signal mixture examples investigated in this work, a value of 10 iterations has proven robust when using an accuracy threshold $\epsilon$ of $10^{-4}$ as indicated. The value could be lowered to remove less flow and raised to remove more clutter if needed. The method of selecting clutter subspace eigenvectors by ordering on decreasing eigenvalue works as long as the clutter to flow signal ratio is relatively high. When the signal power of blood flow becomes comparable to that of tissue, the flow signal may be represented by one of the first major eigenvectors and, consequently, may be removed by the filter. Furthermore, if the first eigenvectors correspond to blood flow, the algorithm may end without including any eigenvectors at all. Both cases result in reduced attenuation of clutter and biased velocity estimates. The problem may appear inside vessel lumens or in the heart ventricle for higher imaging frequencies, i.e., when the Rayleigh scattering from blood flow becomes prominent.

The filter performance examples in Fig. 3.10 shows that the proposed algorithm can provide sufficient attenuation of the clutter signal, even in nonstationary environments, and use lower order filters where needed to retain the blood flow signal. As shown in Fig. 3.11, the bias in velocity and bandwidth estimates induced by the filter is comparable to that of polynomial regression filtering as long as eigenvectors representing blood flow are not included in the filter basis. The bias due to the filter then is located mainly in the stop band of the filter; therefore, it is important that the clutter signal in the filter stop band is attenuated substantially below that of the blood flow signal. Contrary to Legendre polynomial filters, the eigenvector filters need not have infinite suppression of the mean value as shown in Fig. 3.2. To ensure that stationary tissue signal and reverberations are removed, one also could include the first Legendre basis vector in the basis set representing clutter.

Fig. 3.12 shows that, in order to keep the computation time per frame as low as possible, it will be beneficial to work with smaller packet sizes, and to reduce the number of averaging regions. The packet size is limited by the frame rate needed to follow the dynamics of the blood flow; otherwise, it should be as high as possible to achieve a proper separation of clutter and lower variance in velocity estimates (typically 8-16). However, by introducing adaptive averaging regions that remain large in areas of uniform statistics, and that are divided into smaller regions in nonuniform areas, computation time potentially can be saved. There should not be large abrupt changes in filter order between neighboring regions, and the initial presence of such could be used to iteratively divide an area into finer averaging regions.

## 3.6 Conclusion

Adaptive clutter filtering based on the eigenvector decomposition of the signal correlation matrix is feasible for real-time CFI applications using todays desktop computers. A new filter order selection algorithm has been introduced that works satisfactorily in different clutter and flow signal mixtures. By adapting unique filters to regions in a fine averaging grid, improved suppression of clutter is achieved in normal as well as in highly nonstationary tissue environments. Further work needs to be done on optimizing the averaging grid, and to investigate the influence of the algorithm on velocity estimates in more detail.

# References


[1] A. Weyman, *Principles and Practice of Echocardiography.* Philadelphia, USA: Lippincott Williams & Wilkins, 1993.

[2] M. Hennerici and D. Neuerburg-Heusler, *Vascular Diagnosis With Ultrasound: Clinical References With Case Studies.* New York, USA: Thieme Medical Publishers, 1997.

[3] A. Hoeks, J. Vandevorst, A. Dabekaussen, P. Brands, and R. Reneman, "An efficient algorithm to remove low-frequency doppler signals in digital doppler systems," *Ultrason. Imaging*, vol. 13, pp. 135–144, 1991.

[4] A. Kadi and T. Loupas, "On the performance of regression and step-initialized iir clutter filters for color doppler systems in diagnostic medical ultrasound," *IEEE Trans. Ultrason., Ferroelect., Freq. Contr.*, vol. 42, pp. 927–937, 1995.

[5] H. Torp, "Clutter rejection filters in color flow imaging: A theoretical approach," *IEEE Trans. Ultrason., Ferroelect., Freq. Contr.*, vol. 44, pp. 417–424, 1997.

[6] S. Bjaerum, H. Torp, and K. Kristoffersen, "Clutter filter design for ultrasound color flow imaging," *IEEE Trans. Ultrason., Ferroelectr., Freq. Control*, vol. 49, pp. 204–216, 2002.

[7] Y. Yoo, R. Managuli, and Y. Kim, "Adaptive clutter filtering for ultrasound color flow imaging," *Ultrasound Med. Biol.*, vol. 29, pp. 1311–1320, 2003.

[8] L. Thomas and A. Hall, "An improved wall filter for flow imaging of low velocity flow," *Proceedings of the IEEE Ultrasonics Symposium*, vol. 3, pp. 1701–1704, 1994.

[9] S. Bjaerum, H. Torp, and K. Kristoffersen, "Clutter filters adapted to tissue motion in ultrasound color flow imaging," *IEEE Trans. Ultrason., Ferroelectr., Freq. Control*, vol. 49, pp. 693–704, 2002.

[10] D. Kruse and K. Ferrara, "A new high resolution color flow system using an eigendecomposition-based adaptive filter for clutter rejection," *IEEE Trans. Ultrason., Ferroelect., Freq. Contr.*, vol. 49, pp. 1384–1399, 2002.

[11] C. Gallippi and G. Trahey, "Adaptive clutter filtering via blind source separation for two-dimensional ultrasonic blood velocity measurement," *Ultrason. Imaging*, vol. 24, pp. 193–214, 2002.

[12] L. Loevstakken, S. Bjaerum, R. Haaverstad, P. Aadahl, S. Samstad, and H. Torp, "Quality control in off-pump coronary artery bypass surgery using ultrasound color flow imaging with adaptive clutter rejection filters," *Proceedings of the IEEE Ultrasonics Symposium*, vol. 2, pp. 1602–1605, 2003.

[13] H. Torp, K. Kristoffersen, and B. Angelsen, "Autocorrelation technique in color flow imaging, signal model and statistical properties of the autocorrelation estimates," *IEEE Trans. Ultrason., Ferroelect., Freq. Contr.*, vol. 41, pp. 604–612, 1994.

[14] C. Therrien, *Discrete Random Signals and Statistical Signal Processing*. Upper Saddle River, USA: Prentice Hall Inc., 1992.

[15] E. Chornoboy, "Initialization for improved iir filter performance," *IEEE Trans. Signal Process.*, vol. 40, pp. 543–550, 1992.

[16] G. Golub and C. V. Loan, *Matrix Computations*. Baltimore, USA: Johns Hopkins University Press, 1996.

[17] D. O'Leary, G. Stewart, and J. Vandergraft, "Estimating the largest eigenvalue of a positive definite matrix," *Mathematics of Computation*, vol. 33, pp. 1289–1292, 1979.

[18] R. Chesarek, "Ultrasound imaging system for relatively low-velocity blood flow at relatively high frame rates," *US Patent 4888694, Quantum Medical Systems, Inc.*, Dec 19, 1989.

[19] J. Jensen, *Estimation of Blood Velocities Using Ultrasound - A Signal Processing Approach*. New York, USA: Cambridge University Press, 1996.

[20] C. Kasai, K. Namekawa, A. Koyano, and R. Omoto, "Real-time two-dimensional blood flow imaging using an autocorrelation technique," *IEEE Trans. Sonics Ultrason.*, vol. 32, pp. 458–464, 1985.

[21] J. Dongarra, "Performance of various computers using standard linear equations software," *http://www.netlib.org/benchmark/performance.ps*, 2005.

[22] J. Dongarra, P. Luszczek, and A. Petiet, "The linpack benchmark: Past, present, and future," *Concurrency and Computation: Practice and Experience*, vol. 15, pp. 1–18, 2003.

[23] R. Haaverstad, N. Vitale, O. Tjomsland, A. Tromsdal, H. Torp, and S. Samstad, "Intraoperative color doppler ultrasound assessment of lima-to-lad anastomoses in off-pump coronary artery bypass grafting," *Ann. Thorac. Surg.*, vol. 74, pp. S1390–S1394, 2002.

# Chapter 4

# Optimal velocity estimation in ultrasound color flow imaging in presence of clutter

Lasse Løvstakken[1], Steinar Bjærum[2], and Hans Torp[1]
[1] Dept. Circulation and Medical Imaging, NTNU
[2] GE Vingmed Ultrasound, Horten, Norway

In color flow imaging (CFI), the rejection of tissue clutter signal is treated separately from blood velocity estimation, by high-pass filtering the received Doppler signal. The complete suppression of clutter is then difficult to achieve without affecting the subsequent velocity estimates. In this work a different approach to velocity estimation is investigated, based on a statistical model of the signal from both clutter and blood.
An analytic expression for the Cramer-Rao lower bound (CRLB) is developed, and used to determine the existence of an efficient maximum likelihood estimator (MLE) of blood velocity in CFI when assuming full knowledge of the clutter statistics. We further simulate and compare the performance of the MLE to that of the autocorrelation method (ACM) using finite impulse response (FIR) and polynomial regression clutter filters. Two signal scenarios are simulated, representing a central and peripheral vessel.
Simulations showed that by including 3-9 (independent) spatial points, the MLE variance approached the CRLB in both scenarios. The ACM was approximately unbiased only for the central scenario in the clutter filter pass band, then with a variance of up to four times the CRLB. The ACM suffered from a severe bias in the filter transition region, and a significant performance gain was here achieved using the MLE.
For practical use, the clutter properties must be estimated. We finally replaced the known clutter statistics with an estimate obtained from low-rank approximations of the received sample correlation matrix. Used in the model-based framework, this method came close to the performance of the MLE, and may be an important step towards a practical model-based estimator including tissue clutter with optimal performance.

## 4.1 Introduction

Ultrasound imaging of blood flow is an important tool for the diagnosis of the human circulatory system [1, 2]. One particular modality referred to as color flow mapping or imaging (CFI), has proven useful by providing a two-dimensional (2-D) map of flow velocities in real-time, where areas of abnormal flow related to pathology can be detected and further investigated [3, 4]. To achieve a sufficient frame rate for following the dynamics of the flow in the heart and arteries, few temporal samples are available for processing in each sample bin in the image, typically 8-16 samples. Such short ensemble lengths make detection of blood flow and estimation of blood flow velocity a challenge.

Real-time CFI became feasible in the mid-eighties with the introduction of the autocorrelation method (ACM) [5], previously used in weather radar applications [6, 7]. The method estimates the mean Doppler frequency of the received slow-time signal using the phase of the estimated correlation function at lag one. Being a phase-shift estimator, the method suffers from aliasing artifacts. Alternative estimators based on 2-D signal models have been proposed to estimate the mean scatterer velocity with less bias and variance, and beyond the Nyquist limit. Cross-correlation methods have been proposed [8], wideband maximum likelihood estimation [9], a 2-D extension of the autocorrelation technique [10], and the 2-D butterfly search technique [11]. Experimental methods for estimating the lateral as well as the axial velocity component have also been proposed [12–14]. However, due to its low computational complexity, and its adequate performance even in poor signal-to-noise conditions, the autocorrelation approach is still the most commonly used CFI velocity estimation algorithm. The method has further been shown to come close in performance to the cross-correlation technique when averaging over several range gates [15]. In this work a one-dimensional (1-D) signal model estimator is developed and compared to the ACM. For a more in-depth review of common CFI velocity estimators, please refer to [3, 4].

Signal from surrounding tissue is a potential source of estimator bias in all flow estimators proposed. This clutter signal can have a signal power as high as 80 dB compared to that of blood flow, and must be dealt with before the flow velocity and velocity spread can be properly estimated [16]. This issue is conventionally treated separately by high-pass filtering the Doppler signal prior to velocity estimation. FIR, initialized IIR, and polynomial regression type filters have been used for this purpose [16–19]. More advanced adaptive clutter filter techniques have also been proposed [20–23], where the clutter filters are adapted to the tissue movement. However, the small number of temporal samples available results in clutter filters with a long transition band in order to achieve sufficient stop band attenuation. The complete suppression of the clutter signal is therefore difficult without affecting the flow velocity estimates, and often leads to suboptimal performance [16, 19]. The use of estimation schemes that incorporates a clutter signal model, may yield an improvement in estimator accuracy. Such alternative methods of dealing with the clutter have previously been proposed based on auto-regressive and signal subspace based methods [24–26].

In this work we investigate the performance of maximum likelihood estimation of blood velocity, based on a 1-D statistical model of the received Doppler signal from both tissue clutter and blood flow. We first develop an analytic expression for the Cramer-Rao lower bound (CRLB) on estimator variance, and use this as a reference for estimator performance. We then simulate and compare the performance of a maximum likelihood estimator assuming full knowledge of the clutter statistics, to that of the autocorrelation method. Finally, we replace the known clutter statistics with estimates from the received signal. This approximative MLE will be compared to the MLE having full knowledge of the clutter statistics and the ACM. All investigations are carried out by simulations.

Related work on maximum likelihood estimation include that of Ferrara and Algazi [9], who developed a wideband MLE for use in CFI based on a 2-D signal model. This estimator was extended to include a prior knowledge from fluid physics in [27]. A simpler MLE for the CFI setting was described in [28]. A similar small-sample problem exists for weather radar applications, and optimal maximum likelihood estimation have been analyzed among others by Chornoboy [29]. Common to these investigations however is the lack of clutter in the signal model. To the authors knowledge this has not previously been pursued in the literature.

The paper is organized as follows. In Section 4.2, the signal model and the development of the CRLB and estimators are given. Further in Section 4.3, the simulation method and setup is described. The results of the simulation study is given in Section 4.4, and discussed in Section 4.5. Finally in Section 4.6, conclusions are drawn based on the results obtained.

## 4.2 Theory

### 4.2.1 Blood signal model

The signal model for blood used in this simulation study follows that of Torp [30], which is based on a random continuum model of the blood scatterers [31]. A sequence of pulses are fired at intervals of $T_p$, and the received signals are complex demodulated and sampled at intervals of $T_s$. The pulse sequence can described as a two-dimensional complex Gaussian process $x(n,m)$, where $n$ is the sampled signal corresponding to a depth range $r = \frac{c \cdot nT_s}{2}$, and $m$ is the pulse number in the sequence. The Gaussian assumption is justified by the central limiting theorem in the fact that the received signal is a sum of contributions from a large number of independent scatterers. Assuming the pulse and Gaussian shaped lateral beam profiles constant over the sample volume, and assuming rectilinear scatterer movement, the autocorrelation function of the received Doppler signal can be shown to be Gaussian shaped and given by [30]

$$R(n,m) = R(0,0)e^{-\frac{1}{2}Q(n,m)}e^{i\omega_d m}, \tag{4.1}$$

where $\omega_d = 2\pi f_d$ is the received Doppler frequency. $Q(n,m)$ is a transit time expression which determines the bandwidth of the Doppler signal, and is given by

$$Q(n,m) = (\frac{n}{\sigma_1})^2 + 2\rho\frac{n}{\sigma_1}\frac{m}{\sigma_2} + (\frac{m}{\sigma_2})^2, \tag{4.2}$$

where $\sigma_1$ and $\sigma_2$ are the correlation lengths in the radial and temporal direction respectively, and $\rho$ is a cross-correlation coefficient that describes to what extent the same scatterers are imaged by consecutive pulses. These variables are related to the transit times of the scatterers through the insonified sample volume as [30]

$$\begin{aligned} \sigma_1 = &\frac{L}{\sqrt{3}\cdot T_s}, \qquad \sigma_2 = \frac{\rho}{\sqrt{3}\cdot T_p}, \\ &\rho = \Big(\frac{1}{T_r^2} + \frac{1}{T_a^2} + \frac{1}{T_e^2}\Big)^{-\frac{1}{2}}. \end{aligned} \tag{4.3}$$

$T_r$, $T_a$ and $T_e$ are the transit times in the radial, azimuth, and elevation direction respectively, $L$ is the temporal pulse length, and $T_p$ is the pulse repetition time. The transit times are given by imaging system variables as well as the velocity and direction of the scatterers:

$$T_r = \frac{L}{v\cos\theta}, \quad T_a = \frac{D_a}{v\sin\theta\cos\phi}, \quad T_e = \frac{D_e}{v\sin\theta\sin\phi}, \tag{4.4}$$

where $D_a$ and $D_e$ are the beam widths in the azimuth and elevation direction, and $\theta$ and $\phi$ is the scatterer angle of movement compared to the ultrasound beam and azimuthal plane respectively. We further simplify the model by only considering the slow-time signal $x(t_0, m)$ acquired from the pulse sequence at a given radial depth of interest $r_0 = ct_0/2$. The final simplified form of the autocorrelation function is then given by

$$R_b(m) = R_b(0)e^{-\frac{1}{2}(\frac{m}{\sigma_2})^2}e^{i\omega_d m}. \tag{4.5}$$

The power spectrum of the signal model is determined by the Fourier transform of $R(m)$. When neglecting aliasing artifacts this is analytically given by

$$G_b(\omega) = R_b(0)\sqrt{2\pi}\sigma_2 e^{-\frac{1}{2}(w-w_d)^2\sigma_2^2}, \tag{4.6}$$

where the center frequency is given by the Doppler frequency $w_d$, and bandwidth is given by the transit time expression defined by $\sigma_2$ in (4.3).

### 4.2.2 Clutter signal model

Tissue clutter signal is present in the received signal from blood due to beam sidelobes and reverberations from tissue structures. The clutter signal may therefore originate from different regions consisting of tissue with different scattering properties and motion patterns. It can be shown that when the number of scatterers within one resolution cell is large and the phases of the scattered waves are uniformly

distributed, the amplitude of the resulting received complex signal is complex Gaussian distributed [32]. This produces what is called fully developed speckle in ultrasound B-mode images, and occurs in regions of tissue with near homogenous properties. To simplify, we assume this to be the case in our simulations.

In general the velocity of a specific tissue structure is low compared to the pulse repetition frequency (PRF), and will therefore have a narrow Doppler bandwidth. Transit time effects are less prominent than for blood flow, but the bandwidth is increased by the accelerated movement over the heart cycle, and by the vibration of muscle both in the operator holding the probe and inside the patient itself [33]. Because the clutter signal may consist of signal from different tissue regions with different motion patterns, the total clutter Doppler spectrum can be regarded as the sum of the contributions from the different regions, with a given center frequency and bandwidth that varies over the heart cycle. For exact parametric modeling of clutter, this variation should be taken into account. However, to simplify we assume in our examples the clutter signal to be stationary with a Gaussian shaped power spectrum, centered around zero Doppler frequency as given by

$$G_c(w) = G_c(0)e^{-\frac{1}{2}(w/B_c)^2}, \tag{4.7}$$

where $B_c$ is the clutter signal bandwidth. The discrete correlation function for the clutter component is then given on the form

$$R_c(m) = R_c(0)e^{-\frac{1}{2}(m/\sigma_c)^2}, \tag{4.8}$$

where $R_c(0)$ is the clutter signal power, and $\sigma_c = \frac{1}{B_c}$ is the temporal correlation length of the composite clutter signal. The relation between $R_c(0)$ and $G_c(0)$ is given through the Fourier transform of (4.8) as $G_c(0) = R_c(0)\sqrt{2\pi}\sigma_c$. The signal power and bandwidth of the clutter signal are set empirically to match realistic signal scenarios.

### 4.2.3 Imaging context

The general imaging context is illustrated in Fig. 4.1. A vessel is located at a depth $z_0$, at angles $\theta$ compared to the ultrasound beam, and $\phi$ compared to the azimuthal imaging plane. In this vessel, stationary and rectilinear blood flow is assumed. A number of $N_P$ consecutive pulses are fired in a given beam direction, insonifying a sample volume within the vessel, where $N_P$ is referred to as the packet size. The packet size typically consists of 8-16 samples. The received signal information can be regarded as being two-dimensional, consisting of both a signal along a given range gate, and a signal from a specific range between pulse emissions. This is referred to as the fast-time and slow-time signal respectively. In this work, the slow-time signal from each range gate is processed separately.

The resulting received complex signal vector $\boldsymbol{x} = [x_1, x_2, \ldots, x_{N_P}]^T$ is assumed to consist of three components. A clutter component $\boldsymbol{c}$ originating from sound scattered from tissue and acoustic noise sources such as reverberation, an electrical/thermal noise component $\boldsymbol{\eta}$ modeled as white noise, and a blood signal component $\boldsymbol{b}$ originating from sound scattered from the red blood cells. As the clutter and blood signal

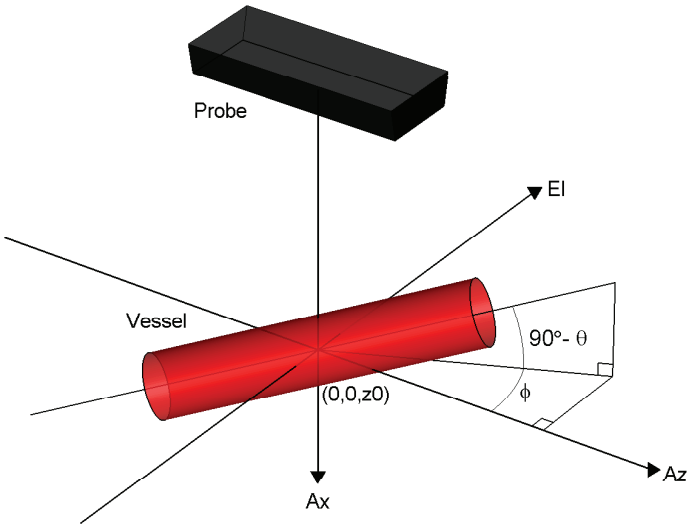


Figure 4.1: Illustration of the imaging context. A vessel is positioned in the tissue at a depth $z_0$, and at angles $\theta$ and $\phi$ relative to the ultrasound beam and azimuthal imaging plane. The flow in the vessel is assumed rectilinear within the insonified sample volume.

components originate from fundamentally different scatterers at different spatial positions, we consider them statistically independent. The general signal component model is then given by

$$\boldsymbol{x} = \boldsymbol{c} + \boldsymbol{\eta} + \boldsymbol{b}, \tag{4.9}$$

which is governed by a multivariate complex Gaussian probability density function (PDF) given by

$$p_x(\boldsymbol{x}) = \frac{1}{\pi^{N_P}|\mathbf{R}_x|} e^{-\boldsymbol{x}^{*T}\mathbf{R}_x^{-1}\boldsymbol{x}}. \tag{4.10}$$

The signal correlation matrix $\mathbf{R}_x = E\{\boldsymbol{x}\boldsymbol{x}^{*T}\}$ is in general parameterized by acquisition parameters related to the ultrasound pulse and beam shape, the tissue and flow scatterer movement, and the tissue and flow signal-to-noise ratios. In our simplified treatment however, we consider only the blood flow velocity magnitude $v$ unknown. This ideal case allows us to develop tractable solutions for the MLE and CRLB, and still allows us to make some interesting observations and estimator comparisons. Assuming independent components, the signal correlation matrix can be written as

$$\mathbf{R}_x(v) = \mathbf{R}_c + \mathbf{R}_\eta + \mathbf{R}_b(v) = \mathbf{R}_c + \sigma_\eta^2\mathbf{I} + \mathbf{R}_b(v), \tag{4.11}$$

where $\mathbf{R}_c$ is the clutter correlation matrix, $\mathbf{R}_b(v)$ is the blood signal correlation matrix parameterized by $v$, $\sigma_\eta^2$ is the thermal noise level, and $\mathbf{I}$ is the identity matrix. The signal correlation matrix is in general Hermitian symmetric. When stationary

conditions are given it also exhibits a Toeplitz structure, and is then completely defined by the signal correlation function of different lags. We assume stationary signal components with known properties, and the correlation matrix $\mathbf{R}_x(v)$ is then for a given noise power $\sigma_\eta^2$ determined by (4.5) and (4.8).

### 4.2.4 Cramer-Rao lower bound

The Cramer-Rao lower bound (CRLB) defines the lower bound of the variance of an unbiased estimator, and is in general given by

$$var(\hat{\boldsymbol{\xi}}) \geq [\mathbf{I}(\boldsymbol{\xi})]^{-1} \tag{4.12}$$

where $\mathbf{I}(\boldsymbol{\xi})$ is the Fisher information matrix, and $\boldsymbol{\xi}$ is a general vector of parameters. For a complex Gaussian signal model with real parameters, an exact expression exists for the Fisher information matrix, which for a zero-mean process is given by [34]

$$\mathbf{I}(\boldsymbol{\xi}) = tr(\mathbf{R}_x^{-1}\frac{\partial \mathbf{R}_x}{\partial \boldsymbol{\xi}}\mathbf{R}_x^{-1}\frac{\partial \mathbf{R}_x}{\partial \boldsymbol{\xi}}). \tag{4.13}$$

By inserting our expression for $\mathbf{R}_x$ in (4.11), we obtain the following simplified and scalar expression for the Fisher information matrix:

$$I(v) = tr(\mathbf{R}_x^{-1}\frac{\partial \mathbf{R}_b}{\partial v}\mathbf{R}_x^{-1}\frac{\partial \mathbf{R}_b}{\partial v}). \tag{4.14}$$

The derivative of $\mathbf{R}_b(v)$ with respect to the scalar parameter $v$ is defined as the derivative of each individual matrix element. Assuming stationary conditions these are completely defined by the derivative of $R_b(m; v)$, the blood flow signal correlation function. Using the simplified model in (4.5), this can be calculated analytically and shown to be given by

$$\frac{\partial R_b}{\partial v} = \frac{1}{v}(iw_d m - (\frac{m}{\sigma_2})^2)R_b. \tag{4.15}$$

When an estimator is unbiased with variance equal to the CRLB, it is called an efficient estimator, and is then by definition optimal in the minimum variance unbiased (MVU) sense. The analytic expression for the CRLB will be used as a reference for finding an approximatively efficient maximum likelihood estimator.

### 4.2.5 Maximum likelihood estimator

Maximum likelihood estimation is a standard technique in statistical estimation theory. The likelihood function $l(\boldsymbol{x}; \boldsymbol{\xi})$ determines how likely it is that a given signal vector realization $\boldsymbol{x}$ originates from a signal model parameterized by a given $\boldsymbol{\xi}$. It is considered a function of the parameters. The maximum likelihood estimator (MLE) is the parameter values that maximizes the likelihood function. The likelihood function is in our case derived using (4.10) and (4.11) [34], and is a function of the flow velocity

$v$ only. It is often practical to evaluate the (negative) log-likelihood function, which for our case is given by

$$-L(\boldsymbol{x};v) = \boldsymbol{x}^{*T}\mathbf{R}_x^{-1}(v)\boldsymbol{x} + \ln|\mathbf{R}_x(v)| + N_P \ln \pi. \tag{4.16}$$

The MLE is then the value of $v$ that minimizes $-L(\boldsymbol{x};v)$, defined as

$$\hat{v}_{ml} = \arg\min_v -L(\boldsymbol{x};v). \tag{4.17}$$

The MLE is asymptotically optimal in the MVU sense, becoming unbiased with variance equal to the CRLB for large data records [34]. The optimal MLE is however not necessarily given for the small-sample restrictions imposed in CFI. By expanding the MLE to include several sample vector realizations, an improved estimate can be achieved. This can in practise be done by including several spatial points in the estimator design. In this work we approximate this scenario by using several independent sample vector realizations, drawn from the same statistical model of clutter and blood. This approximation is valid when one sample is obtained per resolution cell. It is shown in the appendix (Section 4.7) that when expanding the estimator to include $K$ independent sample vectors, the (negative) log-likelihood function is given by

$$\begin{aligned} -L_K(\boldsymbol{x};v) = K\big[&tr(\mathbf{R}_x^{-1}(v)\hat{\mathbf{R}}_K) \\ &+ \ln|\mathbf{R}_x(v)| + N_P \ln \pi\big], \end{aligned} \tag{4.18}$$

where $tr$ indicates the matrix trace operator, and $\hat{\mathbf{R}}_K$ is the sample correlation matrix estimate given by

$$\hat{\mathbf{R}}_K = \frac{1}{K}\sum_{k=1}^{K} \boldsymbol{x}_k \boldsymbol{x}_k^{*T}. \tag{4.19}$$

Although an exact expression exist for the derivative of the log-likelihood function for a complex Gaussian process with real parameters [34], we could not find an explicit expression for $\hat{v}_{ml}$ in our case. We therefore had to resort to numerical procedures to find the maximum likelihood estimate.

### 4.2.6 Autocorrelation estimator

The real-time autocorrelation algorithm was first described for use in diagnostic ultrasound in [5], where the mean Doppler frequency is estimated using the phase of the autocorrelation function of lag one. As shown in [35], the performance of the ACM is improved considerably by averaging the correlation function estimate over several spatial positions. The estimate of the autocorrelation function at lag one is obtained by averaging $N_P - 1$ correlation terms for each packet, over $K$ spatial positions. This results in the expression

$$\hat{R}(1) = \frac{1}{N_P - 1}\sum_{n=1}^{N_P-1} \big[\hat{\mathbf{R}}_K\big]_{n+1,n}, \tag{4.20}$$

where $\left[\hat{\mathbf{R}}_K\right]_{n+1,n}$ is the second lower diagonal of the sample correlation matrix defined in (4.19). The mean velocity estimate is obtained by appropriate scaling of $\hat{\omega}_d = \angle\hat{R}(1)$, given by

$$\hat{v}_{AC} = \frac{c \cdot PRF}{4\pi f_0 \cos\theta} \angle\hat{R}(1), \tag{4.21}$$

where $PRF = 1/T_P$ is the pulse repetition frequency, $f_0$ the received signal center frequency, and $c$ is the speed of sound. We assume the angle of flow known, and therefore angle correct the estimates with the term $cos(\theta)$ to obtain the full velocity magnitude. The ACM estimate can be shown to be equivalent to a first order autoregressive estimate of the mean velocity [36].

To achieve unbiased velocity estimates in presence of clutter, the ACM incorporates a clutter filter. In this work, conventional high-pass FIR and polynomial regression clutter filters are used. FIR filters can be described by an impulse response function $h(n),\ n = 0, \ldots, M-1$, where $M-1$ is denoted the filter order. With an input signal $x(n),\ n = 0, \ldots, N_P - 1$, the output signal $y(n)$ is the convolution sum given by

$$y(n) = \sum_{k=0}^{M-1} h(k)x(n-k), \tag{4.22}$$

where the first $M-1$ output samples are invalid and discarded. The polynomial regression filter models the clutter signal by a set of orthonormal slowly varying polynomial basis functions. Typically, the Legendre polynomials have been used. The filter output is given as the projection of the input signal vector $\boldsymbol{x}$ onto the complement of the clutter signal basis given by

$$\boldsymbol{y} = \big(I - \sum_{k=0}^{M-1} \boldsymbol{b}_k \boldsymbol{b}_k^{*T}\big)\boldsymbol{x} = \mathbf{A}\boldsymbol{x}, \tag{4.23}$$

where $\boldsymbol{b}_k$ are orthonormal basis vectors spanning the clutter signal subspace, and $\mathbf{A}$ is a projection matrix. The filter order is given by $M-1$. For a more in-depth description of conventional clutter filters in CFI, please refer to [16, 19].

### 4.2.7 Low-rank maximum likelihood estimator

The complex origin and motion pattern of the clutter signal may be difficult to model statistically in practise. Also, as the number of total unknown model parameters is increased, it will become more difficult to numerically produce robust maximum likelihood estimates. As an alternative we investigate if the clutter correlation matrix can be estimated directly from the received signal, alleviating the need for complex clutter correlation models. Several authors have proposed the idea of clutter signal representation through eigenanalysis of the received signal correlation matrix. This concept has previously been used in model-based estimation [26, 37], as well as for designing adaptive clutter filters [21, 22]. Due to the dominant and low-bandwidth nature of the clutter Doppler signal, the clutter signal energy is mostly contained in the

signal subspace represented by a smaller set of eigenvectors with large corresponding eigenvalues [21].

We propose to estimate the clutter correlation matrix as a low-rank approximation of the sample correlation matrix for the same reasons. In general, the correlation matrix can be expressed by its eigenvalues and corresponding orthonormal eigenvectors [38], given by

$$\mathbf{R}_x = \sum_{k=1}^{N_P} \lambda_k \boldsymbol{e}_k \boldsymbol{e}_k^{*T}, \tag{4.24}$$

where $\lambda_k$ and $\boldsymbol{e}_k$ are the eigenvalues and corresponding eigenvectors of $\mathbf{R}_x$. By truncating (4.24) to use the $N_{LR} < N_P$ eigenvectors with the largest corresponding eigenvalues, an estimate of the clutter correlation matrix is obtained. This estimate is given by

$$\hat{\mathbf{R}}_c = \hat{\mathbf{R}}_{lr} = \sum_{k=1}^{N_{LR}<N_P} \hat{\lambda}_k \hat{\boldsymbol{e}}_k \hat{\boldsymbol{e}}_k^{*T}, \tag{4.25}$$

where $N_{LR}$ is the desired rank of the estimated clutter correlation matrix, and $\hat{\lambda}_k$ and $\hat{\boldsymbol{e}}_k$ are the estimated eigenvalues and corresponding eigenvectors of the sample correlation matrix in (4.19) sorted on decreasing eigenvalues, $\hat{\lambda}_1 \geq \hat{\lambda}_2 \ldots \geq \hat{\lambda}_{N_P}$.

To see how it will affect the performance of a model-based estimator, we replace the clutter correlation matrix $\mathbf{R}_c$ in the MLE framework with the low-rank estimate $\hat{\mathbf{R}}_{lr}$ in (4.25). We will in subsequent sections refer to this estimator as the *low-rank MLE*. In this work we use a fixed rank for the estimated clutter correlation matrix. In general the tissue movement and signal power will vary in space and time, and the optimal choice of rank will therefore also vary. Methods of rank selection have previously been proposed by thresholding the eigenvalue spectrum [19, 22] and the eigenvalue spectrum slope [39]. To achieve a sample correlation matrix of full rank, the number of independent signal vectors $K$ used to form the estimate in (4.19) needs to at least be equal to the packet size $N_P$. The variance of the sample correlation matrix estimate can be reduced by including more spatial sample vectors when averaging, increasing the accuracy of the low-rank clutter correlation matrix estimate. In a practical situation however, the number of sample vectors one can include is limited in space by varying tissue signal properties and tissue movement.

## 4.3 Method

### 4.3.1 Simulation setup

The simulation setup was divided into two different imaging cases, empirically based on clutter, blood, and noise signal conditions that may occur in realistic settings. Case 1 represents the imaging of a central vessel such as the carotid artery. The imaging object is here located some distance into the tissue (2-4 cm), and a moderate blood-to-noise signal ratio (BNR) and clutter-to-noise signal ratio (CNR) is given. Case 2 represents the imaging of a peripheral vessel such as the radial artery. It is located

**Table 4.1: Default simulation parameters for different cases**

| Parameter | Case 1 | Case 2 |
|---|---|---|
| Clinical object | Central vessel | Peripheral vessel |
| Center frequency | 5 MHz | 10 MHz |
| Pulse duration | 0.8 $\mu$s | 0.2 $\mu$s |
| F# transmit / receive | 2.0 / 1.4 | 2.0 / 1.4 |
| PRF | 4.0 kHz | 0.5 kHz |
| Packet size, $N_P$ | 12 | 12 |
| CNR, BNR | 50dB, 20dB | 50dB, 5dB |
| Clutter BW, $cbw$ | 0.10·$v_{Nyquist}$ | 0.15·$v_{Nyquist}$ |
| Clutter rank, $N_{LR}$ | 3 | 4 |
| $\theta_{blood}$ | 45 deg | 45 deg |
| $v_{Nyquist}$ | 30.8 cm/s | 1.93 cm/s |
| $N_{sim}$ | 5000 | 5000 |

at shallow depths ($<$ 1 cm), and a low BNR and high clutter-to-blood signal ratio is present. In both cases the maximum clutter velocity was set to be in the high end of the velocity range for the given scenario, typically when the vessel wall moves in response to the incoming flow pulse.

The simulation parameters for the two cases are listed in Table 4.3.1. For simplicity we assume the angle compared to the azimuthal imaging plane $\phi = 0$. The one-way beam widths used in the simulations are given by the Rayleigh criterion $F_{\#} \cdot \lambda$, where $F_{\#}$ is the one-way F-number and $\lambda$ is the wavelength of the emitted pulse.

The power spectrum of the different signal components in the two simulation cases are illustrated in Fig. 4.2, together with the FIR and polynomial regression clutter filters used in conjunction with the ACM. As clutter filters we chose the polynomial regression filter order that produced the best results for a given case, and further adapted the FIR filter frequency response to match this response, while keeping the FIR filter order as low as possible. To be able to match the steep transition band of the polynomial regression filters, an order of 8 was needed, leaving 4 samples for velocity estimation after discarding initializing samples. The FIR filters were designed using the minimum-phase method described in [19]. As a reference in the result figures, we define a clutter bandwidth measure as the velocity at which the clutter power spectrum crosses the white noise level, illustrated by $cbw$ in Fig. 4.2. By solving for the frequency argument $\omega$ after setting the expression for the clutter power spectrum in (4.7) equal to the white noise level $\sigma_\eta^2$, we get the following bandwidth measure (scaled to velocity):

$$v_{cbw} = \sqrt{2B_c^2 \ln\left(\frac{G_c(0)}{\sigma_\eta^2}\right)} \cdot \frac{PRF \cdot c}{4\pi f_0}, \tag{4.26}$$

where $G_c(0) = \sqrt{2\pi}\sigma_c R_c(0)$, and $\sigma_c = 1/B_c$.

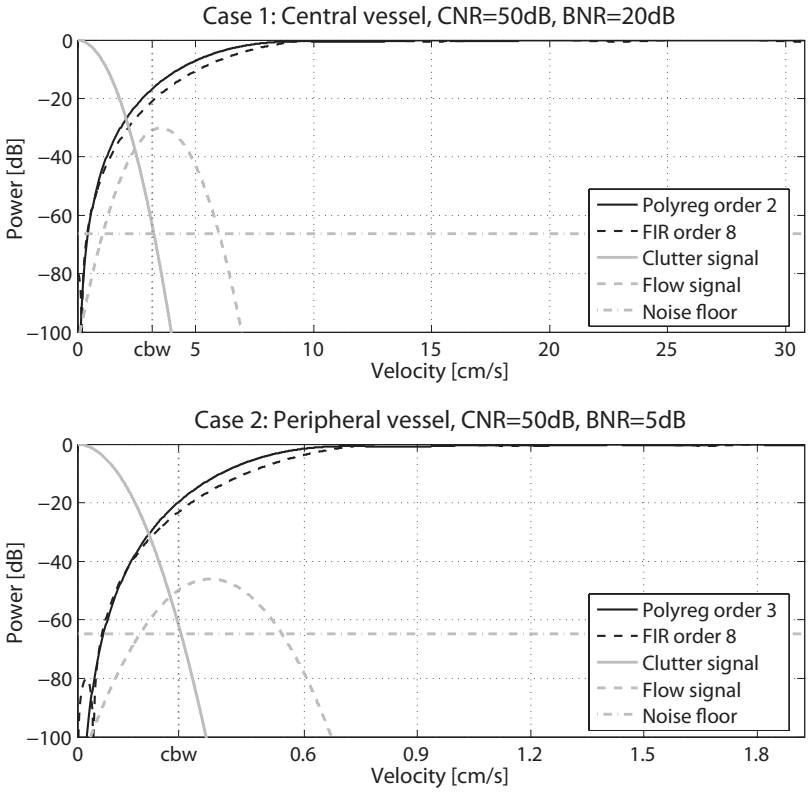


Figure 4.2: The two different simulation cases used for evaluating estimator performance. Case 1 represents signal conditions from a central vessel such as the common carotid artery, while case 2 represents conditions from a peripheral vessel such as the radial artery. The clutter filters used for the given cases are indicated together with the power spectrum for the clutter, blood flow, and thermal noise signal components.

### 4.3.2 Simulation method

Both the tissue and blood flow signal component was simulated using the Gaussian parametric power spectrum model given by (4.6) and (4.7) respectively. The thermal noise component was assumed white. A signal vector realization was generated by a FFT-based method valid for stationary processes. A sequence of 512 complex Gaussian white noise samples was generated, and then shaped using the total power spectrum of the signal components in (4.9). The resulting time domain signal was obtained by selecting the first $N_P$ samples after calculating the discrete inverse Fourier transform. The number of sample vectors realizations $N_{sim}$ used in the simulations were determined by increasing the number until no qualitative difference was observed in the results. A value of $N_{sim} = 5000$ proved sufficient. The maximum likelihood

estimate was found using a golden section search algorithm as described in [40]. This algorithm is based solely on function value evaluations, and avoids the lack of robustness often encountered with iterative methods such as Newton or Fisher scoring algorithms. This was feasible due to the simplified scalar parameter estimation problem given, assuming only the velocity magnitude unknown. As the direction of the flow was assumed known, we performed one-sided comparisons, limiting the signal simulation range from zero to the Nyquist velocity. To avoid aliasing artifacts influencing the estimator comparisons, the ACM estimate was always corrected by phase-unwrapping using the known blood velocity. Similarly, the search range of the MLE was kept one-sided, but extended the simulation range by 10 percent of the Nyquist velocity to each side to avoid bias at the ends of the simulation range.

## 4.4 Results

In the following subsections the simulation results is presented. For each plot we simulated 100 velocities ranging from zero to the Nyquist velocity. The scaling of the figure axes have been adapted to the data to allow a detailed inspection of the results. The same scale have been applied to plots in different figures that are natural to compare. The values on all figure axes are given in percent of the Nyquist velocity, and the clutter bandwidth measure as defined in Section 4.3.1 is shown as a dashed vertical line at velocity *cbw* as a reference in all plots. To enhance the qualitative features in the results, the resulting graphs were smoothed using a seventh order Savinsky-Golay FIR filter with a polynomial order of one [40].

### 4.4.1 The optimal estimator

The optimal property of the MLE is not necessarily given for as small ensemble lengths as that available in CFI. To investigate this asymptotic behavior we first evaluated the MLE performance for an increasing packet size. The more challenging case 2 as shown in Fig 4.2, was used in the evaluation. In the two larger plots in Fig. 4.3, the bias and standard deviation of the MLE using a packet size of 12 and 96 is shown respectively. It can be observed that the MLE is in fact not unbiased for any velocities when using a packet size of 12 for this scenario, and is therefore not the optimal MVU estimator for this example. For a packet size as large as 96 however, the MLE is approximately efficient, and therefore approximately the optimal MVU estimator. In the rightmost smaller plots in Fig. 4.3, the convergence towards the MVU estimator for increasing packet size is shown for two different velocities, $\frac{1}{3}v_{Nyquist}$ and $\frac{2}{3}v_{Nyquist}$. As can be seen, the MLE estimator does not become efficient for any applicable packet size ($< 16$), but is approximately so for packet sizes larger than 72.

As mentioned in Section 4.2.5, another way to increase the performance of the MLE is to include several spatial points in the estimator design. As an approximation to this scenario, we evaluated the MLE performance using several independent sample vectors. The effect of such spatial averaging on the performance of the MLE is shown in Fig. 4.4. As can be observed in the two larger plots, the MLE becomes approximately

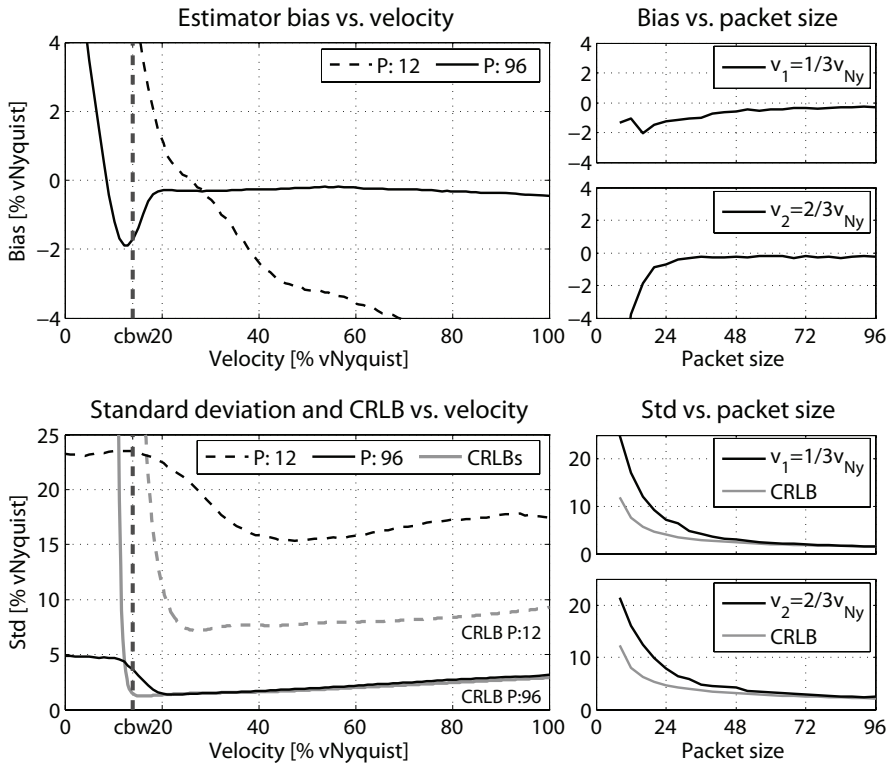


Figure 4.3: The bias and standard deviation of the MLE for case 2, when increasing the packet size. The larger plots show the MLE performance for a packet size of 12 and 96 for all velocities. The smaller plots show the development towards the optimal estimator for two different velocities. As can be observed, the MLE is asymptotically efficient only for large ensemble lengths.

efficient and therefore MVU for only 9 points. The convergence towards the MVU estimator can be followed in the smaller plots to the right as in Fig. 4.3. We may conclude that an near optimal MVU estimator exists for practical packet sizes when including at least 9 independent spatial points in the estimator design for this example. In further estimator comparisons, this amount of spatial averaging will be used in all estimators. For the ACM the averaging is done directly on the autocorrelation function estimates as described in Section 4.2.6.

### 4.4.2 Estimator comparisons

We now compare the performance of the three estimators presented in Section 4.2, the MLE assuming full knowledge of the clutter statistics, the conventional ACM using polynomial regression and FIR clutter filters, and the low-rank MLE using direct

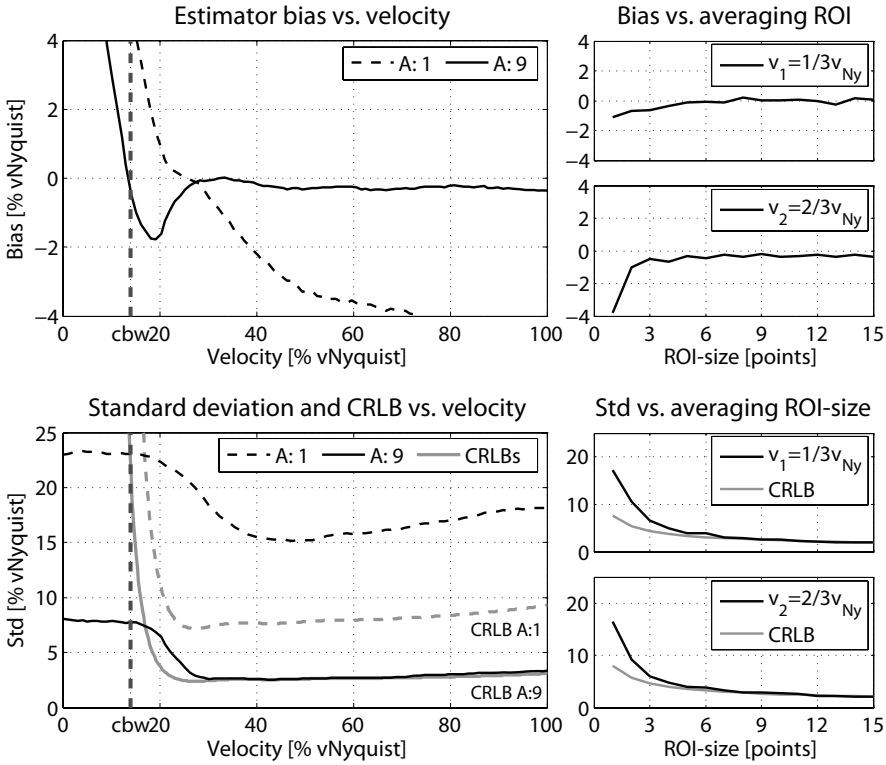


Figure 4.4: The bias and standard deviation of the MLE for case 2, when including several spatial points in the estimator design. The larger plots show the MLE performance for an averaging ROI consisting of 1 and 9 points. The smaller plots show the development towards the optimal estimator for two different velocities. As can be observed, the MLE rapidly becomes efficient when using several points in the estimator design.

estimates of the clutter correlation matrix. The estimator comparisons for case 1 and 2 are shown in Fig. 4.5 and Fig. 4.6. As can be seen, the MLE assuming full knowledge of the clutter statistics is efficient for both cases when the flow velocity is above the clutter bandwidth measure *cbw*. A MLE variance below the CRLB can be explained by the presence of a negligible but non-zero bias. For case 1 the ACM is biased in the transition band of both clutter filters, with a maximum bias of 2.5 and 7.5 percent of the Nyquist velocity for the FIR and polynomial regression filter respectively. The method becomes approximately unbiased above 50 percent of the Nyquist velocity for both filters. In the unbiased range, the mean standard deviation is 3.0 and 2.4 percent of the Nyquist velocity for the FIR and polynomial regression filters, compared to 1.5 percent for the CRLB. For case 2 the ACM suffers from a severe bias in the clutter filter transition band. It also has a moderate bias even in the pass band of the filters,

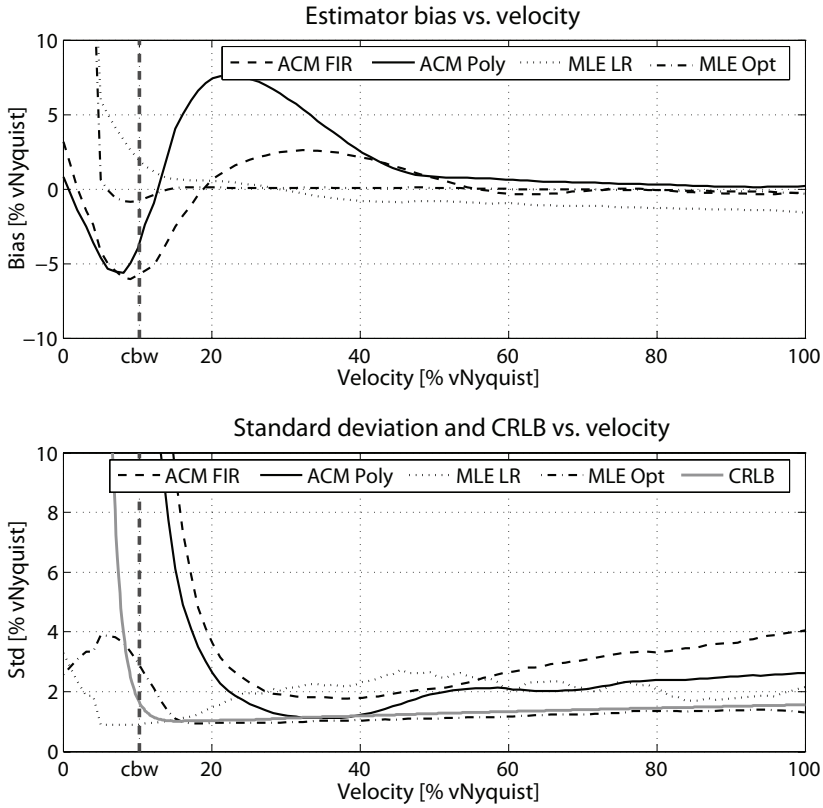


Figure 4.5: The bias and standard deviation of the ACM compared to the optimal and low-rank MLE for case 1. A 2nd order polynomial regression filter and 8th order FIR filter was used, and 9 spatial points were averaged for all estimators. As can be observed the ACM performs adequately compared to the optimal MLE in the filter pass band. In the transition region however, the ACM becomes inferior compared to the ideal and low-rank MLE.

with a mean value of 3.9 and 7.5 percent of the Nyquist velocity for the FIR and polynomial regression filter respectively. The standard deviation in this region has a mean value of 6.3 percent of the Nyquist velocity for FIR and 4.1 percent for the polynomial regression filter, compared to 2.9 percent for the CRLB.

The performance of the low-rank MLE described in Section 4.2.7 is given by the dotted lines in Fig. 4.5 and 4.6. The results were obtained using the minimal amount of averaging signal vectors $K = N_P$ necessary to ensure a correlation matrix of full rank. As can be seen, the bias is improved compared to the ACM in the filter transition regions in both cases. However, a mean negative bias of 1.25 percent compared to the Nyquist velocity for case 1 and 2.8 percent for case 2 is present across the velocity spectrum. The standard deviation of the low-rank MLE is superior in the transition

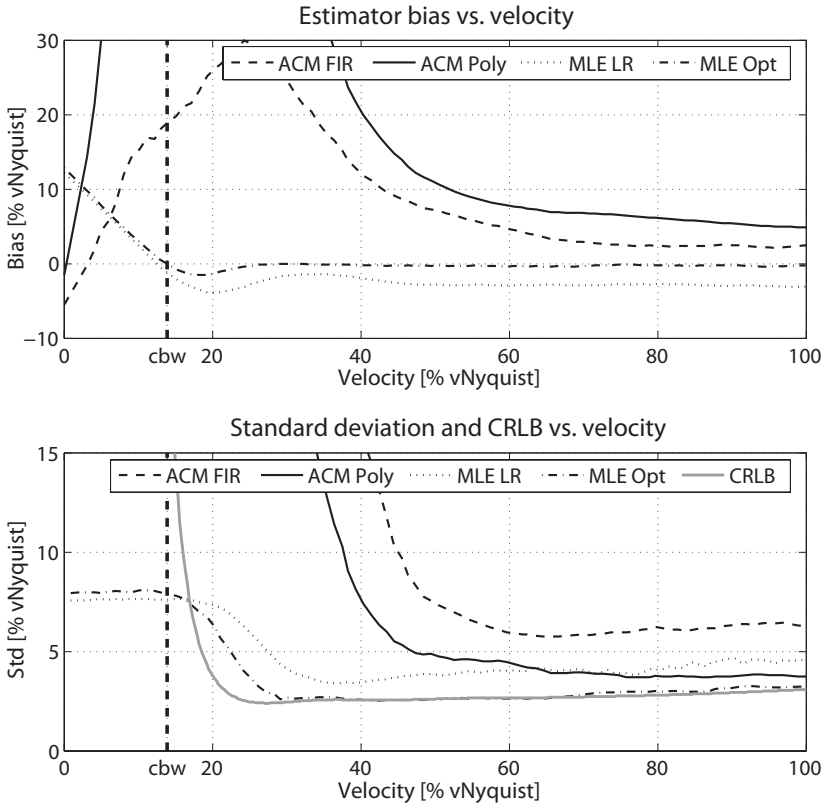


Figure 4.6: The bias and standard deviation of the ACM compared to the optimal and low-rank MLE for case 2. A 3rd order polynomial regression filter and 8th order FIR filter was used, and 9 spatial points were averaged for all estimators. As can be observed the ACM has a severe bias in the clutter filter transition region, and much can here be gained by the model-based estimators.

region, and comes close to the performance of the ACM in the pass band of both cases.

The low-rank MLE results can be improved by expanding the averaging ROI used to estimate the signal correlation matrix. In Fig. 4.7, the results of increasing the averaging ROI for case 2 are shown. In the two larger plots the bias and standard deviation is given for an averaging ROI consisting of 12 and 30 points. As can be seen, the standard deviation of the low-rank MLE using 30 spatial averaging points now has near equal performance as that of the optimal MLE. However, an overall negative bias of 1.0 percent compared to the Nyquist velocity still remains. In the smaller plots, the development of the low-rank MLE performance can be followed for two different velocities, $\frac{1}{3}v_{Nyquist}$ and $\frac{2}{3}v_{Nyquist}$. The performance quickly converges to its final value. In fact, for case 2 the best performance is achieved using less than 25 averaging points.

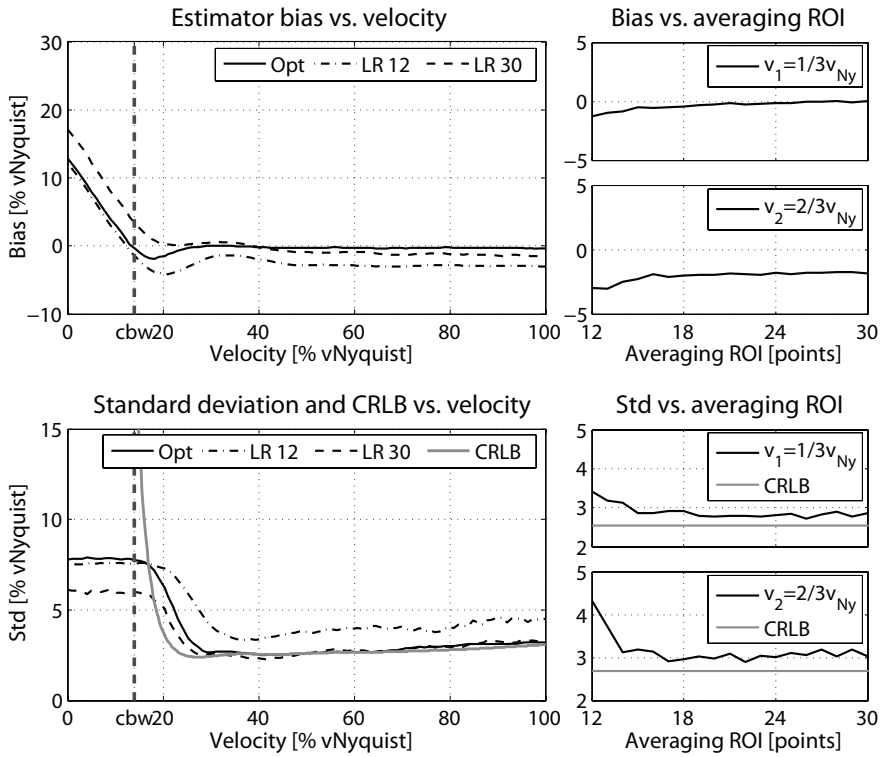


Figure 4.7: The bias and standard deviation of the low-rank MLE for an increasing amount of independent averaging points. The two larger plots show the performance for an averaging ROI of 12 and 30 points. The smaller plots show the development towards the optimal MLE for two different velocities. As can be observed, the low-rank MLE quickly approach the optimal MLE, although a negative bias remains.

## 4.5 Discussion

This work investigates if optimal methods of velocity estimation exist in CFI in presence of clutter. The simulation study was based on simplified models of the received signal from both clutter and blood, which allowed us to develop an analytical expression for the CRLB, and a tractable simulation setup for maximum likelihood estimation. We assumed only the flow velocity magnitude as unknown.

Stationary and rectilinear movement of the blood scatterers were assumed, which is a fair approximation only for very limited spatial extents and very short periods of time. The tissue signal was assumed to be centered around zero Doppler frequency with a given bandwidth. In reality, the tissue may move considerably in the radial direction and its Doppler spectrum may therefore be shifted away from the center. Also, the tissue movement is in general cyclic and therefore accelerated, and the tissue

Doppler bandwidth will then increase and vary with time. For proper parametric modeling of the clutter Doppler spectrum, a varying Doppler shift as well as a varying bandwidth should be taken into account.

Further simplifications made in the signal models would in reality influence the received Doppler signal. Frequency dependent scattering and attenuation were assumed included in the model for the received signal, but must in a practical estimator be estimated from the received signal. As shown by Ferrara [41], this factor affected the results of their MLE as well as the conventional ACM. In a practical model-based estimator, frequency dependent scattering and attenuation should be included. We further assumed Gaussian shaped beam profiles, and neglected beam sidelobes. Gaussian shaped main beam lobes are approximately given when using rectangular apodization, and even more so for smooth apodization functions. Also, as shown in an example in [30], 94 percent of the signal power from blood can be considered to originate from within the $-6$ dB mainlobe of the beam, and helps to rationalize the approximation of neglecting sidelobes.

The results show that we were able to produce an optimal MVU velocity estimator for CFI, even in presence of a severe clutter signal, by using several (independent) spatial points in the estimator design. The MVU estimator for case 2 was approximately ensured for 9 spatial points. However, for the less challenging case 1, using 3 spatial points in the estimator design would have been sufficient. In the estimator comparisons in Fig. 4.5 and 4.6, the FIR filters are less biased than polynomial regression filters for both cases. To achieve comparable filter frequency responses, we had to use an 8th order FIR filter, and only 4 samples were available for velocity estimation. FIR filters therefore exhibited a higher variance than polynomial regression filters. These results have also previously been reported [16, 21]. The negative bias seen for the ACM for low velocities in the filter transition region of Fig. 4.5 can be explained by small remains of clutter signal present after filtering, that become prominent when the blood signal is increasingly attenuated. For asymmetric FIR filters such as the minimum-phase filter used in this work, the standard deviation could be improved by filtering in both the forward and backward direction as described in [21]. For case 2 there is a moderate positive bias even in the pass-band of the clutter filters. This is caused by the high-pass filtering of the thermal noise component, which pulls the mean frequency towards the Nyquist velocity. This problem and a possible solution has been described in [42]. Compared to the MLE assuming full knowledge of the clutter statistics, the ACM averaging 9 correlation function estimates performs quite adequately in the clutter filter pass band for case 1. And although the method is biased for case 2, it still has a low standard deviation in the filter pass band when using a polynomial regression filter. However, in the clutter filter transition regions there is much to be gained compared to the CRLB in both cases.

We investigated the performance of the MLE when incorporating direct estimates of the clutter correlation matrix from the received signal. This concept has several advantages. The clutter Doppler parameters such as mean frequency and bandwidth does not need to be modeled explicitly, and the method will also adapt to variations of these parameters over the heart cycle. The concept can be taken further. The signal variation represented by the remaining eigenvectors not included in the clutter

correlation matrix estimate, may be used for estimating parameters related to the blood and thermal noise component, to further reduce the number of unknowns. Estimation of the blood signal power could be attempted, and it is common to estimate the white noise signal power using the smallest eigenvalues. In our context the noise component can also be estimated from the received signal when turning off the transmitter. These aspects are not pursued in this work, however they may represent further important steps towards a practical model-based blood velocity estimator in presence of clutter. As seen in Fig. 4.5 and 4.6, the low-rank MLE outperforms the ACM in the clutter filter transition region, and is close in performance in the filter pass bands. Further, the results approach that of the MLE when averaging the signal correlation matrix over just a marginally larger area than the minimal required to form a full rank correlation matrix estimate. The same statistical process is assumed when averaging, and in reality the averaging ROI used will be limited by varying signal characteristics over the ultrasound image. The negative bias present for the low-rank MLE can be explained by a deviation in the low-rank estimate of the clutter correlation matrix compared to the actual one. This misrepresentation is perhaps the most serious source of errors in such modeling. The correct choice of clutter signal rank is crucial for the success of method, and must in practise be chosen adaptively due to the time varying characteristics of the clutter and blood signal mixtures.

In this work, we have not explored computationally efficient methods for the implementation of the MLE. However, in [39] we demonstrated a method for real-time eigenanalysis in adaptive clutter filter design. We also proposed a method for selecting the proper clutter rank adaptively based on the slope of the eigenvalue spectrum, and demonstrated its potential through in-vivo examples. This method should also be applicable for estimating the clutter correlation matrix in model-based estimation.

## 4.6 Conclusion

Optimal estimation of blood velocity in CFI was investigated based on simplified models of both clutter and blood. An efficient maximum likelihood estimator of blood velocity was shown to exist in the CFI setting only when including several (independent) spatial points in the estimator design. However, even for severe clutter conditions no more than 3-9 points were needed in our simulations. The ACM was approximately unbiased only for a moderate clutter signal scenario, then only in the clutter filter pass band, and with a variance of up to four times the CRLB. The ACM suffered from a severe bias in the filter transition region, and a significant performance gain was here achieved using the MLE. Adaptive modeling of the clutter signal statistics using low-rank estimates of the signal correlation matrix was investigated, and came close in performance to the MLE assuming full knowledge of the clutter statistics. This may be an important step towards a practical model-based estimator that also includes the clutter signal, and more work should be done to explore computationally efficient approaches to such an estimation scheme.

## 4.7 Appendix: Derivation of log-likelihood function for K independent complex Gaussian signal vectors

The joint likelihood function for $K$ independent complex Gaussian signal vectors is given by

$$\begin{aligned} p(\boldsymbol{x}_1, \boldsymbol{x}_2, \cdots, \boldsymbol{x}_K; v) &= \prod_{k=1}^{K} p_x(\boldsymbol{x}_k; v) \\ &= \Big(\frac{1}{\pi^{N_P}|\mathbf{R}_x(v)|}\Big)^K e^{-\sum_{k=1}^{K} \boldsymbol{x}_k^{*T}\mathbf{R}_x(v)\boldsymbol{x}_k}. \end{aligned} \tag{4.27}$$

Taking the natural logarithm of (4.27) then yields

$$L_K(\boldsymbol{x}; v) = \ln\Big(\frac{1}{\pi^{N_P}|\mathbf{R}_x(v)|}\Big)^K - \sum_{k=1}^{K} \boldsymbol{x}_k^{*T}\mathbf{R}_x(v)\boldsymbol{x}_k. \tag{4.28}$$

The sum of quadratic expressions $\boldsymbol{x}_k^{*T}\mathbf{R}_x\boldsymbol{x}_k$ can be simplified by invoking the vector algebra rule $(\boldsymbol{a}^{*T}\boldsymbol{b}) = tr(\boldsymbol{b}\boldsymbol{a}^{*T})$ [34], where $tr$ is the matrix trace operator. Setting $\boldsymbol{b} = \mathbf{R}_x\boldsymbol{x}_k$ and $\boldsymbol{a} = \boldsymbol{x}_k$, we get

$$L_K(\boldsymbol{x}; v) = \ln\Big(\frac{1}{\pi^{N_P}|\mathbf{R}_x(v)|}\Big)^K - \sum_{k=1}^{K} tr\big(\mathbf{R}_x(v)\boldsymbol{x}_k\boldsymbol{x}_k^{*T}\big). \tag{4.29}$$

Since the sum of matrix traces is equal to the trace of the sum of matrices, we can further write

$$L_K(\boldsymbol{x}; v) = \ln\Big(\frac{1}{\pi^{N_P}|\mathbf{R}_x(v)}\Big)^K - tr(\mathbf{R}_x(v)\sum_{k=1}^{K} \boldsymbol{x}_k\boldsymbol{x}_k^{*T}). \tag{4.30}$$

By using the expression for the sample correlation marix in (4.19), and writing out every expression, we get the final (negative) log-likelihood function:

$$\begin{aligned} -L_K(\boldsymbol{x}; v) = K\big[&tr(\mathbf{R}_x^{-1}(v)\hat{\mathbf{R}}_K) \\ &+ \ln|\mathbf{R}_x(v)| + N_P \ln\pi\big]. \end{aligned} \tag{4.31}$$

# References


[1] A. Weyman, *Principles and Practice of Echocardiography.* Philadelphia, USA: Lippincott Williams & Wilkins, 1993.

[2] M. Hennerici and D. Neuerburg-Heusler, *Vascular Diagnosis With Ultrasound: Clinical References With Case Studies.* New York, USA: Thieme Medical Publishers, 1997.

[3] P. Wells, "Ultrasonic colour flow imaging," *Phys. Med. Biol.*, vol. 39, pp. 2113–2145, 1994.

[4] K. Ferrara and G. DeAngelis, "Color flow mapping," *Ultrasound in Medicine & Biology*, vol. 23, pp. 321–345, 1997.

[5] C. Kasai, K. Namekawa, A. Koyano, and R. Omoto, "Real-time two-dimensional blood flow imaging using an autocorrelation technique," *IEEE Trans. Sonics Ultrason.*, vol. 32, pp. 458–464, 1985.

[6] D. Zrnic, "Spectral moment estimates from correlated pulsed pair," *IEEE Trans. Aerosp. Electron.*, vol. 13, pp. 344–354, 1977.

[7] R. Doviak and D. Zrnic, "Practical algorithms for mean velocity estimation in pulse doppler weather radars using a small number of samples," *IEEE Trans. Geosci. Remote Sensing*, vol. 21, pp. 491–501, 1983.

[8] O. Bonnefous and P. Pesque, "Time domain formulation of pulse-doppler ultrasound and blood velocity estimation by cross correlation," *Ultrason. Imaging*, vol. 8, pp. 73–85, 1986.

[9] K. Ferrara and V. Algazi, "A new wideband spread target maximum likelihood estimator for blood velocity estimation. i. theory," *IEEE Trans. Ultrason., Ferroelec., Freq. Contr.*, vol. 38, pp. 1–16, 1991.

[10] T. Loupas, J. Powers, and R. Gill, "An axial velocity estimator for ultrasound blood flow imaging, based on a full evaluation of the doppler equation by means of a two-dimensional autocorrelation approach," *IEEE Trans. Ultrason., Ferroelec., Freq. Contr.*, vol. 42, pp. 672–688, 1995.

[11] S. Alam and K. Parker, "The butterfly search technique for estimation of blood velocity," *Ultrasound in Medicine & Biology*, vol. 21, pp. 657–670, 1995.

[12] M. Fox, "Multiple crossed-beam ultrasound doppler velocimetry," *IEEE Trans. Sonics Ultrason.*, vol. 25, pp. 281–286, 1978.

[13] G. Trahey, J. Allison, and O. von Ramm, "Angle independent ultrasonic detection of blood flow," *IEEE Trans. Biomed. Eng.*, vol. 34, pp. 965–967, 1987.

[14] J. Jensen and P. Munk, "A new method for estimation of velocity vectors," *IEEE Trans. Ultrason., Ferroelect., Freq. Contr.*, vol. 45, pp. 837–851, 1998.

[15] H. Torp, X. Lai, and K. Kristoffersen, "Comparison between cross-correlation and auto-correlation technique in color flow imaging," *Ultrasonics Symposium, 1993 Proceedings, IEEE 1993*, pp. 1039–1042 vol2, 1993.

[16] H. Torp, "Clutter rejection filters in color flow imaging: A theoretical approach," *IEEE Trans. Ultrason., Ferroelec., Freq. Contr.*, vol. 44, pp. 417–424, 1997.

[17] A. Hoeks, J. Vandevorst, A. Dabekaussen, P. Brands, and R. Reneman, "An efficient algorithm to remove low-frequency doppler signals in digital doppler systems," *Ultrason. Imaging*, vol. 13, pp. 135–144, 1991.

[18] A. Kadi and T. Loupas, "On the performance of regression and step-initialized iir clutter filters for color doppler systems in diagnostic medical ultrasound," *IEEE Trans. Ultrason., Ferroelec., Freq. Contr.*, vol. 42, pp. 927–937, 1995.

[19] S. Bjaerum, H. Torp, and K. Kristoffersen, "Clutter filter design for ultrasound color flow imaging," *IEEE Trans. Ultrason., Ferroelec., Freq. Contr.*, vol. 49, pp. 204–216, 2002.

[20] L. Thomas and A. Hall, "An improved wall filter for flow imaging of low velocity flow," *Proceedings of the IEEE Ultrasonics Symposium*, vol. 3, pp. 1701–1704, 1994.

[21] S. Bjaerum, H. Torp, and K. Kristoffersen, "Clutter filters adapted to tissue motion in ultrasound color flow imaging," *IEEE Trans. Ultrason., Ferroelec., Freq. Contr.*, vol. 49, pp. 693–704, 2002.

[22] D. Kruse and K. Ferrara, "A new high resolution color flow system using an eigendecomposition-based adaptive filter for clutter rejection," *IEEE Trans. Ultrason., Ferroelect., Freq. Contr.*, vol. 49, pp. 1384–1399, 2002.

[23] C. Gallippi and G. Trahey, "Adaptive clutter filtering via blind source separation for two-dimensional ultrasonic blood velocity measurement," *Ultrason. Imaging*, vol. 24, pp. 193–214, 2002.

[24] P. Vaitkus and R. Cobbold, "A new time-domain narrowband velocity estimation technique for doppler ultrasound flow imaging. i. theory," *IEEE Trans. Ultrason., Ferroelec., Freq. Contr.*, vol. 45, pp. 939–954, 1998.

[25] Y. Ahn and S. Park, "Estimation of mean frequency and variance of ultrasonic doppler signal by using second-order autoregressive model," *IEEE Trans. Ultrason., Ferroelec., Freq. Contr.*, vol. 38, pp. 172–182, 1991.

[26] M. Allam, R. Kinnick, and J. Greenleaf, "Isomorphism between pulsed-wave doppler ultrasound and direction-of-arrival estimation. ii. experimental results," *IEEE Trans. Ultrason., Ferroelec., Freq. Contr.*, vol. 43, pp. 923–935, 1996.

[27] M. Schlaikjer and J. Jensen, "Maximum likelihood blood velocity estimator incorporating properties of flow physics," *IEEE Trans. Ultrason., Ferroelec., Freq. Contr.*, vol. 51, pp. 80–92, 2004.

[28] J. Giovannelli, J. Idier, B. Querleux, A. Herment, and G. Demoment, "Maximum likelihood and maximum a posteriori estimation of gaussian spectra. application to attenuation measurements and color doppler velocimetry," *Ultrasonics Symposium, 1994 Proceedings, 1994 IEEE*, vol. 3, pp. 1721–1726 vol.3, 1994.

[29] E. Chornoboy, "Optimal mean velocity estimation for doppler weather radars," *IEEE Transactions on Geoscience and Remote Sensing*, vol. 31, pp. 575–586, 1993.

[30] H. Torp, K. Kristoffersen, and B. Angelsen, "Autocorrelation technique in color flow imaging, signal model and statistical properties of the autocorrelation estimates," *IEEE Trans. Ultrason., Ferroelec., Freq. Contr.*, vol. 41, pp. 604–612, 1994.

[31] B. Angelsen, "A theoretical study of the scattering of ultrasound from blood," *IEEE Trans. Biomed. Eng.*, vol. BME-27, pp. 61–67, 1980.

[32] R. Wagner, S. Smith, J. Sandrik, and H. Lopez, "Statistics of speckle in ultrasound b-scans," *IEEE Trans. Sonics Ultrason.*, vol. 30, pp. 156–163, 1983.

[33] A. Heimdal and H. Torp, "Ultrasound doppler measurements of low velocity blood flow: limitations due to clutter signals from vibrating muscles," *IEEE Trans. Ultrason., Ferroelec., Freq. Contr.*, vol. 44, pp. 873–881, 1997.

[34] S. Kay, *'Fundamentals of Statistical Signal Processing - Estimation theory '*. New Jersey, USA: Prentice Hall, Inc., 1993.

[35] H. Torp, K. Kristoffersen, and A. Angelsen, "On the joint probability density function for the autocorrelation estimates in ultrasound color flow imaging," *IEEE Trans. Ultrason., Ferroelec., Freq. Contr.*, vol. 42, pp. 899–906, 1995.

[36] T. Loupas and W. McDicken, "Low-order ar models for mean and maximum frequency estimation in the context of doppler color flow mapping," *IEEE Trans. Ultrason., Ferroelec., Freq. Contr.*, vol. 37, pp. 590–601, 1990.

[37] P. Vaitkus, R. Cobbold, and K. Johnston, "A new time-domain narrowband velocity estimation technique for doppler ultrasound flow imaging. ii. comparative performance assessment," *IEEE Trans. Ultrason., Ferroelec., Freq. Contr.*, vol. 45, pp. 955–971, 1998.

[38] C. Therrien, *Discrete Random Signals and Statistical Signal Processing.* Upper Saddle River, USA: Prentice Hall Inc., 1992.

[39] L. Løvstakken, S. Bjærum, K. Kristoffersen, R. Haaverstad, and H. Torp, "Real-time adaptive clutter rejection in color flow imaging using power method iterations," *IEEE Trans. Ultrason., Ferroelect., Freq. Contr.*, vol. 53, pp. 1597–1608, 2006.

[40] W. Press, B. Flannery, S. Teukolsky, and W. Vetterling, *Numerical Recipes in C : The Art of Scientific Computing.* Cambridge, Englend: Cambridge University Press, 1992.

[41] K. Ferrara, V. Algazi, and J. Liu, "The effect of frequency dependent scattering and attenuation on the estimation of blood velocity using ultrasound," *IEEE Trans. Ultrason., Ferroelec., Freq. Contr.*, vol. 39, pp. 754–767, 1992.

[42] J. Rajaonah, B. Dousse, and J. Meister, "Compensation of the bias caused by the wall filter on the mean doppler frequency," *IEEE Trans. Ultrason., Ferroelec., Freq. Contr.*, vol. 41, pp. 812–819, 1994.

# Chapter 5

# Blood Flow Imaging - A new real-time 2-D flow imaging technique

Lasse Løvstakken[1], Steinar Bjærum[2], Ditlef Martens[2], and Hans Torp[1]
[1] Dept. Circulation and Medical Imaging, NTNU
[2] GE Vingmed Ultrasound, Horten, Norway

This paper presents a new method for the visualization of two-dimensional (2-D) blood flow in ultrasound imaging systems called blood flow imaging (BFI). Conventional methods of color flow imaging (CFI) and power Doppler (PD) techniques are limited as the velocity component transversal to the ultrasound beam cannot be estimated from the received Doppler signal. The BFI relies on the preservation and display of the speckle pattern originating from the blood flow scatterer signal, and it provides qualitative information of the blood flow distribution and movement in any direction of the image. By displaying speckle pattern images acquired with a high frame rate in slow motion, the blood flow movement can be visually tracked from frame to frame. The BFI is easily combined with conventional CFI and PD methods, and the resulting display modes have been shown to have several advantages compared to CFI or PD methods alone. Two different display modes have been implemented: one combining BFI with conventional CFI, and one combining BFI with PD. Initial clinical trials have been performed to assess the clinical usefulness of BFI. The method especially has potential in vascular imaging, but it also shows potential in other clinical applications.

## 5.1 Introduction

Conventional ultrasound imaging of blood flow is based on the detection and estimation of the Doppler shift caused by blood scatterer movement. The Doppler shift is used to discriminate signal from blood flow scatterer to that of slowly moving muscular tissue. It also is used to quantify the actual blood flow velocity. Unfortunately, this Doppler shift measuring technique is only sensitive to the velocity component along the ultrasonic beam, and potential velocity components transversal to the beam cannot be estimated. This issue is common to all the established Doppler techniques existing in current scanner systems, such as pulsed and continuous wave Doppler (PW, CW), color flow imaging (CFI), and power Doppler (PD). Although these methods have proved to be highly useful clinically in locating abnormal blood flow related to pathology [1, 2], the angle dependency typically leads to an underestimation of the true blood flow velocity, and erroneous results may be displayed.

Several authors have proposed methods for measuring both the axial and lateral flow velocity components using ultrasound. Compound Doppler scanning has been attempted [3, 4], in which several beams from different directions overlap in a region of interest at which a velocity vector is constructed. The beams may originate from different transducers, or from subapertures on a single transducer. The accuracy of the method depends on the angle between the emitted beams, and it can be difficult to get a wide enough angle for sufficient accuracy. When using several transducers, it also can be difficult to get the necessary acoustic windows for beam overlap.

Two-dimensional speckle pattern tracking techniques also have been proposed [5, 6]. These methods rely on correlation techniques to track the displacement of the speckle pattern in small regions from image to image. The velocity is found using the estimated displacement and the time between image acquisitions. The decorrelation of the speckle pattern in a region over time degrades the accuracy of the method; therefore, it can be difficult to get proper estimates in the presence of out-of-plane movement, flow gradients, and turbulence.

Another way of estimating the lateral flow velocity component by using lateral coherent processing was introduced for ultrasound applications by Anderson [7] and Jensen [8]. By using more advanced aperture apodization and focusing schemes, the lateral beam pattern can be modulated. Quadrature sampling and processing of the received signal in the lateral direction then can be used to estimate the lateral flow velocity. Issues exist limiting the usability of the methods, including a reduced sensitivity due to a high degree of aperture apodization, a relatively poor lateral resolution, and a measurement accuracy that decreases when both axial and lateral flow is present due to axial-lateral inter-modulation.

Common to all methods mentioned is that they are still experimental, and relatively few or no publications showing the potential clinical use of the methods exist. A new method for visualizing blood flow with ultrasound that has reached clinical use is the B-flow technique introduced by Chiao et al [9]. The method uses coded excitation and temporal high-pass filtering to simultaneously show B-mode images of tissue and flow based on the same data without using overlays. Using coded excitation, a high resolution can be achieved while retaining sensitivity, and the display mode better

indicates the vessel wall to flow borderline compared to established methods. The method also may indicate hemodynamic properties and the lateral direction of flow through speckle pattern movement. However, a low imaging frame rate compared to the flow movement limits the perception of the true blood flow direction.

This paper describes a new method for visualizing both the axial and lateral blood flow, called blood flow imaging (BFI), which is a technique that relies on the preservation and display of the speckle pattern originating from the blood flow signal. By using a slow motion display of speckle pattern imaged at a very high frame rate, it is possible to visually track the speckle movement from frame to frame in any direction. The speckle movement and distribution correlates with that of the corresponding blood scatterer for short time periods, providing qualitative information of the hemodynamics. The method is most comparable to B-flow, as both methods are using B-mode processing for the imaging of flow, and neither method attempts to estimate the actual flow velocity. However, BFI has been combined with conventional Doppler techniques to also provide quantitative flow velocity information. As will be shown, this combined modality differs in several aspects compared to conventional CFI, PD, and B-flow that may be advantageous clinically.

The method described in this paper was first introduced by Bjærum [10], and some of the material and figures used have been taken from his work. The method has further been described in two proceeding papers [11, 12]. Since the original method description, a real-time implementation has been made. Based on this experience, the method has been further optimized and evaluated for different clinical settings. The aim of this paper is to present the BFI data acquisition, signal processing, and display modes. And further, to compare the new display modes to conventional CFI and B-flow. These aspects are described in Sections II, III, and IV, respectively. Results of basic BFI processing and an initial evaluation of a real-time implementation of BFI with examples of potential clinical use are included in Section V. In Section VI, the current status of the BFI modality is discussed. And in Section VII, initial conclusions are drawn.

## 5.2 Data acquisition

The data acquisition in BFI is basically the same as in conventional CFI and PD modalities. The ultrasonic beam is scanned over the flow region to be imaged, and a series of $N$ pulses (typically 8-16) are transmitted in each beam direction, which forms the basis for further blood flow detection and velocity estimation. This acquisition scheme is referred to as packet acquisition, and the number of pulses $N$ as the packet size. For each flow image, one tissue B-mode scan is performed, and the flow and B-mode images are combined to visualize both the blood flow and the tissue structures simultaneously. The data acquisition in BFI is restricted by the same model for ensuring the safety of patients as in conventional CFI and meets all requirements set by the FDA in these regards.

In BFI the goal is to ensure a good visual perception of the flow movement in axial and lateral directions using images of the speckle pattern. There are some concerns

regarding the data acquisition for this to succeed. One concern deals with frame rate requirements. As the decorrelation of the speckle pattern from blood flow scatterer is rapid, a high frame rate is needed to be able to capture the speckle pattern movement. This frame rate requirement can be attained using packet acquisition as in conventional methods as described above, in which the frame rate for speckle pattern imaging then is the pulse repetition frequency (PRF) used during acquisition. It also is important that the time between the acquisition of neighboring beams is small compared to the PRF, so that snapshots of the speckle movement are acquired. This means that the beam sweep velocity must be much higher than the flow velocity. In B-Flow imaging [9], this is not the case, and the flow velocity is often comparable to the sweep velocity of the imaging system. The speckle movement then will not be apparent between images. In BFI, a high sweep rate compared to the flow velocity is made possible by using beam interleaving techniques [13] that can be described as follows. The ultrasonic pulse needs to propagate a distance equal to twice the image depth $d_{max}$ before a new pulse can be transmitted. The maximum possible PRF is thus given by:

$$\mathrm{PRF}_{\max} = \frac{1}{T} = \frac{c}{2d_{\max}}, \tag{5.1}$$

where c is the sound velocity. By decreasing the PRF with a factor $k$, there is time to acquire data in $k-1$ other beam directions before transmitting the next pulse in the initial direction. These $k$ beams form an interleave group (IG), and the number $k$ is called the interleave group size (IGS) which can be expressed by:

$$\mathrm{IGS} = \left\lfloor \frac{\mathrm{PRF}_{\max}}{\mathrm{PRF}} \right\rfloor \cdot \mathrm{MLA}, \tag{5.2}$$

where MLA is the number of parallel beams acquired, and $\lfloor \cdot \rfloor$ means rounding off to the nearest integer towards $-\infty$. The number of interleave groups $N_{\mathrm{IG}}$ in one image is given by:

$$N_{\mathrm{IG}} = \frac{N_{\mathrm{beams}}}{\mathrm{IGS}}, \tag{5.3}$$

where $N_{\mathrm{beams}}$ is the number of beams determined by the image width and the lateral resolution. The principle of beam interleaving is illustrated in Fig. 5.1, where the numbers in the different beam directions indicate the timing of the transmitted pulses.

Another concern that needs to be addressed is the requirement for spatial resolution. To ensure a proper perception of movement, the speckle pattern needs to be fine-grained in both the axial and lateral direction of the image. In the axial direction this is given if the pulse bandwidth is sufficiently high, which for conventional pulses corresponds to a short pulse length during acquisition. In the lateral direction of the image this property is ultimately given if the beam width achieved during acquisition is sufficiently narrow and the beam overlap is sufficiently high. Compared to typical CFI and PD applications both the axial and lateral resolution often has to be improved for BFI to work properly.

The timing of pulse transmissions compared to the generation of image samples for conventional CFI / PD and BFI is shown in Fig. 5.2. In conventional CFI and PD,

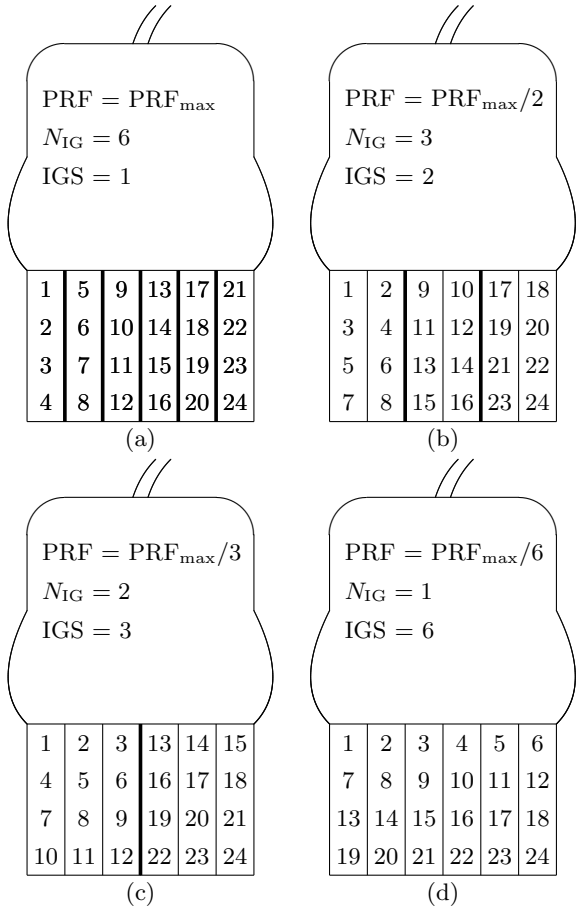


Figure 5.1: Beam interleaving in 2-D Doppler acquisition with 6 beam directions and packet size $N = 4$. The numbers indicate the sequence of the 24 pulses.

one image sample is generated for each packet acquired. In BFI each packet sample corresponds to one speckle image sample; therefore, several images are generated for each packet frame acquired. These speckle images are displayed uniformly in time during the capture of one complete packet frame, and the frame rate in BFI is thus increased compared to conventional CFI or PD methods. This BFI frame rate is approximatively given by

$$BFI_{\mathrm{FR}} = CFI_{\mathrm{FR}} \cdot N_{\mathrm{BFI}} \approx \frac{PRF_{\max}}{N_{\mathrm{b}} \cdot N} \cdot (N - N_{\mathrm{F}}), \tag{5.4}$$

where $CFI_{\mathrm{FR}}$ is the frame rate using CFI / PD methods, $N_{\mathrm{BFI}}$ is the number of BFI frames calculated for each packet of data, $N$ is the packet size, $N_{\mathrm{b}}$ is the number of beams used during acquisition, and $PRF_{\max}$ is the maximum PRF available. $N_{\mathrm{F}}$ is

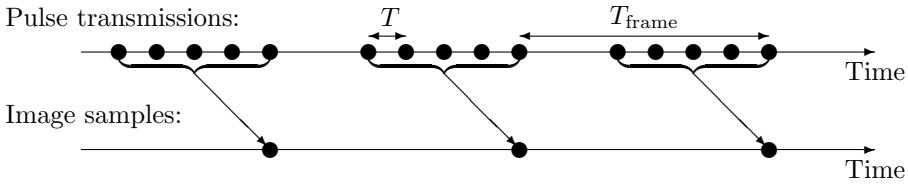


(a) Pulse transmissions and image sample generation in CFI/PD

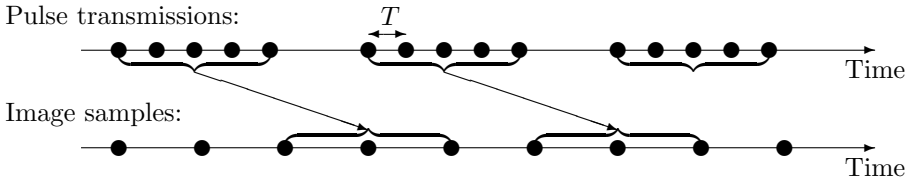


(b) Pulse transmissions and image sample generation in BFI

Figure 5.2: The timing of pulse transmissions vs. image samples. During the time $T_{\text{frame}}$, packet data in all beam directions as well as tissue B-mode data are acquired. In conventional CFI/PD methods, one image sample is calculated per packet of data. In BFI, several image samples are calculated per packet of data, providing a higher imaging frame rate.

the number of samples lost due to clutter filtering. Using a finite impulse response filter (FIR) as described in Section 5.3 this number equals the filter order (typically 3-5 samples). The time it takes to capture a separate tissue B-mode image has been neglected in the equation.

As the speckle images are acquired with a frame rate equal to the PRF of the system and displayed uniformly during the capture of one entire packet frame, the speckle pattern movement is displayed in slow motion. This is necessary to allow the human eye to perceive the movement. A slow motion factor can be calculated, showing how fast the speckle pattern and hence blood flow scatterer are moving during display compared to its actual velocity, and is given by

$$n_{\text{SM}} = \frac{BFI_{\text{FR}}}{PRF} \cdot 100\%. \tag{5.5}$$

Typical values for the slow motion factor $n_{\text{SM}}$ are about 5-10% of the actual speckle image velocity.

Following acquisition the input data available for processing are complex demodulated and time-gain compensated IQ signals arranged in packets. Each packet of data corresponds to time samples from one sample volume in the image, sampled at the PRF of the system. These time samples form a complex valued signal vector with dimension equal to the packet size $N$, where the samples have a zero-mean complex Gaussian probability density function (PDF). In Section 5.3, the signal processing performed on the input data will be described.

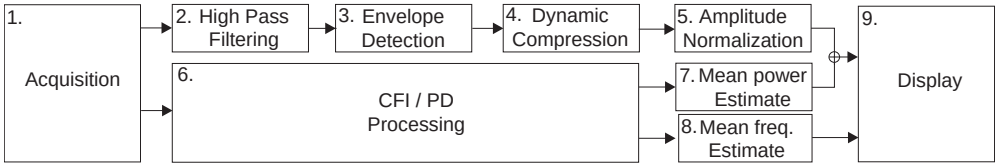


Figure 5.3: A diagram showing the basic signal processing blocks used in BFI and how the BFI processing can be combined with conventional CFI or PD methods.

## 5.3 Signal processing

A block diagram showing the basic form of BFI processing is given in Fig. 5.3. Using this block diagram as a reference, the signal processing in BFI will be described in the following subsections.

### 5.3.1 Basic processing

As seen in block 1-4 in Fig. 5.3, the basic signal processing in BFI is similar to conventional B-mode processing. However, in BFI the speckle pattern from the blood flow signal is to be displayed, and for this to be possible it is necessary to filter out signal from stationary or slow-moving tissue. Therefore, the first stage in BFI processing is clutter filtering. This can be done by high-pass filtering the signal vector obtained from a given sample volume. The result of such an operation is shown in Fig. 5.4, where B-mode image processing has been performed on image data of the carotid artery before and after high-pass filtering. Potential clutter filters include FIR filters, infinite impulse response (IIR) filters with different types of initialization [14, 15], and polynomial regression filters [16–18]. Polynomial regression filters and IIR filters using initialization are not time invariant. As BFI performance depends on the similarity of the speckle pattern in subsequent images, the processing should be the same for all signal vectors. Thus, FIR filters have been preferred being the only filters that are time invariant for signals of finite length [19]. Using a FIR filter will ensure that the visual perception of movement from image to image is not degraded by the clutter filtering operation.

A FIR filter can be described by an impulse response function $h(n),\ n = 0, \ldots, L-1$ , where $L-1$ is the filter order. With an input signal $x(n),\ n = 0, \ldots, N-1$, the output signal $y(n)$ is the convolution sum given by

$$y(n) = \sum_{k=0}^{L-1} h(k)x(n-k). \tag{5.6}$$

This means that each output sample $y(n)$ is a weighted sum of the previous $L$ input samples $x(n), \ldots, x(n-L+1)$. The first output sample that does not depend on any $x(n)$ for $n < 0$ is $y(L-1)$, which implies that the first $L-1$ output samples needs to be discarded. With a packet size equal to $N$, the number of samples after the high-pass filtering process is reduced to $M = N-(L-1)$. This reduction in the

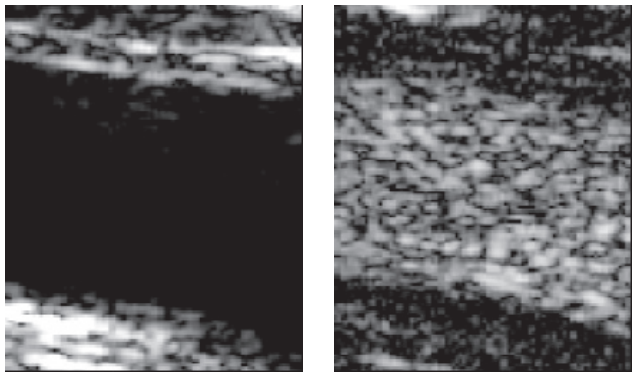

(a) (b)

Figure 5.4: Carotid artery. (a) Tissue B-mode image. (b) Tissue B-mode image calculated from temporally high-pass filtered data.

number of speckle images calculated per packet frame may degrade the perception of movement. Not removing the clutter signal properly results in stationary speckle signal present in areas of blood flow. However, FIR filters of order 3-5 have been made that sufficiently separate the blood flow speckle pattern, while ensuring that enough samples are available for giving the perception of movement. Examples of such FIR filters are given in [19], and the magnitude response of the particular fourth order filter used to generate the examples in this paper is shown in Fig. 5.5.

As shown in block 3 in Fig. 5.3, envelope detection is the next stage in the BFI processing. Having the complex envelope available, this can be accomplished by calculating the squared magnitude $|y(n)|^2$ of the complex signal samples. This detection procedure produces the power envelope of the signal, which form the basis for the speckle image to be displayed. The expected value of $|y(n)|^2$ is the mean power of the signal, and is equal to the autocorrelation function at lag zero, $R(0) = E\{|y(n)|^2\}$. When taking the magnitude squared of the signal, the phase information is discarded, and therefore not used during image formation. The advantages of designing a FIR filter with a minimum-phase response can thus be used. This property is useful as a better stop-band attenuation for a given filter order then can be achieved [19]. It also can be important if a combination of the CFI autocorrelation method with BFI is made based on the same clutter filtered signal vectors, as the CFI processing is very dependent of effective clutter filtering in order to obtain unbiased velocity estimates.

The final step in basic BFI processing is dynamic compression, performed to reduce the dynamic range to a level at which both weak and strong echoes can be visualized simultaneously.

### 5.3.2 Amplitude normalization

As shown in Fig. 5.2 there is a gap in time between the acquisition of signal data packets. This time gap produces discontinuities in the signal and causes visible flashing

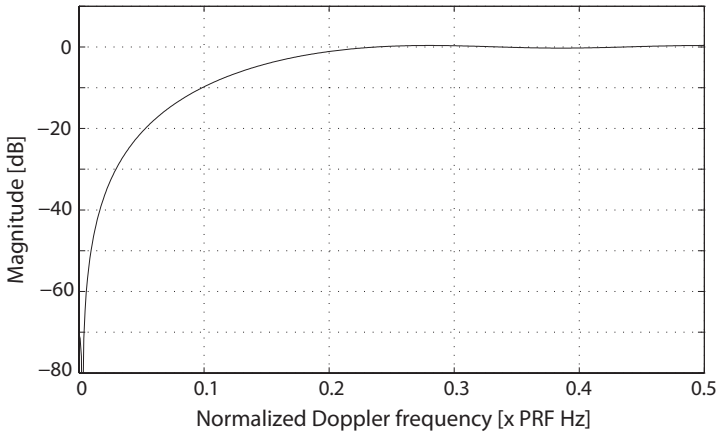


Figure 5.5: The magnitude response of a fourth order minimum phase FIR filter that would work for BFI purposes.

artifacts in the speckle images. The squared magnitude of the high-pass filtered signal from a representative sample volume is shown in Fig. 5.6, where it can be seen that the mean power varies significantly from packet to packet. To get a smooth temporal display, this fluctuation in the mean power needs to be compensated for.

The IQ signal is a stochastic signal with a zero mean complex Gaussian probability distribution. As the high-pass FIR filtering operation is linear, the signal $y(n)$ at the filter output is also a zero mean complex Gaussian process, given by:

$$y(n) = u(n) + iv(n), \tag{5.7}$$

where $u(n)$ and $v(n)$ are zero mean real Gaussian processes that are statistically independent [20]. The expected mean square value is given by:

$$\begin{aligned} E\left\{|y(n)|^2\right\} =& E\left\{u(n)^2\right\} + E\left\{v(n)^2\right\} \\ =& \sigma_u^2 + \sigma_v^2 = 2\sigma_u^2 = 2\sigma_v^2, \end{aligned} \tag{5.8}$$

where $\sigma_u^2 = \sigma_v^2$ are the variances of $u(n)$ and $v(n)$ respectively. Normalizing the squared magnitude by the mean we get:

$$z(n) = \frac{|y(n)|^2}{E\{|y(n)|^2\}} = \frac{1}{2}\left(\frac{u(n)^2}{\sigma_u^2} + \frac{v(n)^2}{\sigma_v^2}\right). \tag{5.9}$$

The random variable $2z(n)$ is $\chi^2$-distributed with 2 degrees of freedom since it is the sum of the square of two independent Gaussian variables with zero mean and variance equal to one [21]. In decibel-scale, the normalized signal becomes:

$$\begin{aligned} w(n) &= g(z(n)) = 10\log(z(n)) \\ &= 10\log(|y(n)|^2) - 10\log\left(E\{|y(n)|^2\}\right). \end{aligned} \tag{5.10}$$

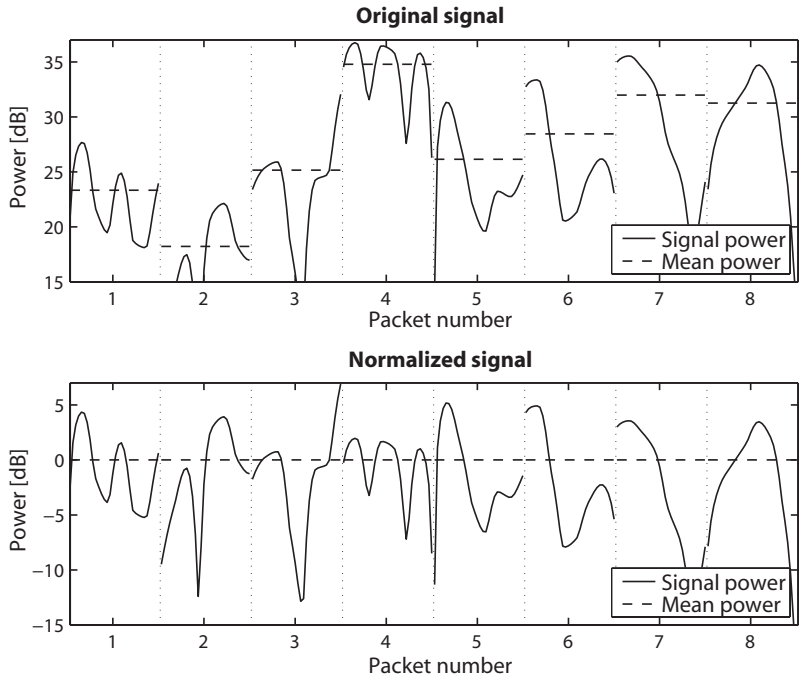


Figure 5.6: The squared magnitude of the original (top) and normalized (bottom) signal in decibel scale. The original signal was normalized by subtracting the sample mean in the log-domain.

The inverse of this transformation is given by $z(n) = h(w(n)) = 10^{w(n)/10}$, and the PDF of $w(n)$ can then be found by [21]:

$$\begin{aligned} f_W(w) =& |h'(w)| \cdot f_U(h(w)) \\ & \frac{\ln(10)}{10} 10^{w/10} e^{-10^{w/10}}. \end{aligned} \tag{5.11}$$

Knowing the actual PDF of the normalized signal allows us to determine the dynamic range needed to capture a desired amount of variation in the signal.

The normalization method corresponding to (5.10) is done by subtracting the mean power estimated by:

$$\hat{R}(0) = \frac{1}{M} \sum_{m=0}^{M-1} |x(m)|^2, \tag{5.12}$$

from the speckle signal in the log domain. This procedure is shown in Fig. 5.6. The estimates then are interpolated to match the number of speckle image samples, smoothed, and limited to a maximum value set by the desired dynamic range for display. The final BFI signal is obtained by adding the normalized speckle signal to the processed mean power estimates. The mean power processing and the final BFI

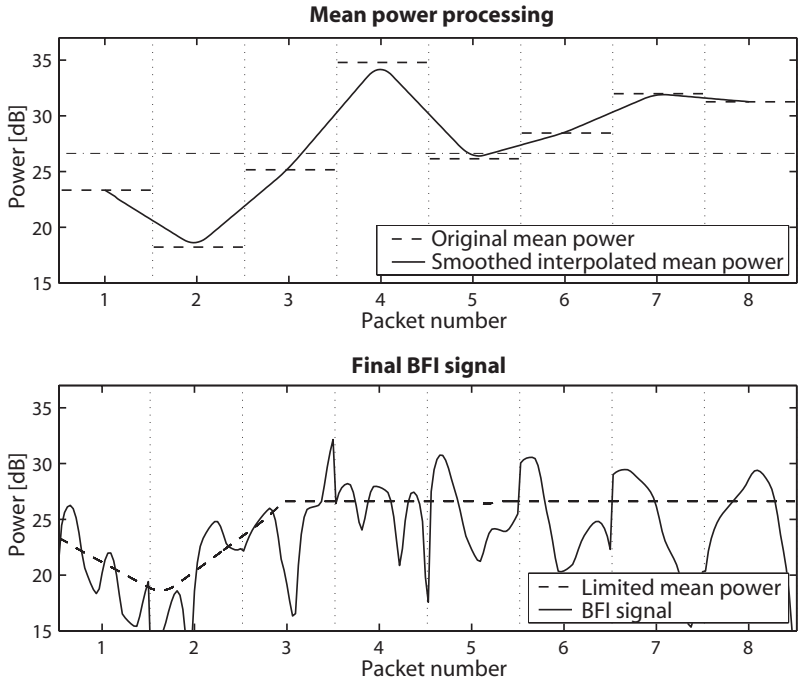


Figure 5.7: The upper plot illustrates the interpolation and smoothing performed on the mean power estimates. The horizontal line indicates the limiting value for these estimates. The lower plot shows the final BFI signal obtained by adding the normalized signal to the processed mean power estimates.

signal is illustrated in Fig. 5.7. Compared to the non-normalized signal in Fig. 5.6 the BFI signal has less variation in mean power while retaining the signal fluctuations.

## 5.4 Display modes

The most basic form of BFI display is a simple mixture of the B-mode tissue image with the BFI speckle image. This modality is in itself interesting, providing blood flow detection and 2-D directional information. However, more powerful modalities emerge when the BFI speckle signal is combined with the output of conventional CFI or PD techniques. In addition to the processing described in Section. 5.3, it is possible to use the same data acquired to perform conventional autocorrelation techniques [22] in parallel. These methods typically estimate the mean power and frequency of the received Doppler signal, which can be modified by the BFI speckle data in a way that allows for both display modes simultaneously. The most apparent combination has been to modify the mean power estimates, which typically represents the brightness of the color display. The processed mean power estimates shown in Fig. 5.7 then are

equal to the mean power estimates from CFI or PD processing.

Two different display modalities have been developed and implemented in real time for evaluation: one combining BFI with CFI, and one combining BFI with PD. All properties of conventional CFI and PD are present, in addition to the information offered by BFI. A mixing parameter can be used to control the amount of speckle pattern that is mixed with the power estimates of CFI or PD. This allows the operator to adjust the display mode to show as much speckle as needed for optimal perception of movement. Setting the mixing parameter to zero would mean that a regular CFI or PD display is shown.

To get satisfactory performance when combining the tissue and flow images, a decision needs to be made whether a certain pixel represents flow or tissue. Without such an arbitration scheme the final image would suffer from flashing artifacts due to ineffective clutter filtering. Normally, a decision is made resulting in a pixel representing either tissue or flow. An alternative to arbitration is to mix the two images together according to amounts given by mixing rules for the red, green, and blue color components. In this way, a transparent view of flow on top of the B-mode image can be made, allowing for both flow and tissue pixels to be shown simultaneously. One example of how the RGB-components can be calculated is given by:

$$\begin{aligned} \mathrm{R} &= 4 \times \mathrm{BFI} + 2 \times \mathrm{tissue}, \\ \mathrm{G} &= \mathrm{BFI} + 4 \times \mathrm{tissue}, \\ \mathrm{B} &= 4 \times \mathrm{tissue} \end{aligned} \tag{5.13}$$

giving a high contrast between blood flow and the surrounding tissue. A new display mode combining BFI with PD using the new additive arbitration scheme has been implemented, which may have advantages when imaging slow flow, or when imaging in poor signal-to-noise ratio conditions.

## 5.5 Results

In the following subsections, results showing the performance of the BFI display modes will be given, including a look at the potential advantages of BFI in different clinical settings. When presenting the BFI display, it is natural to compare the results to the performance of existing modalities. The relevant modalities for comparison includes CFI, PD, and B-flow, which are typically targeted for the same clinical applications. For the initial clinical results, all images were acquired in real time using a Vivid 7 scanner (GE Vingmed Ultrasound, Horten, Norway) system. The BFI is now commercially available as a vascular imaging modality for this system. The probes used during imaging were standard probes normally used for the given application. All recordings were done within FDA limits for thermal and mechanical aspects related to patient safety.

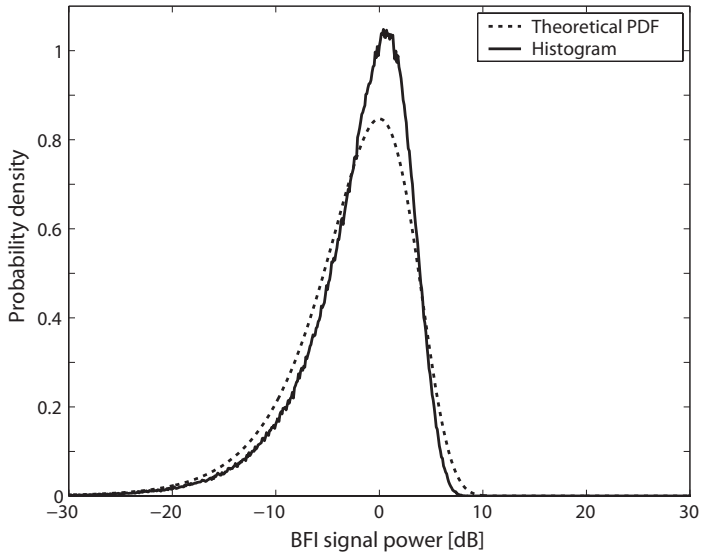


Figure 5.8: The PDF $f_W(w)$ together with a histogram of the data from a representable image frame. The close agreement indicates the validity of the analysis in Section 5.3.2

### 5.5.1 Amplitude normalization

Results of the normalization analysis in Section 5.3.2 is given in Fig. 5.8, in which the PDF in (5.11) is shown together with a histogram of the transformed data from a representable image frame. The figure shows a close agreement between the experimental data and the theoretical PDF, indicating the validity of the analysis. The benefit of using amplitude normalization can be observed in Fig. 5.9, where gray scaled M-mode images generated from high-pass filtered data from a healthy carotid artery is shown. The upper M-mode image was normalized by the procedure given in Section 5.3.2 prior to display; the lower was not. It can be observed that the variation in brightness, corresponding to the signal power level, is reduced between packets as expected.

### 5.5.2 Display modes

The differences between the real-time BFI display modes developed and the comparable modalities CFI and B-flow, can be seen in Fig. 5.10. In Fig. 5.10, images for all the comparable modalities were generated from the same data set of a healthy brachial vein. To simulate the B-flow modality, the method described in [9] was followed, in which the coded excitation acquisition scheme was replaced by conventional imaging using high bandwidth pulses. This was justified by the fact that the signal-to-noise ratio was not an issue for the case used in the comparisons.

The information offered by BFI has several advantages compared to conventional CFI, PD, or B-flow. A more intuitive and detailed view of the blood flow distribution

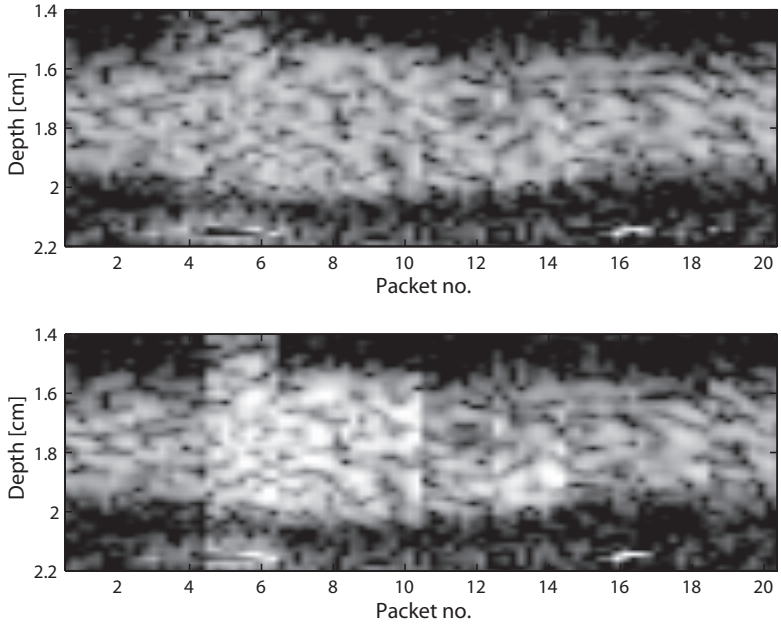


Figure 5.9: M-mode images of high pass filtered data from a healthy carotid artery. The upper image has been normalized prior to display, but the lower image has not. Notice how this procedure removes the variation in mean power level between packets.

and movement is given. Both lateral and axial flow is presented, and at a higher frame rate. Artifacts in conventional CFI or PD such as the coloring of vessel walls are more easily identified. Because the speckle is stationary in these areas, the separation between the vessel wall and blood flow is more visible. Also, the higher frame rate has positive implications in applications requiring a high spatial resolution, as more visual feedback is available.

### 5.5.3 Clinical applications

In this subsection, clinical BFI examples are given for vascular, cardiac, and abdominal applications. The data was acquired using a GE Vingmed Vivid 7 ultrasound scanner, and standard probes were used for the given application. The probes and acquisition parameters used to generate BFI images for the different clinical examples are given in Table 5.1 as a reference.

#### Vascular imaging

BFI has been successfully applied in vascular imaging. The 2-D directional information not available with regular CFI or PD methods may be valuable in many contexts, and in general a more intuitive view of the blood flow is presented. The real channel of the

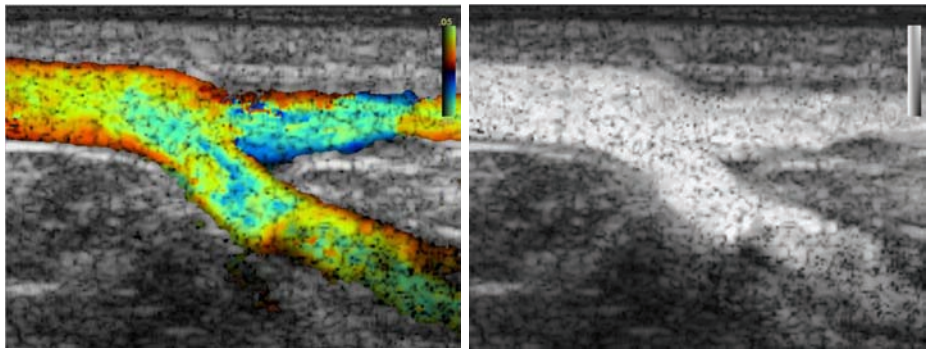

(a) BFI + CFI (b) BFI + PD

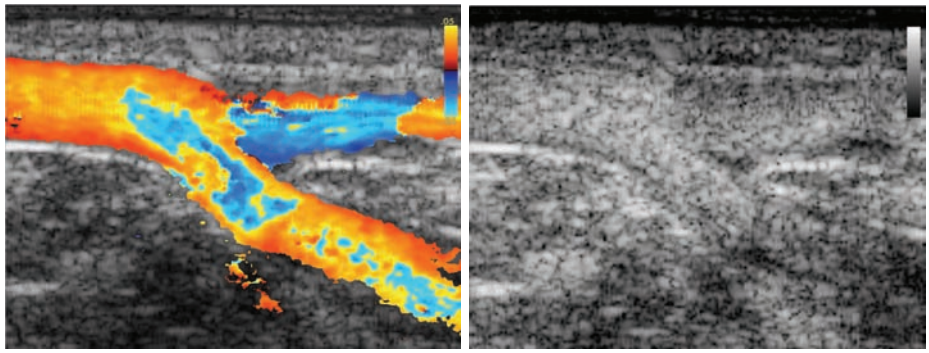

(c) CFI (d) B-Flow

Figure 5.10: The two real-time BFI display modes compared to CFI and B-flow. The images were generated from the same data acquired of a healthy brachial vein bifurcation.

flow across a stenosis, or the flow along a thrombus, can for example be visualized with more detail. Also, disturbed flow patterns may be more easily detected than they are with CFI because both the color and speckle pattern are altered. Fig. 5.11 shows an example of a carotid artery bifurcation in which a stenosis has occurred in the external carotid artery branch. It was imaged in real time using a GE M12L 1.25D linear array probe (GE Healthcare, Waukesha, WI), designed for high resolution vascular imaging. The complex flow in the branching, and across and after the stenosis, can be observed. The turbulence occurring after the stenosis causes eddies that can be observed in the speckle pattern movement.

### Cardiac imaging

The blood flow inside the heart is more complicated than the flow in peripheral vessels. Flow transversal to the imaging plane, a reduced PRF due to the large imaging depth,

**Table 5.1: Acquisition parameters used in clinical BFI examples**

| Parameter | Vascular | Cardiac | Abdominal |
|---|---|---|---|
| Clinical object | Carotid artery | Heart | Kidney |
| Probe | GE M12L | GE 3S | GE 3.5C |
| Probe type | Linear array | Phased array | Curvilinear array |
| Center frequency | 5.7 MHz | 2.5 MHz | 3.6 MHz |
| Sample volume | 0.4 mm | 1.0 mm | 0.6 mm |
| F# transmit / receive | 1.7 / 1.4 | 3.0 / 1.3 | 2.0 / 1.2 |
| Beam overlap | 60 % | 60 % | 65 % |
| PRF | 2.0 kHz | 4.5 kHz | 1.0 kHz |
| Packet size | 12 | 10 | 12 |
| FIR clutter filter order | fourth | fourth | fourth |

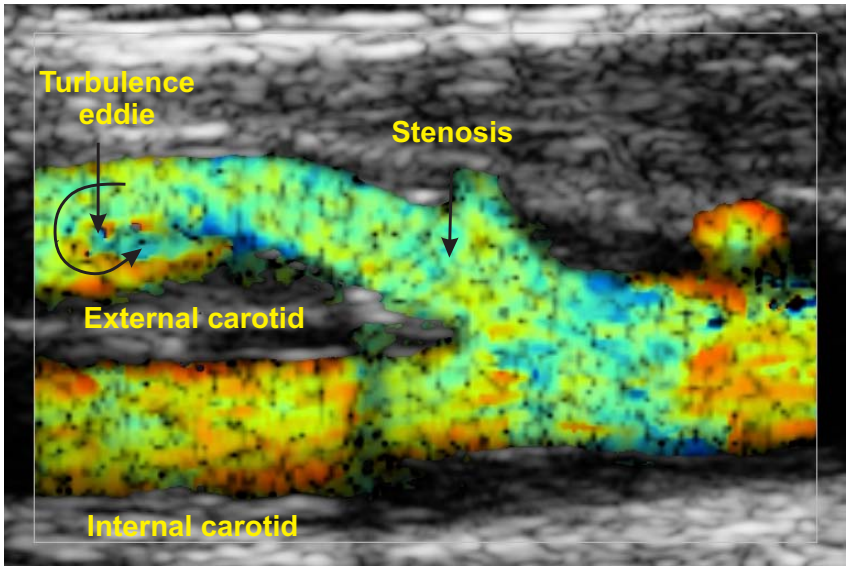


Figure 5.11: BFI used for vascular imaging of the carotid artery branch, with a stenosis in the internal carotid artery. The complex flow pattern in the branching and across and after the stenosis is more detailed in the BFI images compared to CFI.

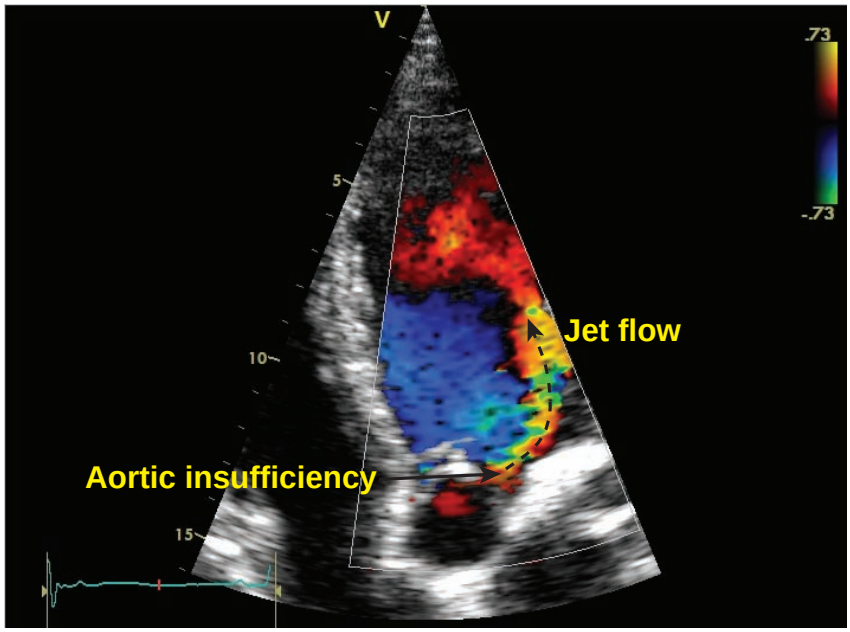


Figure 5.12: BFI used for cardiac imaging of jet due to aortic insufficiency. The speckle fluctuations enhance areas with complex flow dynamics.

and a small interleave group size increase the decorrelation of the speckle pattern from frame to frame. Therefore, it is hard to visually track the speckle pattern when imaging flow inside the heart. However, there will be an even stronger speckle decorrelation in regions with disturbed flow resulting from valve stenosis or insufficiencies than in regions with more regular flow. This increase in speckle fluctuations might ease the detection of small jets. Fig. 5.12 shows an example of imaging a patient with an aortic insufficiency. The image data was acquired using a GE 3S phased array probe (GE Healthcare), designed for cardiac imaging. It is not possible to see detailed blood flow directions at all times during the heart cycle. However, the complex flow dynamics causes fluctuations in the speckle pattern that enhances these areas in the image.

Other possibilities may be present for transesophageal or pediatric imaging. The probe may be placed closer to the heart, allowing for a higher spatial resolution during imaging. Therefore, a more detailed speckle pattern may be visualized, revealing more information about the complex 2-D flow pattern inside the heart. With the improved ability of BFI to visualize disturbed flow, we hope that it can ease the detection of shunts and other abnormalities in pediatric imaging.

### Abdominal imaging

Abdominal imaging with BFI has been tried out briefly on healthy subjects. An example is given in Fig. 5.13 in which an image of a healthy kidney is shown. For

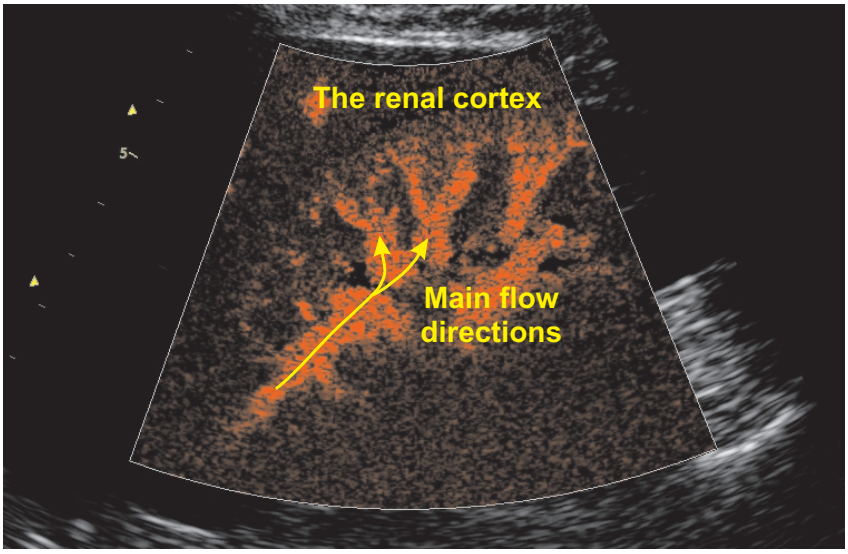


Figure 5.13: BFI used for abdominal imaging of a healthy kidney. The main directions of the kidney arterial blood flow can be observed as it ripples out in the renal cortex.

this example, the speckle images have been combined with PD techniques. The data was acquired using a GE 3.5C curvilinear array probe (GE Healthcare), designed for standard abdominal imaging. Although the flow details are not perceptible, it is possible to observe the main directions of the renal blood flow as it ripples outward in the renal cortex.

#### Other applications

BFI has been tried out in intraoperative imaging during off-pump heart surgery, in which the complex flow in coronary artery bypass grafts is a challenge for the conventional CFI modality. The 2-D directional information offered by BFI can in this case more accurately uncover what actually happens during the heart cycle. This may provide a better quality control of the bypass grafts and a more complete understanding of the physiology of the flow dynamics after surgery.

## 5.6 Discussion

The BFI technique relies upon the human eye perceiving movement in the speckle pattern images displayed. These speckle pattern images are generated by processing the temporally high-pass filtered signal packets, and the movement between images is correlated to the blood flow scatterer movement and distribution for short periods of time. Attempts have been made to quantify this movement by tracking the speckle pattern using image pattern matching techniques as described in [5, 6]. However,

the success of this approach has not yet been sufficient to qualify for clinical use. The approach taken in BFI is qualitative, as no attempt is made to estimate the 2-D velocity vector of the blood flow. The method relies upon the human eye to do the tracking, and many factors are involved for this to work properly.

First, the degree of decorrelation of the speckle pattern between frames needs to be limited. The amount of decorrelation is mainly given by the complexity of the flow dynamics and the degree of out-of-plane movement. Therefore, the direction of movement may be harder to observe when imaging flow with large spatial velocity gradients or a high degree of turbulence. However, the speckle pattern fluctuations which arise in these situations emphasize these areas in the image, and, therefore, may still offer valuable information in detecting abnormal flow.

Second, the ability to capture the speckle pattern movement requires a high imaging frame rate and a short acquisition time between neighboring beams compared to the PRF. This has been solved by using conventional packet acquisition and interleaving techniques as described in Section 5.2. The amount of correlated speckle pattern displayed is related to the number of neighboring beams acquired rapidly in succession. This number is given by the size of the IGS and decreases according to depth and PRF values as given by (5.1) and (5.2) in Section 5.2. As the IGS decrease, the amount of uncorrelated speckle pattern displayed increase. Therefore, a small interleave group size may cause problems for the perception of speckle movement. As seen by the equations, the IGS is larger for smaller depths and for lower PRF values, and, therefore, the method works best when imaging peripheral flow. In cardiac imaging, the large imaging depths and the high PRF needed to avoid aliasing results in a small IGS, making it hard to perceive the speckle movement from blood flow inside the heart. As mentioned in Section 5.2, the success of BFI is dependent on the slow-motion display of the speckle movement. The human eye would not be capable of recognizing any movement if the speckle images were displayed as fast as acquired. This is an important difference between the B-flow and BFI technique. In B-flow the slow motion factor would equal 100%, meaning that the images are displayed as fast as acquired. Even if the speckle movement initially was captured with the B-flow acquisition, it still is displayed too fast for any perception of motion in the images.

In addition to the limiting properties of the human eye, the exact display rate needed to ensure a proper perception of movement is dependent on several other factors. The flow velocity and the amount of decorrelation of the speckle pattern from image to image are two limiting factors. Therefore, rapid, complex, or pulsatile flow seems to require a lower display rate than slow, stationary, or laminar flow. As seen by (5.4) and (5.5) in Section 5.2, several parameters affect the display rate of the speckle pattern images in BFI. Empirically, the display rate obtained using default parameters for most vascular applications allows for the perception of movement during real-time scanning. In addition, the PRF also can be used to slow down or speed up the real-time display rate to some extent. In replay mode, it is possible to slow down the display of speckle images by lowering the overall system frame rate to a level at which the speckle movement becomes apparent in the cineloop.

In general, BFI has similar characteristics and demands for spatial resolution and lateral sampling as B-mode imaging. To ensure a proper perception of speckle

movement, the PSF of the imaging system must be small enough to give defined speckle structures within the dimensions of the flow area of interest. This granularity of the speckle pattern is given by the bandwidth of the imaging pulse; therefore, short pulses are preferred. Unfortunately, using short pulses also may reduce the sensitivity to below that needed in clinical settings. However, pulse lengths commonly used in conventional CFI has successfully been used in vascular imaging of vessels as deep as the carotid artery, with proper perception of speckle movement. When imaging vessels lying deeper in the tissue, it may not always be possible to get the desired sensitivity and sufficiently short pulse for BFI to work properly. One way to solve this problem would be to use coded excitation [23]. Chirp pulses can, for example, be long while at the same time having a large bandwidth. By deconvolution filtering at reception, sufficient resolution and sensitivity may be achieved simultaneously. This is a subject for further work.

The two different display modes implemented have different advantages. Combining speckle images with CFI gives Doppler velocity estimates and 2-D directional information. A drawback may be that a fluctuating color display sometimes can confuse and degrade the perception of movement. This problem does not exist with the PD combination. Furthermore, using the PD display mode with the new additive arbitration technique, more sensitivity to low blood flow and a less obstructive view of the color overlay may be achieved. The BFI processing and display techniques can be applied in all combinations of imaging modalities in which conventional color flow is used. Examples are M-mode and spectrum Doppler. The combination with spectrum Doppler is of special interest because accurate angle correction is easier to perform when the lateral blood flow is visualized.

The major limitations of the traditional Doppler methods are related to angle dependence and aliasing. The BFI method also is dependent on Doppler information for separating the blood flow signal. However, the method still works for perpendicular flow as parts of the flow signal is retained after filtering due to the lateral bandwidth of the imaging system. Although altered by the bandwidth reduction caused by the clutter filtering, the speckle pattern still can be followed from frame to frame. Aliasing does not seem to have any effect on the perception of the speckle pattern movement.

The BFI seems to have potential in different clinical settings as shown in Section 5.5. In vascular applications BFI can show the flow channel along a stenosis or a thrombus with more detail, and combined with PW-Doppler more correct angle correction can be made. The method is currently being evaluated to find out more about the potential in vascular applications. In cardiac imaging, the speckle pattern fluctuations may enhance jets and abnormal blood flow patterns; however, more work needs to be done to verify this hypothesis. The same goes for abdominal imaging, for which so far few attempts have been made to map the clinical value of BFI.

## 5.7 Conclusion

A new method for 2-D blood flow visualization with ultrasound has been introduced. The method preserves, enhances, and visualizes the speckle pattern movement

originating from the red blood cell movement and distribution, and it is sensitive to flow in all directions. The method is qualitative, as no attempt is made to estimate the 2-D velocity component. The BFI provides a more intuitive and detailed display of the flow direction in peripheral vessels. However, the method also may ease the detection of disturbed flow in cardiac and abdominal applications. A real-time implementation offering two different display modes has been made in which conventional CFI and PD has been extended to also display speckle images. Clinical trials are currently being performed to map the potential of real-time BFI in vascular applications. Further work is currently in process to find the degree and implications of speckle pattern decorrelation in BFI as a function of imaging system parameters and factors related to hemodynamics and the geometry of vessel to probe placement.

# References


[1] A. Weyman, *Principles and Practice of Echocardiography.* Philadelphia, USA: Lippincott Williams & Wilkins, 1993.

[2] M. Hennerici and D. Neuerburg-Heusler, *Vascular Diagnosis With Ultrasound: Clinical References With Case Studies.* New York, USA: Thieme Medical Publishers, 1997.

[3] M. Fox, "Multiple crossed-beam ultrasound doppler velocimetry," *IEEE Trans. Sonics Ultrason.*, vol. 25, pp. 281–286, 1978.

[4] W. Wei-qi and Y. Lin-xin, "A double beam doppler ultrasound method for quantitative blood flow velocity measurement," *Ultrasound Med. Biol.*, vol. 8, pp. 421–425, 1982.

[5] G. Trahey, J. Allison, and O. von Ramm, "Angle independent ultrasonic detection of blood flow," *IEEE Trans. Biomed. Eng.*, vol. 34, pp. 965–967, 1987.

[6] L. Bohs, B. Geiman, M. Anderson, S. Gebhart, and G. Trahey, "Speckle tracking for multi-dimensional flow estimation," *Ultrasonics*, vol. 38, pp. 369–375, 2000.

[7] M. Anderson, "Multi-dimensional velocity estimation with ultrasound using spatial quadrature," *IEEE Trans. Ultrason., Ferroelect., Freq. Contr.*, vol. 45, pp. 852–861, 1998.

[8] J. Jensen and P. Munk, "A new method for estimation of velocity vectors," *IEEE Trans. Ultrason., Ferroelect., Freq. Contr.*, vol. 45, pp. 837–851, 1998.

[9] R. Chiao, L. Mo, A. Hall, S. Miller, and K. Thomenius, "B-mode blood flow (b-flow) imaging," *Proceedings of the IEEE Ultrasonics Symposium, 2000*, vol. 2, pp. 1469–1472, 2000.

[10] S. Bjærum, *Detection and visualization of moving targets in medical ultrasound imaging, paper H: Blood Motion Imaging: A new blood flow imaging technique.* Ph.D. Thesis, Norwegian University of Science and Technology, 2001.

[11] S. Bjærum, D. Martens, K. Kristoffersen, and H. Torp, "Blood motion imaging - a new technique to visualize 2d blood flow," *Proceedings of the IEEE Ultrasonics Symposium*, 2002.

[12] L. Løvstakken, S. Bjærum, D. Martens, and H. Torp, "Real-time blood motion imaging, a 2d blood flow visualization technique," *Proceedings of the IEEE Ultrasonics Symposium*, 2004.

[13] R. Chesarek, "Ultrasound imaging system for relatively low-velocity blood flow at relatively high frame rates," *US Patent 4888694, Quantum Medical Systems, Inc.*, 1989.

[14] R. Fletcher and D. Burlage, "Initialization technique for improved mti performance in phased-array radars," *Proceed. IEEE*, vol. 60, pp. 1551–1552, 1972.

[15] E. Chornoboy, "Initialization for improved iir filter performance," *IEEE Trans. Signal Process.*, vol. 40, pp. 543–550, 1992.

[16] H. Torp, "Clutter rejection filters in color flow imaging: A theoretical approach," *IEEE Trans Ultrason Ferroelectr Freq Control*, vol. 44, pp. 417–424, 1997.

[17] A. Kadi and T. Loupas, "On the performance of regression and step-initialized iir clutter filters for color doppler systems in diagnostic medical ultrasound," *IEEE Trans Ultrason Ferroelectr Freq Control*, vol. 42, pp. 927–937, 1995.

[18] A. Hoeks, J. Vandevorst, A. Dabekaussen, P. Brands, and R. Reneman, "An efficient algorithm to remove low-frequency doppler signals in digital doppler systems," *Ultrason. Imaging*, vol. 13, pp. 135–144, 1991.

[19] S. Bjærum, H. Torp, and K. Kirstoffersen, "Clutter filter design for ultrasound color flow imaging," *IEEE Trans. Ultrason., Ferroelect., Freq. Contr.*, vol. 49, pp. 204–216, 2002.

[20] C. Therrien, *Discrete Random Signals and Statistical Signal Processing.* Upper Saddle River, USA: Prentice Hall Inc., 1992.

[21] A. Papoulis, *Probability, Random Variables and Stochastic Processes.* New York, USA: McGraw-Hill Inc., 2001.

[22] C. Kasai, K. Namekawa, A. Koyano, and R. Omoto, "Real-time two-dimensional blood flow imaging using an autocorrelation technique," *IEEE Trans. Sonics Ultrason.*, vol. 32, pp. 458–464, 1985.

[23] B. Haider, P. Lewin, and K. Thomenius, "Pulse elongation and deconvolution filtering for medical ultrasonic imaging," *IEEE Trans. Ultrason., Ferroelect., Freq. Contr.*, vol. 45, pp. 98–113, 1998.

# Chapter 6

# Clinical applications of BFI

Lasse Løvstakken et al
Dept. Circulation and Medical Imaging, NTNU

The limitations of conventional color flow imaging (CFI) related to angle-dependency and velocity aliasing may often obscure information about the true blood flow. A new real-time flow mapping technique called Blood Flow Imaging (BFI) has been introduced, able to visualize the two-dimensional vector flow direction, not limited by aliasing. In three clinical and one experimental pilot study, we evaluated potential benefits of the new method. In cardiovascular surgery, the BFI potential was evaluated as a tool for intraoperative quality control of flow in coronary anastomoses in an experimental setting. In a porcine model, technically patent as well as pathological anastomoses were created. BFI was shown to more properly portrait the complex flow conditions, and to require less interpretation than CFI.
In neurovascular surgery, the potential of BFI combined with navigation technology was evaluated for intra-operative flow visualization in cerebral aneurisms and arteriovenous malformations (AVM). The directional information provided by BFI was shown to increase certainty in separating arteries from veins in AVMs, and to reduce the amount of interpretation needed for identifying vessels of interest in the complex vascular architecture.
The flow through atrial septal defects (ASD) in children may be difficult to detect due to overlapping B-mode and color images, caused by trade-offs between spatial resolution and frame rate. The increased frame rate and directional information provided by the speckle pattern movement in BFI showned potential for increasing the certainty of these evaluations, by more properly visualizing the movement of blood across the septum, and for separating true flow across the septum from color artifacts.
In treatment of tendinosis, imaging of vessels on a scale of millimetres is needed to guide needle incisions. Conventional tissue-flow arbitration may then potentially obscure flow due to strong clutter components and low blood velocities. A new transparent arbitration technique combined with the BFI speckle movement was shown to more properly visualize the small vessels.

## 6.1 Application no. 1:

# Blood Flow Imaging - A new 2-D ultrasound modality for enhanced intraoperative visualization of blood flow patterns in coronary anastomoses

Lasse Løvstakken[1], Khalid S. Ibrahim[1,2], Nicola Vitale[1,2], Siren Torsvik Henriksen[1], Idar Kirkeby-Garstad[1,3], Hans Torp[1], and Rune Haaverstad[1,2]
[1] Dept. of Circulation and Medical Imaging, NTNU, Trondheim, Norway
[2] Dept. of Cardiothoracic Surgery, Trondheim University Hospital, Norway
[3] Dept. of Anaesthesia, Trondheim University Hospital, Norway

### 6.1.1 Introduction

Coronary artery disease (CAD) occurs when atherosclerotic plaques line the wall of the arteries that provide blood supply to the heart. This atherosclerotic process may cause a significant narrowing in one or more coronary arteries, leading to an inadequate blood supply to areas of the myocardium. Untreated CAD generally results in progressive angina, myocardial infarction, left ventricular dysfunction, and ultimately death.

Of all patients diagnosed with CAD about 10% are candidates for revascularization using coronary artery bypass grafting (CABG) surgery [1], which in 2003 amounted to about one half of a million cases in the United States alone [2]. The long term survival of these patients after CABG surgery, is directly related to the patency of distal anastomoses [3]. Modern coronary bypass series report perioperative graft occlusion rates as high as 11 percent [3, 4], especially in off-pump CABG where grafting is technically more demanding [4]. The construction of a technically perfect anastomosis at the time of surgery is therefore an important determinant of graft patency. Technical errors in bypass graft construction by the operating surgeon are primarily responsible for early failures. However, there is currently no standard approach for identifying these errors using any form of intraoperative graft assessment (i.e. angiography, ultrasound Doppler scanning, transit-time flowmetry), and it is not routine clinical practice in most centers.

Epicardial imaging with ultrasound is a reliable and simple method of intraoperative assessment of coronary grafts and anastomoses [5]. High-frequency B-mode imaging provides images of sufficient quality for measuring dimensions and for identifying abnormalities related to the anatomy. Another indicator of graft patency is the blood flow fields in the anastomosis. Ultrasound color flow imaging (CFI) has previously been used for mapping these flow fields [6, 7]. However, due to the complex vessel geometry and small vessel dimensions the flow fields in the anastomosis are complex, and Doppler images produced by CFI may then require a great deal of interpretation [8]. The new real-time blood flow imaging (BFI) modality can provide angle-independent directional flow information which is not limited by aliasing [9], and may overcome these limitations. With this in mind, the aim of the present study

was to evaluate the application of BFI versus CFI for the assessment of blood flow in the left internal mammary artery (LIMA) to left anterior descending (LAD) coronary anastomosis in a pig model.

### 6.1.2 Materials and methods

#### Pig model

A total of nine pigs (weight 60-85 kg) underwent off-pump grafting of LIMA-LAD under general anaesthesia. All operations were carried out by the same senior surgeon (RH). The coronary surgery was aimed at creating patent anastomoses without technical failures. Animals received humane care in accordance with the European convention on Animal care and the Norwegian national regulations; the Norwegian Ethics Committee on animal research approved the protocol.

In all nine pigs epicardial ultrasound assessment of the anastomosis was carried out with the LAD snared proximally from the anastomotic site, with the intention to simulate the standard condition of a graft anastomosis placed below a significant stenosis. Furthermore, in three pigs, after the assessment in the standard condition was completed, one untoward situation that might occur in clinical practice was created in each pig: 1) the LAD was unsnared in one pig, mimicking an anastomosis constructed below a non-significant stenosis; 2) by placing an extra deep stitch at the toe of the anastomosis, a failed severely stenotic anastomosis occurred in the second pig; 3) the LAD was snared distally to the anastomotic site in the third pig, as to reproduce an anastomosis placed proximally to a significant stenosis. These three different experimental settings are referred to as special case 1, 2 and 3, respectively.

#### Data acquisition and processing

The imaging setup is shown in Fig. 6.1. The epicardial ultrasound images of the LIMA-LAD anastomoses were acquired using a GE Vingmed Vivid 7 ultrasound scanner (GE Vingmed, Horten, Norway) equipped with a GE i13L linear array probe (GE Healthcare, Waukesha, USA), operating at frequencies of 7-14 MHz. For each B-mode recording, CFI and BFI data were also stored. Recordings of transit-time LIMA flow was obtained using a MediStim Butterfly unit (MediStim ASA, Oslo, Norway).

Cineloops from the two different flow modalities were generated off-line from the same data recordings. The color images were therefore the same for both modalities which allowed proper comparisons. An example of the B-mode image quality obtained is given in Fig. 6.2, where also dimensions used to validate the quality of the anastomosis is indicated [7]. The images were rated good when the LIMA-LAD anastomosis and the LAD proximal and distal run-off could be well visualized by the B-mode and CFI in the longitudinal plane. The anastomoses were assessed by the following measurements: length of the anastomosis proper ($D_A$), diameter of the LAD at the toe of the anastomosis ($D_1$) and 5 mm distally to the anastomosis ($D_2$). $D_2$ was defined as the reference diameter and the ratio $D_1/D_2$, was calculated; a $D_1/D_2$ value around 1 indicates no anastomotic stricture at the toe [7].

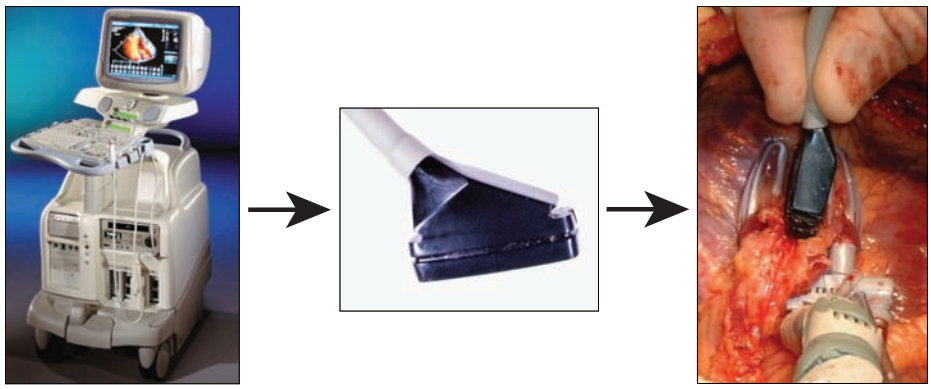


Figure 6.1: The ultrasound imaging setup. A stabilized area around the LIMA-LAD anastomosis is imaged using a GE Vingmed Vivid7 ultrasound scanner (GE Vingmed Ultrasound, Horten, Norway) and a high-frequency i13L linear array (GE Healthcare, Waukesha, USA).

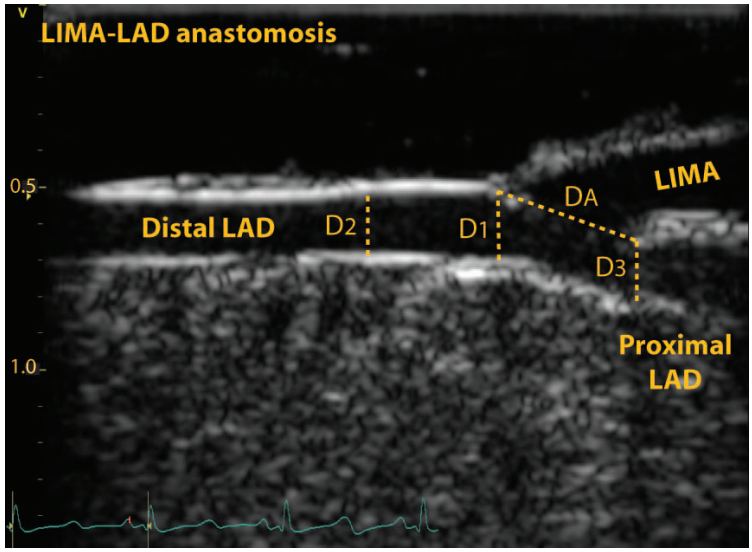


Figure 6.2: B-mode image of the left internal mammary artery (LIMA) to left anterior descending (LAD) coronary anastomosis as obtained in the study. Diameter measurements indicated were used to determine the quality of the anastomosis. $D_A$, the length of the anastomosis proper; $D_1$, the diameter of the anastomosis toe; $D_2$, the diameter 5 mm distally to the anastomosis; and $D_3$, the diameter of the anastomosis heel.

#### Data analysis

Cineloops from the two modalities were assessed by three independent observers all familiar with CFI. The cineloops were presented to the observers in random order, and different aspects related to flow direction and velocity magnitude were evaluated. The following questions were asked:

**Question 1:** Based on the flow information presented, to what degree of certainty can you assess the direction of flow:

**a)** from the LIMA to the distal part of the LAD?

**b)** from the LIMA to the proximal part of the LAD?

**Question 2:** Based on the flow information presented, to what degree of certainty can you assess competitive flow in the anastomosis?

**Question 3:** Based on the flow information presented, to what degree of certainty are you able to assess flow pulsatility?

**Question 4:** Based on the flow information presented, to what degree are you influenced by velocity aliasing in assessing:

**a)** flow direction?

**b)** flow velocity?

The observer evaluations was scored from 0-100. For question 4a and 4b, the scale was reversed so that the method least influenced by aliasing scored higher. To quantify the visual evaluation of the observers a visual analogue scale (VAS) was employed.

#### Statistical analysis

The general null hypothesis for the different evaluations was that there is no difference in the assessment of a specific flow aspect when using the information provided by either CFI or BFI respectively. Statistical analysis was performed using the exact two-sided Wilcoxon signed rank test of paired measurements. The outcome of the evaluations was displayed in dot-plots. The statistical analysis and plotting was performed using the numerical MATLAB software with the statistical toolbox (The MathWorks, Natick, MA).

### 6.1.3 Results

All nine anastomoses were rated good and patent by B-mode ultrasound measurements as described in Section 6.1.2. Mean transit-time flow of LIMA grafts was $34.7 \pm 4.2$ ml/min, at a mean arterial blood pressure of $76 \pm 6.3$ mmHg. In special case 3, the mean measurements of the purposely failed anastomosis were as follows: $D_A = 2.2mm$; $D_1 = 1.8mm$; $D_2 = 2.7mm$. The $D_1/D_2$ ratio was equal to 0.67, indicating a severe stenosis at the anastomotic toe.

#### Modality comparisons

In Fig. 6.3, the standard case of a technically perfect anastomosis is imaged with CFI and BFI, respectively. In this case, a significant occlusion is induced proximally in the LAD by snaring. Artifacts in the color image of this example, relating to the Doppler limitations of angle-dependency and velocity aliasing, are indicated by arrows in the CFI (upper) image. The dashed arrows in the BFI (lower) image indicate the observed movement of the speckle pattern.

#### Special case 1: Unsnared anastomosis

Imaging of an anastomosis without proximal snaring of the LAD using BFI is shown in Fig. 6.4. This case was produced to mimic the clinical situation where the graft is constructed below a non-significant stenosis, causing flow competition between the LIMA and LAD. Complex flow patterns resulting from this competition is observed within the anastomosis.

#### Special case 2: Stenosed anastomosis

Imaging of a stenosed anastomosis using BFI is shown in Fig. 6.5. This case was produced to mimic the clinical situation of technical error where the stitch is placed too deep, causing a stenosis in the toe of the anastomosis. An increased amount of flow from the LIMA proximally into the LAD, and jet-like post-stenotic flow patterns can be observed.

#### Special case 3: Distally snared anastomosis

Imaging of a distally snared anastomosis using BFI is shown in Fig. 6.5. This case was produced to mimic the clinical situation where the graft is placed proximally to a significant stenosis. A substantial increase in the amount of flow from the LIMA proximally into the LAD can be observed.

#### Observer evaluations

The results from the three observers evaluations are presented in Fig. 6.7. The corresponding p-values. A difference in favor of BFI can be observed for most aspects with regards to median and range of VAS scores. A non-significant result was found only for observer 2 in the assessment of flow from the LIMA directed to the distal part of the LAD.

### 6.1.4 Discussion

With the exception of coronary artery bypass surgery, virtually all other interventions on the heart, including cardiac valve repair and coronary stenting, are usually accompanied by diagnostic imaging on completion to ensure a satisfactory result. There is currently no standard imaging method for intraoperative identification of technical errors in coronary surgery.

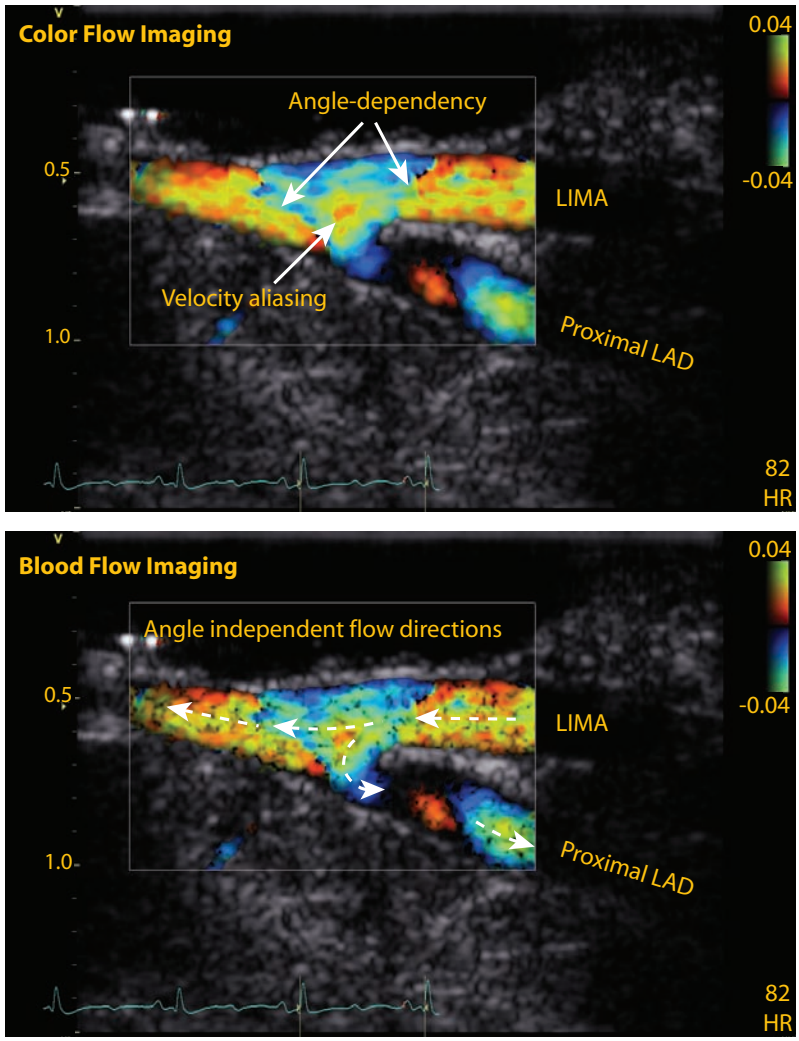


Figure 6.3: The standard imaging case of a technically perfect and fully patent LIMA-LAD anastomosis imaged with CFI and BFI respectively. Artifacts present in the Doppler image relating to angle-dependency and velocity aliasing are indicated by the arrows in the CFI (upper) image. The dashed arrows in the BFI (lower) image indicate the observed direction of the speckle movement.

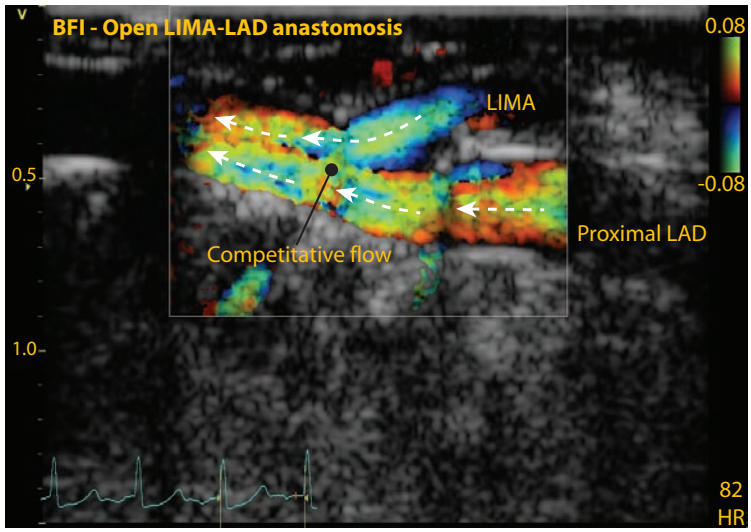


Figure 6.4: An unsnared LIMA-LAD anastomosis imaged with BFI. As no significant stenosis exists neither proximally or distally in the LAD, competitive downstream flow can be observed.

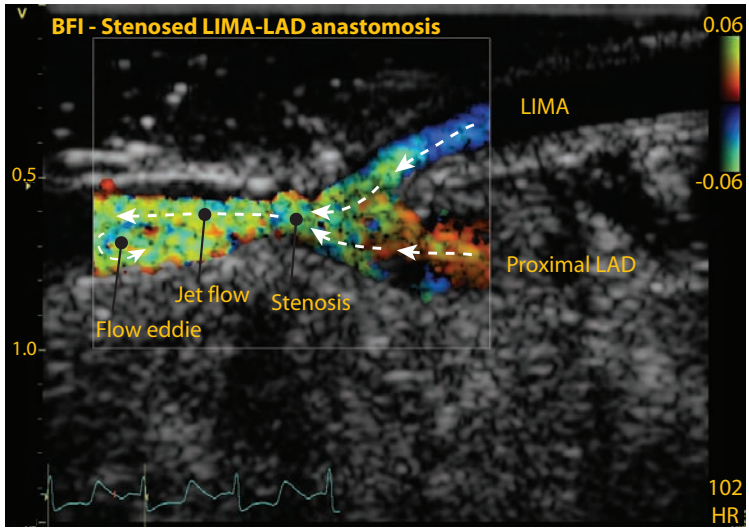


Figure 6.5: A stenosed LIMA-LAD anastomosis imaged with BFI. As shown here in the diastolic phase of the cardiac cycle, jet flow through the stenosis in the toe of the anastomosis as well as flow turbulence and eddies distally to the anastomosis can be observed (post-stenotic flow patterns). In the systole, an increased amount of flow was seen proximally into the LAD caused by the increased resistance in the stenosis (pre-stenotic flow patterns).

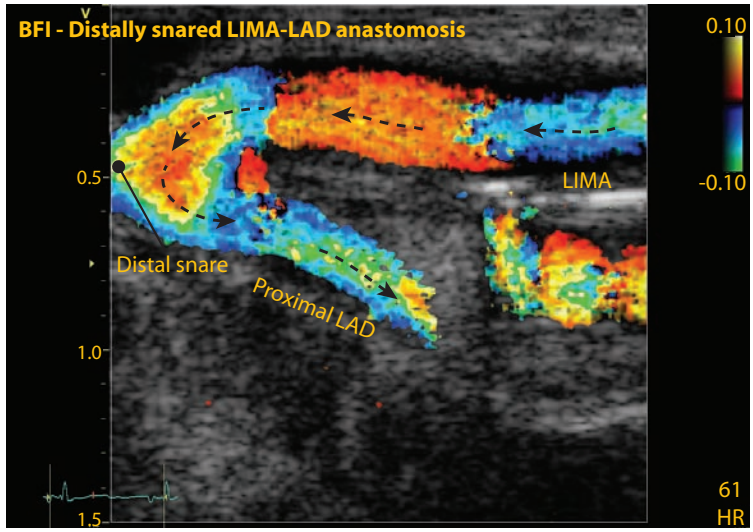


Figure 6.6: A distally snared LIMA-LAD anastomosis imaged with BFI. Due to the distal occlusion, an increased amount of flow from the LIMA directed proximally into the LAD can be observed (indicated by dashed arrows).

Intraoperative ultrasound has shown potential for clinical use in coronary bypass surgery [5, 7]. In addition to the evaluation of the anastomosis geometry, the evaluation of flow patterns inside the anastomosis is important. Ideally, when the anastomosis is correctly placed distal to a significant stenosis, the blood should run from the graft through the anastomosis and then into the distal and proximal coronary artery, providing adequate blood supply to the ischemic myocardium. The small dimensions of the vessels involved (1 to 2 mm) coupled with the dynamic changes in the cardiac cycle increases the complexity of the flow fields, and requires both a high spatial resolution and a high frame rate for adequate imaging.

In this study we compared the conventional CFI modality with Doppler measurements of axial flow velocity and direction, to the BFI modality that in addition provides a qualitative visualization of the movement of blood that is not affected by the Doppler limitations of angle-dependency and velocity aliasing. For intraoperative assessment, one can argue that the use of information presented in the color images is mainly qualitative, i.e. to get an impression of the overall flow conditions in the anastomosis. In this respect, the BFI modality can provide a more intuitive and detailed image, with less demands of image interpretation. Based on the independent observer evaluations of different aspects related to the imaging of flow direction and velocity dynamics, our findings indicate this to be the case. The new modality more adequately portrayed the complex flow in the anastomosis, and may therefore increase the certainty and efficiency of flow evaluation in the operating room.

The evaluation of flow direction in the anastomosis is important to validate a satisfactory transportation of blood from the graft to the ischemic areas of the

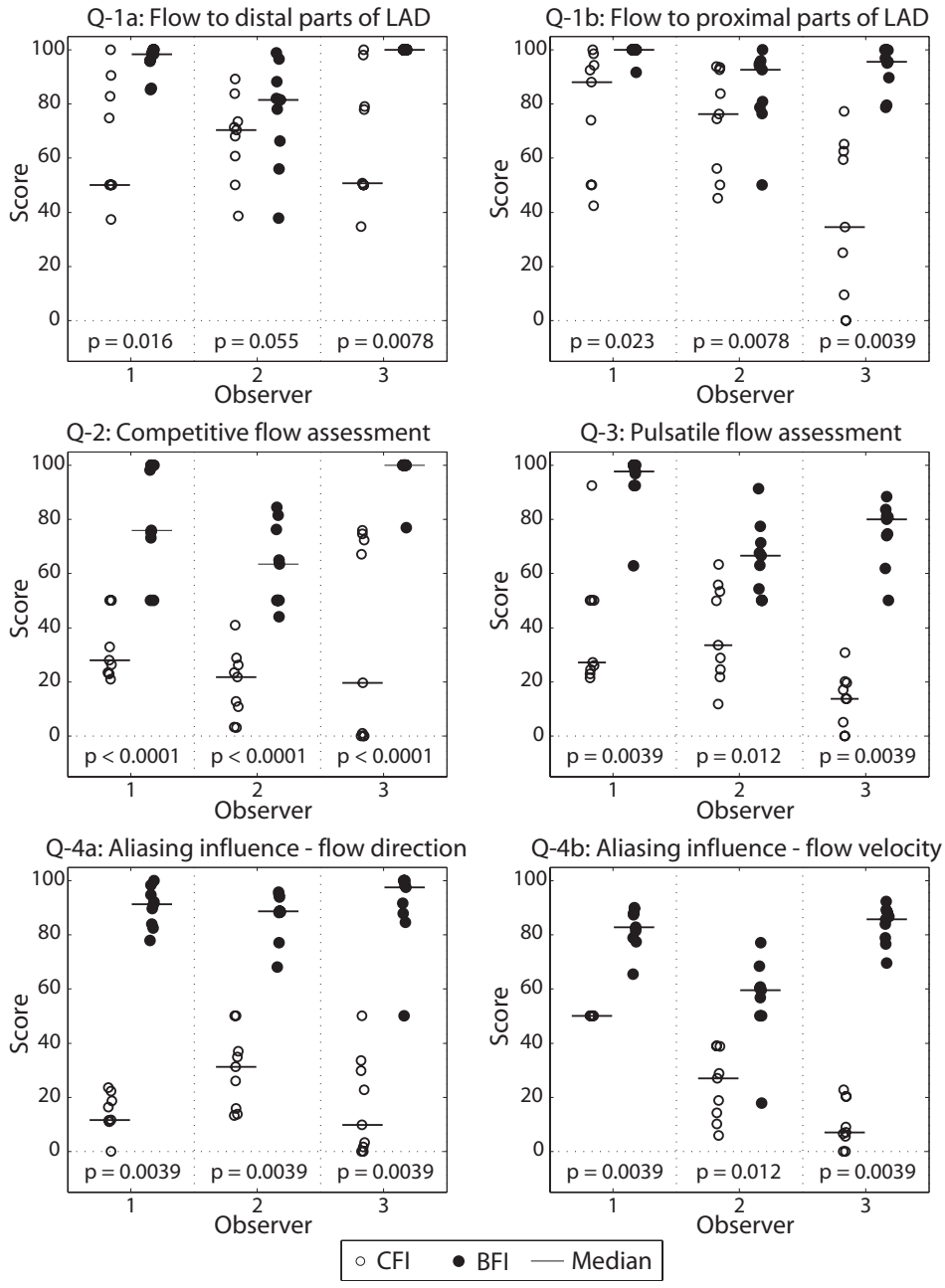


Figure 6.7: Dot plots showing the observer's visual analogue score assessments of BFI versus CFI for the assessment of flow in the standard case (perfect) LIMA-LAD anastomosis (N=9). The corresponding p-values for each individual observer has been indicated for each evaluation.

myocardium. The near transverse angle and tortuous nature of the coronary artery compared to the ultrasound beam may lead to unreliable Doppler measurements, and an image that is prone to interpretation due to angle-dependencies. We asked the observers to evaluate the modalities with respect to imaging of flow directed from the LIMA distally and proximally into the LAD, and with respect to competitive flow in the anastomosis. As evident from Fig. 6.7, the BFI modality was generally rated higher than CFI with regards to these aspects. All results were statistically significant, with the exception of one observation in the evaluation of the distal flow direction.

The impression of the dynamics of flow velocity magnitude is important to detect the occurrence of stenoses, turbulence, and flow pulsatility due to abnormal changes in flow resistance. Pulsatility measurements has previously been used as an indicator for the evaluation of flow conditions [10]. Although the speckle visualization technique provided by BFI is not based on quantified blood velocities, relative velocities in different parts of an image and throughout the cardiac cycle are properly visualized. In fact, all observers rated BFI as superior in the assessment of flow pulsatility, which indicates that the speckle movement in BFI provide a display with a higher dynamic range of velocities. This has potential benefits when assessing highly dynamic flow as present in the coronary arteries.

Due to the high dynamics of the flow through the anastomosis, aliasing artifacts obscured the Doppler information in all clips in some parts of the cardiac cycle. Different pulse repetition frequencies (PRF) were used in the image recordings shown to the observers, and the Doppler velocity range and amount of aliasing present in the images therefore varied. As the color images were identical for both CFI and BFI in the clips generated offline, an equal amount of aliasing was present for both modalities. When asked how influenced they were with aliasing when assessing flow direction and velocity, the observer evaluations was consistently less influenced when the BFI speckle movement was included. This advantage of BFI may reduce the need to adapt the velocity scale during the intraoperative evaluation of the flow in the coronary arteries and anastomoses.

In ultrasound imaging the demands of frame rate often compromise the image quality. This becomes particulary relevant when imaging the coronary arteries due to their small dimensions and the high dynamics of flow. In our BFI application, eight speckle images were generated for each color image. This eightfold increase in frame rate provided more information of the flow in the LIMA-LAD anastomosis, and an increase in spatial resolution was also confirmed applicable while retaining a sufficiently smooth display of flow information.

The results from the observer evaluation of flow conditions in the standard case are expected to also be applicable clinically. To investigate the clinical application, the properties of BFI was further examined in three special cases where realistic abnormalities had been induced. In the unsnared anastomosis, flow from the proximal parts of the LAD can be observed mixing with the LIMA flow. Such competitive flow patterns might be an indication of technical error in the placement of the graft. In the stenosed case, an increased flow into the proximal LAD in the systole, and an accelerated stenotic flow in the diastole was clearly visualized. Further, in the post-stenotic flow, jet-like flow qualities and flow turbulence can be observed. For the

distally snared anastomosis, the directional flow information provided by BFI clearly visualized an increased amount of blood moving from the LIMA proximally into the LAD.

**Limitations of study**

As no gold standard is available to provide a reference regarding flow conditions, the evaluations were based upon expert opinions, and the results must be viewed in light of this. Although all observers were experts in interpreting color flow images, they had different professional backgrounds which may have influenced the results.

### 6.1.5 Conclusion

The BFI modality offers new information about flow conditions in the LIMA-LAD anastomosis not readily available with conventional CFI. Being more intuitive, a more instant appreciation of the flow condition can be obtained in the operating room. As the conventional Doppler information is also present, we conclude that the BFI modality may replace CFI in the evaluation of anastomosis flow in the future. The BFI modality may also have potential for improved imaging of flow in other areas of cardiothoracic surgery, as for instance in the evaluation of flow through prosthetic heart valves and for interpretation of blood flow in patients with aortic dissection. Further investigations should be performed to establish this potential.

**Acknowledgements**

We thank the observers for their efforts. We also thank Eirik Skogvoll and Stian Lydersen for advice on the statistical analysis.

# References


[1] A. Michaels and K. Chatterjee, "Cardiology patient pages. angioplasty versus bypass surgery for coronary artery disease," *Circulation*, vol. 106, pp. e187–e190, 2002.

[2] T. Thom, N. Haase, W. Rosamond, V. Howard, J. Rumsfeld, T. Manolio, Z. Zheng, K. Flegal, C. O'Donnell, S. Kittner, D. Lloyd-Jones, D. Goff, Y. Hong, R. Adams, G. Friday, K. Furie, P. Gorelick, B. Kissela, J. Marler, J. Meigs, V. Roger, S. Sidney, P. Sorlie, J. Steinberger, S. Wasserthiel-Smoller, M. Wilson, and P. Wolf, "Heart disease and stroke statistics–2006 update: a report from the american heart association statistics committee and stroke statistics subcommittee," *Circulation*, vol. 113, pp. e85–151, 2006.

[3] F. Grover, R. Johnson, G. Marshall, and K. Hammermeister, "Impact of mammary grafts on coronary bypass operative mortality and morbidity. department of veterans affairs cardiac surgeons," *Ann. Thorac. Surg.*, vol. 57, pp. 559–68 discussion 568–9, 1994.

[4] G. D'Ancona, H. Karamanouikan, T. Salerno, S. Schmid, and J. Bergsland, "Flow measurement in coronary surgery," *Heart Surg. Forum*, vol. 2, pp. 121–124, 1999.

[5] R. Haaverstad, N. Vitale, R. Williams, and A. Fraser, "Epicardial colour-doppler scanning of coronary artery stenoses and graft anastomoses," *Scand. Cardiovasc. J.*, vol. 36, pp. 95–99, 2002.

[6] A. Kenny, N. Cary, D. Murphy, and L. Shapiro, "Intraoperative epicardial echocardiography with a miniature high-frequency transducer: imaging techniques and scanning planes," *J. Am. Soc. Echocardiogr.*, vol. 7, pp. 141–149, 1994.

[7] R. Haaverstad, N. Vitale, O. Tjomsland, A. Tromsdal, H. Torp, and S. Samstad, "Intraoperative color doppler ultrasound assessment of lima-to-lad anastomoses in off-pump coronary artery bypass grafting," *Ann. Thorac. Surg.*, vol. 74, pp. S1390–S1394, 2002.

[8] N. Vera, D. Steinman, C. Ethier, K. Johnston, and R. Cobbold, "Visualization of complex flow fields, with application to the interpretation of colour flow doppler images," *Ultrasound Med. Biol.*, vol. 18, pp. 1–9, 1992.

[9] L. Løvstakken, S. Bjærum, D. Martens, and H. Torp, "Blood flow imaging - a new real-time, 2-d flow imaging technique," *IEEE Trans. Ultrason., Ferroelec., Freq. Contr.*, vol. 53, pp. 289–299, 2006.

[10] D. Leong, V. Ashok, A. Nishkantha, Y. Shan, and E. Sim, "Transit-time flow measurement is essential in coronary artery bypass grafting," *Ann. Thorac. Surg.*, vol. 79, pp. 854–7 discussion 857–8, 2005.

## 6.2 Application no. 2:

## Blood Flow Imaging - A new angle-independent ultrasound modality for intraoperative assessment of flow dynamics in neurovascular surgery

Frank Lindseth[1] and Lasse Løvstakken[2], Geir A. Tangen[1], Ola M. Rygh[3], Hans Torp[2], and Geirmund Unsgaard[3]
[1] SINTEF Health Research, Trondheim, Norway
[2] Department of Circulation and Medical Imaging, NTNU, Trondheim, Norway
[3] Department of Neurosurgery, Trondheim University Hospital, Trondheim, Norway

### 6.2.1 Introduction

The imaging of blood flow in neurosurgery is important to avoid the damage of important blood vessels, and for quality control in neurovascular interventions. Ideally, the surgeon would like to steer the surgical instruments in the context of a high-resolution three-dimensional (3-D) navigation scene that properly portrait not only the vessel geometry but also flow velocity and direction. However, due to the complex neurovascular architecture, this is a challenging task. Furthermore, while navigation technology has revolutionized many aspects of neurosurgery, brain shifts occuring when opening the patient skull and during resection remains a serious limitation [1]. Intraoperative imaging is therefore important to allow for navigation using updated data, and to offer the possibility of observing the immediate effects of surgery for quality control.

Multi-slice CT, high-field MRI, 3-D rotational angiography and high-quality 3D ultrasound are all relatively new achievements potentially important for the future of intraoperative imaging [2–5]. Of these, many currently consider intraoperative MRI to be the gold standard in neurosurgery. However, intraoperative MRI requires high investments and is logistically challenging. Intraoperative ultrasound imaging is a cost-effective, time-efficient, and user-friendly alternative for most neurosurgical departments, especially when integrated with navigation technology and preoperative MRI data for overview, interpretation and brain shift visualization [6, 7]. Brain shift compensation of the high-resolution preoperative MR images is further possible using 3-D ultrasound [8–11], which further makes the combination of the two modalities an attractive solution.

Knowing the vascular anatomy in detail is of great importance for a neurosurgeon. It is crucial to know the exact location of important vessels relative to the surgical instruments at all times in order to perform a safe radical resection. This is important for instance during tumor surgery, where intraoperative 3-D ultrasound in combination with navigation technology has been shown to be a powerful tool [12]. In other contexts, not only the presence but also the velocity and direction of blood flow can provide important information. This is for instance the case for intracranial aneurysms

and arteriovenous malformations. An intracranial aneurysm is an abnormal dilatation of a blood vessel caused by a weakening of the vessel wall, that may infer serious consequences if ruptured. The main goals in aneurysm treatment is the occlusion of the lesion and to maintain a sufficient blood flow in the parent and branching vessels. This goal is however not always achieved [13], and intraoperative flow imaging for immediate correctional surgery is valuable [14]. An arteriovenous malformation (AVM) is an abnormal cluster of blood vessels with direct arterial to venous connections, that when ruptured can cause an intracranial hemorrhage. The goal when treating an AVM is to completely close off the abnormal vessel supply (also called the feeding vessels/arteries) to relieve flow pressure prior to resection of the nidus. Surgery is the mainstay of treatment for many cases, and it is then important to obtain information about the nidus configuration, its relationship to surrounding vessels, and the location of feeding arteries and draining veins.

Current methods of real-time ultrasound flow imaging in neurosurgery include spectral-Doppler, power-Doppler (PD), and color flow imaging (CFI) methods, and have previously been used to investigate the hemodynamics in intracranial aneurysms and AVMs [15–20]. The CFI and PD modality both provide an image of the presence of blood flow in a distributed region of interest, and are preferred for the visual assessment of blood flow. The CFI modality also provides Doppler measurements of blood velocity. Spectral-Doppler methods can further provide the visualization of the full velocity spectrum within smaller parts of this region. The CFI modality is inherently limited by an angle-dependency in only being able to measure the axial velocity component of blood flow. Due to the complex neurovascular architecture, the resulting images may then be difficult to interpret. Two-dimensional contrast enhanced ultrasound imaging has been proposed to offer a more detailed evaluation of flow conditions in cerebral aneurysms [15]. In this way the blood flow patterns inside the aneurysm sack could be properly visualized, and also quantified offline [21]. However, this imaging method increases the time and cost needed to perform an investigation.

Blood Flow Imaging (BFI) is a new two-dimensional (2-D) ultrasound modality that in addition to Doppler measurements offers an angle-independent visualization of flow that could be beneficial in the neurosurgical setting [22]. When further integrated with 3-D navigation technology, this modality may be a step towards the ideal visualization for surgical needs. The aim of this preliminary study is to investigate the clinical applicability of intraoperative BFI for flow assessment in cerebral aneurysms and AVMs. We explore the clinical usefulness of the modality, state our preliminary results, and discuss various features important for the future use of the proposed technique.

### 6.2.2 Materials and Methods

#### Patient material

Six patients undergoing cerebrovascular surgery, three media aneurysms and three AVMs, were investigated. In two of the AVM cases, navigational information was not available. Informed consent was given by each patient before the treatment.

### Equipment and experimental setup

The experimental setup used in the operating room can be seen in Fig. 6.8. The illustration shows how key personnel and equipment were located relative to each other as well as the main connections that were used between the systems. As can be seen, only the tracking and display hardware of the ultrasound-based neuronavigation system SonoWand [6] (MISON AS, Trondheim, Norway) was used. The built-in ultrasound scanner was replaced by a stand-alone GE Vingmed Vivid 7 system (GE Vingmed Ultrasound, Horten, Norway), equipped with a GE 10S phased array probe (GE Healthcare, Waukesha, USA). The probe had a pre-calibrated tracking frame attached [23]. Furthermore, the built-in navigational computer was replaced by a stand-alone laptop (PowerBook G4, Apple Computer Inc., Cupertino, USA), running an in-house navigation software capable of presenting an integrated 3D navigation scene to the surgeon. A standard RS-232 cable connected the optical tracking system (Polaris, NDI, Canada) to the navigation laptop, and real-time ultrasound data was obtained from the Vivid 7 scanner using a S-video cable connected to a Firewire-based frame-grabber.

Two computer screens were presented to the surgeon in an adjustable and convenient manner. The left screen contained the integrated navigation scene visualizing the preoperative MR-images and the position of the real-time 2-D ultrasound image planes (for overview), and the right screen duplicated the ultrasound scanner BFI display (for details). The technical assistant used the laptop screen and the scanner monitor for optimizing the navigation display and ultrasound acquisition settings respectively.

### Data acquisition and processing

**Preoperative:** Magnetic resonance angio (MRA) scanning of the patients were obtained one day before surgery using a 1.5T MR scanner (Siemens, Erlangen, Germany). Prior to MR scanning, five skin fiducials were attached to the patient's head for later image to patient registration. The MRA data was loaded into the in-house navigation system software, and the fiducials were localized and marked in the dataset. Also, the cerebrovascular tree was obtained by segmenting the MRA data using a region growing technique, from which a surface model of the vessels around the lesion was generated using the marching cubes algorithm. The whole image registration and segmentation step took from 5 to 30 minutes depending on the complexity of the vessels surrounding the lesion.

**Intraoperative:** The patient head position was fixed and the navigation system was calibrated to match using the skin fiducials. After the opening of the dura, navigated 2-D ultrasound scans were first performed to give an updated image of the aneurysm or AVM position, and to detect the degree of brain-shift occuring. Ultrasound flow images were further obtained of the aneurysm or AVM throughout the procedure. For each recording, B-mode and both CFI and BFI raw data was stored. Synchronized video recordings of the 3-D scene that matched the ultrasound acquisitions were also obtained. The ultrasound images

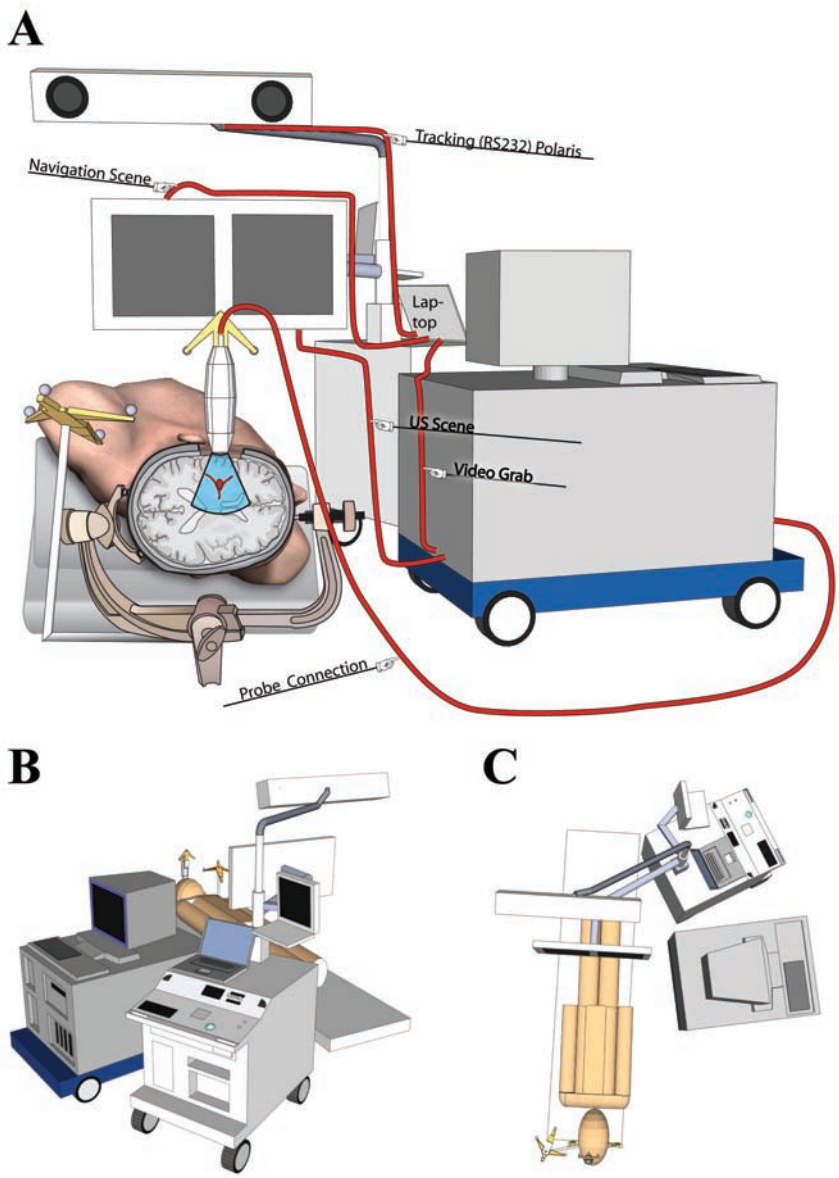


Figure 6.8: Technical and clinical setup in the OR. A) Surgeon's view. The main connections between the systems used are shown in red. B) Researchers view. The two systems (the US scanner and the navigation laptop) controlled by the researcher are shown. C) Top view. The relative locations between key personal and equipment are shown.

were acquired using the Vivid 7 ultrasound system (GE Vingmed Ultrasound, Horten, Norway) using the 10S phased array probe operating at frequencies from 5 to 10 MHz (GE Healthcare, Waukesha, USA).

**Postoperative:** Post surgery, cineloops for both the CFI and BFI modality were generated from the same data recording. This allowed for proper comparisons between the different modalities. The recorded video of the 3-D scene were matched to corresponding ultrasound acquisitions for offline evaluation.

### 6.2.3 Results

#### Imaging modality comparison

A comparison of the different image modalities in question is shown imaging an AVM in Fig. 6.9. In the upper left image, a three-dimensional MR-angio image is shown, providing a larger view of the AVM distribution, including the nidus and communicating vessels. Identified feeding arteries and draining veins are indicated by solid arrows. The flow directions in the different vessel branches as observed by the speckle movement in the BFI images have further been indicated by the dashed arrows. In the upper right image, a CFI view of a smaller part of the AVM is shown, which includes Doppler measurements of the mean axial flow velocity inside the AVM vessels. Some apparent artifacts present in the color image due to Doppler method limitations have been indicated by arrows. As can be observed, the Doppler image alone does not portrait the complete picture of the flow conditions. In the lower corresponding images, two different BFI modalities are shown. The lower left BFI modality extends conventional CFI with speckle pattern movement, while the lower right extends the power-Doppler modality with speckle pattern movement. The latter modality was preferred by the surgeon, and will be used as the main BFI modality in further examples. In the BFI images, the flow directions observed from the speckle pattern movement have been indicated by the dashed arrows.

#### Imaging of cerebral aneurysms

An example of a middle cerebral artery aneurysm imaged with BFI is shown in Fig. 6.10. In the upper image (A), the aneurysm region is imaged before clipping of the aneurysm sack, and in the lower image (B), the aneurysm region is imaged after clipping. In addition to the BFI image, the corresponding CFI and the composite 3-D scene are given in the smaller upper right and left views respectively.

Before clipping, the flow direction can be observed from the speckle pattern movement in the median artery as well as the aneurysm sack and the distal branches. In the aneurysm sack, the flow direction can be observed to be of circular form. The velocity magnitude in the middle cerebral artery (M1 segment) can be observed to be substantially higher than in the distal branches (M2 segments) and in the aneurysm sack. After clipping, a clear flow direction was observed only in the middle cerebral artery and its distal branches.

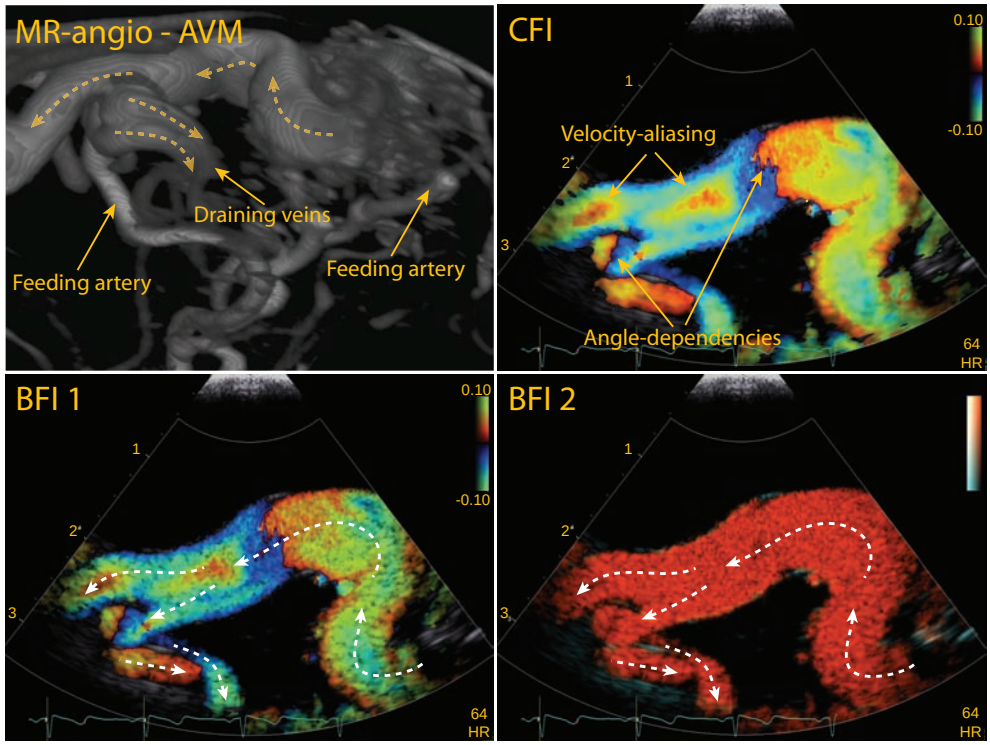


Figure 6.9: Image modality comparisons. *Upper left:* MR-angio image of AVM with feeding arteries and draining veins indicated by arrows. The dashed arrows further indicate the observed flow directions with BFI. *Upper right:* Image produced by the CFI modality. *Lower left:* The BFI modality combined with Doppler velocity and power estimates. *Lower right:* The BFI modality combined with Doppler power estimates only. The speckle movement in BFI is indicated by the dashed arrows. As can be observed, the color information provided by Doppler measurements do not satisfactory portrait the complete flow picture.

### Imaging of arteriovenous malformations

An example of an arteriovenous malformation imaged with BFI is shown in Fig. 6.11. In the upper image (A), a region covering parts of the AVM nidus and connected vessels is shown. The corresponding CFI image is given in the upper right view, and the composite 3-D scene is shown in the upper left view. The direction of flow and other flow characteristics such as velocity magnitude and pulsatility can be assessed from the speckle movement. In the lower image (B), a region covering parts of the AVM nidus and a feeding vessel is shown. As can be observed in the corresponding CFI view, the true directions of flow can be difficult to interpret based on the Doppler information alone.

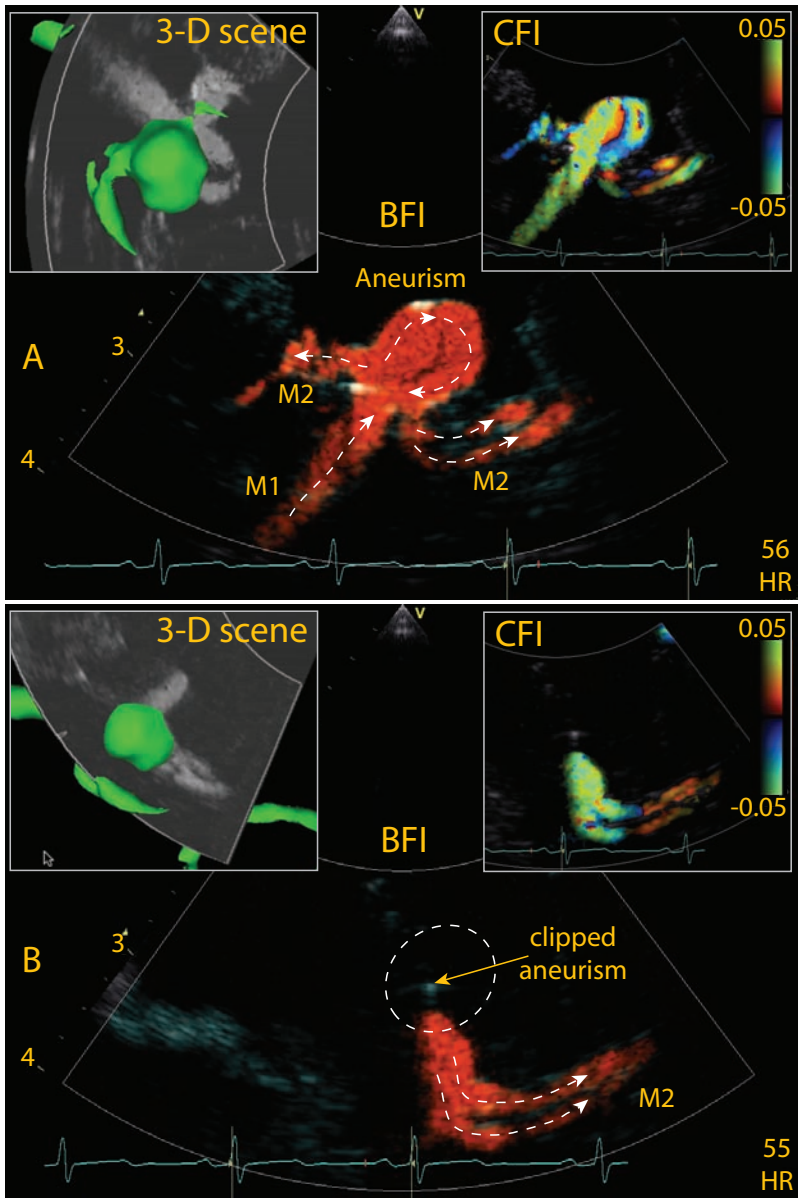


Figure 6.10: Imaging of a cerebral aneurysm. *A:* Before clipping, and *B:* After clipping of the aneurysm sack. The dashed arrows indicate the direction of speckle movement in the BFI images. The corresponding CFI image and synchronized navigation scene is shown in the upper right and left corner respectively.

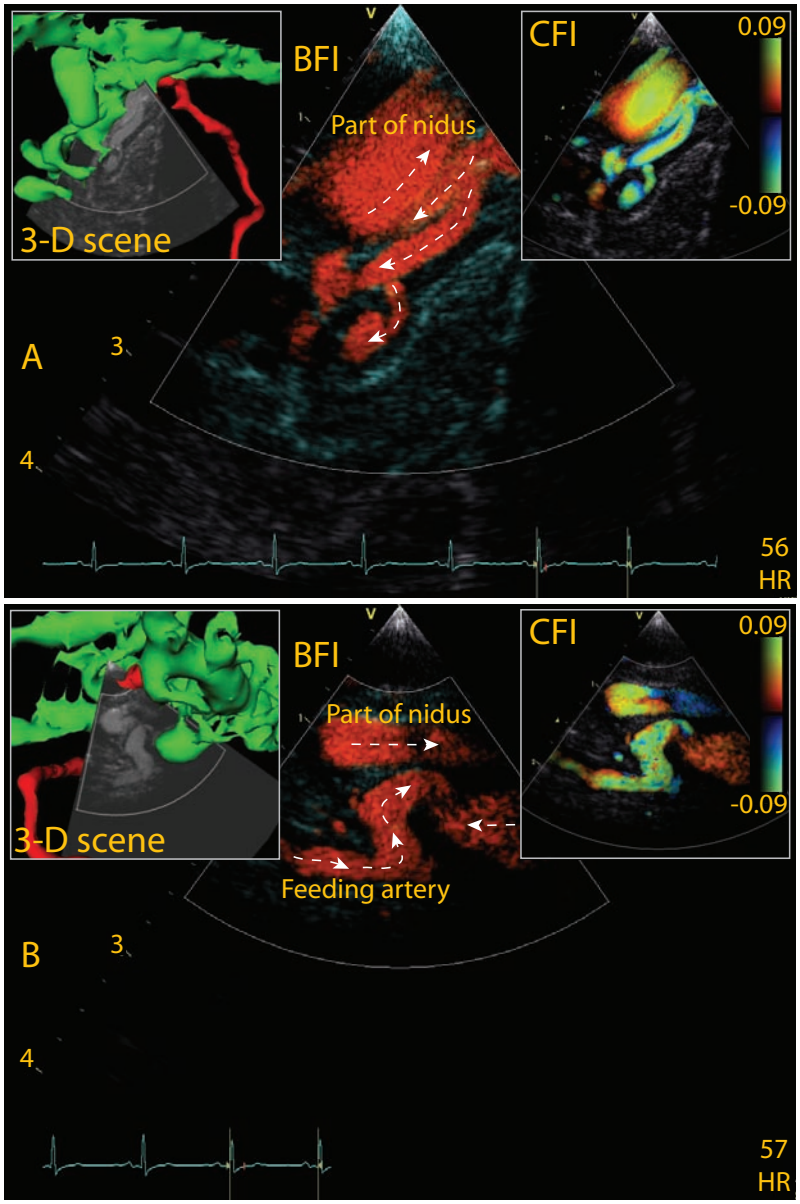


Figure 6.11: Two different image views of the same arteriovenous malformation. *A:* A view that covers parts of the nidus and surrounding vessels can be observed. The speckle movement observed is indicated by the dashed arrows. *B:* A view that covers parts of the nidus and a feeding artery. As can be observed in the corresponding CFI view, the true directions of flow can be difficult to interpret based on the Doppler information alone.

### 6.2.4 Discussion

The preliminary results from this study indicate that BFI can provide important information in the neurosurgical context, information that is not readily available using conventional CFI. The flow direction in the neurovascular vessels was properly visualized in all cases using BFI, and the use of navigation technology further allowed for identification of vessels of interest despite the presence of potential brain shift. Further, the surgeon found BFI to give a more intuitive image of the flow conditions compared to conventional CFI methods, requiring less interpretation. This is an important aspect in the operating room.

The flow conditions in the aneurysm and its surrounding vascular tree was properly visualized in all three cases, both before and after clipping. This allowed for quality control of sufficient flow in all distal arteries. Compared to CFI, having full two-dimensional directional information available made it easier to discern the true distal branches from nearby vessels. The speckle movement in the aneurysm branch was in two cases more difficult to perceive after clipping. This could be due to the more rigid vessel geometry and more complex flow conditions resulting from the clip placement. It could also be due to distortion effects of the reflected ultrasonic waves from the metallic clip.

The flow characteristics observed through the BFI speckle movement in the middle cerebral artery, the aneurysm sack, and the distal branches, correlated well to that described in previous studies using pulsed wave (PW) Doppler [16], contrast agent enhanced ultrasound imaging [15], and from computational and in-vitro studies [21, 24, 25]. In the aneurysm sack it could be observed that the flow was quite regular and non-turbulent. Also, a circular flow movement around the aneurysm sack could be observed. In the middle cerebral artery the flow velocity was observed to be of higher magnitude compared to the distal branches.

Work has previously been done to estimate how the flow pressure is distributed in saccular aneurysms using computer and in-vitro models [21, 25], to investigate where rupture is most probable to first occur. The speckle information provided by BFI can portrait local changes in the flow velocity in any direction of the image plane, and may therefore indicate areas where the flow pushes against the vessel wall. This subject has however not been investigated, and remains to be established. In [15], the movement of contrast microbubbles in the B-mode ultrasound images was tracked offline using digital particle image velocimetry (DPIV) methods, and quantified measurements of the flow velocity field in aneurysms could therefore be obtained. Speckle tracking procedures have previously been proposed to quantify flow velocity non-invasively in ultrasound [26]. These methods could be applicable for imaging the flow in saccular aneurysms, and should be further explored. As the flow movement is inherently three-dimensional, a tracking method should ideally be applied on 3-D ultrasound image acquisitions. This is an approach currently receiving research attention for the tracking of tissue using ultrasound [27–29].

When imaging arteriovenous malformations, the two-dimensional directional information provided by BFI has a clear clinical value. The aim is to identify the feeding vessels of the nidus, which is indicated directly by the flow direction. Navigated

BFI properly visualized the flow conditions in the nidus and the direction of flow in the complex vessel architecture connected to the AVM. This made it possible to discern between feeding arteries and draining veins with an increased confidence compared to CFI, and to control the complete nidus resection. Different flow characteristics could be observed in the nidus and connected vessels. In the nidus, a slow and more regular flow could be observed from the speckle movement. In the feeding vessels, a substantially increased velocity magnitude could further be seen.

The visualization of two-dimensional ultrasound image planes in the three-dimensional MR-angio scene made the two-dimensional ultrasonic flow assessment more easy and certain. Although brain shift complicated the assessment, the vessels surrounding the nidus and the aneurysm and corresponding vessels could still be identified and imaged using the navigated ultrasound modality. The segmentation algorithms used when processing the preoperative MR images sometimes missed smaller vessels of interest connected to the AVM. An update using three-dimensional intraoperative imaging with ultrasound could then have provided the additional information needed, as well as compensate for brain shift [2, 30]. The accuracy of the proposed method of navigated BFI was evaluated in a water bath, where the 3-D error was found to be on the order of 1 mm. The main error source was attributed to the ultrasound probe calibration [23, 31]. In addition, the tracking system is also associated with a small error. The main error sources associated with the MR model of the vascular tree, as depicted by the mismatch with corresponding vessels seen in the ultrasound image compared to the navigation scene, are related to patient registration and brain shift.

The navigated two-dimensional flow imaging modality proposed cannot replace the need for intraoperative three-dimensional imaging, but is considered very useful on its own, and should also be an option in future systems. As a surgical imaging tool the modality is based on simultaneous imaging and navigation. This increases the operating complexity compared to three-dimensional imaging, where the navigation can be performed after the image acquisition. An extension of the BFI modality to three dimensions is challenging due to the high frame rate demands of the speckle pattern image acquisition [22]. However, with future ultrasound technology, sufficient parallel receive beamforming may provide the means for approaching this concept.

Although indications are given of the usefulness of BFI in the neurosurgical context, a larger patient material is needed to properly establish the clinical value of the method. Vascular abnormalities located deep in the brain tissue have not yet been investigated using BFI. As the method's performance degrade with an increasing scan depth [22], it may not provide a suitable visualization for all patient cases. This subject should be further explored.

### 6.2.5 Conclusion

BFI seems to be a promising modality for flow visualization, which combined with navigated image acquisitions can portrait the true flow direction in cerebral aneurysms and AVMs, visualized in an intuitive manner. This property may provide the surgeon with a valuable tool for intraoperative quality control and safer interventions in

vascular neurosurgery. However, further work is needed to establish the clinical usefulness of the proposed imaging setup.

# References


[1] M. Reinges, H. Nguyen, T. Krings, B. Hútter, V. Rohde, and J. Gilsbach, "Course of brain shift during microsurgical resection of supratentorial cerebral lesions: limits of conventional neuronavigation," *Acta Neurochir. (Wien)*, vol. 146, pp. 369–77 discussion 377, 2004.

[2] G. Unsgaard, O. Rygh, T. Selbekk, T. Müller, F. Kolstad, F. Lindseth, and T. Hernes, "Intra-operative 3d ultrasound in neurosurgery," *Acta Neurochir. (Wien)*, vol. 148, pp. 235–53 discussion 253, 2006.

[3] A. Raabe, J. Beck, S. Rohde, J. Berkefeld, and V. Seifert, "Three-dimensional rotational angiography guidance for aneurysm surgery," *J. Neurosurg.*, vol. 105, pp. 406–411, 2006.

[4] B. Albayrak, A. Samdani, and P. Black, "Intra-operative magnetic resonance imaging in neurosurgery," *Acta Neurochir. (Wien)*, vol. 146, pp. 543–56 discussion 557, 2004.

[5] C. Nimsky, O. Ganslandt, B. von Keller, and R. Fahlbusch, "Intraoperative high-field mri: anatomical and functional imaging," *Acta Neurochir. Suppl. (Wien)*, vol. 98, pp. 87–95, 2006.

[6] A. Gronningsaeter, A. Kleven, S. Ommedal, T. Aarseth, T. Lie, F. Lindseth, T. Langø, and G. Unsgård, "Sonowand, an ultrasound-based neuronavigation system," *Neurosurgery*, vol. 47, pp. 1373–9 discussion 1379–80, 2000.

[7] W. Tirakotai, D. Miller, S. Heinze, L. Benes, H. Bertalanffy, and U. Sure, "A novel platform for image-guided ultrasound," *Neurosurgery*, vol. 58, pp. 710–8 discussion 710–8, 2006.

[8] V. Coenen, T. Krings, J. Weidemann, F. Hans, P. Reinacher, J. Gilsbach, and V. Rohde, "Sequential visualization of brain and fiber tract deformation during intracranial surgery with three-dimensional ultrasound: an approach to evaluate the effect of brain shift," *Neurosurgery*, vol. 56, pp. 133–41 discussion 133–41, 2005.

[9] U. Sure, L. Benes, O. Bozinov, M. Woydt, W. Tirakotai, and H. Bertalanffy, "Intraoperative landmarking of vascular anatomy by integration of duplex and

doppler ultrasonography in image-guided surgery. technical note," *Surg. Neurol.*, vol. 63, pp. 133–41 discussion 141–2, 2005.

[10] I. Reinertsen, F. Lindseth, G. Unsgaard, and D. Collins, "Clinical validation of vessel-based registration for correction of brain-shift," *Submitted to Medical Image Analysis*, 2006.

[11] I. Rasmussen, F. Lindseth, O. Rygh, E. Berntsen, T. Selbekk, J. Xu, T. Hernes, E. Harg, A. Håberg, and G. Unsgaard, "Functional neuronavigation combined with intra-operative 3d ultrasound: Initial experiences during surgical resections close to brain areas and future directions in automatic brain shift compensation of preoperative data," *Submitted to Acta Neurochirurgica*, 2006.

[12] O. Rygh, T. N. Hernes, F. Lindseth, T. Selbekk, T. B. Muller, and G. Unsgaard, "Intraoperative navigated 3-dimensional ultrasound angiography in tumor surgery," *Surg. Neurol.*, vol. 66, pp. 581–592, 2006.

[13] I. Feuerberg, C. Lindquist, M. Lindqvist, and L. Steiner, "Natural history of postoperative aneurysm rests," *J. Neurosurg.*, vol. 66, pp. 30–34, 1987.

[14] T. Alexander, R. Macdonald, B. Weir, and A. Kowalczuk, "Intraoperative angiography in cerebral aneurysm surgery: a prospective study of 100 craniotomies," *Neurosurgery*, vol. 39, pp. 10–7 discussion 17–8, 1996.

[15] T. Hölscher, J. Rodriguez-Rodriguez, W. Wilkening, J. Lasheras, and H. U, "Intraoperative brain ultrasound: a new approach to study flow dynamics in intracranial aneurysms," *Ultrasound Med. Biol.*, vol. 32, pp. 1307–1313, 2006.

[16] J. Gilsbach and W. Hassler, "Intraoperative doppler and real time sonography in neurosurgery," *Neurosurg. Rev.*, vol. 7, pp. 199–208, 1984.

[17] J. Rubin, M. Hatfield, W. Chandler, K. Black, and M. DiPietro, "Intracerebral arteriovenous malformations: intraoperative color doppler flow imaging," *Radiology*, vol. 170, pp. 219–222, 1989.

[18] M. Woydt, K. Greiner, J. Perez, A. Krone, and K. Roosen, "Intraoperative color duplex sonography of basal arteries during aneurysm surgery," *J. Neuroimaging*, vol. 7, pp. 203–207, 1997.

[19] M. Woydt, J. Perez, J. Meixensberger, A. Krone, N. Soerensen, and K. Roosen, "Intra-operative colour-duplex-sonography in the surgical management of cerebral av-malformations," *Acta Neurochir. (Wien)*, vol. 140, pp. 689–698, 1998.

[20] G. Unsgaard, S. Ommedal, O. Rygh, and F. Lindseth, "Operation of arteriovenous malformations assisted by stereoscopic navigation-controlled display of preoperative magnetic resonance angiography and intraoperative ultrasound angiography," *Neurosurgery*, vol. 56, pp. 281–90 discussion 281–90, 2005.

[21] G. Cantón, D. Levy, and J. Lasheras, "Hemodynamic changes due to stent placement in bifurcating intracranial aneurysms," *J. Neurosurg.*, vol. 103, pp. 146–155, 2005.

[22] L. Løvstakken, S. Bjærum, D. Martens, and H. Torp, "Blood flow imaging - a new real-time, 2-d flow imaging technique," *IEEE Trans. Ultrason., Ferroelec., Freq. Contr.*, vol. 53, pp. 289–299, 2006.

[23] L. Mercier, T. Langø, F. Lindseth, and D. Collins, "A review of calibration techniques for freehand 3-d ultrasound systems," *Ultrasound Med. Biol.*, vol. 31, pp. 449–471, 2005.

[24] C. Gonzalez, Y. Cho, H. Ortega, and J. Moret, "Intracranial aneurysms: flow analysis of their origin and progression," *AJNR. Am. J. Neuroradiol.*, vol. 13, pp. 181–188, 1992.

[25] J. Boissonnat, R. Chaine, P. Frey, G. Malandain, S. Salmon, E. Saltel, and M. Thiriet, "From arteriographies to computational flow in saccular aneurisms: the inria experience," *Med. Image Anal.*, vol. 9, pp. 133–143, 2005.

[26] L. Bohs, B. Geiman, M. Anderson, S. Gebhart, and G. Trahey, "Speckle tracking for multi-dimensional flow estimation," *Ultrasonics*, vol. 38, pp. 369–375, 2000.

[27] G. Bashford and O. von Ramm, "Ultrasound three-dimensional velocity measurements by feature tracking," *Ultrasonics, Ferroelectrics and Frequency Control, IEEE Transactions on*, vol. 43, pp. 376–384, 1996.

[28] X. Chen, H. Xie, R. Erkamp, K. Kim, C. Jia, J. Rubin, and M. O'Donnell, "3-d correlation-based speckle tracking," *Ultrason. Imaging*, vol. 27, pp. 21–36, 2005.

[29] F. Veronesi, C. Corsi, E. Caiani, A. Sarti, and C. Lamberti, "Tracking of left ventricular long axis from real-time three-dimensional echocardiography using optical flow techniques," *IEEE Trans. Inf. Technol. Biomed.*, vol. 10, pp. 174–181, 2006.

[30] F. Lindseth, J. Kaspersen, S. Ommedal, T. Langø, J. Bang, J. Hokland, G. Unsgaard, and T. Hernes, "Multimodal image fusion in ultrasound-based neuronavigation: improving overview and interpretation by integrating preoperative mri with intraoperative 3d ultrasound," *Comput. Aided Surg.*, vol. 8, pp. 49–69, 2003.

[31] F. Lindseth, T. Langø, J. Bang, and T. N. Hernes, "Accuracy evaluation of a 3d ultrasound-based neuronavigation system," *Comput. Aided Surg.*, vol. 7, pp. 197–222, 2002.

## 6.3 Application no. 3:

# Blood Flow Imaging - A new angle-independent ultrasound modality for the visualization of flow in atrial septal defects in children

Siri Ann Nyrnes[1], Lasse Løvstakken[2], Hans Torp[2], and Bjørn Olav Haugen[2]
[1] Dept. of Pediatrics,University Hospital of Trondheim, Norway
[2] Dept. of Circulation and Medical Imaging, NTNU, Norway

### 6.3.1 Introduction

An atrial septal defect (ASD) is an abnormal hole in the septum between the right and left atria of the heart. Oxygenated blood from the left atrium passes through the hole and mixes with deoxygenated blood in the right atrium. This results in an increased blood flow to the right ventricle and lungs. An ASD is a congenital heart anomaly, accounting for approximately 7-12 percent of all congenital heart disorders [1, 2]. The defect is often asymptomatic until adulthood, and is one of the most common congenital cardiac anomalies in adults [3].

The functional consequences of the defect are related to the anatomic location, its size, and the presence or absence of other cardiac anomalies. Potential complications include pulmonary hypertension, right ventricular failure, paradoxical embolization, cerebral abscess, and atrial arrhythmias [1, 3]. Approximately 70 percent of all ASDs are secundum defects, which may close spontaneously, remain unchanged or enlarge as the child grows [4–6]. When ASDs are clinically significant, follow up with echocardiography is mandatory to follow the hemodynamic consequences, to ensure that closure can be done at an optimal time, or to confirm spontaneous closure.

Transthoracic echocardiography (TTE) combined with color flow imaging (CFI) is diagnostic in the majority of patients with ASD [7], providing dynamic images of the atrial septum anatomy and flow conditions in multiple planes. Transesophageal echocardiography (TEE) provide better images of the interatrial septum compared to TTE [8, 9]. But TEE applicability is limited by the need for general anesthesia in children, and is mostly used to guide catheter closure. Recent studies have also presented real-time 3-D echocardiography [10] and magnetic resonance imaging (MRI) [11, 12] as useful imaging modalities. But the need for sedation and the fact that these modalities are time consuming limits the use of these methods in daily clinical practice. Despite of all new modalities for ASD-visualization, 2-D TTE still is the most cost-effective and commonly used technique for ASD imaging.

To obtain a sure diagnosis of ASD with TTE, one often have to rely on the flow images provided by CFI. However, due to a false coloring of the interatrial septum from overlapping color and B-mode images (color blooming artifacts), the flow through atrial septal defects are not always easy to determine, especially when 2-D images are suboptimal and when defects are small. Also, Doppler-shift techniques are only able to

measure velocities along the ultrasound beam, and are thus angle dependent. Often a priori knowledge of the anatomy and ultrasound beam angle is required to interpret the information presented. Further, when the Nyquist limit for blood velocity is reached, aliasing artifacts will obscure the true velocity and the direction of flow [13].

The Blood Flow Imaging (BFI) modality provides, in addition to quantitative Doppler measurements, angle-independent directional flow information not limited by aliasing, at a higher frame rate than CFI [14]. In this study we investigate if BFI can more properly portrait the ASD flow, and thereby increase the certainty of diagnosis of ASD in children.

### 6.3.2 Materials and methods

#### Patient material

This pilot study was performed at the Pediatric Department, University Hospital of Trondheim, Norway. A total of 13 children with the diagnosis of ASD were evaluated between March and August 2006. The inclusion criterion was ASD sized 4 mm or more at the time of diagnosis. Patients were recruited in the outpatient clinics and from the hospital ward, and both newly diagnosed and previously diagnosed patients were included. The reason for referral to a pediatric cardiologist in most of the patients was the presence of a heart murmur. In one patient, hemiparesis and cerebral infarction led to further investigation with echocardiography. One patient previously diagnosed having ASD was excluded due to late closure of the defect discovered at the time of study inclusion.

An ethical committee approval was obtained, and the parents of all study subjects provided written informed consent for participation in the study.

#### Data acquisition and processing

The blood flow through the atrial septal defects was first studied in a conventional TEE examination using CFI, establishing the presence and size of the ASD. We further supplemented with BFI as a part of the same examination. A pediatric cardiologist and an accompanying ultrasound technician performed the scans. Subcostal views were utilized because this imaging plane has been shown to be most sensitive [15]. All the TTEs were performed using a GE Vingmed Vivid 7 (GE Vingmed, Horten, Norway) with a GE M4S cardiac probe (GE Healthcare, Waukesha, USA). An example of B-mode image quality obtained is given in Fig. 6.12.

When all patient data had been collected, CFI and BFI cineloops for each patient were prepared offline based on the same data obtained in the BFI recording for side-by-side comparisons. The color image information presented was therefore identical in both modalities.

Two different cineloops were prepared for review for each modality. In one cineloop the color images were first optimized for best possible visualization of the flow through the ASD for a given case. In a second cineloop, the amount of flow gain was increased to simulate color blooming artifacts often present when using CFI. This concept

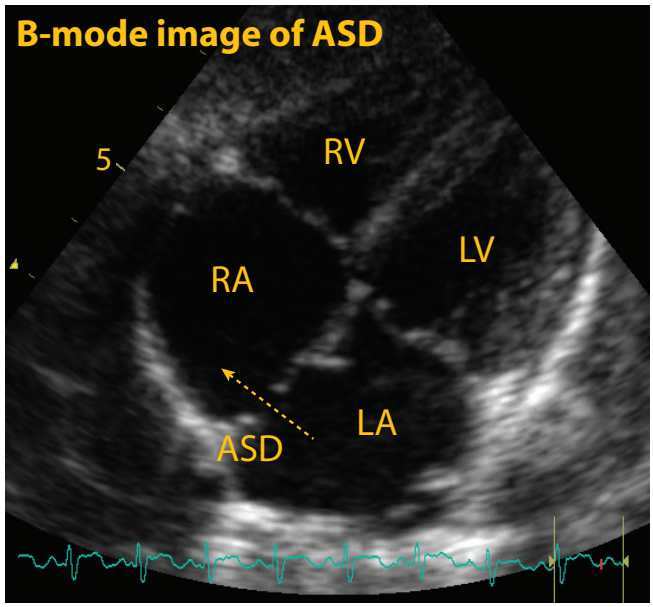


Figure 6.12: Ultrasound B-mode image quality obtained. The anatomy of and the atrial septal defect has been indicated. Oxygen rich flow from the systemic left side flows across the ASD to the pulmonary system, decreasing the overall function of the heart.

was introduced in order to evaluate the potential of BFI when the CFI images were suboptimal.

### Data analysis

The cineloops were independently reviewed by two pediatric cardiologists, one adult cardiologist and one physician with ultrasound research experience, who all were otherwise uninvolved in the study. The two pediatric cardiologists had no previous experience with BFI, but were introduced to the concept prior to evaluation. The other observers were familiar with the technique from vascular applications.

The images from the two modalities were presented to the observers in random order, and they were asked to review the image information by answering the following question:

**Question:** Based on the flow information presented, how certain are you that there is flow going between the atria?

The observer certainty was scored from 0-100. To quantify the visual evaluation of the observers a visual analogue scale (VAS) was employed, which previously have been used in evaluations subjective matters such as image quality. The four observer evaluations were analyzed separately.

#### Statistical analysis

The null hypothesis was formulated:

$H_0$ : There is no difference between CFI and BFI for the assessment of interatrial flow.

The recorded scores for the two image modalities were compared using the exact two-tailed Wilcoxon signed-rank test for paired samples [16]. The level of significance was chosen at $p < 0.05$. The analysis was done independently for the two cases of optimal and suboptimal color images. The statistical analysis and plotting was done in the numerical MATLAB software with the statistics toolbox (The MathWorks Inc., Natick, USA).

### 6.3.3 Results

#### Patient Characteristics

The patient material is described in Table 6.1. One patient had a primum ASD and the others had secundum defects. The ASD size ranged from 2-9 mm. Two of the patients had two defects. One patient had a bidirectional shunt, the others had left-to-right shunting across the ASD. In one patient the recordings with BFI revealed two ASDs and not one as first suspected in the prior CFI recording. Eight of the patients were girls. Seven patients had additional cardiac anomalies. One of the patients had total atrioventricular (AV) block, while the others had sinusrythm. Three patients had significant right ventricular volume overload. The 12 months old girl had experienced stroke, and had a 5 mm secundum ASD.

#### ASD flow imaging

All ASDs visualized using CFI in the examinations were confirmed using BFI. In one patient the recordings with BFI revealed two ASDs and not one as first suspected in the prior CFI recording. BFI imaging prolonged the echocardiographic examination with approximately five minutes. No children needed sedation during the ultrasound examination.

*Example 1 - double ASD:* In one patient, a double ASD was present which had not detected in a previous examination using TTE with CFI. Using BFI however, it was more clearly visualized. An optimized image of using CFI and BFI of this case is shown in Fig. 6.13. The ASDs are indicated in the CFI image to the left. The arrows in the BFI image to the right indicate the direction of flow as visualized by the speckle pattern movement in BFI. As in many cases, the atrial septum anatomy in the frame shown is almost completely covered by the color image.

*Example 2 - 9mm ASD:* In this case, a relatively large ASD was present. An optimized CFI and BFI image is shown in Fig. 6.14. As can be seen, again the color image covers the septum almost completely. The extra information provided by the speckle movement in BFI, may here offer an increased certainty that apparent flow across the atrial septum is not due to color artifacts.

**Table 6.1: Patient characteristics**

| # | Age | **Diagnosis** | **ASD size** | **Other cardiac anomalies** |
|---|---|---|---|---|
| 1 | 9 years | Secundum | 7 mm | Small patent ductus arteriosus |
| 2 | 12 months | Secundum | 5 mm | |
| 3 | 22 months | Secundum | 4 and 2 mm | Pulmonary hypertension |
| 4 | 4 months | Primum | 6 mm | Atrioventricular septal defect |
| 5 | 1 month | Secundum | 4 mm | Muscular ventricular septum defect |
| 6 | 13 months | Secundum | 3 mm | Pulmonary valve stenosis |
| 7 | 19 months | Secundum | 4 mm | Pulmonary valve stenosis |
| 8 | 2 weeks | Secundum | 4 mm | Perimembranous VSD |
| 9 | 2 months | Secundum | 3 mm | |
| 10 | 3 years | Secundum | 9 mm | |
| 11 | 21 months | Secundum | 6 and 3 mm | |
| 12 | 5 days | Secundum | 4 mm | Grade III atrioventricular block |
| 13 | 6 weeks | Secundum | 4 mm | |

#### Observer evaluations

The four observer evaluations are presented in Fig. 6.15. When the color image was optimized for each clip, the certainty of interatrial flow was significantly higher for two of the observers (p-values are given in the figure). When the color images were suboptimal with regards to color blooming, the p-values decreased in the favor of BFI for all observers, and the certainty that interatrial flow was present became significantly higher for three of the observers.

### 6.3.4 Discussion

This study is to the authors knowledge the first to evaluate BFI in cardiac imaging. The results obtained indicate that the new angle-independent BFI modality may improve the visualization of blood flow trough the atrial septum in children compared to the conventional CFI method.

As BFI adds the speckle images to the Doppler images available with CFI, all information available in previous examinations using CFI is still provided. The added speckle movement information provided by BFI may have several advantages when imaging ASD flow. As the ASD flow only occurs during a limited time interval of the cardiac cycle, the frame rate should be high in order to properly capture these events. The limited frame rate in CFI may then be insufficient. The speckle

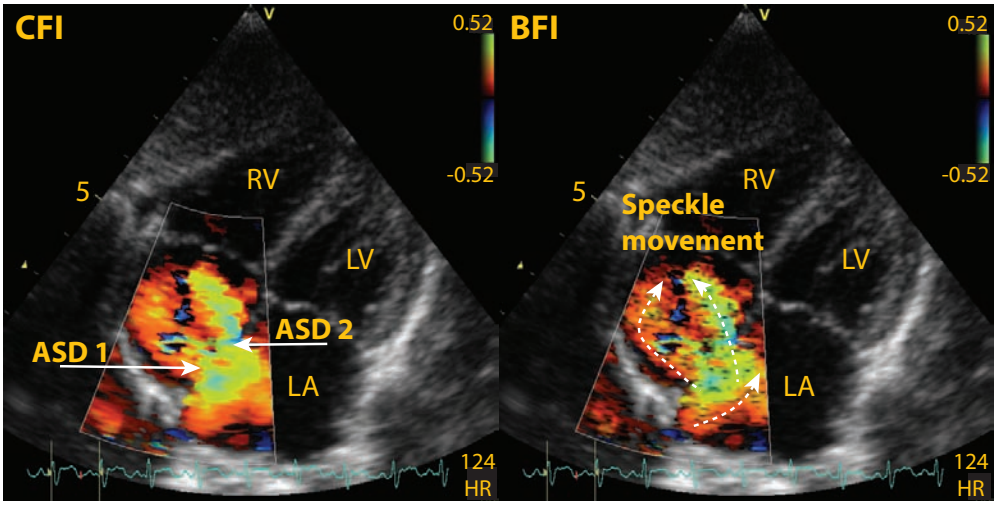


Figure 6.13: Imaging of a double ASD with CFI (left) and BFI (right) respectively. The two ASDs are indicated by the dashed arrows in the CFI image. The arrows in the BFI image indicate the direction of flow as visualized by the speckle pattern movement.

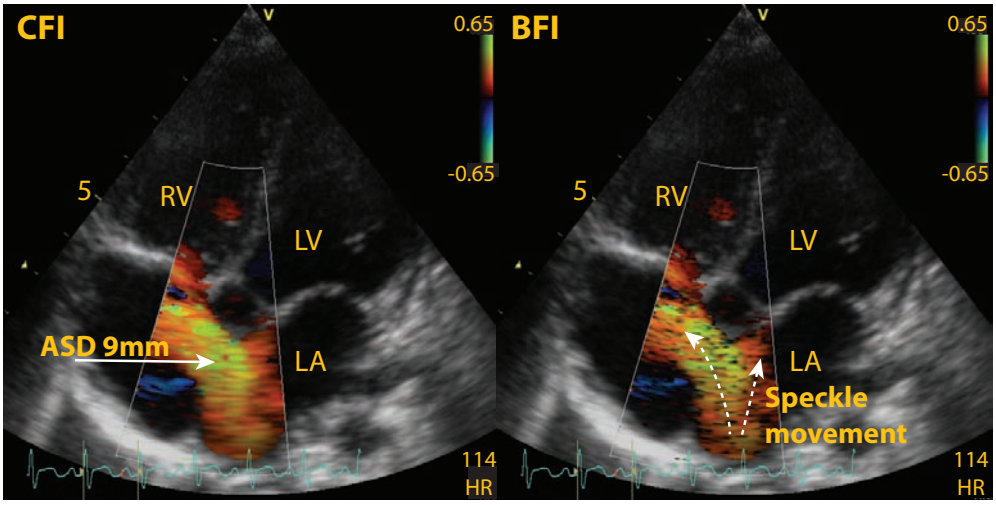


Figure 6.14: Imaging of a 9 mm ASD with CFI (left) and BFI (right) respectively. As can be observed, the color image almost covers the complete atrial septum. The dashed arrows in the BFI image indicate the direction of flow as visualized by the speckle pattern movement.

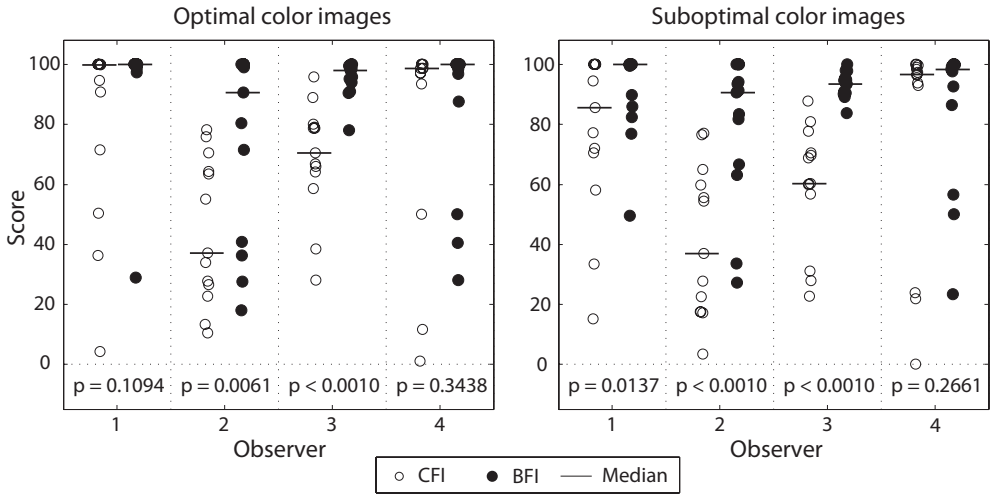


Figure 6.15: Dot plots showing the observer assessments of BFI versus CFI for the imaging of ASD flow. The corresponding p-values are indicated in the plots. Random noise was added to enhance the visual quality.

movement provided by BFI has an increased frame rate compared to the color images. This increased amount of information is especially important when imaging children, due to their higher heart rates compared to adults. Further, BFI is able to provide information of flow in any direction of the image plane, and therefore provide more detailed information of interatrial blood flow than CFI alone. This may increase the certainty of ASD diagnosis, especially when the color images are suboptimal. In one particular patient in this study, BFI imaging revealed two ASDs and not one defect as first suspected in a prior CFI examination. This is important information for instance when planning catheter based device closure.

Several aspects make the visualization of speckle movement more challenging in cardiac imaging. As the BFI technique relies on human perception of speckle movement between images, it is dependent on a degree of similarity between the speckle images. These similarities are degraded by flow accelerations and out-of-plane flow movement, and the speckle movement of blood flow inside the heart may therefore be harder to perceive than in peripheral vessels [14]. The BFI speckle visualization is further dependent on beam interleaving techniques for obtaining sub-images of the speckle pattern at a high frame rate [14]. The sub-image width then decrease with an increasing scan depth, and with an increasing velocity scale as determined by the pulse repetition frequency. In adult TTE imaging, the width of the sub-images may become too small for the perception of the lateral speckle movement. In pediatric imaging, the ultrasound transducer is positioned closer to the heart, and we found that both the axial and lateral speckle pattern movement of flow in the atria could be visualized.

Several investigators have used CFI to estimate the size of the ASD [7, 17]. But even if the CFI jet-visualization width give an indication of ASD size, reliability of

using color images for predicting size is limited by variability in gain settings and alignment of the scanning plane relative to the shunt [1]. In addition, estimation of the jet-width diameter does not take into account shunt flow due to associated anomalous pulmonary connections. We do not know if the use of BFI may improve the sizing of ASDs, but this study indicates that a better visualization of blood flow is obtained, especially when there are color blooming artifacts.

2D-TTE-CFI has limitations in detecting small secundum ASD, sinus venosus defects and associated anomalous pulmonary venous return. TEE is superior to TTE for imaging these types of ASDs in adults [9]. In children, routine transthoracic studies are generally adequate for diagnosis, but TEE may be used in patients with poor image quality. Also, TEE imaging of the entire heart is the preferred modality during guidance of catheter-based treatments of atrial septal defects in children [18]. The use of TEE and BFI may provide an improved visualization of blood flow. As the probe is then placed even closer to the heart, a more detailed speckle pattern movement may then also be visualized. To establish this, further studies are necessary.

The images in this study were presented to three experienced cardiologists and one physician with cardiac ultrasound experience from research. The four observers were otherwise uninvolved in the study, and should therefore be objective in their evaluation. When the color images were suboptimal (i.e. color blooming artifacts were created), the rating differences between BFI and CFI were enlarged in favor of BFI for all the tree cardiologists. This finding indicates that BFI may be especially useful in situations with suboptimal images such as in presence of color blooming artifacts, which often occurs in daily clinical practice.

#### Limitations of the study

A limitation of the study was that the images that were presented for the observers did not include a control group without ASD. We therefore do not know if false positive findings may occur when using BFI. Previous studies with CFI have not indicated problems with false positive findings. On the contrary, false negative results in the detection of ASD have been reported [9], and BFI may help further reduce the amount of false negative findings. No patients in our study had sinus venosus defect or coronary sinus defect, and further investigations remains to find out if the use of BFI may simplify the diagnosis of these defects. BFI is promising in the visualization of known ASD, but the applicability of BFI during routine screening echocardiography remains to be evaluated. Further investigation is necessary to study the sensitivity and specificity of the method. To accomplish this, BFI should be compared to the gold standard of ASD visualization which at present is balloon sizing during catheterization.

### 6.3.5 Conclusion

Using BFI to visualize ASD flow in children can be done as part of an ordinary 2D-TTE examination. The images can be done quickly with no need for post processing offline and without sedation. This pilot study indicates that BFI gives a better visualization of blood flow through the atrial septum than conventional CFI, and we believe the

method could be a useful supplement to CFI in the diagnosis and follow up of children with ASD.

**Acknowledgements**

We thank the observers for their efforts. We also thank Eirik Skogvoll for advice on statistics.

# References


[1] R. Anderson, E. Baker, F. Macartney, M. Rigby, E. Shinebourne, and M. Tynan, *Peadiatric Cardiology, 2nd edition*. London: Churchill Livingstone, 2001.

[2] S. Stephensen, G. Sigfusson, H. Eiriksson, J. Sverrisson, B. Torfason, A. Haraldsson, and H. Helgason, "Congenital cardiac malformations in iceland from 1990 through 1999," *Cardiol. Young*, vol. 14, pp. 396–401, 2004.

[3] J. Therrien, G. Webb, D. Zipes, and P. Libby, *Congenital heart disease in adults*. Philadelphia, PA: W.B. Saunders Company, 2004.

[4] H. Helgason and G. Jonsdottir, "Spontaneous closure of atrial septal defects," *Pediatr. Cardiol.*, vol. 20, pp. 195–199, 1999.

[5] C. McMahon, T. Feltes, J. Fraley, J. Bricker, R. Grifka, T. Tortoriello, R. Blake, and L. Bezold, "Natural history of growth of secundum atrial septal defects and implications for transcatheter closure," *Heart*, vol. 87, pp. 256–259, 2002.

[6] A. Hanslik, U. Pospisil, U. Salzer-Muhar, S. Greber-Platzer, and C. Male, "Predictors of spontaneous closure of isolated secundum atrial septal defect in children: a longitudinal study," *Pediatrics*, vol. 118, pp. 1560–1565, 2006.

[7] F. Faletra, S. Scarpini, A. Moreo, G. Ciliberto, P. Austoni, F. Donatelli, and V. Gordini, "Color doppler echocardiographic assessment of atrial septal defect size: correlation with surgical measurements," *J. Am. Soc. Echocardiogr.*, vol. 4, pp. 429–434, 1991.

[8] K. Morimoto, M. Matsuzaki, Y. Tohma, S. Ono, N. Tanaka, H. Michishige, K. Murata, Y. Anno, and R. Kusukawa, "Diagnosis and quantitative evaluation of secundum-type atrial septal defect by transesophageal doppler echocardiography," *Am. J. Cardiol.*, vol. 66, pp. 85–91, 1990.

[9] D. Hausmann, W. Daniel, A. Múgge, G. Ziemer, and A. Pearlman, "Value of transesophageal color doppler echocardiography for detection of different types of atrial septal defect in adults," *J. Am. Soc. Echocardiogr.*, vol. 5, pp. 481–488, 1992.

[10] A. van den Bosch, D. T. Harkel, J. McGhie, J. Roos-Hesselink, M. Simoons, A. Bogers, and F. Meijboom, "Characterization of atrial septal defect assessed by real-time 3-dimensional echocardiography," *J. Am. Soc. Echocardiogr.*, vol. 19, pp. 815–821, 2006.

[11] Z. Wang, G. Reddy, M. Gotway, B. Yeh, and C. Higgins, "Cardiovascular shunts: Mr imaging evaluation," *Radiographics*, vol. 23 Spec No, pp. S181–S194, 2003.

[12] C. Piaw, O. Kiam, A. Rapaee, L. Khoon, L. Bang, C. Ling, H. Samion, and S. Hian, "Use of non-invasive phase contrast magnetic resonance imaging for estimation of atrial septal defect size and morphology: a comparison with transesophageal echo," *Cardiovasc. Intervent. Radiol.*, vol. 29, pp. 230–234, 2006.

[13] K. Ferrara and G. DeAngelis, "Color flow mapping," *Ultrasound in Medicine & Biology*, vol. 23, pp. 321–345, 1997.

[14] L. Løvstakken, S. Bjærum, D. Martens, and H. Torp, "Blood flow imaging - a new real-time, 2-d flow imaging technique," *IEEE Trans. Ultrason., Ferroelec., Freq. Contr.*, vol. 53, pp. 289–299, 2006.

[15] C. Shub, I. Dimopoulos, J. Seward, J. Callahan, R. Tancredi, T. Schattenberg, G. Reeder, D. Hagler, and A. Tajik, "Sensitivity of two-dimensional echocardiography in the direct visualization of atrial septal defect utilizing the subcostal approach: experience with 154 patients," *J. Am. Coll. Cardiol.*, vol. 2, pp. 127–135, 1983.

[16] B. Rosner, *Nonparametric methods, Fundamentals of Biostatistics, 5th edition*, pp. 331–353. Pacific Grove, USA: Duxbury, Brooks/Cole, 2000.

[17] C. Pollick, H. Sullivan, B. Cujec, and S. Wilansky, "Doppler color-flow imaging assessment of shunt size in atrial septal defect," *Circulation*, vol. 78, pp. 522–528, 1988.

[18] C. Kleinman, "Echocardiographic guidance of catheter-based treatments of atrial septal defect: transesophageal echocardiography remains the gold standard," *Pediatr. Cardiol.*, vol. 26, pp. 128–134, 2005.

## 6.4 Application no. 4:

# Blood Flow Imaging - Enhanced visualization of low-velocity peripheral flow for treatment of tendinosis

Agnar Tegnander[1], Lasse Løvstakken[2], and Hans Torp[2]
[1] Dept. of Orthopedics,University Hospital of Trondheim, Norway
[2] Dept. of Circulation and Medical Imaging, NTNU, Norway

### 6.4.1 Introduction

The treatment of tendinopathies has changed during the past years as a result of new knowledge of the pathophysiology. In 1995, Åström and Rausing reported histological findings from 163 operated patients with chronic Achilles tendinopathy [1]. The most important features were a lack of inflammatory cells and a poor healing response. They found however degenerative changes (tendinosis) characterized by abnormal fiber structure, focal hypercellularity, and vascular proliferation. It has also been suggested that this more accurately should be described as failed healing response due to mechanical overload. This process decreases tendon strength and leaves it less able to tolerate load and thus, vulnerable to further injury [2].

In 1998, Alfredson and co-workers reported good results after heavy-loaded eccentric calf muscle training for the treatment of chronic Achilles tendinosis [3]. They found later that in all patients with a painful nodular thickening of the Achilles tendon, blood vessels (neovascularisation) were seen in close relation to the widened part of the tendon [4]. In normal controls, no such blood vessels could be identified. Furthermore they showed with a microdialysis technique a significant increase of the neurotransmitter glutamate in Achilles tendinopathy suggesting formation of new nerves. Based on these studies Öhberg and Alfredson started with ultrasound-guided sclerosis of these neovessels, and documented good effect in 8 out of 10 patients [5]. Later several authors have shown neovascularisation in other tendons [6–10].

The detection of neovascularization and needle navigation has been based on flow visualization using ultrasound color flow imaging (CFI). This method has potential disadvantages when used in this context. When imaging peripheral flow the velocity of the surrounding tissue and flow may become comparable, resulting in disturbing flashing artifacts. Further, the current arbitration method used for mixing tissue and flow information in CFI may further conceal vessels of interest. In the Blood Flow Imaging (BFI) modality [11], a new transparent mixing technique is available, in which no flow information is lost. In this preliminary study we investigate the potential advantages of BFI compared to CFI for the visualization of neovascularisation and needle navigation in the treatment of tendinosis.

### 6.4.2 Materials and methods

#### Patient material

Nineteen patients with tendinopathy a mean duration of 40 months were asked to participate in this pilot study. The location and duration of symptoms were registered, and any earlier treatment was also noted. Patients with neovascularisation were also asked to participate in the sclerosing treatment with Polidocanol (Aethoxysklerol 1% from Kreussler Pharma, Germany). A written consent explaining the procedure and imaging technique was signed by all patients.

#### Data acquisition and processing

The ultrasound acquisition was performed using a GE Vivid 7 ultrasound scanner (GE Vingmed Ultrasound, Horten, Norway), with a M12L linear array probe (GE Healthcare, Waukesha, USA). Images and cineloops for both CFI and BFI were produced offline from the same data recording for comparisons.

### 6.4.3 Results

Thirteen men and 6 women were examined with both methods. They have had symptoms from 2 to 156 months (mean 40 months), and their mean age was 32 years (range 17-50). Ten of the patients had symptoms from the Patellar tendon (Jumper's knee), 8 from the Achilles tendon and 1 patient had symptoms from the origin of the extensor tendons of the forearm (tennis elbow). In 15 patients (79%) we found neovascularisation of the tendon with both CFI and BFI, and 4 (21%) did not show any in either method.

#### Case 1

Male alpine skier with symptoms of jumper's knee for 6 months. He reported pain in the proximal part of the Patella tendon with exercise and on palpation. He had earlier been treated with non-steroid anti-inflammatory drugs, acupuncture, friction massage, concentric and eccentric training programs including stretching. Fig. 6.16 shows images using CFI and BFI before, during, and immediate after first sclerosing therapy. Vessels details were more accurately portrayed using BFI, and flashing artifacts were less disturbing compared to CFI.

#### Case 2

Highly ranked Swedish male orienteering runner with Achilles tendinosis for 2 months. Treated with eccentric and concentric training programs, but still pain near the insertion of the tendon to the heel bone. Fig. 6.17 shows images using CFI and BFI before, during, and after an injection. Flashing artifacts occurred repeatedly during the probe navigation, needle guidance, and during injection. Imaging with BFI increased the certainty of blood vessel removal after of the procedure.

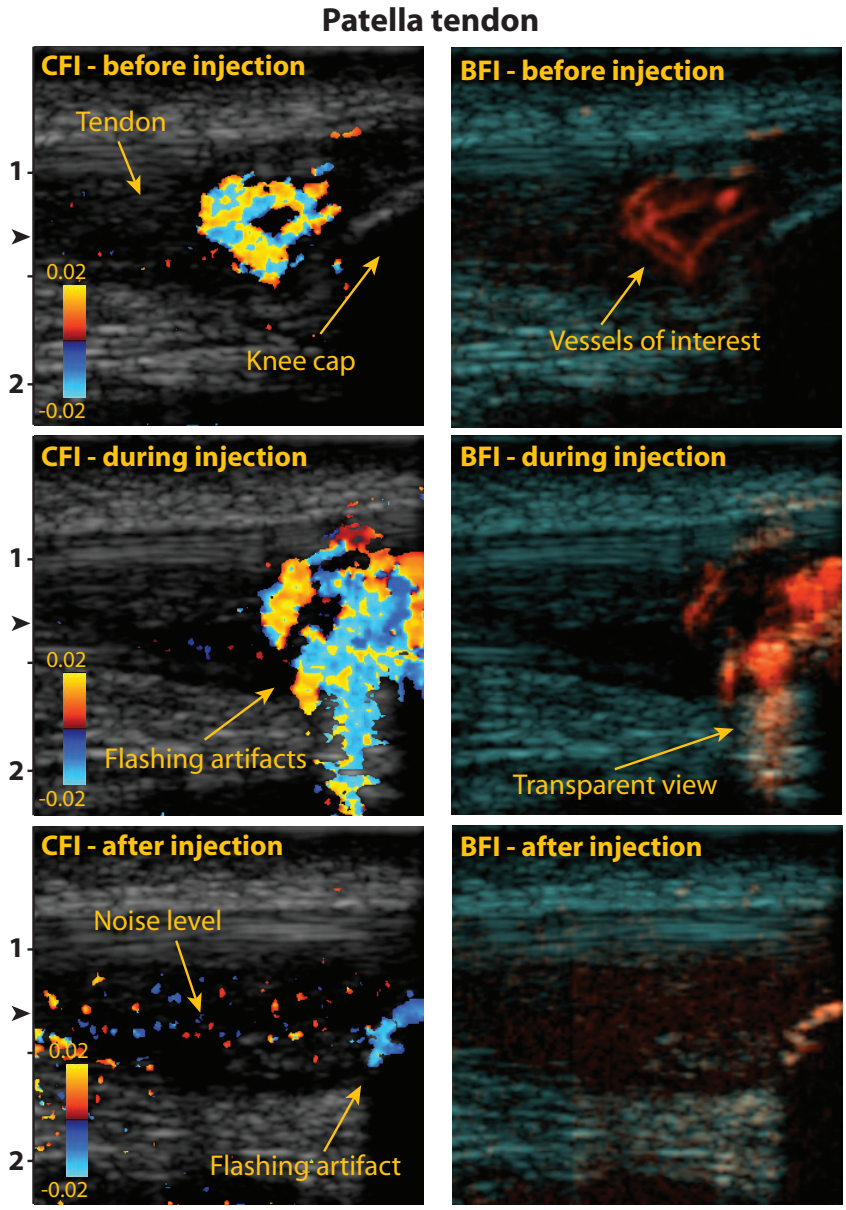


Figure 6.16: The intervention and imaging of a patella tendon before, during, and after the injection of sclerotic medium. In the top images, observe the spatial smearing of the color images in CFI compared to BFI. In the middle images, observe the difference in appearance of flashing artifacts for the two modalities. In the lower image, observe the appearance of the noise level in CFI compared to the transparent view in BFI.

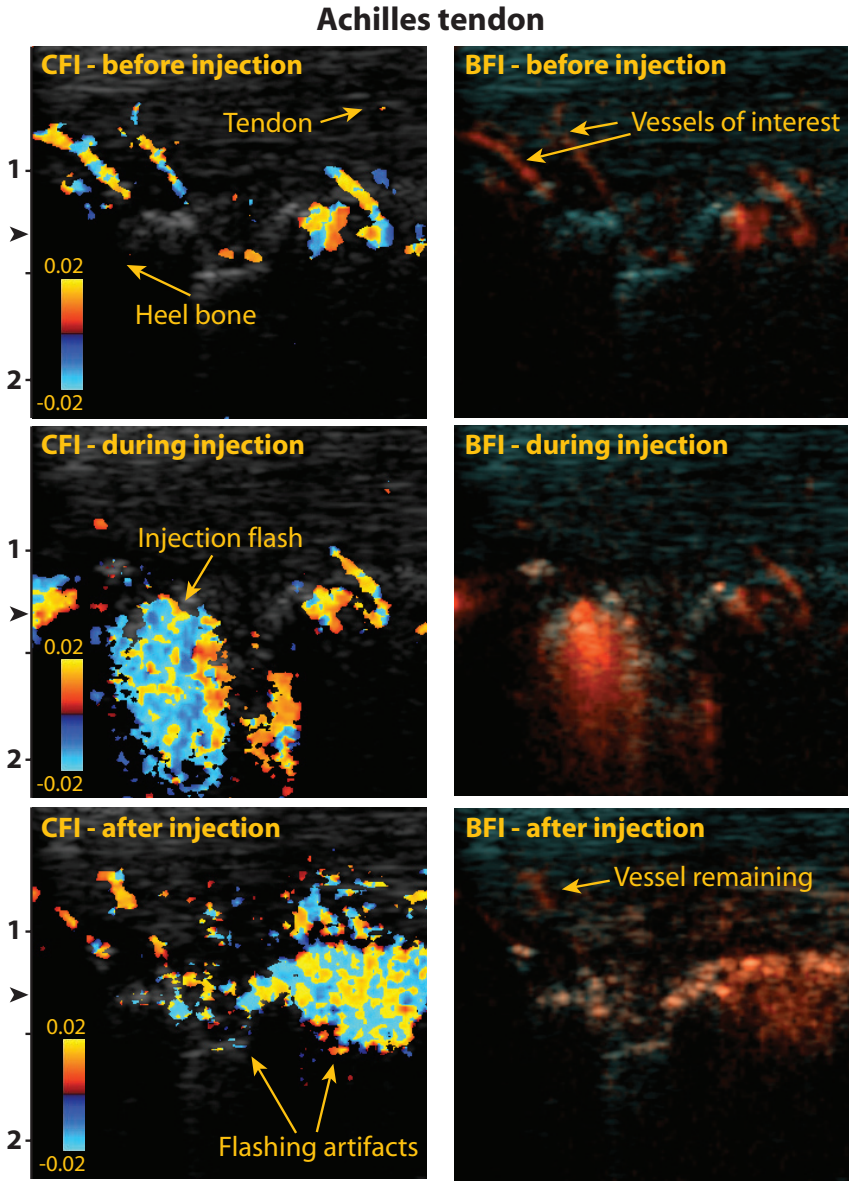


Figure 6.17: The intervention and imaging of an Achilles tendon before, during, and after the injection of sclerotic medium. Observer how the flashing artifacts may influence the detection of small vessels differently in CFI and BFI respectively. In BFI the tissue is still visible underneath the false coloring artifacts.

### 6.4.4 Discussion

Recent studies have shown promising results of sclerosing therapy in the treatment tendinosis in jumper's knee, Achilles, and tennis elbow conditions [6, 10, 12, 13], all studies reporting a satisfactory treatment of approximately 80% of the cases. In patients with unsatisfactory results, remaining neovascularisation has been reported [5, 12], even after as many as five sclerosing treatments. One reason for this could be due to limitations in the imaging of the low-flow neovessels, which prohibits a proper detection and needle guidance.

In our investigations, both CFI and BFI could be used to successfully image the small vessels using a high-frequency transducer operating at 7-14 MHz. One of the main imaging challenges was that small movements of the probe could potentially shift the tiny vessels in or out of the imaging plane. Due to the movement of the patient and challenges related to simultaneous imaging and needle guidance, a high degree of probe navigation was required during the investigation. Further, in order to be able to detect the low Doppler shifts, the imaging pulse repetition frequency (PRF) was set low ($< 500$ Hz). This made the imaging very susceptible to flashing artifacts from the relative tissue and probe movement, and also from the movement of the needle.

While CFI strictly visualized either flow or tissue information in a given image point, a transparent mixing of both was available in BFI. This transparent view helped reduce the impact of the flashing artifacts compared to CFI. Being able to view the underlying tissue, artifacts could more easily be identified, and areas of flow otherwise concealed could be observed. The artifacts further appeared less dramatic than with CFI, and it was possible to more properly navigate the needle tip while imaging.

The arbitration rules in CFI may further fail, and conceal areas of actual flow in favor of tissue, especially when imaging small vessels barely visible in the tissue B-mode image. In BFI, all flow information is present at all times, and this limitation is not present. Another advantage of the transparent view in BFI is that the flow gain can be increased until the noise level is apparent. The smooth appearance of noise did not influence the imaging, while further ensuring that no flow information was missed.

An advantage of the CFI display, is that a high contrast between tissue and flow information is given. The color visualization used for CFI was based on the mean Doppler frequency only, arguably the default mode on most commercial scanner systems. By also encoding the color using the Doppler power estimates, image noise can be shown in darker colors, and its appearance may then be reduced.

The BFI visualization used was based on the power-Doppler modality, and did not include any quantitative measurements of flow velocity or direction. Although angle-independent speckle pattern movement was also available, this had a limited value as it was often hard to perceive the speckle movement in the small vessels. It did however help discern real flow from artifacts, as the speckle movement in actual flow had a distinct direction, compared to a random movement for noise. A transparent modality including Doppler frequency information could be useful, and should be explored.

### 6.4.5 Conclusion

Both CFI and BFI could be used to image the small vessels in the treatment of tendinosis. The transparent view of flow and tissue information available in BFI is less influenced by flashing artifacts, and more properly allows for simultaneous imaging and needle guidance compared to CFI. As the flow information acquired is always visualized, the method further adds an increased confidence to a successful procedure.

# References


[1] M. Aström and A. Rausing, "Chronic achilles tendinopathy. a survey of surgical and histopathologic findings," *Clin. Orthop.*, pp. 151–164, 1995.

[2] J. Cook, K. Khan, and C. Purdam, "Achilles tendinopathy," *Man. Ther.*, vol. 7, pp. 121–130, 2002.

[3] H. Alfredson, T. Pietilá, P. Jonsson, and R. Lorentzon, "Heavy-load eccentric calf muscle training for the treatment of chronic achilles tendinosis," *Am. J. Sports Med.*, vol. 26, pp. 360–366, 1998.

[4] L. Ohberg, R. Lorentzon, and H. Alfredson, "Neovascularisation in achilles tendons with painful tendinosis but not in normal tendons: an ultrasonographic investigation," *Knee Surg. Sports Traumatol. Arthrosc.*, vol. 9, pp. 233–238, 2001.

[5] L. Ohberg and H. Alfredson, "Ultrasound guided sclerosis of neovessels in painful chronic achilles tendinosis: pilot study of a new treatment," *Br. J. Sports Med.*, vol. 36, pp. 173–5 discussion 176–7, 2002.

[6] E. Zeisig, L. Ohberg, and H. Alfredson, "Sclerosing polidocanol injections in chronic painful tennis elbow-promising results in a pilot study," *Knee Surg. Sports Traumatol. Arthrosc.*, vol. 14, pp. 1218–1224, 2006.

[7] M. Walther, S. Radke, S. Kirschner, V. Ettl, and F. Gohlke, "Power doppler findings in plantar fasciitis," *Ultrasound Med. Biol.*, vol. 30, pp. 435–440, 2004.

[8] H. Chiou, Y. Chou, J. Wu, C. Hsu, D. Huang, and C. Chang, "Evaluation of calcific tendonitis of the rotator cuff: role of color doppler ultrasonography," *J. Ultrasound Med.*, vol. 21, pp. 289–95 quiz 296–7, 2002.

[9] T. Torp-Pedersen, S. Torp-Pedersen, and H. Bliddal, "Diagnostic value of ultrasonography in epicondylitis," *Ann. Intern. Med.*, vol. 136, pp. 781–782, 2002.

[10] H. Alfredson, H. Harstad, S. Haugen, and L. Ohberg, "Sclerosing polidocanol injections to treat chronic painful shoulder impingement syndrome-results of a two-centre collaborative pilot study," *Knee Surg. Sports Traumatol. Arthrosc.*, vol. 14, pp. 1321–1326, 2006.

[11] L. Løvstakken, S. Bjaerum, D. Martens, and H. Torp, "Blood flow imaging–a new real-time, 2-d flow imaging technique," *IEEE Trans. Ultrason., Ferroelect., Freq. Contr.*, vol. 53, pp. 289–299, 2006.

[12] H. Alfredson and L. Ohberg, "Sclerosing injections to areas of neo-vascularisation reduce pain in chronic achilles tendinopathy: a double-blind randomised controlled trial," *Knee Surg. Sports Traumatol. Arthrosc.*, vol. 13, pp. 338–344, 2005.

[13] A. Hoksrud, L. Ohberg, H. Alfredson, and R. Bahr, "Ultrasound-guided sclerosis of neovessels in painful chronic patellar tendinopathy: a randomized controlled trial," *Am. J. Sports Med.*, vol. 34, pp. 1738–1746, 2006.